2018 SUMMER RESEARCH PROGRAM FOR HIGH SCHOOL JUNIORS

AT THE

UNIVERSITY OF ROCHESTER'S

LABORATORY FOR LASER ENERGETICS

STUDENT RESEARCH REPORTS

PROGRAM DIRECTOR

Dr. R. Stephen Craxton

2018 SUMMER RESEARCH PROGRAM FOR HIGH SCHOOL JUNIORS

AT THE

UNIVERSITY OF ROCHESTER'S

LABORATORY FOR LASER ENERGETICS

STUDENT RESEARCH REPORTS

PROGRAM DIRECTOR

Dr. R. Stephen Craxton

LABORATORY FOR LASER ENERGETICS
University of Rochester
250 East River Road
Rochester, NY 14623-1299

During the summer of 2018, 13 students from Rochester-area high schools participated in the Laboratory for Laser Energetics' Summer High School Research Program. The goal of this program is to excite a group of high school students about careers in the areas of science and technology by exposing them to research in a state-of-the-art environment. Too often, students are exposed to "research" only through classroom laboratories, which have prescribed procedures and predictable results. In LLE's summer program, the students experience many of the trials, tribulations, and rewards of scientific research. By participating in research in a real

environment, the students often become more excited about careers in science and technology. In addition, LLE gains from the contributions of the many highly talented students who are attracted to the program.

The students spent most of their time working on their individual research projects with members of LLE's scientific staff. The projects were related to current research activities at LLE and covered a broad range of areas of interest including computer modeling of implosion physics, experimental diagnostic modeling, cryogenic target characterization, physical chemistry, computational chemistry, laser beam modeling, laser flash-lamp diagnostics, web-based data analysis, and the adaption of a technique developed to visualize laser damage to high-school life-science education. The students, their high schools, their LLE supervisors, and their project titles are listed in the table. Their written reports are collected in this volume. By working through several iterations of their project reports, incorporating feedback from their supervisors and the Program Director, the students experience most of the steps involved in preparing a scientific paper for publication.

The students attended weekly seminars on technical topics associated with LLE's research. Topics this year included laser physics, fusion, holography, nonlinear optics, the National Ignition Facility, scientific measurement techniques, and pulsed power. The students also received safety training, learned how to give scientific presentations, and were introduced to LLE's resources, especially the computational facilities.

The program culminated on 29 August with the "High School Student Summer Research Symposium," at which the students presented the results of their research to an audience including parents, teachers, and LLE staff. Each student spoke for approximately ten minutes and answered questions. At the symposium LLE presented its 22nd annual William D. Ryan Inspirational

Teacher Award. The recipient this year was Mrs. Jennifer Vibber, a mathematics teacher at Penfield High School. This award honors a teacher, nominated by alumni of the LLE program, who has inspired outstanding students in the areas of science, mathematics, and technology. Mrs. Vibber was nominated by Claire Guo, a participant in the 2017 Summer Program.

A total of 377 high school students have participated in the program from its inception in 1989 through 2018. The students in 2018 were selected from approximately 50 applicants. Each applicant submitted an essay describing his or her interests in science and technology, a copy of his or her transcript, and a letter of recommendation from a science or math teacher.

In the past, several participants of this program have gone on to become scholars (formerly known as "semifinalists") and finalists in the prestigious Regeneron (formerly Intel) Science Talent Search. This tradition of success continued this year with the selection of Maia Raynor and Anirudh Sharma as two of the 300 Regeneron Scholars chosen from nearly 2000 applicants nationwide.

LLE plans to continue this program in future years. The program is strictly for students from Rochester-area high schools who have just completed their junior year. Application information is mailed to schools and placed on the LLE web site in January with an application deadline near the middle of March. For more information about the program, please contact Dr. R. Stephen Craxton at LLE.

Table I: High School Students and Projects—Summer 2018.

Name	High School	Supervisor	Project Title
Aditya Bhargava	Victor	M. J. Guardalben	Measurement Accuracy of the Harmonic Energy Diagnostic on OMEGA EP
Steven Booth	Brighton	W. A. Bittle and V. Anand	Analysis Tools for Current Characteristics of Pulse-Forming Networks Driving High-Energy Flash Lamps
Carwyn Collinsworth	Brighton	M. D. Wittman and D. H. Edgell	Real-Time X-Ray Analysis of Liquid-DT Fill Level in Full-Tube Capsules to Control Solid-Layer Thickness
Matthew Cufari	Pittsford Sutherland	P. B. Radha and O. M. Mannion	Modeling Charged-Particle Spectra to Diagnose Asymmetries in OMEGA Implosions
Audrey DeVault	Penfield	C. J. Forrest	Spectral Moment Analysis of the Deuterium–Deuterium Neutron Energy Distribution from Inertial Confinement Fusion on OMEGA
Katherine Glance	Pittsford Sutherland	W. T. Shmayda and M. Sharpe	Measuring Isotherms of the Hydrogen-Palladium System
Katherine Kopp	Victor	S. G. Demos	Microscopy with Ultraviolet Surface Excitation in Life Science Education
Hannah Lang	Rush Henrietta	K. L. Marshall	Computational Chemistry Modeling of Photoswitchable Liquid Crystal Alignment Materials
Maia Raynor	Brighton	W. T. Shmayda and C. Fagan	Oxidation of Copper Zinc Alloy
Margaret Rudnick	Pittsford Mendon	K. L. Marshall	Protective Polymer Coatings for Laser Optics
Aidan Sciortino	Wilson Magnet	R. W. Kidder	A Containerized Approach for Data Analysis on Omega
Anirudh Sharma	Webster Schroeder	R. S. Craxton	Optimization of Cone-in-Shell Targets for an X-Ray Backlighter on the National Ignition Facility
Alan Tu	Pittsford Sutherland	A. B. Sefkow	Complex Ray Tracing and Cross-Beam Energy Transfer for Laser-Plasma Simulations

Analysis Tools for Current Characteristics of Pulse-Forming Networks Driving High-Energy

Flash Lamps

Steven Booth

Brighton High School

LLE Advisors: Wade Bittle, Vinitha Anand

Laboratory for Laser Energetics

University of Rochester

January 2019

1. Abstract

High-intensity flash lamps are used to excite laser glass amplifiers on the OMEGA and OMEGA EP lasers. These flash lamps are driven by high-energy current pulses created by pulse-forming networks in power-conditioning units (PCUs). The electrical current waveforms directly correlate to the laser output energy and hence can adversely affect the beamline gain. Analyzing and correlating flash-lamp current data can highlight trends that can help locate failures, predict potential failures, and provide information for preventive maintenance. In this work, Python programs were developed to analyze PCU diagnostic current data. The first program – a diagnostic information tool – calculates summary metrics from the current data stored for each laser system shot in the power conditioning database and compiles them into Excel files. With the files created by this program, the second program – a PCU health program – can display useful information for each PCU on a per-shot basis and summary metric trends over time.

2. Introduction

Currently, maintenance on the flash-lamp systems of the OMEGA and the OMEGA EP lasers is done in reaction to part failures. This approach is inefficient and requires extensive labor. This also results in failed laser shots and downtime on the laser. Developing software tools that use available data to predict part failures or determine when parts should be serviced is valuable because such software will decrease the downtime of the laser by indicating when maintenance for the flash-lamp systems is needed. Although most of the data analysis for this project was devoted to the OMEGA EP (extended performance) laser system, similar analysis routines can be easily applied to the OMEGA laser system.

The OMEGA EP laser system produces light pulses of kilojoule energies at picosecond widths, resulting in ultrahigh petawatt (10^{15} W) powers. The Omega EP beam lines consist of neodymium-doped glass excited by xenon flash lamps. The power conditioning system provides the high-energy pulses required to power the flash lamps. This involves converting ac power to high voltage dc, storing the energy in charge-storage capacitor banks, and delivering precisely timed high-current pulses to the flash lamps. The amplified laser beams can be delivered to targets within the OMEGA target chamber as well as an independent chamber within the OMEGA EP target area.[1] Each beamline includes a main amplifier containing 11 laser disk modules (shown in Figure 1) and a booster amplifier containing 7 laser disk modules. Since each laser disk module requires one power-conditioning unit (PCU), each beamline requires 18 PCUs, each of which powers the 36 flash lamps required for one laser disk module.
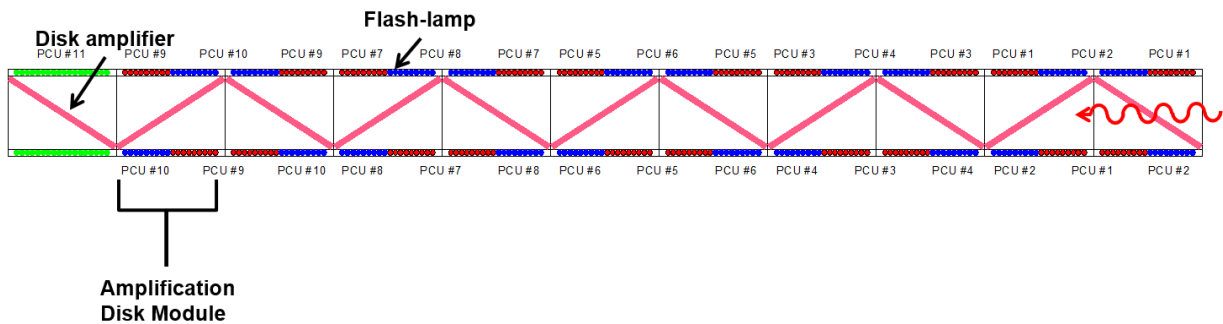

Figure 1: OMEGA EP main-amplifier configuration.

Figure 2 depicts a block diagram of a PCU, including the PCU control module (PCM), the waveform digitizer module (WDM), and charging, trigger, and switching circuits. There are two trigger generator modules: one for the pre–ionization and lamp check (PILC) and another to trigger the main pulse. Each PCU includes 12 pulse-forming networks (PFNs) that create the electrical pulse shape used to drive the flash lamps.
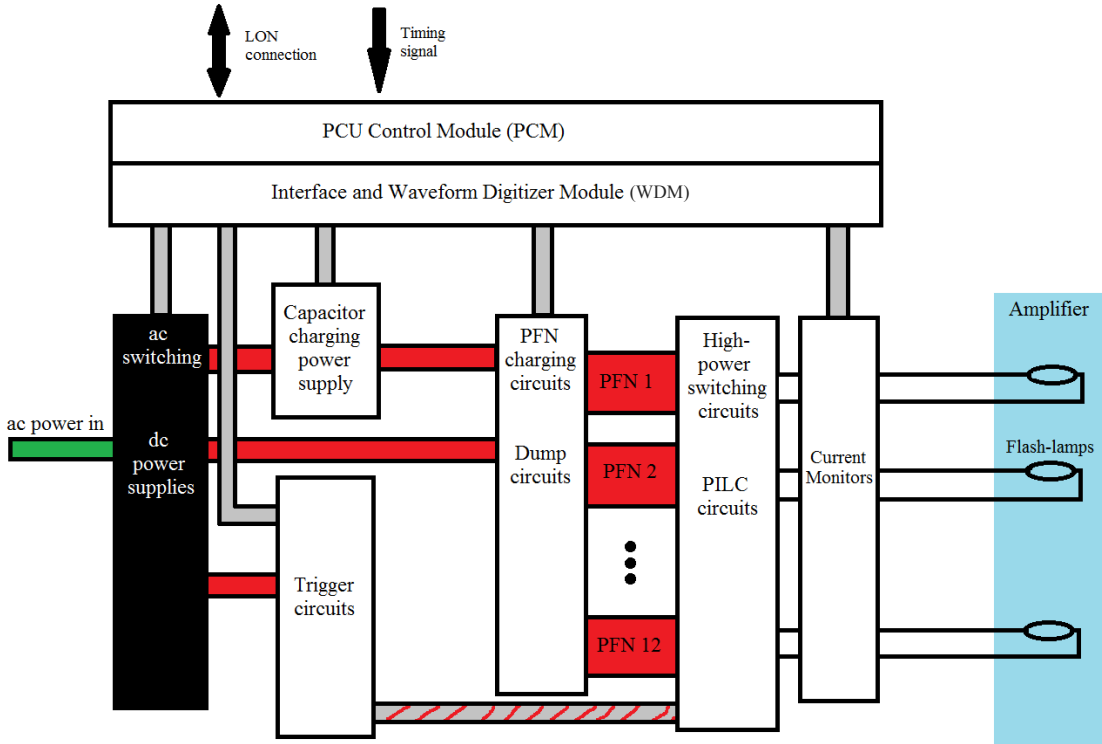
3

Figure 2: Power-conditioning unit (PCU) block diagram. Red represents power transfer, while grey represents control signals. ac power from the power grid enters the PCU and is converted to high voltage dc power, which charges the capacitors that provide the power for the pulse-forming networks (PFNs) and the trigger circuits used to initiate the pulses. A short time after a timing signal is received from the power control executive, the trigger circuits initiate the PILC (pre-ionization and lamp check) pulse, and then shortly thereafter the main pulse. The current through the PFNs is recorded by current monitors and sent to the Waveform Digitizer Module (WDM) for later analysis.

Once the PFNs are charged and a shot is about to occur, the power conditioning executive sends a timing signal to each PCU's PCM to synchronize their firings. Once the timing signal is received, the pre-ionization and lamp check (PILC) circuits discharge. This low intensity pulse determines if there have been any lamp failures and reduces the mechanical shock of the main pulse and x ray production from the rapid ionization of xenon. Approximately 250 microseconds after the PILC trigger is received, the main PFNs discharge as well. The primary purpose of the WDM is to digitize and store PFN current waveforms during the shot sequence (Figure 3). The WDM records the current for each of 15 assigned channels twice per microsecond. The 16th

channel is reserved as a space for future development. After this, the residual stored energy is discharged through dump circuits, and the current data recorded by the WDM is sent to the power conditioning executive control program and exported to an Excel file. The data quantity per shot per PCU is very large and stored in a spreadsheet format. These large Excel spreadsheets typically comprise 16 columns, one for each of the 12 PFNs, the ground buss bar, and several other diagnostic signals. Each file has 6000 rows, one for each 500 ns spaced sample. The magnitude of these spreadsheets makes analyzing the data by hand an insurmountable task.

The current work involved the development of two computer programs. The first, a diagnostic information program, calculates useful summary metrics from the raw data recorded in the database. The second, a PCU health program, displays these metrics in a format that can be used to determine which PCUs or PFNs need servicing.
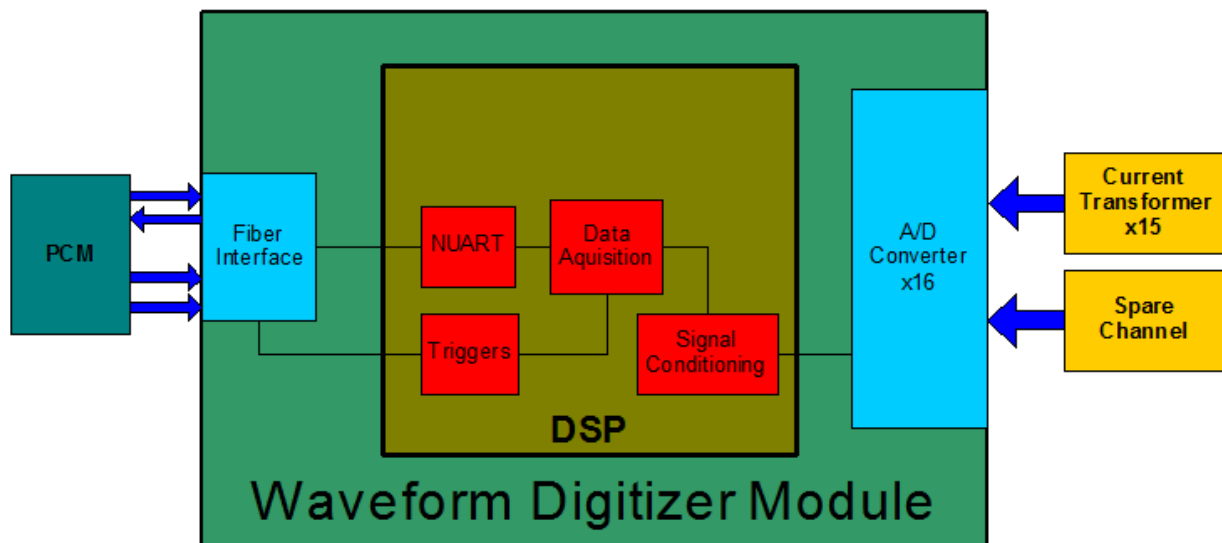

Figure 3: Waveform Digitizer Module (WDM) block diagram. The WDM uses analog-to-digital converters to sample the current from the 12 PFNs and several other parts in the PCU. This information is sent through digital signal processing (DSP) and travels to the PCM through a fiber interface. After each shot, the PCU control module (PCM) communicates the information with the power conditioning executive, and later stores the data acquired in Excel files.

3. Program Development

Python was selected as the primary programming language for its flexible packages and strong data analysis capabilities. The main packages used for data analysis were Pandas, NumPy, and Matplotlib. Pandas is a well-rounded data manipulation package, and interfaces well with the other two packages used for data analysis. NumPy supports large, multidimensional arrays and matrices, and hosts a suite of high-level mathematical functions to operate on these structures. Matplotlib produces quality graphs that are easily embedded in the graphical user interface (GUI). Tkinter was selected for its simplicity and functionality and was used to make the GUIs for the two programs.

4. Data Analysis

Every time a shot is performed on OMEGA or OMEGA EP, the records of all the gathered data are stored in LLE's databases which can then be accessed for analysis. The Excel files produced from the WDMs' data are stored on the LLE network drive Redwood. While these files are typically 16 columns by 6000 rows, their length depends on whether the shot was successful or not. Lamp failures or other circuit components breaking can result in shortened data recording or atypical waveforms. Some shots are PILC only and are used for diagnostics of the systems. These shots also result in atypical pulse shapes. Such shots are ignored by the diagnostic information program. Figure 4 is a plot produced by the PCU health program for a successful shot, showing a typical PFN current waveform with definitions of the summary metrics (the time from the trigger firing to the peak current, the magnitude of the peak current, and the width of the peak when it is at one-third of its maximum current).
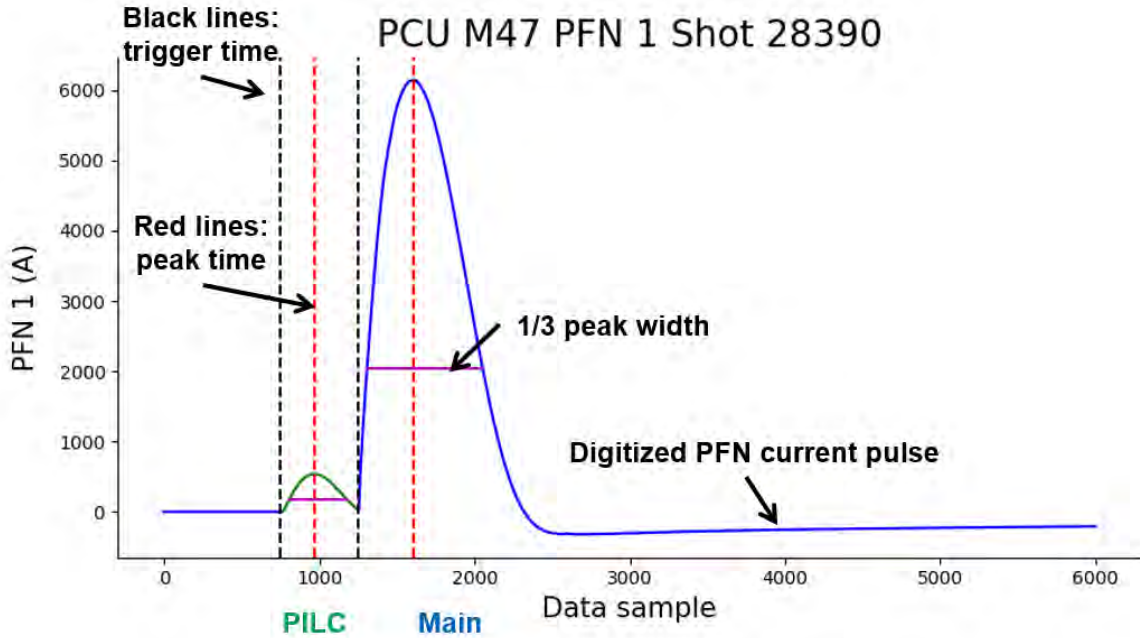
Figure 4: Typical shot waveform. The small green peak is the PILC (pre-ionization and lamp check) pulse, while the large blue one is the main pulse. The two dotted black lines show the times of the triggers for the PILC and the main pulse, while the two dotted red lines show the time of the peaks for each pulse. The time to peak is the distance between these two values for each pulse. The peak current is the highest value for each pulse. The solid horizontal purple lines show the 1/3 width measurement, which is the width of the curve at 1/3 of its peak current.

5. Programs developed

When launched, the diagnostic information program GUI prompts the user to select the PCUs to calculate summary metrics for. The diagnostic information program then retrieves the requested data from the Redwood database and calculates the summary metrics for every successful shot in that PCU. The calculated metrics are stored in an Excel file, which contains the peak current, time from the trigger to the peak, and width of the curve at a third of its peak current for each PFN. Failed shots are left out of the final output and are reported in an error log text file.

When launched, the PCU health program prompts the user to input the Redwood folder (for single-shot information), and the folder containing the files produced by the diagnostic information program (for long-term trends). The single-shot metrics page allows the user to see waveforms and summary metrics for specific shots, and to see how each PFN performed compared to the PCU's average (Figure 5). This comparison is useful because the most underperforming PFN is likely the one that needs servicing. While the single-shot page can graph failed or PILC-only shots as well, it does not enable metrics to be calculated for those shots.
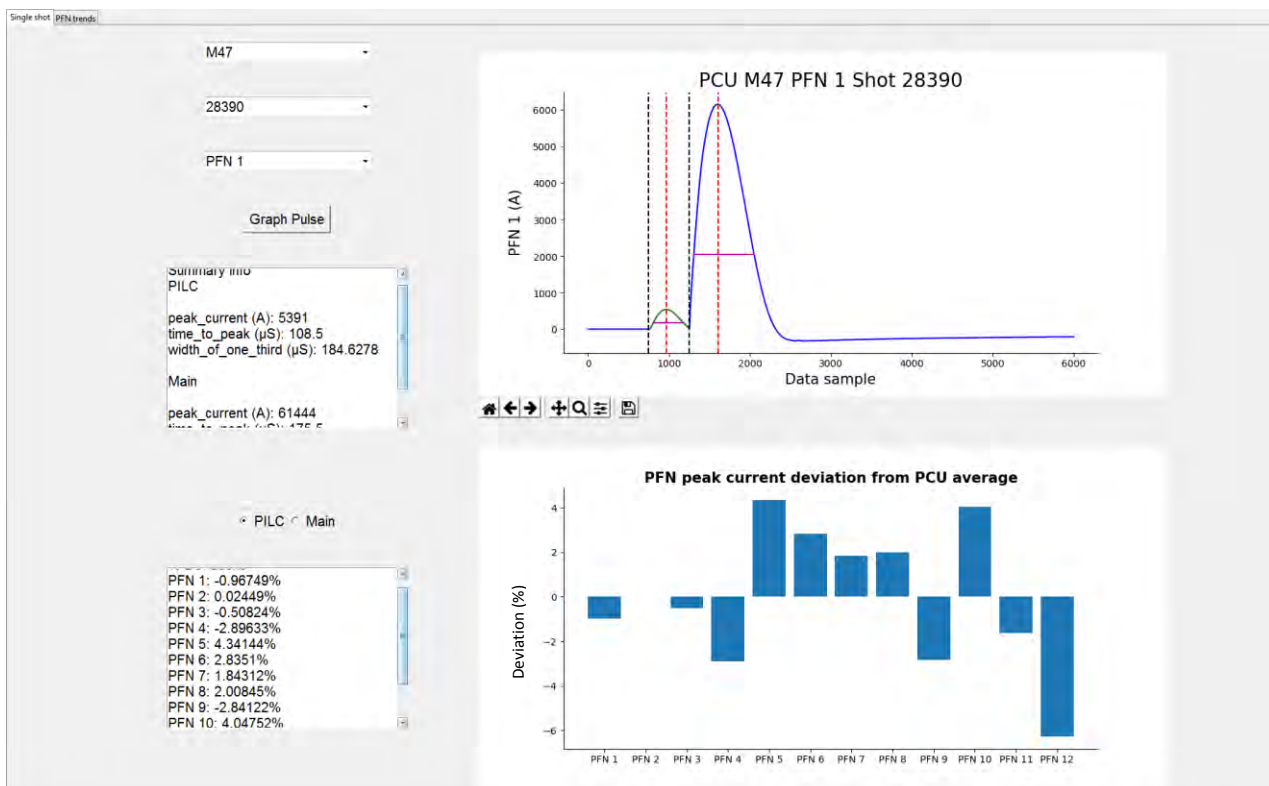

Figure 5: Single shot metrics. The user inputs the PCU, shot number, and PFN number, and the program graphs the waveform. For the selected shot, it also displays each PFN's percent deviation from the PCU's average peak current.

The PCU health program also features long-term trend plotting to show how pulse metrics are changing over time for PCUs or PFNs. As shown in Figure 6, using the summary metrics calculated by the diagnostic information program, the GUI can display trends in any of the three summary metrics for either specific PFNs or PCU averages. This information can be plotted over any date range or shot number range the user selects and can be used to give a good overview of how PFN health is changing over time. This can be used to help technicians choose when to perform maintenance on PCUs and trends can be studied to mitigate future degradation.
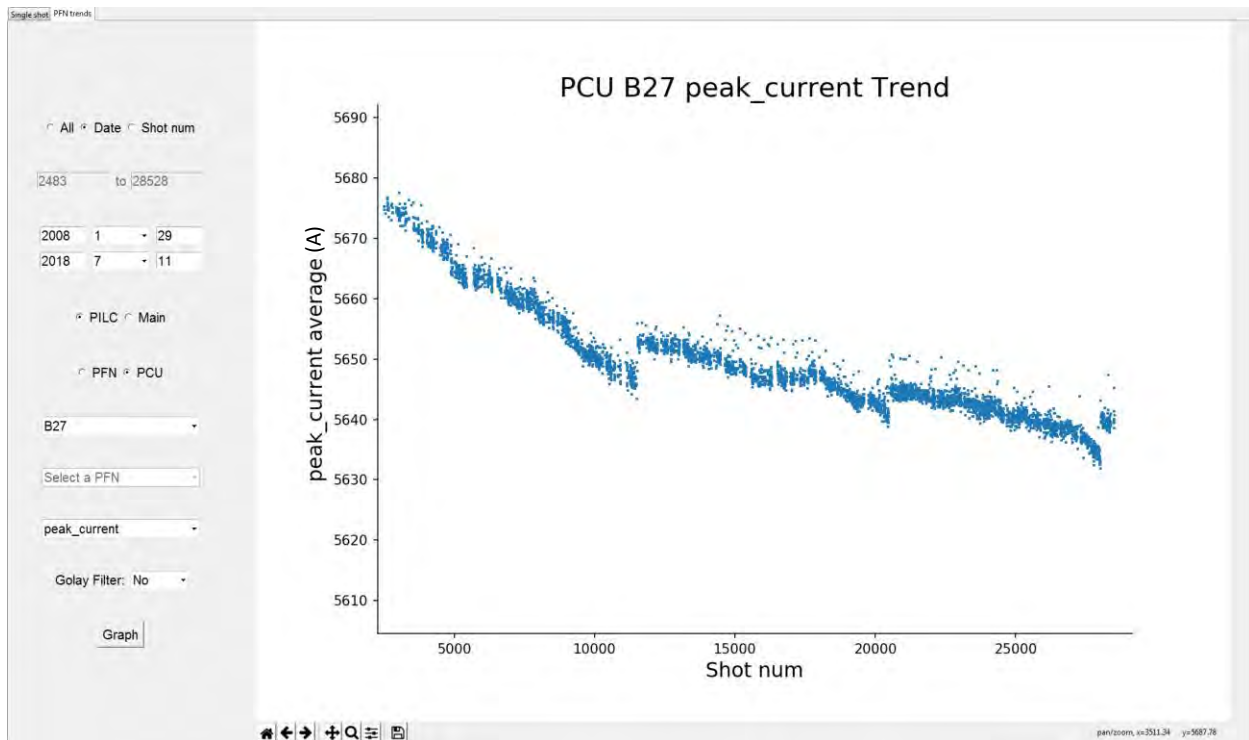

Figure 6: Long-term trend panel. The graph is interactive, and can be plotted for different PFNs, PCUs, date ranges, and statistics.

6. Conclusion

Python programs were developed that analyze PCU diagnostic data to help technicians determine when preventative maintenance is required. Using the current data stored after each shot in the power conditioning database, the diagnostic information program calculates summary metrics and compiles them into Excel files. The PCU health program reads these files and displays useful information on a per-shot basis and summary metric trends for multiple shots over time. Its easy-to-use GUI can help technicians decide which PFNs need to be serviced. Future development could expand on this functionality by allowing the program to automatically predict when critical failures could occur. With more diagnostic information and further development, such programs could replace the current reactive maintenance approach with a predictive preventative maintenance approach that would greatly increase the operational efficiency of the laser system.

7. Acknowledgements

I would like to thank Dr. Craxton for his work to give me and the rest of the interns this opportunity. I would also like to thank Jack Kelly, Greg Brent, and the power conditioning group for their help throughout the project. I would like to give special thanks to Vinitha Anand and Wade Bittle. I'm grateful for their patient guidance and support, without which I would have been unable to perform this work.

8. References

[1] University of Rochester - Laboratory for Laser Energetics. OMEGA Power Conditioning - Laboratory for Laser Energetics, www.lle.rochester.edu/omega_facility/omega_ep/.

Real time x-ray analysis of liquid-DT fill level in fill-tube capsules to control solid-layer
thickness

Carwyn Collinsworth

Brighton High School

Rochester, NY

Advisors: Mark Wittman, Dana Edgell

1. Abstract

The current permeation capsule-filling technique limits the capsule materials to polymers. Future OMEGA experiments will use spherical capsules filled via a fill tube to allow variability in capsule materials. In the filling process, spherical fill-tube capsules are first cooled to cryogenic temperatures and filled with liquid deuterium-tritium (DT), which is then frozen to form a uniformly distributed layer of solid DT on their interior. During initial filling, the liquid level is observed via x-ray phase-contrast imaging normal to the direction of gravity, presenting a meniscus symmetric about the gravitational axis. A series of MATLAB programs were developed to control the liquid-DT fill level in fill tube capsules. The main program acquires near real time phase-contrast images and uses an algorithm to compute the solid thickness when uniformly frozen. The program achieves the desired fill level from user input using a proportional integral derivative (PID) controller. Once the program stabilizes the estimated final thickness within ±1 μm of the desired thickness for a specified time period, the program rapidly freezes an ice plug in the fill tube, blocking any liquid from leaving or entering the capsule. Since a small amount of liquid leaves the capsule when the ice plug forms due to its contraction, a bias is calculated, the capsule is heated back into the liquid phase of DT, and the process is repeated taking the bias into account. The program was successfully implemented to deterministically control capsule filling, and it was proven to be reproducible with a <30 min settling time to achieve the fill required to produce the desired thickness.

2. Introduction

Nuclear fusion offers the prospect of an environmentally friendly energy source with an almost infinite fuel source – deuterium (D) from seawater and tritium (T) bred in a reactor. To achieve fusion, elemental hydrogen isotopes deuterium and tritium must be heated to millions of degrees and compressed to hundreds of Gbar [1]. This causes the D-T hydrogen nuclei to overcome the electrostatic repulsion force between them and combine to form a helium nucleus, and release energy in the form of an energetic neutron.

The University of Rochester's Laboratory for Laser Energetics (LLE) has the mission of conducting fusion research. Inertial-confinement fusion is one method of fusion, implemented at LLE, in which a microscopic target is irradiated by high-power lasers. The energy from the laser is delivered uniformly onto the surface of the target, rapidly heating the shell, and causing ablation of the outer surface that drives implosion of the inner surface. The implosion of the shell compresses the DT to the high pressure required for fusion.

As the deuterium-tritium (DT) filled capsules are imploded by OMEGA's 60 laser beams, both the uniformity of the laser beams and the quality of the capsule are extremely important. A lack of uniformity causes hydrodynamic instabilities, which contribute to mixing of the shell and fuel in the target and spoiling the efficiency of the fusion reactions.

Efforts are being made to optimize the surface uniformity of the capsule. The current permeation-filling process may be leaving debris on the target shells and causing radiation damage to the polymeric capsules that releases condensable contamination (CH_4, CO, CO_2) on their interior. Another advantage of the fill-tube filling method is that it allows for the use of alternate ablators such as beryllium, silicon, and high-density carbon (HDC) [2] which are not permeable to DT. Both the possibility of permeation filling causing imperfections and the desire from scientists to experiment with alternative capsule materials necessitate the development of the fill-tube filling method.
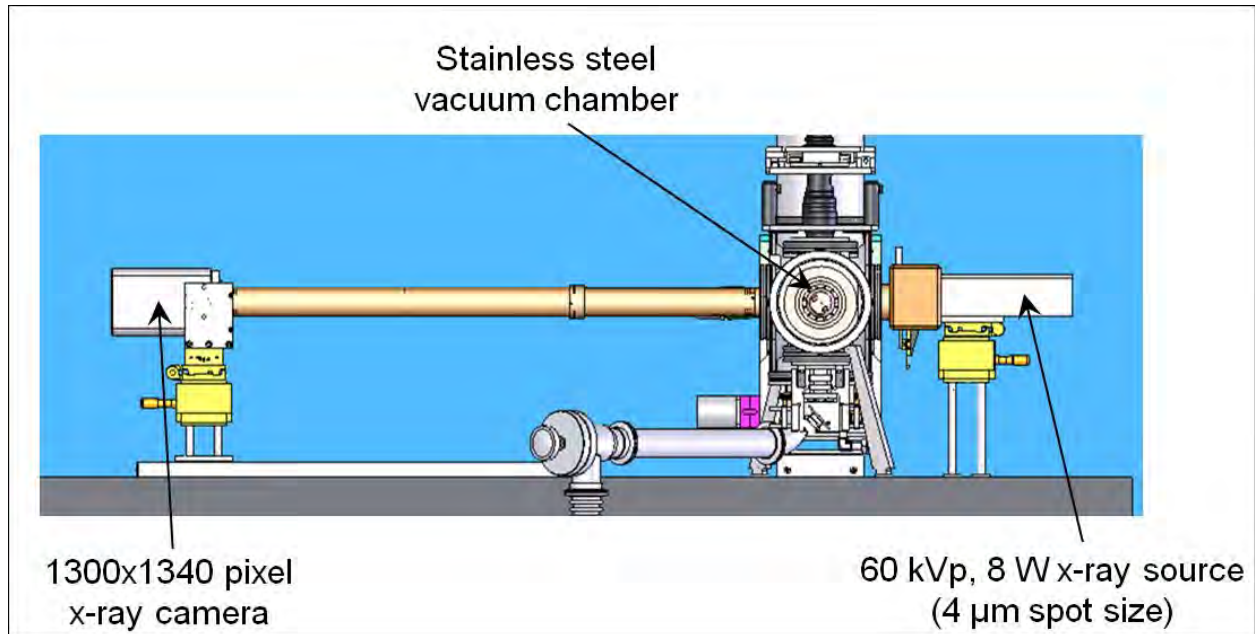
2.1. Cryogenic Fill-tube Test Facility (CFTF)

Figure 1. CAD representation of the x-ray phase-contrast system in the fill-tube experimental apparatus.

Figure 1 depicts the CFTF which researchers at LLE use to determine the parameters required to produce high-quality targets using the fill-tube method. The stainless-steel vacuum chamber contains the capsule. During the filling process, the capsule is illuminated by an x-ray source and imaged onto an x-ray camera to observe the filling process. This viewing is in near real time; multiple three-second long frames are acquired and averaged during image collection to reduce noise in the process.
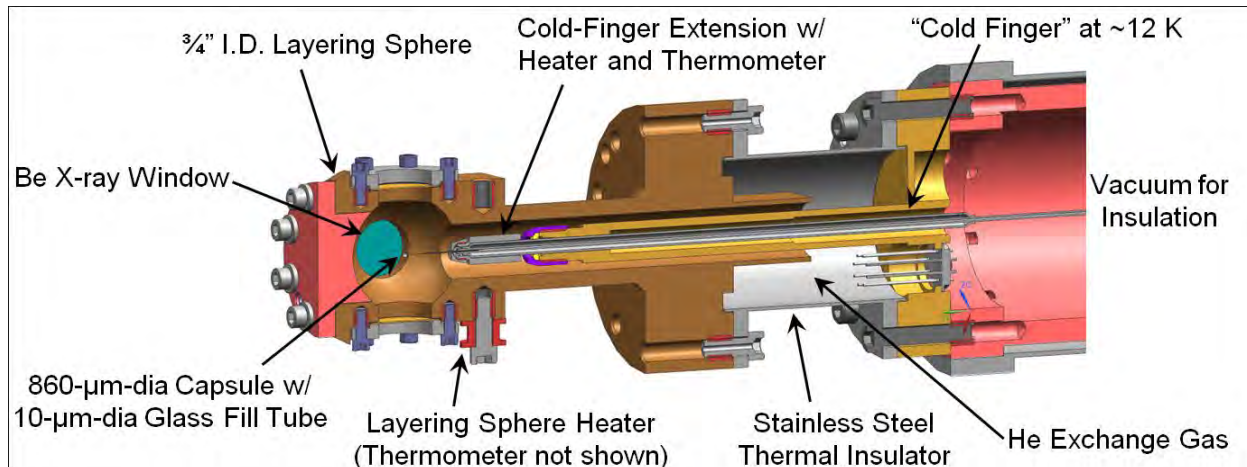
Figure 2. CAD cross section representation of the layering sphere that houses the fill-tube target.

Figure 2 depicts the layering sphere assembly inside of the stainless-steel vacuum chamber displayed in Figure 1. The orientation of this apparatus is horizontal, and situated such that the x-ray camera in Figure 1 views through the beryllium (Be) viewing window. The capsule, held within the ¾-inch-diameter layering sphere, is an 860-μm-diameter polymeric capsule with an 8-μm-thick wall. Holding the capsule in place is a 10-μm-diameter glass fill tube, which connects to a stainless-steel capillary tube exiting the right of the diagram to a gaseous-DT reservoir. To control the fill level in the capsule, the layering sphere's temperature is controlled using a heater and thermometer connected to it. The temperature of the layering sphere is initially controlled at ~19 K and the gaseous DT condenses into the liquid phase as it enters the capsule. An increase in layering-sphere temperature causes the pressure of the DT vapor above the liquid inside the capsule to increase, driving the liquid DT out of the capsule. The opposite effect occurs when the layering sphere is cooled; this process allows filling or emptying the capsule with very fine control using mK temperature changes.

Unfortunately, the relationship between the temperature of the layering sphere and the liquid level in the capsule is not necessarily deterministic. There is no reproducible temperature for any liquid level due to fluctuations in the ratio of deuterium and tritium in the reservoir and the initial pressure in the reservoir. As a result of this, programming an automated capsule filling process must include a

temperature control loop with feedback from the x-ray camera.

One other important feature of the apparatus is the cold finger extension. This is a subset of the cold finger (the element cooling the entire system), which surrounds the fill tube. It is used to control the state of the DT in the fill tube close to the capsule. This metal "bullet" has the ability to heat and cool rapidly, allowing an ice plug to form nearly instantaneously within the fill tube when heat is removed. This gives the ability to terminate any DT flow to or from the capsule once the desired liquid level has been achieved. Unfortunately, there is a slight amount of liquid DT that leaves the capsule when the ice plug forms due to contraction of the liquid during solidification; this must be accounted for. Once the desired thickness is obtained within one micrometer, and checked after the ice plug is formed, the capsule is slowly cooled so that a single DT seed crystal grows and converts the liquid to the solid phase.

This freezing process takes place over a period of up to fifteen hours both to slowly form a single crystal and to allow for beta layering. Beta layering occurs when radioactive tritium releases an energetic beta particle. The beta particle deposits its energy into the solid DT to produce volumetric heating. Thicker regions of the solid receive more energy than thinner regions. Sublimation of the DT occurs – thicker regions sublime and redeposit in the thinner regions; this results in a uniform layer of solid DT on the inside surface of the capsule. The thickness of the layer must be uniform within 1-µm-rms and must be within one micrometer from the desired thickness.

3. Automation Process

The main objective of this work was to automate the fill process of a fill-tube capsule to make it more efficient than the current "human control loop" running the process at LLE. This includes filling the capsule to a desired thickness, creating an ice plug, and compensating for any bias occurring during the ice-plug freezing process. A MATLAB program was developed for this purpose and is structured as shown in Figure 3.
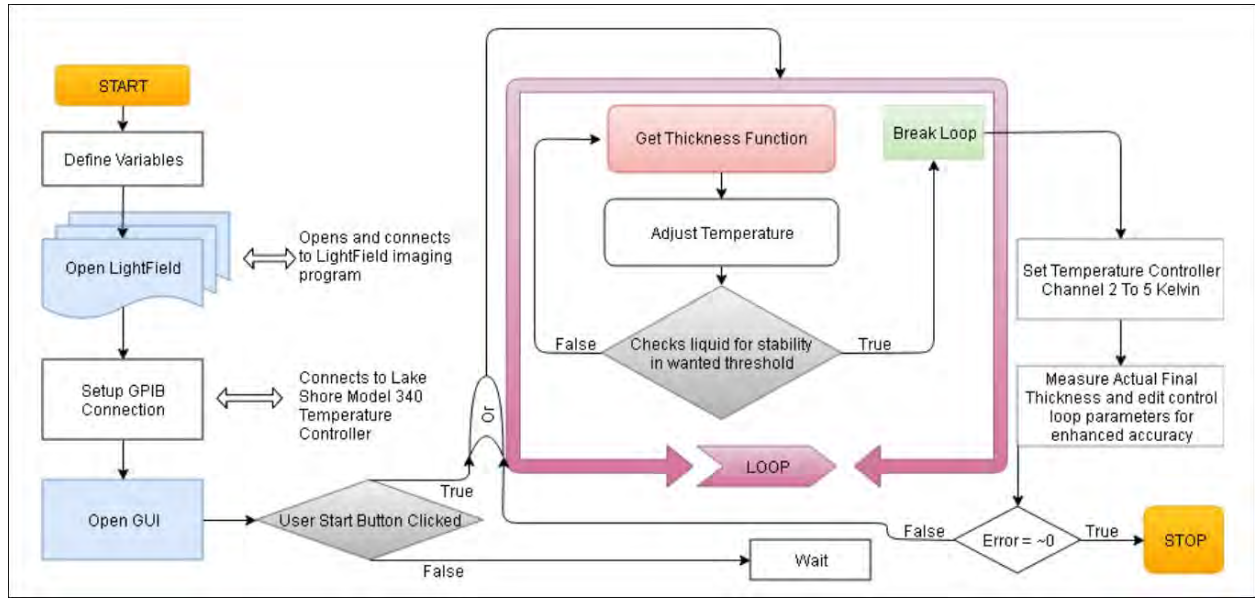
Figure 3. Flowchart diagram outlining high level logic flow of the program used to automate the fill process.

The program begins by setting multiple global variables. These variables such as current time and current estimated thickness are used throughout the program and in most functions, so globalizing them is practical. The program then connects to the necessary systems: First, the program opens an instance of LightField®, an imaging program designed to be used with the x-ray camera in the experimental setup, and connects it with the MATLAB program so it is running in parallel. Next, the program sets up a general purpose interface bus (GPIB) connection with the LakeShore® Model 340 temperature controller, allowing information to be sent to it and received from it. This connection allows the program to acquire and set the current temperature of the layering sphere and the cold-finger extension. Following these initial connections, the program opens a graphical user interface (GUI) so the user can input the desired thickness, image options, and various other important parameters. Once the user clicks a button labeled "Start" on the GUI, the program begins.

The program enters the main loop, where it spends most of its time running. The loop continually estimates the final thickness of the current liquid-filled capsule and adjusts the temperature to empty or fill the capsule. If it reads that the estimated final thickness is within one micrometer of the desired thickness for three iterations of the loop, shown by the "Checks liquid for stability in wanted threshold"

7

diamond in the flowchart, it breaks the loop. The program then sets channel 2 of the temperature controller to 5 K. Channel 2 controls the cold finger extension, so lowering this temperature creates a freeze plug in the fill tube, restricting all liquid flow. Due to the small amount of liquid that escapes from the capsule as the ice plug contracts, the program estimates the final thickness once more after the freeze plug is formed, and calculates a bias representing the amount of liquid that escaped while the fill tube was freezing. The program then accounts for this by adding the bias to the desired thickness value, remelts the freeze plug, and attempts to acquire the desired thickness repeatedly until it is achieved.

3.1. Image Acquisition - The Get Thickness Function

The get thickness function is portrayed as a red rectangle in Figure 3, and is situated as the first element within the loop. This function contains various elements shown in Figure 4.
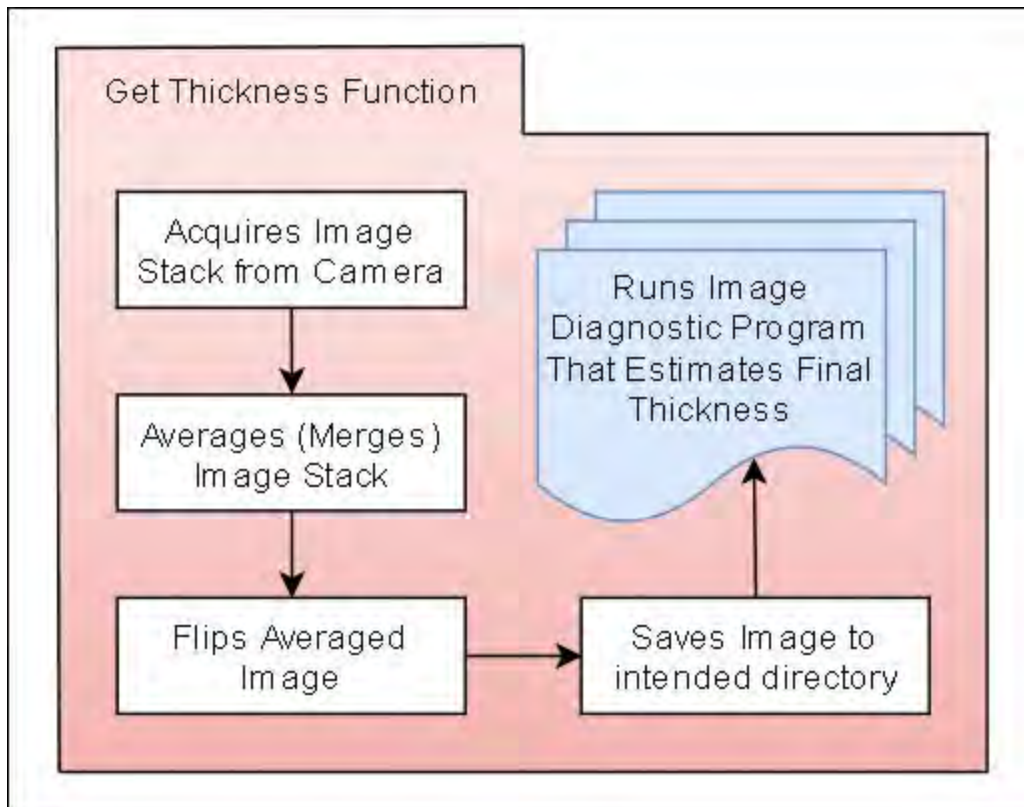

Figure 4. Get Thickness function flow diagram.

To begin the function, the program acquires an image stack, a tagged image format file (TIFF) which stores multiple images within one file. The program's connection with LightField® makes this

simple, taking only one line of code. These images are deconstructed into separate value arrays, with only one layer of the third dimension due to them being black and white (not colored). Then, each pixel (X, Y) is averaged with pixels in other images (X_n, Y_n). This produces an "averaged" image, with well-defined gradients. Since the x-ray camera is mounted upside down with respect to gravity, the image is then flipped. This edited image is saved for future reference, and is run through a diagnostic program. The diagnostic program uses Gaussian fit models and gradient image-evaluation techniques to identify the lines in the left image of Figure 5 representing the capsule shell and liquid-vapor DT boundary. The program then assumes rotational symmetry around the gravitational axis and uses both geometric techniques and the density difference between liquid and solid to estimate the solid thickness if the liquid DT in the capsule was completely frozen into a uniform layer. This is indicated by *t* in the right image of Figure 5.
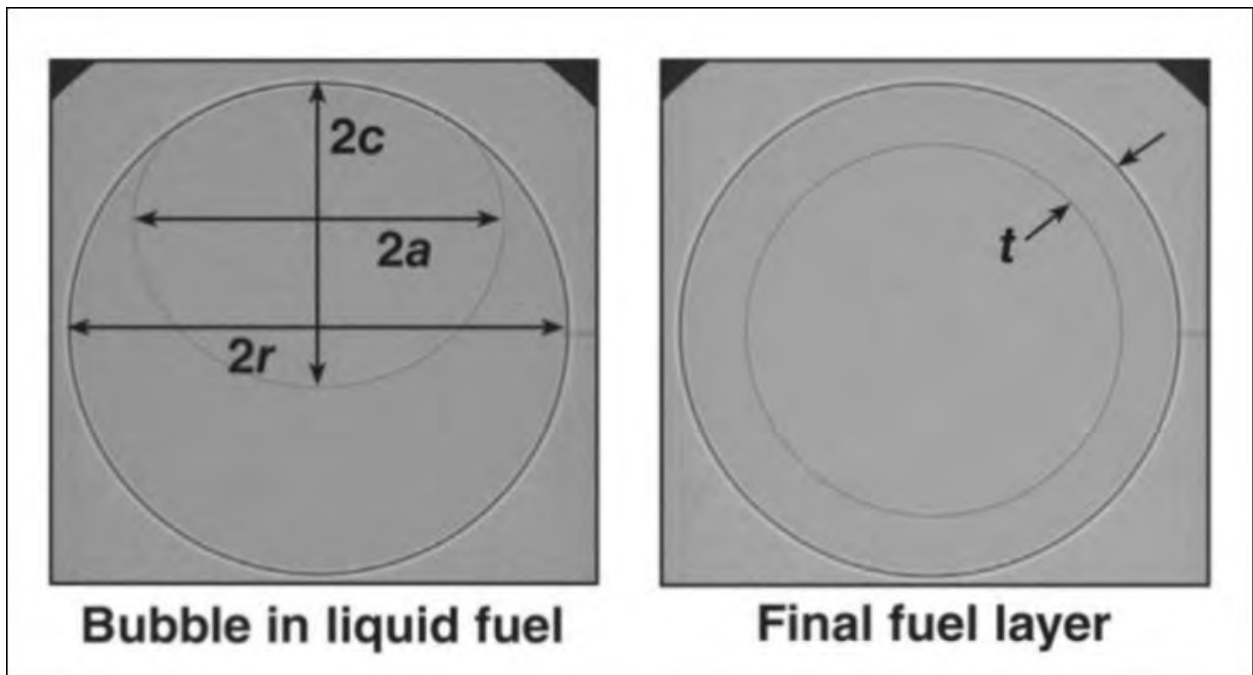

Figure 5. DT-filled fill tube capsules.
The left image is a liquid-DT-filled capsule. The liquid meniscus forms an elliptical bubble; the capsule's perimeter is the outer circle. The right image is the solid-DT-filled capsule; the solid DT forms a symmetric layer within the capsule. Both images show the fill tube on the right.

3.2 Temperature Adjustment - PID Control Loop

Following the image recognition and thickness estimation stage, the program adjusts the temperature of the layering sphere, indirectly controlling the thickness of liquid DT in the capsule. A proportional integral derivative (PID) controller was implemented to best achieve the desired thickness.
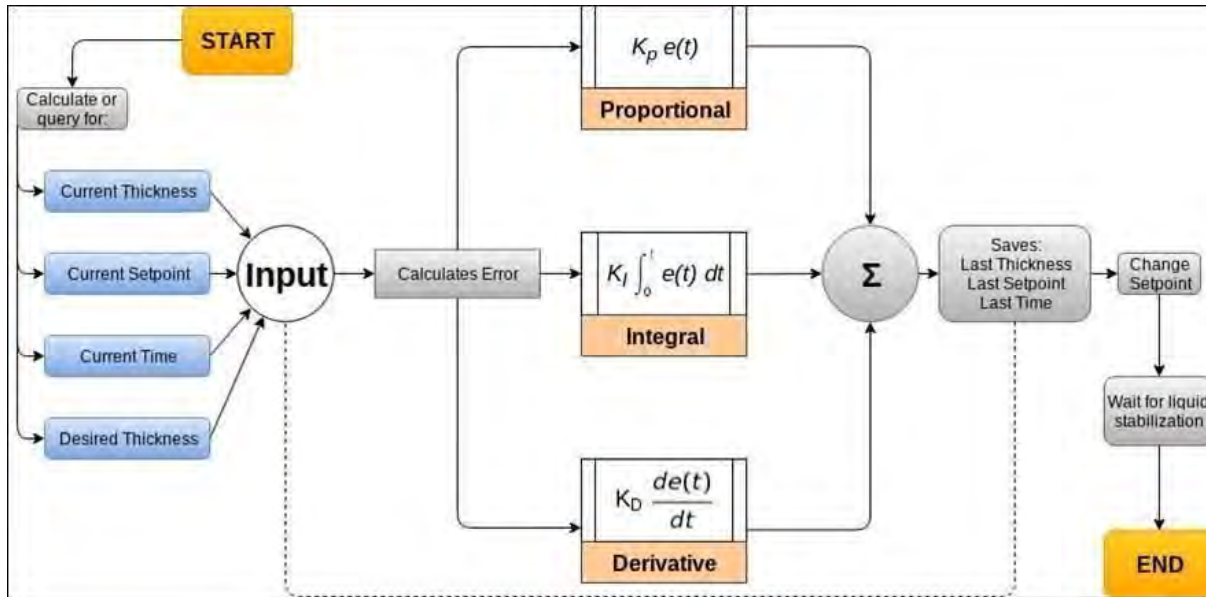

Figure 6. Temperature Adjustment flow diagram.
A PID loop is integrated into the temperature adjustment block of the general program flow diagram.

To determine the temperature change of the layering sphere required to meet the desired thickness, three terms of an error function were implemented, as indicated in Fig. 6. The error function *e(t)* is a function of time based on the difference between the desired thickness and the current estimated solid thickness. The first term of the temperature change is the proportional term. This element calculates a proportion of the error between the desired thickness and the current estimated solid thickness, and sets its input to the temperature change to this. Unfortunately, this term alone will cause the calculated thickness to either oscillate around or to approach but never reach the desired thickness; the integral and derivative terms fix this. The derivative term estimates the next thickness after the same temperature change as the previous temperature change, and uses this to either increase (if the next estimated thickness is still below the desired thickness) or decrease (if the next estimated thickness is above the desired thickness) the temperature change. Finally, the integral term sums up the area under the error vs time

10

graph. This term makes it so that the desired thickness is rapidly achieved rather than being approached asymptotically over a long period of time. After these three are calculated, they are summed to give a logical temperature change. The program logs the new temperature, setpoint, and time, changes the setpoint, and waits for the liquid to stabilize for one minute before continuing the loop. The wait time, indicated as the stabilization time in Figure 7, was initially set to sixty seconds, and is an approximation to the time it takes for the liquid level to settle after the setpoint of the layering sphere is changed. This is necessary so each setpoint change has its own observable independent effect on the layer thickness.

4. Results

Initially, arbitrary values were used as constant coefficients of the proportional, integral, and derivative terms; as a result, the desired thickness was never achieved. The thickness versus time graph displayed oscillatory tendencies around the desired thickness. After appropriately tuning the PID controller, the subsequent test runs with various initial fill levels proved successful. Examples of successful runs are shown in Figures 7-9.
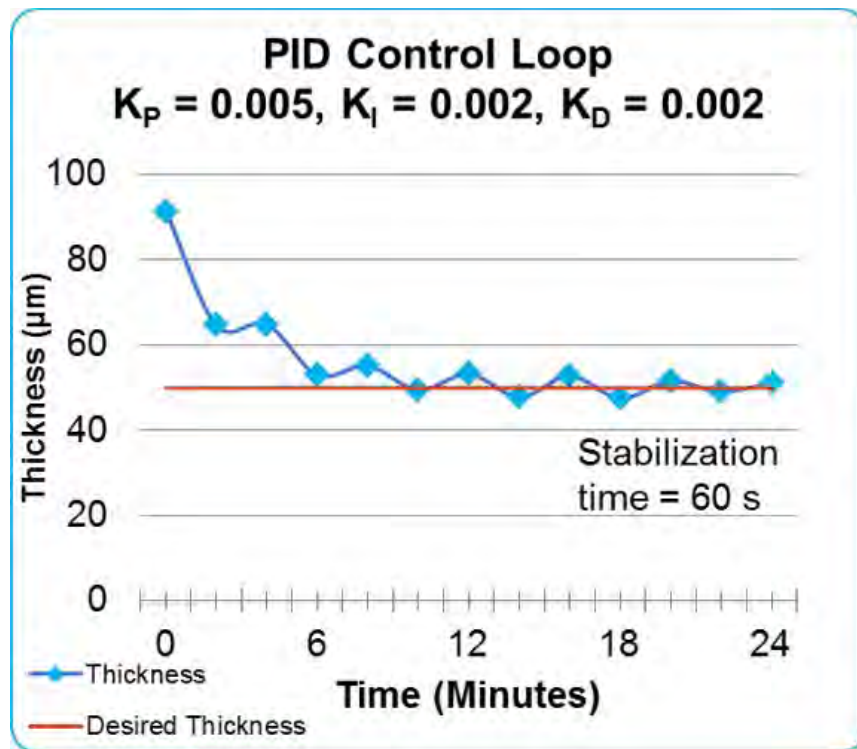

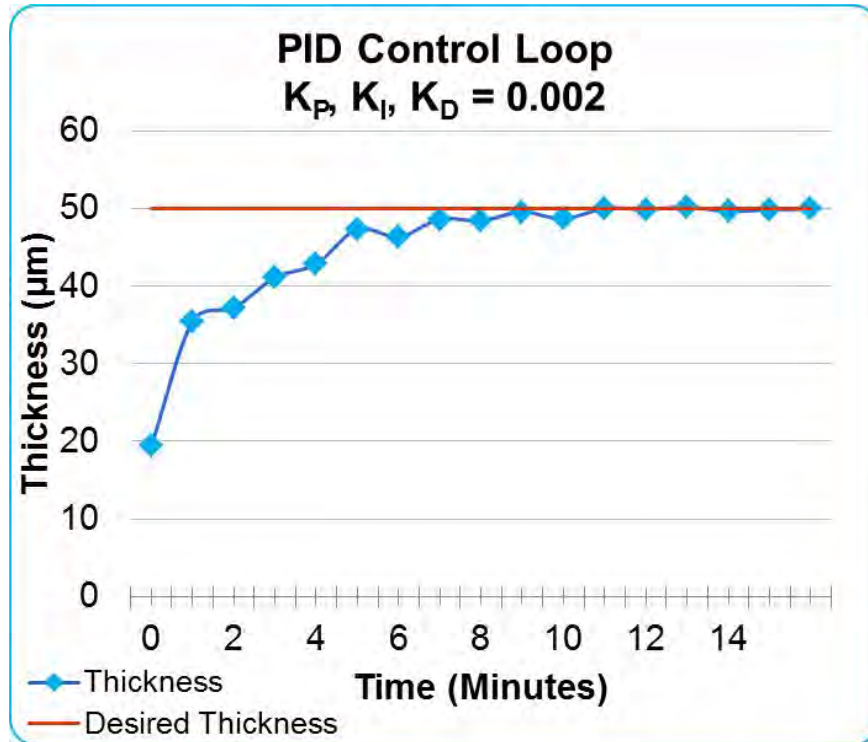**Figure 7. Estimated solid thickness vs time graph with an untuned PID controller.**

Figure 8. Estimated solid thickness vs time graph after tuning
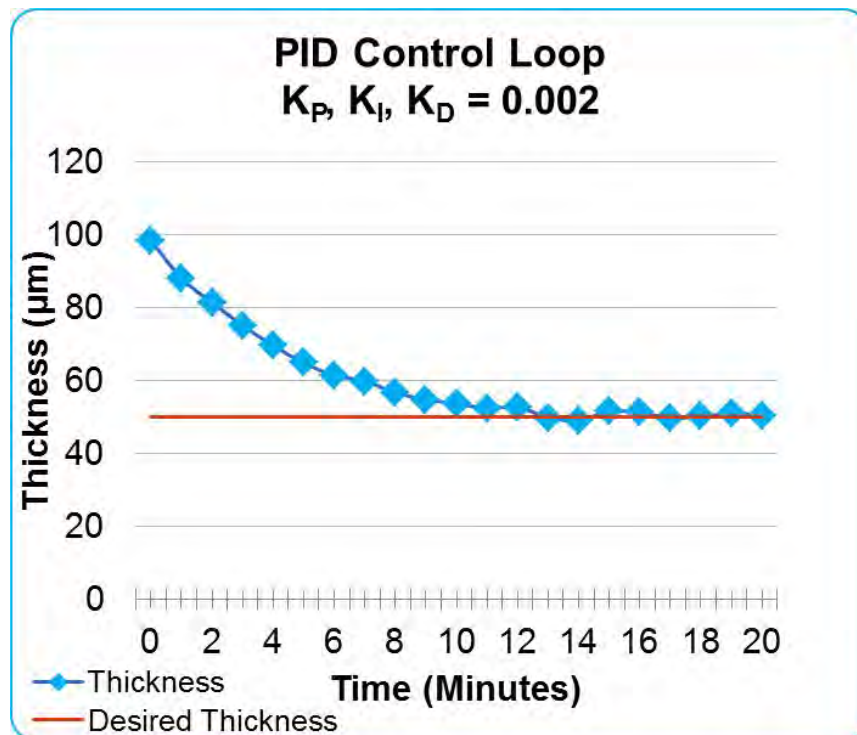Successful underfilled approach.

Figure 9. Estimated solid thickness vs time graph after tuning
Successful overfilled approach

Decreasing the stabilization time from sixty seconds to thirty seconds resulted in a decreased time to achieve the desired thickness as shown in Figure 10.
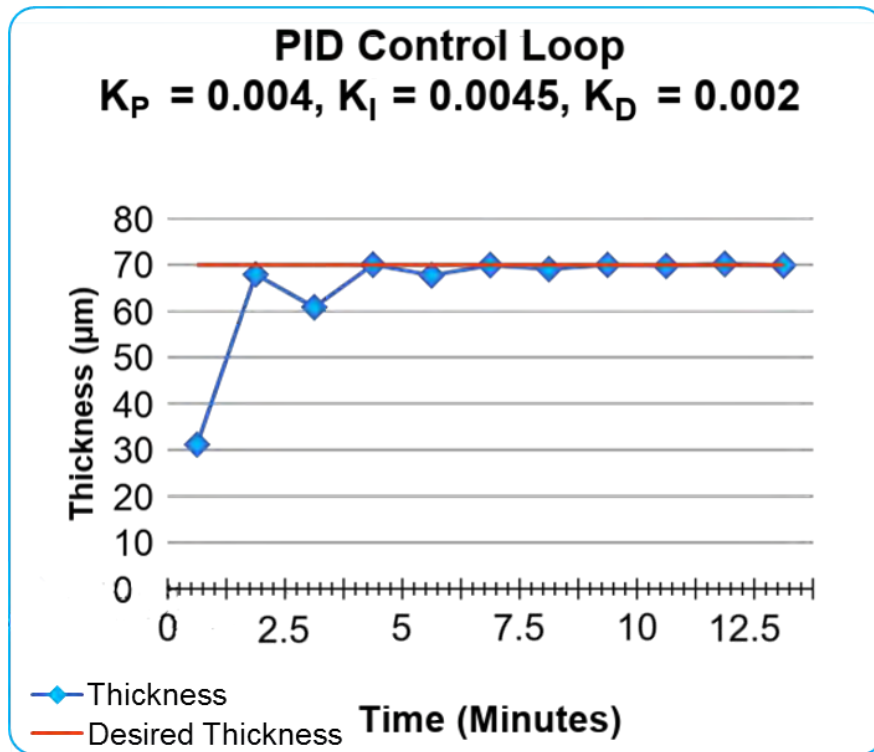

Figure 10. Estimated solid thickness vs time graph after tuning
Successful run after decreasing liquid stabilization time.

The program has the ability to successfully fill a capsule to a desired state from any initial liquid level, above or below the desired thickness. On average, the program can achieve a desired thickness within one micrometer in one to three attempts after determining the bias required to compensate for contraction in the fill tube as the ice plug forms. Each attempt takes from ten to twenty minutes, making this method of fill-tube capsule filling much more deterministic than the previous manual-estimation method.

5. Conclusion

A series of programs were written to automate the fill process for fill-tube capsules. An x-ray camera was used to observe the capsule during the fill process, and a temperature controller was used to control the liquid-DT fill level within the capsule.

A graphical user interface was implemented to allow a user to easily use the system, and an underlying computational model was used to accurately obtain the desired solid-DT final thickness. The computational model incorporated a PID controller to adjust the temperature of the layering sphere, which adjusted the liquid fill level accordingly.

The program was able to produce a liquid meniscus that would result in the desired solid-layer thickness from an overfilled or underfilled state. By tuning the PID controller, this goal was able to be achieved within only thirty minutes - comprising three freeze plug attempts of ten minutes each. It is anticipated that with additional investigation of the coefficients of each PID term, the system can be further optimized to converge in a still shorter time.

6. Acknowledgements

7. References

1. J. Nuckolls, L. Wood, A. Thiessen, and G. Zimmerman, "Laser compression of matter to super-high densities: Thermonuclear (CTR) applications," Nature 239, 139 (1972).

2. B. Rice, J. Ulreich, C. Fella, J. Crippen, P. Fitzsimmons, & A. Nikroo, "Permeation fill-tube design for inertial confinement fusion target capsules." High Power Laser Science and Engineering, 5, E6, (2017).

3. G. Gillard. "An Introduction and Tutorial for PID Controllers." *Mr. Smith's Classes : West Salem High School Computer Science, Engineering and Robotics*, 10 May 2012.

Modeling Charged-Particle Spectra to Diagnose Asymmetries in OMEGA Implosions

Matthew Cufari

Pittsford Sutherland High School

Pittsford, NY

Advisors: Radha Bahukutumbi and Owen Mannion

Laboratory For Laser Energetics

University of Rochester

Rochester, NY

January 2019

Abstract:

Charged-particle spectra are used to diagnose implosion asymmetries in inertial confinement fusion (ICF) experiments on OMEGA. These asymmetries can be the result of numerous imperfections including beam mispointing, beam mistiming, and target offset and manifest as variations in the areal density of the target. These asymmetries cause reduced implosion performance and result in a less efficient conversion of laser energy to hot spot energy. For room-temperature D_2 experiments, the areal density can be inferred from the average energy of detected secondary protons. Asymmetries can then be inferred by comparing areal density measurements along multiple lines of sight. In cryogenic DT experiments, the areal density can be inferred from the knock-on deuteron energy spectrum. The Monte-Carlo code IRIS3D has been extended to simulate charged particles including secondary protons from D_2 targets and knock-on deuterons from DT targets. This was accomplished by integrating a stopping-power physics package into IRIS3D. IRIS3D generates energy spectra for secondary protons and knock-on deuterons by transporting charged particles in straight-line trajectories out of the ICF target to a synthetic detector. For room temperature implosions, IRIS3D computes the average energy of secondary protons along multiple lines of sight to infer areal density asymmetries around the target. In order to diagnose areal density asymmetries in cryogenic targets, an algorithm was developed to infer areal density based on the knock-on deuteron spectrum generated by IRIS3D. By post-processing hydrodynamic simulations with IRIS3D, direct comparisons can now be made with experimental data to infer areal density asymmetries.

1. Introduction:

Charged particle spectra are used to infer the extent of nonuniformity growth in OMEGA targets [1,2,3]. Room-temperature targets can be filled with D_2 gas surrounded by a plastic ablator. These targets are typically positioned within 5 μm of the desired position [4]. Positioning targets consistently within 5 μm of the desired position allows for very controlled experiments. In order to create a plasma, the target is irradiated by the OMEGA laser which heats the target and causes the plastic shell to ablate off, compressing the gas. As the target is compressed it heats the deuterium fuel to temperatures that enable the ions to fuse. D_2 fusion yields neutrons and ^{3}He nuclei. Some of the ^{3}He nuclei then collide with the background deuterium and fuse to form alpha particles and protons. The formed protons are referred to as secondary protons because they are the product of fusion from a primary D_2 fusion product. These protons escape the plasma and can be detected using various charged particle detectors such as wedge-range filters or charged-particle spectrometers. As these protons escape the plasma, they undergo a phenomenon called stopping-power whereby they are slowed down and lose some of their kinetic energy to the surrounding plasma [5]. Areal density is the dominant factor for determining the extent of the energy loss the secondary protons experience. Areal density is defined as

$$\rho R = \int_0^R \rho dr \qquad (1)$$

where ρ is mass density and R is the radius of the target. Energy loss increases linearly with areal density to values of approximately 250 mg/cm^2 for secondary protons.

The Monte-Carlo code IRIS3D is used to post-process hydrodynamic simulations by simulating the reactions that take place during an OMEGA implosion [6]. This is accomplished by simulating a fraction of the actual fusion reactions and tracking the fusion products to a synthetic detector. Increasing the number of simulated particles allows for higher resolution results, but also increases computation time. In this work,
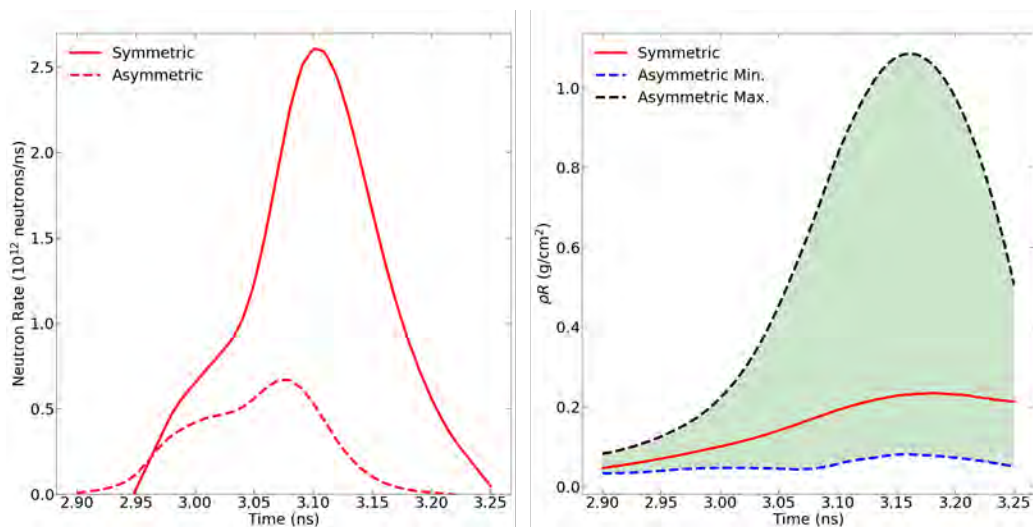

Figure 1: Neutron rate (left) and areal density (right) for a target at target chamber center (symmetric) and a target offset by 40 μm (asymmetric).

IRIS3D was extended to include a stopping-power physics package which computes the energy loss of charged particles over the simulation domain. As a charged particle is transported through the mesh to adjacent regions, the path the particle takes is broken into subsections over which the energy loss is computed. The particle may elastically collide with other fusion products in the mesh resulting in a change in direction and energy. This transport process is repeated until the particle enters a detector located outside of the target.

A set of room temperature D_2 targets were intentionally offset 40 μm from target chamber center to study the charged-particle spectra and target nonuniformity growth in large-offset shots. Post shot simulations have been processed through IRIS3D. Figure 1

compares the neutron rates and areal densities from IRIS3D simulations of a centered target and an offset target. In the offset shot the total neutron yield is reduced, and the time of peak neutron production occurs earlier as a result of the nonuniform compression of the target. The asymmetric target areal density min/max curves demonstrate that the areal density is different along different lines of sight. In the case of Figure 1, the maximum areal density curve is along the line of sight in the direction of the offset, and the minimum is along the line of sight opposite the direction of the offset. This curve demonstrates that charged particle energy spectra are dependent on the lines of sight. Nonuniformities can be inferred by comparing these spectra.

Cryogenic targets are filled with deuterium-tritium (DT) gas surrounded by a layer of DT ice. A plastic ablator encloses the target. In recent OMEGA cryogenic implosions, 86% of targets were positioned within 15 μm of the desired position [4]. Cryogenic targets implode and fuse, and the deuterium-tritium fuel forms neutrons and alpha particles as fusion products. The neutrons collide with and elastically scatter background deuterium and tritium ions [1,3]. Similar to secondary protons, these knock-on deuterons are slowed down as they travel through the plasma due to their non-zero electric charge. The knock-on deuteron energy spectra can then be used to diagnose nonuniformities in the target [1,3]. Scientists at MIT's Plasma Science and Fusion Center are currently working to use a comparison between detected knock-on deuteron spectra and simulated spectra to diagnose areal density asymmetries in OMEGA implosions.

2. Secondary Protons:

Room temperature implosions use gaseous fuel surrounded by a plastic shell. The targets are irradiated, and the plastic shell is ablated off driving the compression of
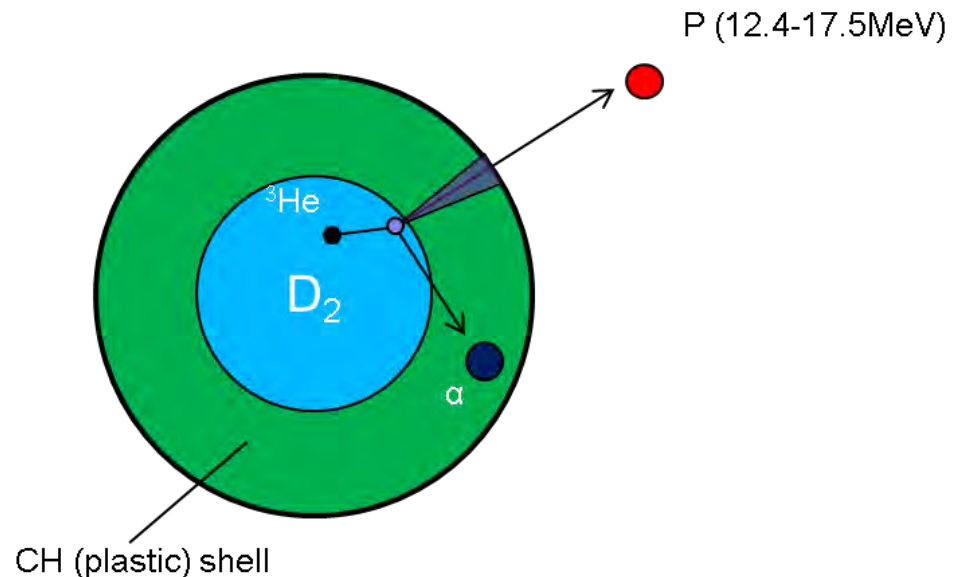

P (12.4-17.5MeV)

³He

D₂

α

CH (plastic) shell

Figure 2: Cross section of a room temperature D₂ target. Both the ³He and secondary proton undergo stopping power, losing energy to the surrounding plasma as they travel through the target.

the fuel. This compression produces conditions with sufficiently high temperatures and pressures that enable the fuel to undergo thermonuclear fusion. D₂ gas fuses according to the equation,

$$D + D \rightarrow {}^{3}He(0.82 \text{ MeV}) + n(2.45 \text{ MeV}) \tag{2}$$
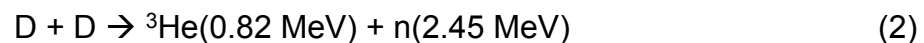
The resulting ³He is capable of then fusing with background deuterium plasma forming an alpha particle and a proton (P) [2].

$$^{3}He(< 0.82 \text{ MeV}) + D \rightarrow \alpha \ (1.7\text{-}6.6 \text{ MeV}) + P(12.4\text{-}17.5 \text{ MeV}) \tag{3}$$
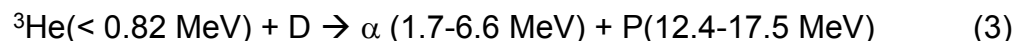
The ³He product is produced at an initial energy of 0.82 MeV but loses energy quickly as a result of having a +2 nuclear charge. Due to its relatively low energy, ³He does not travel a significant distance before stopping in the plasma. Figure 2 shows a ³He

particle created in the D_2 fuel and undergoing a secondary reaction near the D_2/plastic

interface. The secondary proton is slowed down while passing through the plastic shell.

IRIS3D uses spherically symmetric iceblock profiles as benchmarks before post-

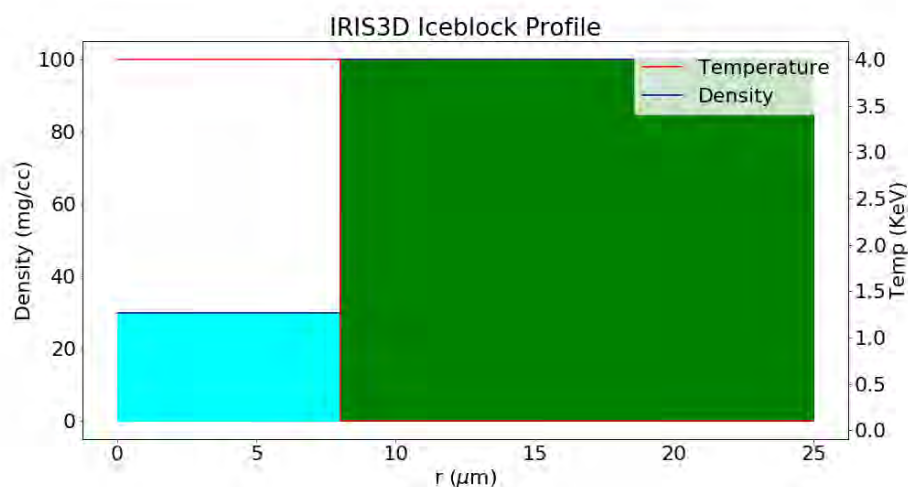processing hydrodynamic simulations. The stopping-power algorithm was optimized and

Figure 3: Simplified temperature and density plot for an imploded target. Cyan is D_2 gas. Green is the plastic shell. In the gaseous region of the profile, the density is low compared to the plastic region.

tested using iceblock models. An example of an iceblock profile is shown in Figure 3.

The profile is characterized by temperature, density, and the ratio of elemental

components. For example, the plastic may be composed of a 1:1 carbon to hydrogen

ratio. In Figure 3, the iceblock model is characterized by a region of D_2 fuel of density 30

mg/cc that forms a sphere of radius 8 μm. Beyond the D_2 fuel, the iceblock model

shows the plastic shell, which is much higher in density, 100 mg/cc, and lower in

temperature, 0.1 keV. The plastic shell extends beyond 25 μm. More energy loss occurs

in the shell due to the higher density compared to the fuel. Figure 3 is the first iceblock

model in a series used to quantify a relationship between areal density and energy loss.

Additional iceblocks have profiles with densities as large as 35 g/cc with radii which

extend to 100 μm.

Areal density, defined in equation (1), is a useful quantity which can be used to infer target nonuniformity. In the absence of asymmetries, the plasma would have the same areal density at any viewing angle. Nonuniform compression, such as that which occurs when the target is offset, leads to areal density variations around the target. By comparing areal density measurements from different lines of sight, nonuniformities can be inferred.

Secondary protons are produced at locations near the hotspot of the plasma where ^{3}He fusion occurs. Secondary protons are emitted isotropically and will travel a path length which is different from the radius of the target. The secondary protons will experience an areal density given by,

$$\rho L = \int_0^L \rho dl \qquad (4)$$

where L is the distance the proton travels from its birth location to the detector. In IRIS3D simulations, secondary protons are typically produced within 5 μm of the birth location of a ^{3}He. Spectra from these secondary protons are useful for inferring ρR_{fuel}, ρR_{Shell}, and ρR_{total} [2]. This is accomplished by comparing the measured proton energy and birth proton energy. Using this comparison, it is possible to compute the ρR of a target up to values where secondary protons are unable to escape the plasma.

The stopping power model used in IRIS3D is the Li-Petrasso stopping power

model [5]. As a result of stopping power, particles in higher ρR targets will lose a greater

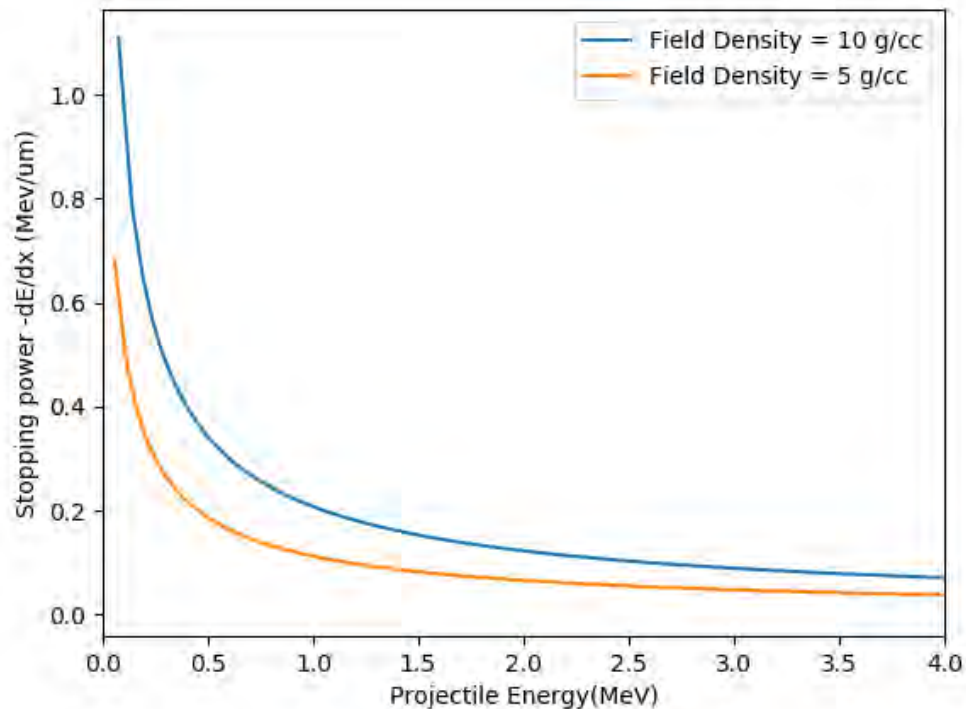**Stopping Power as a Function of Energy for Varying Field Density**

Figure 4: Plot showing energy loss for a proton with an initial energy of 4 MeV in differing field densities. The magnitude of stopping power is much larger for particles at low energies. As a result, particles born at low energies are less likely to be detected. Increased plasma density contributes to an overall increase in stopping power at all particle energies.

amount of energy compared with lower ρR targets. Figure 4 shows a plot of the

magnitude of stopping power for a 4.0 MeV proton in two different plasma densities.

Figure 4 demonstrates that the magnitude of the stopping power increases as particles

lose energy to the surrounding field and that increased plasma density results in an

increase in stopping power. Furthermore, charged particles in high areal density

implosions may become trapped in the plasma. For example, secondary protons can

escape areal densities below ~350 mg/cm^2. This makes secondary protons especially

useful as a diagnostic for ρR asymmetries in implosions with areal densities less than

350 mg/cm^2.

Stopping power is highly linear at high particle energies and low ρR values. By

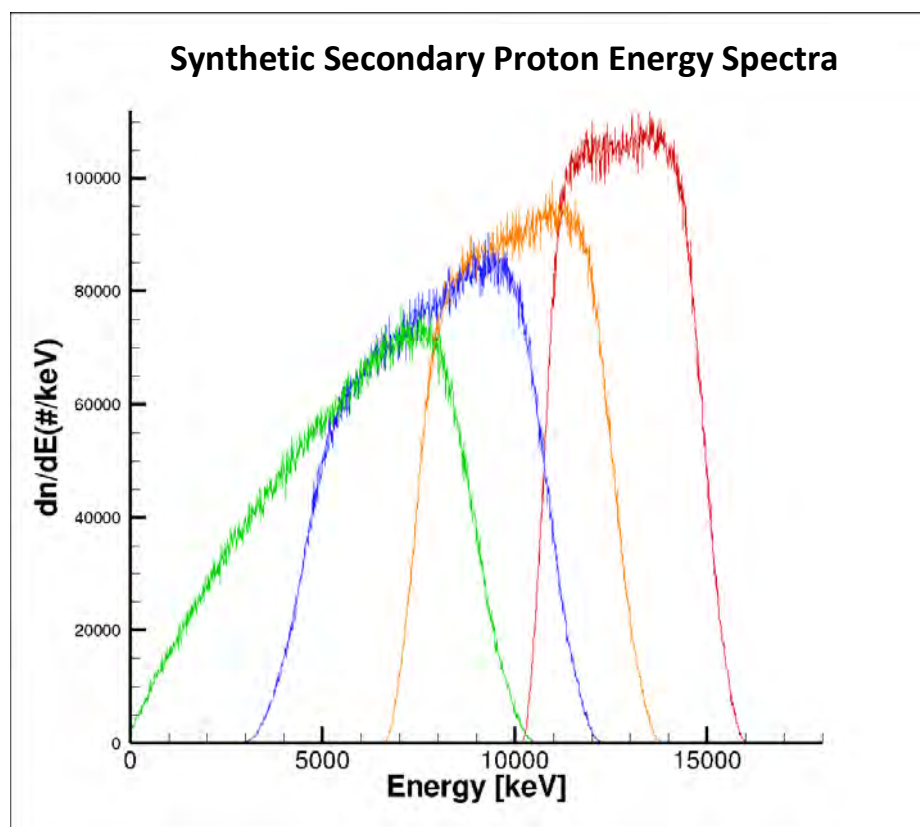comparing the mean energy of secondary protons with varying areal density in iceblock

Figure 5: A plot showing secondary proton energy spectra for varying areal-density values. 50 mg/cm^2 (red), 100 mg/cm^2 (orange),150 mg/cm^2 (blue), 200 mg/cm^2 (green). Spectra were calculated from IRIS3D iceblock models of varying plasma density.

models, a one-to-one function was derived between areal density and average

secondary proton energy. The correlation between average energy and areal density is

apparent in Figure 5: secondary protons in a simulated implosion with areal density

50 mg/cm^2 have an average energy of ~12.5 MeV (red curve) whereas secondary

protons in a simulated implosion with areal density 100 mg/cm^2 have an average energy

of ~10.3 MeV. As areal densities approach values of ~200 mg/cm^2, some secondary

protons are unable to escape the plasma, resulting in a bias in the average energy. The

average energy is only computed for those protons which have trajectories and initial

energies that are sufficient to escape the plasma and be detected, resulting in a

positively skewed calculation.

Figure 6 shows the mean energy of secondary protons in symmetric targets for

increasing values of ρR. For low areal densities, the temperature of the plasma has little

effect on the mean energy of the secondary protons. However, as areal densities

increase, the resulting energy of the secondary protons becomes comparable to the
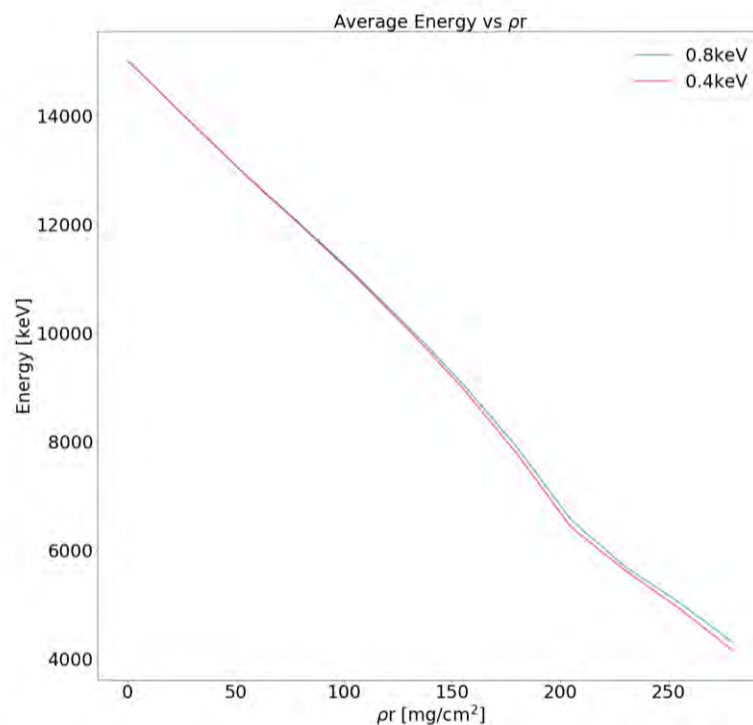
Figure 6: Plot of average energy of secondary protons vs areal density. The blue curve shows secondary protons in a plasma with a temperature of 0.8 keV and the red curve is for secondary protons in a plasma with a temperature of 0.4 keV

energy of the particles in the plasma. The change in functional form occurs abruptly at

~200 mg/cm^2 because some secondary protons produced at energies of ~12.4 MeV are

unable to escape the target at this areal density. As a result of the increased stopping

power in lower temperatures, cooler plasmas have a lower ρR threshold at which the

secondary proton diagnostic remains viable. At lower energies and cooler temperatures,

stopping power becomes increasingly model dependent [7].

A linear fit to the graph in Figure 6 provides a relationship between mean energy

and areal density of the form,

$$E(\rho R) = m * \rho R + Eo \tag{5}$$

where E(ρR) is the mean energy as a function of ρR, m is energy loss in keV/mg/cm^2,

Eo is the mean energy in keV of a secondary proton at birth (14,950 keV). m has a

value of ~ -41.186 keV/mg/cm^2. In order to infer the areal density of a target along a

particular line of sight, the mean energy of the secondary protons is calculated from the

detected spectra and the areal density is then computed using the inverse of the

function above, which has the form,

$$\rho R(E) = \frac{E - Eo}{m} \tag{6}$$

where E is the average energy from the detector.

Figure 7 shows a hydrodynamic profile calculated by the code DRACO for an

offset target at peak neutron production. DRACO is a two-dimensional hydrodynamic

code which simulates the physics of the implosion. The hydrodynamic simulation is then

post-processed by IRIS3D. IRIS3D generates synthetic spectra which can be compared

with measured spectra from the implosion. In order to post-process DRACO

simulations, which are two-dimensional, IRIS3D assumes rotational symmetry in phi.

For shot 88581, target offset is the dominant source of nonuniformity. The target offset

results in an *l=1* mode which is rotationally symmetric in phi [4]. The offset resulted in a

region of high density in the direction of the offset, which corresponds to a higher
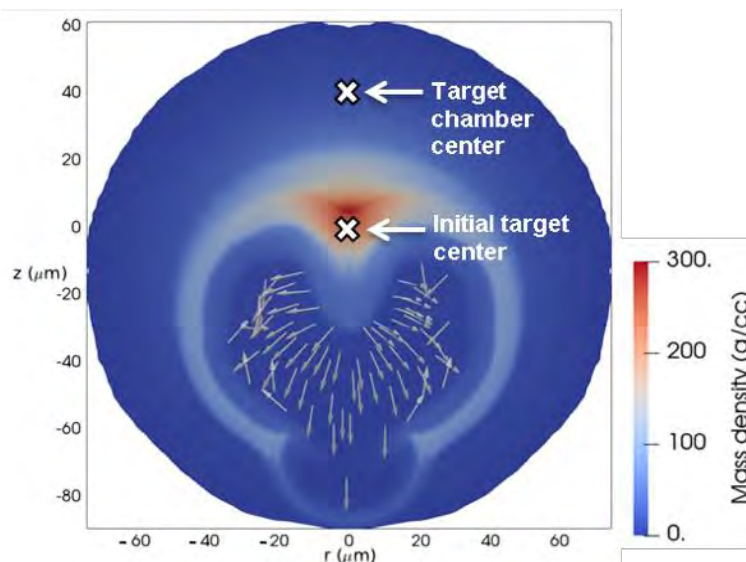
DRACO Profile of Shot 88581 at Peak
Neutron Production

Figure 7: A 2-D DRACO profile for shot 88581, which had a 40 um offset along the line of sight of detector TIM 6. The shot was reoriented in IRIS3D such that the offset was 40 um in the direction of the north pole of the target. IRIS3D assumes symmetry in phi in order to post-process the 2D simulation

expected ρR value along a line of sight aimed at the north pole.

Figure 8 shows the inferred areal density values from post-shot simulations of shot 88581 and the positions of the wedge range filters (WRF) around the target. The inferred areal density values were computed using Eq. (6) by post-processing the DRACO simulation of shot 88581 to obtain the mean energy values. Based on this plot, WRF3, near the south pole of the target, should observe a spectrum that is significantly different than the spectrum seen observed by WRF2, which is near the north pole facing a high-density region. The secondary proton spectrum at WRF2 should be significantly downshifted and broadened compared to WRF3. The spectrum at WRF3 is expected to

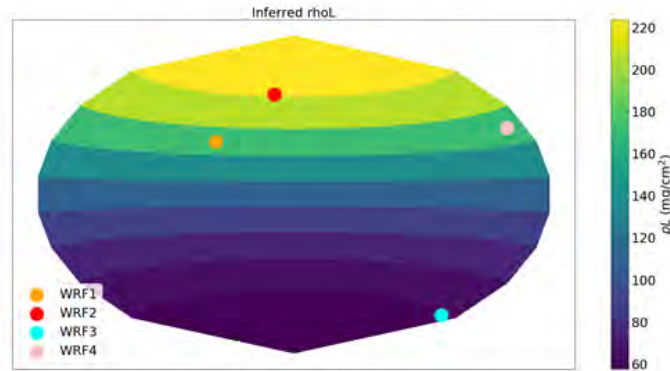yield a mean energy value of ~12.5 MeV. Future work will be done to compare the measured and simulated spectra.

Figure 8: Hammer plot showing inferred ρL for shot 88581. The inferred areal density values were computed from equation (6)

3. Knock-on deuterons:

Knock-on deuterons are the product of an elastic collision between a neutron produced from DT fusion and a deuterium nucleus. Knock-on deuterons are produced in cryogenic targets and are useful for diagnosing areal-density asymmetries. Deuterium and tritium fuse according to,

$$D + T \rightarrow n (14.1 \text{ MeV}) + \alpha \tag{7}$$
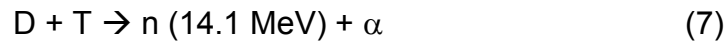
while under high pressure and temperature [1]. The neutron may then collide with background deuterium nuclei in an elastic collision,

$$D + n(14.1 \text{MeV}) \rightarrow D'(\leq 12.5 \text{ MeV}) + n'. \tag{8}$$
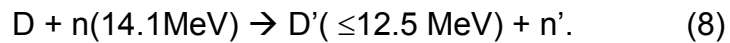
The resulting energy loss of D' as it exits the target makes the knock-on deuteron energy spectra useful for computing target areal densities. The unshifted deuteron energy spectrum is characterized by a peak formed between 12.5 MeV and 9.6 MeV. The spectrum trends upward from 9.6 to 0.0 MeV (the black curve in Figure 10 shows

the unshifted spectrum). Integrating under the peak of the unshifted knock-on deuteron spectrum yields an effective number of particles which contains ~15.7% of the knock-on yield [1,3].

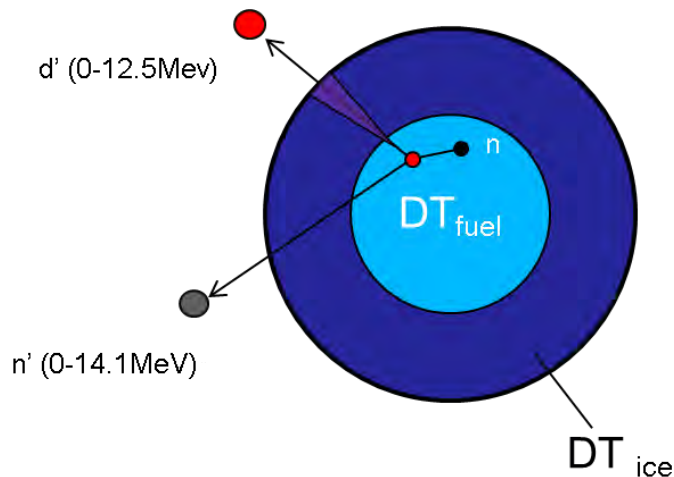As target ρR increases, the effective number of particles increases in proportion

Figure 9: Schematic of production of a knock-on deuteron (denoted by d'). The knock-on-deuteron is formed from an elastic collision with a primary DT neutron. The deuteron experiences energy loss due to stopping power because of its positive charge.

to ρR [3]. However, as areal densities reach values >80 mg/cm^2, the characteristic peak is no longer identifiable as a result of the distortion of the knock-on deuteron spectrum from stopping power [1,3].

In a collision between a deuterium nucleus and a 14.1 MeV neutron, the deuterium nucleus scatters off with an energy between 0 MeV and 12.5 MeV. Figure 9 shows the knock-on deuteron losing energy to the background plasma due to stopping power, similar to the secondary proton. As the spectrum is downshifted, the ratio between the effective number of particles (the area beneath the peak) and total knock-on yield (area beneath the entire spectrum) grows in direct proportion to the ρR of the target [1,3].

Knock-on deuteron spectra are useful for diagnosing areal density asymmetries because the spectrum changes shape for small differences in ρR for areal densities greater than 80 mg/cm^2. At these higher areal densities, the peak of the unshifted knock-on deuteron spectrum (9.6 MeV-12.5 MeV), is washed out by the stopping power of the plasma. However, the spectrum is sensitive to small changes in areal densities and is therefore a useful tool for diagnosing target asymmetries. By comparing two spectra from different detectors with simulated spectra, one can infer the extent of nonuniformity.
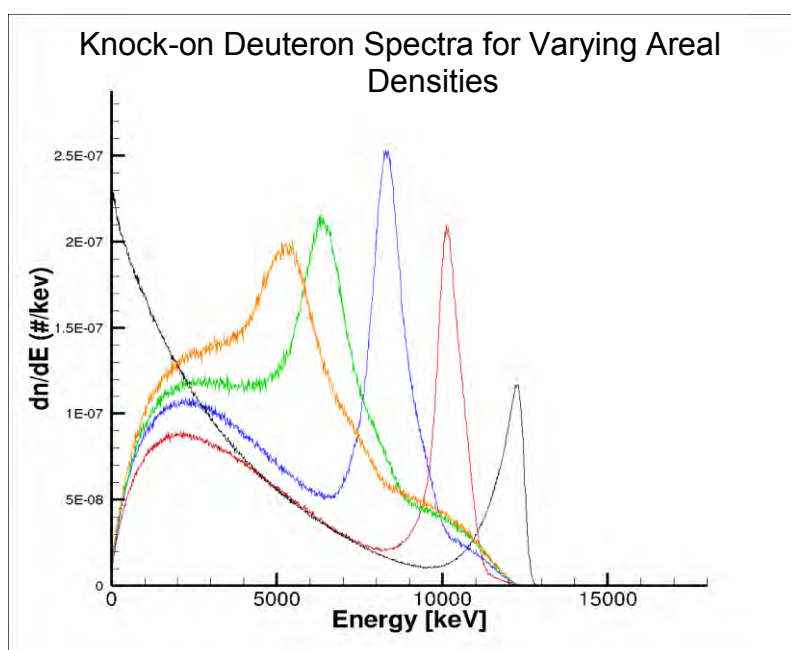

Figure 10: Knock-on deuteron spectra for varying areal density values. 0 mg/cm^2 (black), 15 mg/cm^2 (red), 30 mg/cm^2 (blue), 45 mg/cm^2 (green), 60 mg/cm^2 (orange). The peak becomes difficult to distinguish as areal density increases beyond 80 mg/cm^2. Spectra were produced using iceblock models.

Knock-on deuteron spectra, as shown in Figure 10, are characterized by a distinct peak in low-areal-density implosions. The peak becomes downshifted and broadened by stopping power as the areal density of the target increases. The total
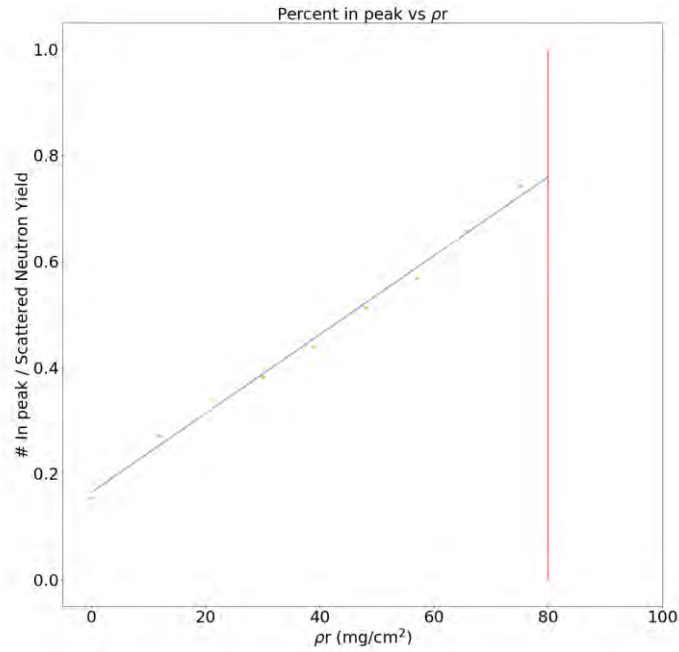
Figure 11: A scatter plot (orange points) showing the ratio between the knock-on deuteron yield within the peak and the total scattered neutron yield with a best fit line (blue) drawn. The red line corresponds to the areal density at which the peak is no longer distinguishable within the knock-on deuteron spectrum.

knock-on deuteron yield increases in proportion to areal density. The equation,

$$Y_{eff}/Y_{KOD} = k * \rho R + r_0 \tag{9}$$

is then deduced where the ratio of the yield underneath the peak to the total yield is given by Y_{eff}/Y_{KOD} and r_0 (=15.7%) is the ratio for a target with $\rho R = 0$ [1], Y_{eff} is defined as

$$Y_{eff} = \int_a^b N(E)dE \tag{10}$$

where N(E) represents the knock-on deuteron yield at energy E, and a and b are the bounds on the peak of the spectrum. To determine the areal density of targets with an areal density ≤ 80 mg/cm^2 the equation can be rearranged into the form,

$$\rho R = (Y_{eff}/Y_{KOD} - r_0) * k^{-1} \tag{11}$$

where k is a constant that corresponds to the change in the ratio between the effective yield and total yield with respect to a change in areal density.

In implosions where the areal density exceeds ~80 mg/cm^2, the knock-on deuteron spectrum is no longer characterized by a well-defined peak. Figure 11 illustrates that the ratio of the yield under the peak (Y_{eff}) to the total scattered neutron yield increases linearly with areal density until the peak of the knock-on deuteron spectrum is no longer distinguishable. Similar to the secondary proton spectrum, as areal density values increase, the number of knock-on deuterons unable to escape the plasma increases. It is possible to diagnose asymmetries by comparing the inferred areal density and shapes of the knock-on spectra from several detectors around a target.

4. Conclusion:

The Monte-Carlo particle tracking code IRIS3D was extended to model the behavior of charged particles in OMEGA implosions in order to develop two diagnostics for implosion asymmetries. Asymmetries in ICF implosions result in less efficient conversion of laser energy to hot spot energy, decreasing the total neutron yield.

One diagnostic applies to deuterium-deuterium fusion. Secondary protons formed from the fusing of a helium-3 with a background deuterium nucleus are slowed

down from their birth energy as they leave the target by a phenomenon called stopping power. The amount of energy secondary protons lose while travelling through the target is directly proportional to the areal density of the target at high energy and low areal density. Therefore, an areal density can be inferred by comparing the mean energy of secondary protons emitted from the target. Asymmetries can then be diagnosed by comparing multiple measurements of secondary proton mean energy along different lines of sight.

The second diagnostic applies to deuterium-tritium cryogenic targets. Knock-on deuterons are deuterium nuclei that collide elastically with a neutron formed from deuterium-tritium fusion. After colliding, the knock-on deuteron will travel through the target and lose energy as a result of stopping power. The unshifted knock-on deuteron energy spectrum is characterized by a sharp peak between 9.6 MeV and12.5 MeV which can be seen in Figure 10. The energy range of the peak becomes downshifted and broadened in proportion to areal density. The effective yield is computed by integrating the area under the peak. The ratio between the effective yield and total knock-on yield is directly proportional to areal density. By comparing the ratio at varying areal density values, a linear fit was produced which can be used to determine the ρR of a target. The linear fit is only a viable diagnostic for areal densities less than ~80 mg/cm^2 because at areal densities greater than this threshold, the effective yield is indistinguishable within the knock-on spectrum. However, the knock-on deuteron energy spectrum remains useful for areal densities greater than 80 mg/cm^2 because the spectrum changes noticeably for small changes in areal density. In order to diagnose asymmetries in high-areal-density targets, one must compare the shape of the knock-on

deuteron spectrum from detectors around the target with simulated data to determine if the areal densities vary significantly. Future work will compare the simulated knock-on and secondary proton data with experiment for the first time.

References:

1. C.K. Li et al., *Study of direct-drive, deuterium–tritium gas-filled plastic capsule implosions using nuclear diagnostics at OMEGA,* Phys. Plasmas **8,** 4902 (2001)

2. F.H. Seguin, et al., *Using secondary-proton spectra to study the compression and symmetry of deuterium filled capsules at OMEGA.* Phys. Plasmas **9,** 2725 (2002)

3. P.B. Radha et al., *A novel charged-particle diagnostic for compression in inertial confinement fusion targets.* Phys. Plasmas **7,** 1531 (2000)

4. O. Mannion, Private communication

5. C.K. Li and R. D. Petrasso, *Charged-Particle Stopping Powers in Inertial Confinement Fusion Plasmas,* Phys. Rev. **70,** 3059 (1993)

6. F. Weilacher et al., *Three-dimensional modeling of the neutron spectrum to infer plasma conditions in cryogenic inertial confinement fusion implosions,* Phys. Plasmas 25, 042704 (2018)

7. Lowell S. Brown, Dean L. Preston, and Robert L. Singleton Jr, *Charged Particle Motion in a Highly Ionized Plasma*. Phys. Plasmas 0501084 (2007).

Spectral Moment Analysis of the Deuterium-Deuterium Neutron Energy

Distribution from Inertial Confinement Fusion on OMEGA

A. DeVault

Penfield High School

Advisors: C. J. Forrest, O. Mannion

Laboratory for Laser Energetics, University of Rochester, 250 East River Road

*Rochester, New York 14623-1299, USA*

December 2019

ABSTRACT

Nuclear diagnostics are essential for inferring the conditions of the deuterium-deuterium (DD) fuel during compression for inertial confinement fusion experiments. The plasma temperature and velocity influence the neutron energy distribution emitted from the fusing target. Bulk flow of the plasma affects the first spectral moment (mean) while the ion temperature affects the second spectral moment (variance). These signatures indicate the presence of fluid motion during hot-spot formation as well as the temperature of the plasma, both of which are important metrics to assess implosion performance. A forward-fit analysis technique was developed to obtain the ion temperature and bulk flow velocity from a primary (DD) neutron energy distribution obtained from a neutron time-of-flight spectrometer. This approach was utilized in a recent campaign to measure the effect of low-mode nonuniformities induced through intentional target offsets. The technique was tested using existing data and simulations and was found to be relatively accurate in determining ion temperatures and bulk flow velocities. A positive, linear relationship was found to exist between offset and bulk flow velocity. A low-mode asymmetry introduced by a systematic offset/imbalance in the laser-target system can be mitigated using a standardized offset based on this relationship.

I. INTRODUCTION

Studying inertial confinement fusion (ICF) is a primary objective at the Laboratory for Laser Energetics (LLE). ICF targets are made out of a thin spherical ablator shell less than 1 millimeter in diameter with both solid and gaseous fuel within.

The energy deposition required to trigger nuclear fusion is achieved through the use of high-power UV lasers. The 60 OMEGA UV laser beams deliver up to 30 kJ of energy onto the ICF target during a nominal 1-ns square pulse. The symmetric illumination rapidly heats and ablates the thin shell. Following Newton's third law, every action has an equal and opposite reaction, and thus the force exerted by the ablating shell provides an inward compressive force upon the target, which, in this work, is filled with deuterium–deuterium (DD) fuel. In an ideal, symmetric implosion, all kinetic energy from the ablator would be transferred to ion thermal energy, heating the very center of the imploding target (the hot spot) to reach the extreme temperature and pressure conditions required to initiate fusion. Temperatures of approximately 100 million Kelvin and pressures exceeding 200 billion atm must be reached in order to overcome the repulsive Coulomb force between two light nuclei and trigger fusion. However, in a realistic implosion, imperfections and asymmetries lead to imperfect translation of kinetic energy to thermal energy, leading to residual kinetic energy in the system, which manifests as flow velocities during the formation of the hot spot.

Bulk flow velocity is characterized as the net velocity of the fusing plasma. Flow velocities are a symptom of asymmetrical implosions, typically caused by unbalanced energy deposition. In order to detect bulk flow velocities, the spectra of energetic neutrons emitted by the fusing plasma can be analyzed. Equation 1 illustrates the relevant neutron-producing fusion reaction of deuterium-deuterium, along with the approximate energies of the products.

$$^{2}\text{H} + {}^{2}\text{H} \gg n(2.45 \text{ MeV}) + {}^{3}\text{He}(0.81 \text{ MeV}) \tag{1}$$
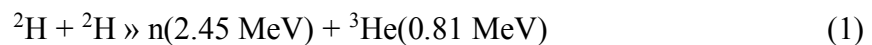
The neutron spectra can be detected by a neutron time-of-flight (nTOF) spectrometer, which relies on a scintillator and photomultiplier tube to relay a signal relative to the number of neutrons incident on the detector. If the time of the implosion is known relative to the neutron detection signal, and the detector is at a known distance from the target, then the velocity and therefore energy of the neutrons can be determined. Since deuterium-deuterium fusion is known to emit approximately monoenergetic neutrons, any deviation from this mean energy can be treated as a Doppler shift in order to determine the velocity of the fusing plasma towards or away from the detector. While bulk flow contributes to shifts in mean energy, ion temperature (T_{ion}) affects the mean energy to a small degree [1], but mainly influences the broadening of the spectra. Since the neutron spectrum for deuterium-deuterium fusion can be fit using a modified gaussian, its mean energy and broadening (which are used to determine bulk flow velocity and T_{ion}, respectively) can be described as spectral moments, with the first spectral moment being the mean, and the second spectral moment being the variance (broadening).

In order to measure the effect of asymmetries on an ICF target, campaigns have been held utilizing intentional target offsets to induce low modes of nonuniformity. Offsetting the target will shift the focus of the laser power away from the center of the target but will not alter the laser power balance relative to the focus of the beams. Experiments designed with induced modes and asymmetries help scientists to better understand asymmetries in the laser-target system that may be preventing ideal implosions. Induced modes can potentially serve as a tool for correcting any inherent

asymmetries in the laser, as these induced modes can be used to counteract unbalanced energy deposition.

An analysis technique was developed in order to explore the effect that these induced modes have on the bulk flow, yield, and ion temperature of deuterium-deuterium fusion experiments. Utilizing data retrieved by neutron time-of-flight spectrometers, a neutron energy distribution was modeled and subsequently used to determine the spectral moments of the data. Using this analysis, dozens of nominal shots were analyzed to identify correlations between known variables such as shell thickness, and ion temperature or bulk flow velocity. The technique was also used on campaign shots to determine the relationship between target offset and the bulk flow velocity of the fusing plasma (an indicator of the symmetry of the implosion).

II.   FUSION NEUTRON SPECTRA

DD fusion's single, approximately monoenergetic, gaussian neutron distribution allows for accurate curve fitting and analysis. In DD fusion, two hydrogen isotopes combine to form Helium-4 before instantly decaying into Helium-3 and a 2.45 MeV neutron (Equation 1). In a perfectly symmetric implosion under ideal conditions, a neutron distribution as pictured in Figure 2.1(a) would be expected. However, when asymmetries are induced, the presence of bulk flow velocity will alter the energy distribution (as pictured in Figure 2.1(b)). As a bulk flow velocity away from the detector is observed, lower mean energies will be interpreted (as represented by the
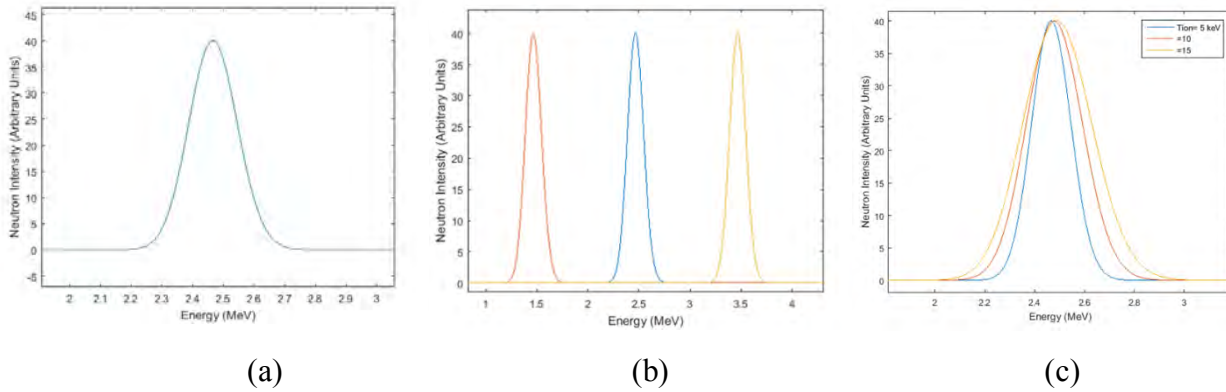
(a)　　　　　　　　　　(b)　　　　　　　　　　(c)

Figure 2.1(a): The neutron energy distribution expected from a symmetrical implosion.
(b): A highly exaggerated display of the effect that a bulk flow velocity will have on a gaussian neutron distribution.
(c): A display of the broadening and slight shifting of the neutron energy distribution as the ion temperature increases from 5 to 15 keV

orange curve), while velocities towards the detector will result in higher measured mean energies (as represented by the yellow curve). As T_{ion} increases (Figure 2.1(c)), the mean energy will shift slightly towards higher energies, and broadening will increase. The simulated effect of variable bulk flow velocity and ion temperature shown in Figures 2.1(a)-2.1(c) can be used to deduce the mean ion temperature and bulk flow velocity of experimental implosions. The effects of bulk motion and ion temperature on neutron distribution used here are consistent with those identified by Munro at the National Ignition Facility [2].

By utilizing induced modes through target offset, a bulk flow velocity of 0 can be pursued, indicating a more symmetric implosion along the line of sight of the detector, minimizing the residual kinetic energy present and improving the implosion efficiency.

III.   EXPERIMENTAL DETAILS

In terms of detecting asymmetries, the most insightful diagnostic is the neutron time-of-flight (nTOF) signal. Figure 3.1 shows the location of an nTOF detector on OMEGA and a schematic of its key components. Using a scintillator and a photomultiplier tube (PMT), the number of neutrons incident upon the scintillator can be measured as a function of time, allowing for the deduction of the neutron velocity spectrum and therefore the energy spectrum. The neutron energy distribution (dN/dE) determined by the nTOF signal can be used to determine the approximate ion temperature of the fusing plasma and the bulk flow velocity of the target.

Figure 3.1 shows that there is a clear line of sight from the fusing target to the nTOF detector, 13.4 m away. The xylene scintillator luminesces when struck by neutrons, allowing for a conversion of neutrons to photons. The photon signal is strengthened by a PMT and then digitized using an oscilloscope. While the analysis performed was based on the measurements and specifications of LLE's facilities, it may be easily altered to fit the specifications of other laboratories.
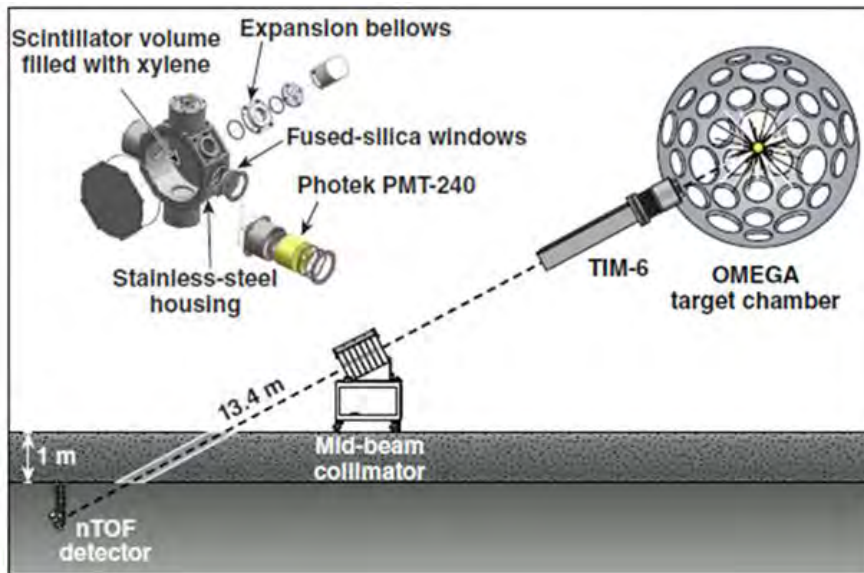

Figure 3.1 Location of a nTOF detector on OMEGA. It uses a xylene scintillator at a distance of 13.4 m from the site of fusion

As nTOF diagnostics and the deduction of neutron energy spectra rely entirely on the measurement of the time it takes for neutrons to reach a scintillator, the timing of the devices is crucial. The raw data must be placed in the lab frame of time, and absolutely timed with the time of fusion as '0'. The timing of the scintillator was calculated with a series of x-ray shots, performed by using targets that, upon irradiation, predictably emit x rays over a short time period (<100 ps). Since x rays travel at a constant, known speed over the known distance, their expected time of arrival could be compared with the arbitrary time units (τ) recorded by the scintillator in order to develop absolute timing. In order to place the arbitrarily timed signal in a reference frame zeroed at the time of emission, the equation [3]:

$$t = \tau - \left(\tau_0 + \Delta t_{laser} + \Delta t_{bang} \right) - \Delta t_{cal} - \Delta t_{att},$$

(2)

is used, where t is the true TOF of a signal; τ is the arbitrary time units; τ_0 is the time of a measured fiducial (in this case the fiducial consists of a train of eight gaussian pulses) of the recorded signal; Δt_{laser} is the delay between the start of the laser pulse (defined as 2% of the maximum laser power) and the fiducial as reported by a P510 streak camera; Δt_{bang} is the delay between the neutron/x-ray bang time and the beginning of the laser pulse as reported by an NTD (neutron temporal diagnostic); Δt_{cal} is a calibration constant accounting for any inherent delays and mistiming in the detector device; and Δt_{att} accounts for additional delays in the signal timing if a signal attenuator is used. Δt_{cal} was calculated using x-ray shots, but was then applied to DD fusion shots as a timing constant.

The instrument response function (IRF) of the scintillator, photomultiplier tube, cables, and oscilloscope also plays an important role in the calibration of the nTOF diagnostics. It represents the measured signal generated by a single incident neutron on the complete detector system [4]. The IRF was calibrated with ten x-ray shots, and was found to be extremely stable. A typical IRF is shown in Figure 3.2, and resembles
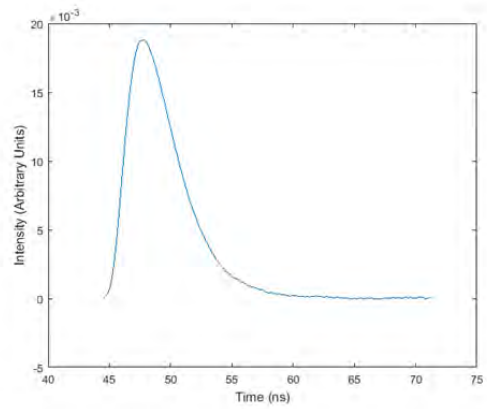

Figure 3.2
Absolutely timed IRF curve from an x-ray shot. It is important to note that the pulse duration of the x-ray shot is much smaller than the timescale shown here.

an exponentially modified Gaussian. It is necessary to determine and account for this curve when fitting the raw data as it will influence the timing and shape of the data.

IV. FORWARD FIT METHOD

In order to fit the "raw" neutron time-of-flight data and determine the ion temperature and bulk flow velocity, a number of factors must be considered. The Matlab function "nlinfit" or "Nonlinear fit" allowed for the parametrization of dN/dE (the neutron energy distribution) so that the fitting procedure would independently determine values for the mean energy shift and ion temperature.

The standard form for the neutron energy distribution as determined by Ballabio [1] is as follows:

9

$$dN/dE = I_0 \exp\left(-\frac{2\bar{E}}{\sigma^2}(\sqrt{E} - \sqrt{\bar{E}})^2\right) \tag{2}$$

where

$$\bar{E} = \langle E \rangle \left[1 - \frac{3}{2}\left(\frac{\sigma_{\text{th}}}{\langle E \rangle}\right)^2\right]^{\frac{1}{2}} \tag{3}$$

$$\sigma^2 = \frac{4}{3}\langle E \rangle^2 \left\{\left[1 - \frac{3}{2}\left(\frac{\sigma_{\text{th}}}{\langle E \rangle}\right)^2\right]^{\frac{1}{2}} - \left[1 - \frac{3}{2}\left(\frac{\sigma_{\text{th}}}{\langle E \rangle}\right)^2\right]\right\} \tag{4}$$

$$= \frac{4}{3}\bar{E}[<E> - \bar{E}] \tag{5}$$

$$E = E_0 + \Delta E_{\text{th}} \tag{6}$$

In Ballabio's semi-relativistic formula, the neutron distribution dN/dE (Equation 2) can be determined using I_0, a parameterized function of the standard deviation (ion temperature); σ^2 as defined in Equations 4 and 5; E as defined in Equation 6; and $\bar{E}$ as defined in Equation 3, representing the mean energy. Equations 3, 4 and 5 rely on $<E>$ and σ_{th}, which are parameterized functions of ion temperature (standard deviation). Equation 6 is in terms of E_0, representing the expected energy (2.45 MeV per neutron), and ΔE_{th}, the expected energy shift as a function of ion temperature, yielding the expected mean energy without compensating for the mean energy shift from bulk flow velocity. To determine the value of the mean energy shift that is derived from a bulk flow velocity, the difference between $\bar{E}$ and E is evaluated as a parametrized function of bulk flow velocity. Once the small shift in mean energy due to ion temperature is accounted

for, the remaining Doppler shifting of the mean velocity and, by extension, the neutron energy distribution, is dictated by the bulk flow velocity. By comparing the expected energy value of 2.45 MeV with the shifted energy value, a velocity shift can be derived by converting to the time-scale, and this velocity shift is indicative of the bulk flow velocity. [5]

The analysis discussed herein utilizes Ballabio's formulas to determine dN/dE and derive values for mean energy shift and ion temperature. In order to match the "raw" data, the parameterized neutron energy distribution must be multiplied by the non-linear light output of the scintillator, and translated to the time/velocity scale of the data through the use of the relativistic energy equation, in which KE represents the energy of the neutrons, m_0 represents neutron mass, c is the speed of light, and v is the velocity of the neutrons.

$$KE = m_0 c^2 \left[\frac{1}{\sqrt{1 - \frac{v^2}{c^2}}} - 1 \right] \quad (7)$$

Once the neutron distribution is translated to the time axis, it must be convolved with a neutron response and instrument response (as pictured in Figure 3.2) in order to accurately match the signal recorded by the oscilloscope. The neutron response function also accounts for the difference between the instrument response functions measured on x-ray shots and fusion shots [6].
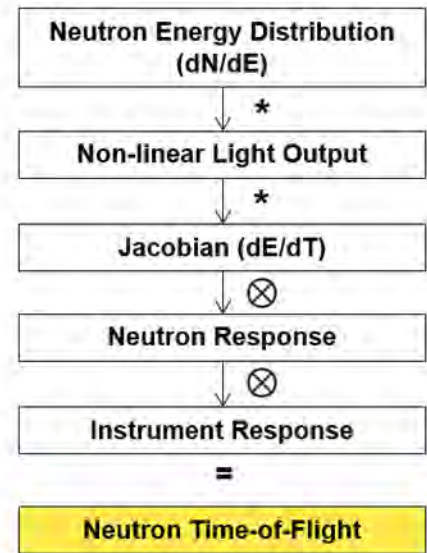

Figure 4.1
Flow chart representing the inputs that contribute to the "raw" nTOF data.

A convolution is a mathematical function defined by the equation:

$$f(t) * g(t) \equiv \int_{-\infty}^{\infty} f(u)g(t-u)du \tag{8}$$

Convolutions function to incorporate characteristics of both input curves into a single output curve. This is especially useful when dealing with response functions as it allows for rapid application of response functions to complex inputs (i.e. the modified gaussian that serves to approximate the neutron energy distribution).

A step-by-step flowchart displaying how each of the functions contributes to the nTOF data that is being fit is presented in Figure 4.1, allowing for a better understanding of how this data is being reconstructed in terms of the desired parameters. The produced neutron time-of-flight curve I(t) is in terms of the parameters of ion temperature and mean energy shift, and therefore can be used as a fit function for MATLAB 's nonlinear fit tool. The nonlinear fit tool requires initial approximate test values for all parameters in order to more quickly and correctly fit the given function. Simulated predictions (~ 3 keV) were used as starting values for the fit. Once functional, the MATLAB code allowed for the rapid determination of ion temperature and mean energy shift from a neutron time of flight signal.
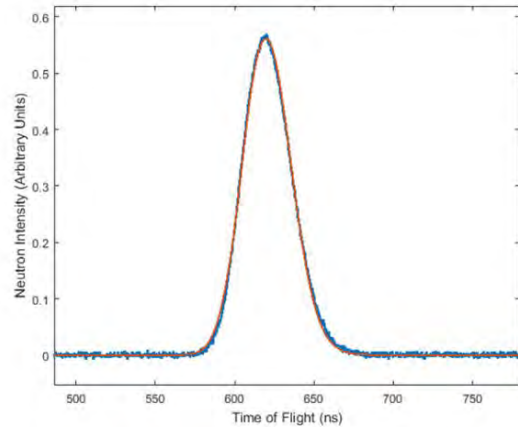

Figure 5.1
The neutron time-of-flight signal data (blue) and parameterized fit from MATLAB (orange) on an induced-mode shot. The two curves are almost indistinguishable.

12

V. APPLICATION OF ANALYSIS TO EXPERIMENTAL DATA

The fitting procedure described in Section IV was utilized to evaluate the ion temperature and bulk flow velocity of 35 nominal, well positioned shots and an induced-mode shot campaign investigating target offset. As seen in Figure 5.1, the signal and the parameterized fit for an induced-mode shot agree extremely well, indicating the quality of the fit.

Figure 5.2 shows the velocities obtained from 12 nominal shots. All analyzed shots yielded a strong positive bulk flow velocity, indicating an inherent asymmetry

Sampled Bulk Flow Velocities

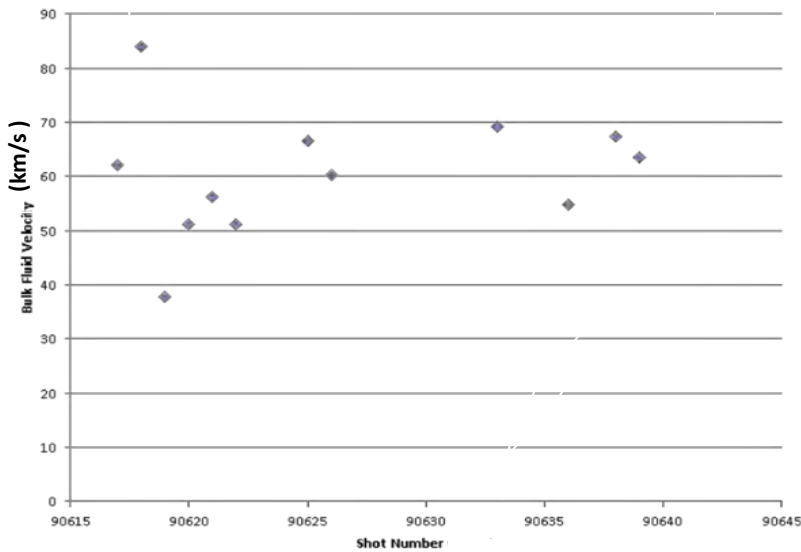
Figure 5.2
A sample of bulk flow velocities plotted with respect to shot number. Nominal shots tended to have strong positive bulk flow velocities.
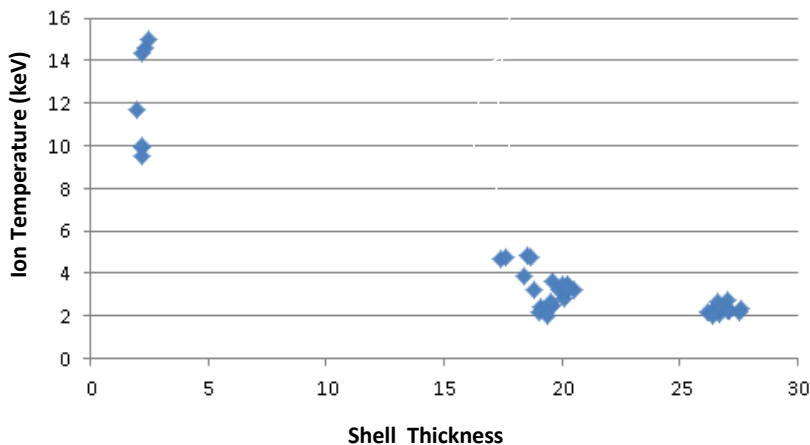
Tion(shell thickness)

Figure 5.3
Measured ion temperature as a function of shell thickness.

along the line of sight of the nTOF detector. It was also found that ion temperature was inversely related to shell thickness (Figure 5.3).

In addition to being applied to nominal shots, the analysis method was utilized to determine characteristics of plasmas in an induced-mode campaign in which intentional target offsets were applied. Since these shots were performed long before the timeframe of the research described herein, radiation hydrodynamic simulations such as Figure 5.4 for a 40-um offset had already been developed for the series of shots, and expected values for the bulk flow velocity had been determined. The experimental data from these shots was analyzed, and the agreement between the expected and experimental values was close (Figure 5.5). Just as the nominal shots had all yielded a positive bulk flow velocity, most of the experimentally determined velocities consistently overshot the simulated values by amounts that ranged from 10 km/s to 45 km/s (Figure 5.5).
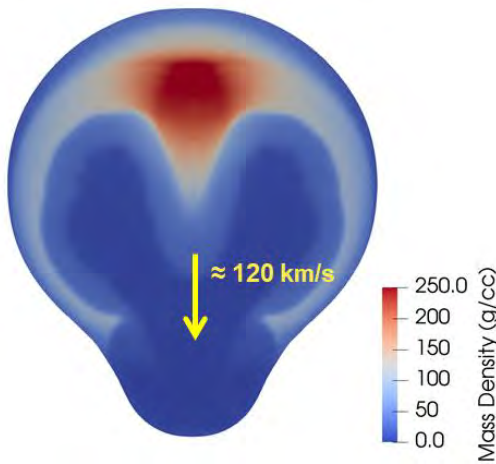

Figure 5.4
DRACO simulation of plasma density on a target with a 40 micron offset in the positive y-direction. [7]
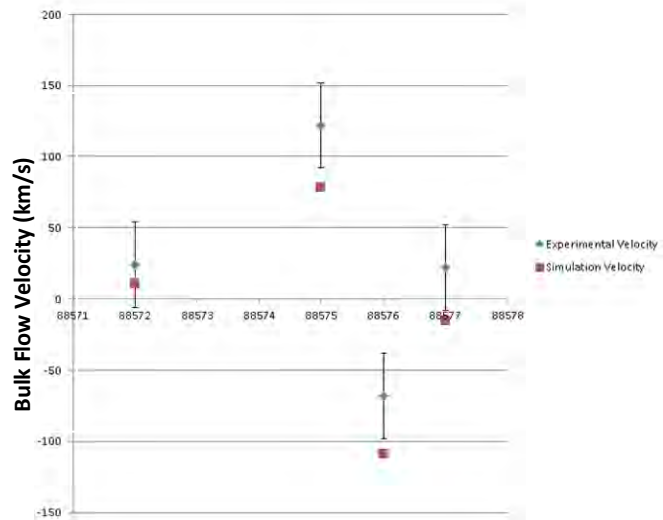
Figure 5.5
Experimental and simulated values for bulk flow velocity for four shots with various target offsets. Agreement is clear, but a consistent positive shift of experimental values indicates a systematic imbalance.

14

Experimental induced-mode shots could provide data with which to correct the inherent asymmetry in the system suggested by Figures 5.2 and 5.5. As seen in Figure 5.6, which plots data from the same four shots as a function of target offset, bulk flow velocity is directly related to the target offset. The average bulk flow velocity found on 0-offset control shots of the target-offset campaign is approximately 30 km/s as seen
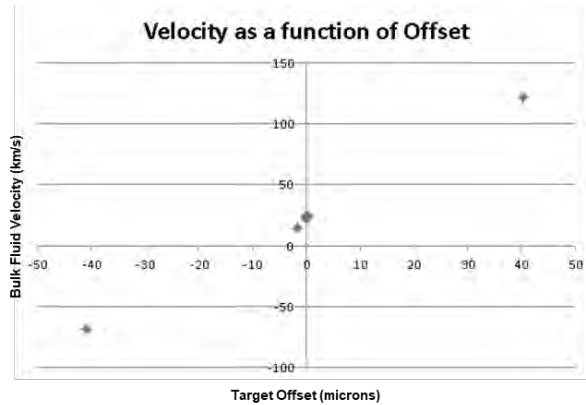

Figure 5.6
Bulk flow velocity as a function of target offset for the four shots plotted in figure 5.5. A direct linear relationship between target offset and bulk flow velocity is clearly visible even with minimal data.

in Figure 5.6, which is less than the bulk flow velocity found on 0-offset nominal shots. More data is therefore required to accurately determine the bulk flow velocity produced by a 0-offset shot. By performing more experimental shots and gathering more data, a linear trend line can be approximated for a plot similar to Figure 5.6, with the x-intercept yielding a target offset that would counteract the inherent asymmetry of the system.

VI. CONCLUSION

A forward-fit analysis technique was developed to evaluate the ion temperature and bulk flow velocity of a primary (DD) neutron energy distribution from a neutron time-of-flight spectrometer. This approach was utilized in a recent campaign to measure the effect of intentional target offset. Through comparison with existing data and simulations, the technique was found to be relatively accurate in determining ion temperatures and bulk flow velocities, the latter indicating an inherent asymmetry in the

laser-target system. In the future, more data from target-offset shots could potentially provide enough information to design a standardized offset to eliminate the inherent asymmetry.

VII. ACKNOWLEDGEMENTS

I would like to thank Chad Forrest, my project advisor who so patiently and expertly taught me everything I needed to know. I would like to thank Owen Mannion who kindly helped debug my code on multiple occasions and served as a resource for when I was stuck. I would like to thank the other participants in the High School program, for providing much-needed moral support and always being willing to offer a fresh set of eyes or a new mathematical trick. Finally, I would like to thank Dr. Stephen Craxton, who made the High School Research Program what it is today, and so patiently aided in the editing and revision of this report.

References

1. L. Ballabio, J. Källne, and G. Gorini, Nucl. Fusion **38**, 1723 (1998).

2. D. H. Munro et al., Phys. Plasmas **24**, 056301 (2017).

3. O.M. Mannion, Review of Scientific Instruments **89** 10I131 (2018).

4. X. Y. Peng, Review of Scientific Instruments **87**, 11D836 (2016).

5. B. Appelbe and J. Chittenden, Plasma Phys. Control. Fusion **53**, 045002 (2011).

6. R. Hatarik, Journal of Applied Physics **118**, 184502 (2015).

7. D. Keller, T. J. B. Collins, J. A. Delettrez, P. W. McKenty, P. B. Radha, B. Whitney, and G. A. Moses, Bull. Am. Phys. Soc. **44**, 37 (1999)

Measuring Isotherms of the Hydrogen-Palladium System

Katherine Glance

Pittsford Sutherland High School

Pittsford, NY

Advisors: Walter T. Shmayda and Matthew Sharpe

Abstract:

Palladium is a metal that absorbs and reacts with hydrogen and its isotopes to form palladium hydride at temperatures below 610 K. Palladium absorbs a significant amount of hydrogen within its crystal lattice and can act as a storage medium for hydrogen. The equilibrium residual hydrogen pressure over palladium was measured as a function of the hydrogen-to-palladium atom ratio (H:Pd) at fixed temperatures, producing isotherm curves. In the present work, equilibrium pressures have been measured for H:Pd ratios between 0.0 and 0.8 and temperatures between 293 K and 393 K. The van't Hoff plot of the present data shows consistency with literature data, regarding the standard enthalpy change ΔH and the standard entropy change ΔS. The ΔH was measured to be -36.8 kJ/mol and the ΔS was measured to be -143.9 J/mol*K. This experiment validates prior data on the hydrogen-palladium system.

1. Introduction:

   Palladium has long been used as a means of storing hydrogen and its isotopes. Prior to this work, the data known for palladium hydride was spread out across a wide temperature range and there was inconsistency in the literature. This paper's data fills in temperature gaps in that range, thus creating a denser and more filled in series of isotherms, which are curves relating pressure and H:Pd atom ratio at various temperatures.

   The study of the behavior of palladium hydride and palladium deuteride is important to the Laboratory for Laser Energetics (LLE) because of its mission to study inertial confinement fusion reactions. A typical test involves filling a cryogenic target with deuterium and tritium in order to establish the fuel density necessary for fusion conditions. In order to do this, a stock of gaseous deuterium and tritium is required for charging. A palladium sponge would make the targets' fuel delivery method involve simply alternating the temperature of the palladium, which is a simpler and cheaper alternative to the current approach. Precise measurements of pressure over palladium hydride are important to ensure that the delicate targets are not crushed due to a rapid pressure excursion. The purpose of creating these isotherms is to study the vapor pressure of hydrogen and deuterium above the palladium bed during the hydriding process. The focus of the current work is on the formation of palladium hydride at modest temperatures.

2. Theory:

   Palladium is part of a special group of metals called getters, which chemically combine with gas molecules upon contact. Getters are used in vacuum systems to remove gas from evacuated space in order to complete and maintain the vacuum. Palladium is non-reactive with oxygen at standard temperatures, and

therefore does not tarnish in air. As a hydrogen getter, palladium is able to absorb and react with hydrogen, motivating further study of palladium's viability as a storage medium for hydrogen and its isotopes. The formation of palladium hydride is a reversible reaction, given by:

(1)

$$\frac{x}{2} H_2(g) + Pd(s) \rightleftarrows H_x Pd(s)$$
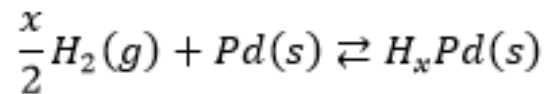
where g indicates the gaseous state, s indicates the solid state, and x indicates the moles of hydrogen contained in palladium hydride.

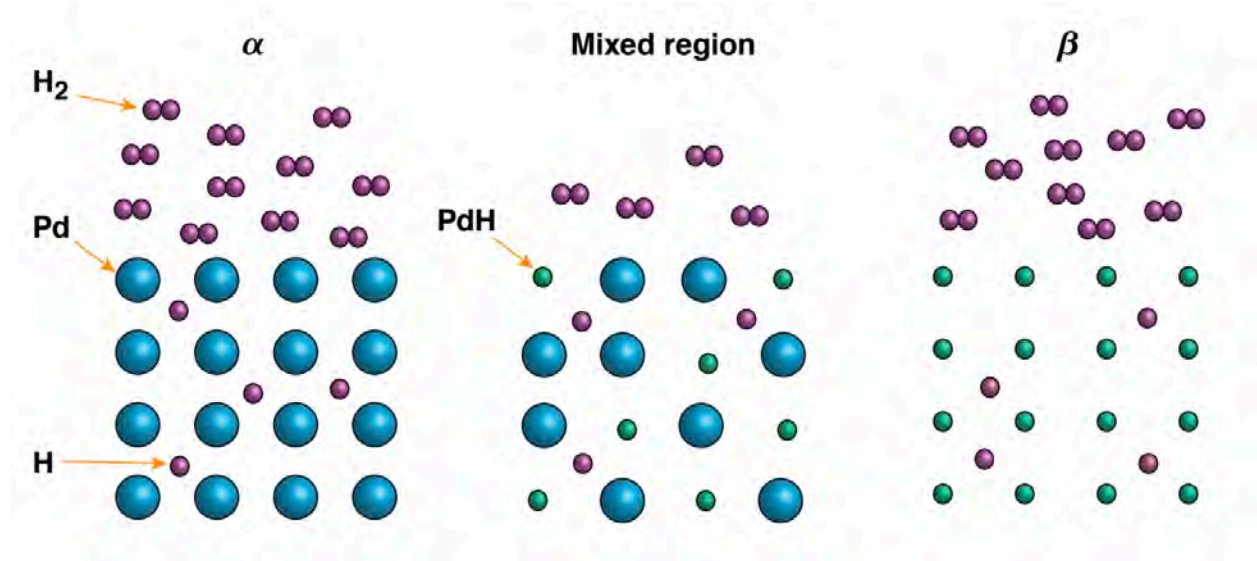*Figure 1: Visual representation of the alpha, mixed, and beta regions on an atomic level. Each region demonstrates unique interactions between hydrogen and palladium.*

Palladium absorbs hydrogen atoms in the three stages shown in figure 1. The first stage is the alpha region, where hydrogen molecules dissociate on the palladium surface and the hydrogen atoms are absorbed into the palladium matrix.

As seen in figure 2, the hydrogen vapor pressure at a constant temperature increases rapidly over the palladium as more hydrogen is added to the system. In this stage, hydrogen atoms occupy interstitial locations between palladium atoms in the palladium lattice but have not chemically bonded to palladium atoms. The second stage is the mixed region (alpha and beta region) where a fraction of the hydrogen atoms continue to be absorbed interstitially in the palladium, and the remaining fraction begins to chemically bond to palladium atoms within the crystal lattice. Hydrogen pressure above the palladium remains relatively constant with increasing H:Pd ratio in this stage. Hydrogen pressure above the palladium bed will increase in the mixed region as metal temperature increases. The third stage is the beta region where all possible hydrogen-palladium bonds have formed. As a result, the pressure increases significantly with increasing hydrogen-to-metal ratios. High pressures are required to insert gas in the beta region because additional hydrogen atoms are no longer bonding to palladium, but rather occupying the interstitial locations within the crystal lattice of the new material: palladium hydride.
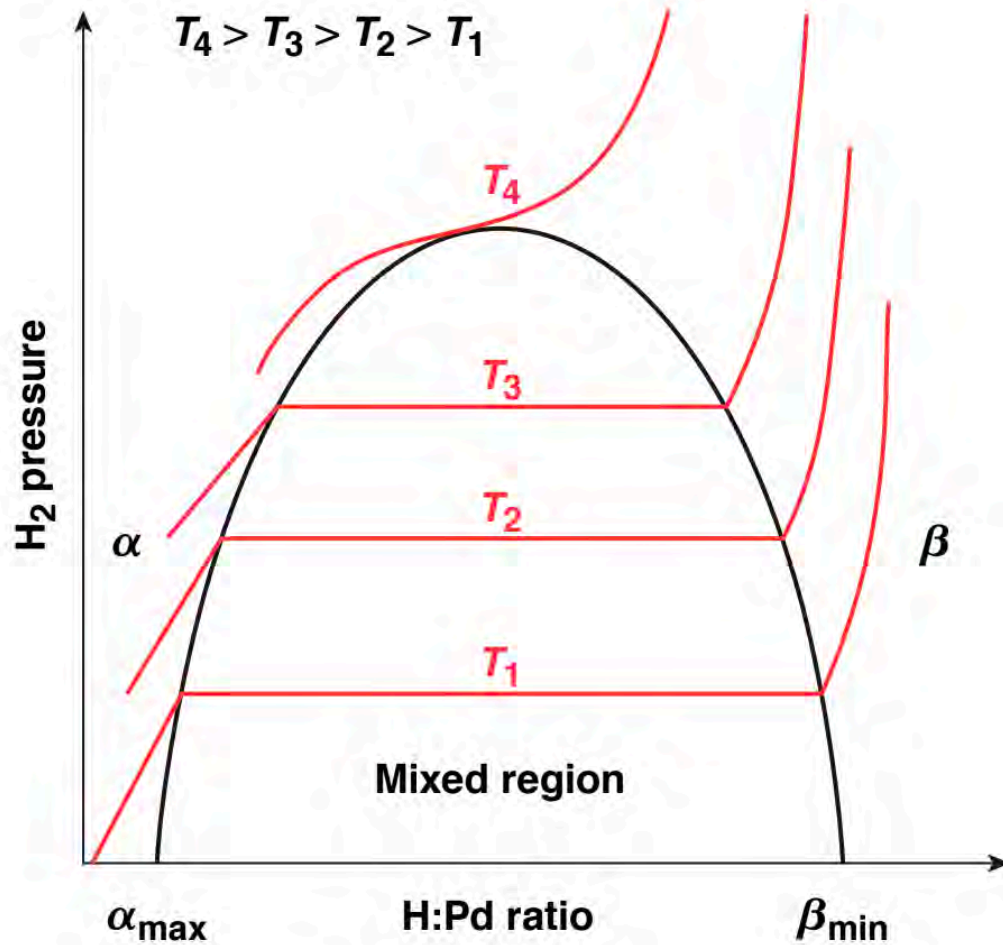
Figure 2: Isotherms indicating the relationship between pressure and composition at increasing temperatures, T_1-T_4. The parabola serves to show the three regions of palladium hydride: left of the parabola represents the alpha region, under the parabola represents the mixed region, and right of the parabola represents the beta region. Alpha max represents the part of the parabola that separates the alpha region of the isotherm from the mixed region. Beta min is the part of the parabola that separates the mixed region of the isotherm from the beginning of the beta region. (from Ref. 1)

Higher temperature isotherms have higher pressures and smaller mixed regions. This indicates that the hydriding reaction is exothermic, where H_2 (g) is favored at higher temperatures.

At standard temperature, a metal hydride can store 5.7 millimoles of gaseous hydrogen per cubic centimeter of metal at 0.5 atm. To store the same number of moles of hydrogen in a cubic centimeter container, the gas would have to be at a pressure of 130 atm. Using a metal getter as a storage mechanism and pump for hydrogen requires substantially less space, pressure, and money than using gaseous containers. Storing hydrogen in getters rather than containers also eliminates many dangers associated with pressurized hydrogen gas, such as laboratory fires or injuries caused by improper use of pressurized gas.

The mixed region of the isotherms can be used to perform van't Hoff analysis. The van't Hoff equation is used to determine the enthalpy and entropy of reaction. The van't Hoff equation can be used to predict the pressure required to obtain a given H:Pd ratio at a given temperature. The van't Hoff equation is given by:

$$\ln(p_{H_2}) = \frac{2\Delta H^\circ}{xRT} - \frac{2\Delta S^\circ}{xR} \tag{2}$$

where P_{H2} (also referred to as P_{eq}) indicates residual hydrogen pressure over palladium, R indicates the ideal gas constant, T indicates temperature, x indicates the number of moles of hydrogen contained in palladium hydride, ΔH° indicates

enthalpy of formation, and $\Delta S°$ indicates entropy of formation. Enthalpy is the total heat content of the system and entropy is the degree of disorder of the system.

Using van't Hoff analysis, one can plot $\ln(P_{eq})$ vs. $1/RT$ and obtain the enthalpy and entropy of formation. To plot the van't Hoff curve, one data point from each isotherm must be chosen at a set H:Pd ratio. This plot should be linear. The slope of the plot represents the enthalpy of formation. The intercept of the line is proportional to the entropy of formation.

3. Experimental Setup:

The experimental setup was designed for the purpose of studying the formation of palladium hydride and palladium deuteride at temperatures between 293 K and 393 K, as well as cryogenic temperatures. The system (figures 3 and 4) introduces hydrogen or deuterium into an evacuated bed containing palladium powder. The experimental setup comprises a palladium bed, a hydrogen or deuterium tank, a reference volume (V_{Ref}), an MKS pressure gauge, a Hastings pressure gauge, an ion gauge, a turbo vacuum pump, a scroll vacuum pump, and a series of valves connected by stainless steel pipes and Swagelok fittings. The valves are abbreviated as follows: hydrogen/deuterium valve ($V_{H/D}$), palladium valve (V_{Pd}), pressure valve (V_P), reference volume valve (V_{Ref}), vacuum valve (V_{Vac}), helium valve (V_{He}), air valve (V_{Air}). Temperature, pressure, and volume calibrations were performed to reduce systematic errors in the data.
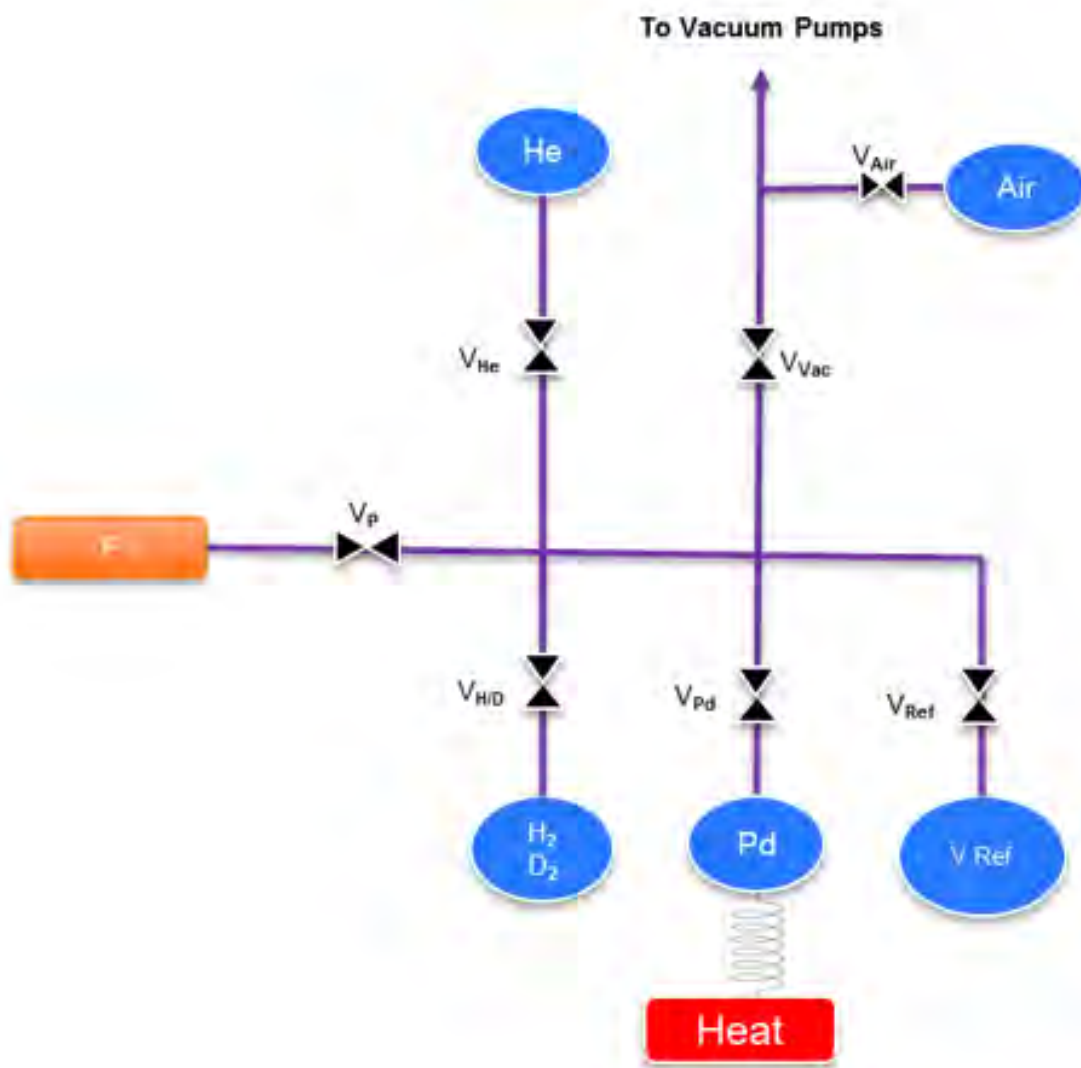
Figure 3: Schematic drawing of the experimental setup.
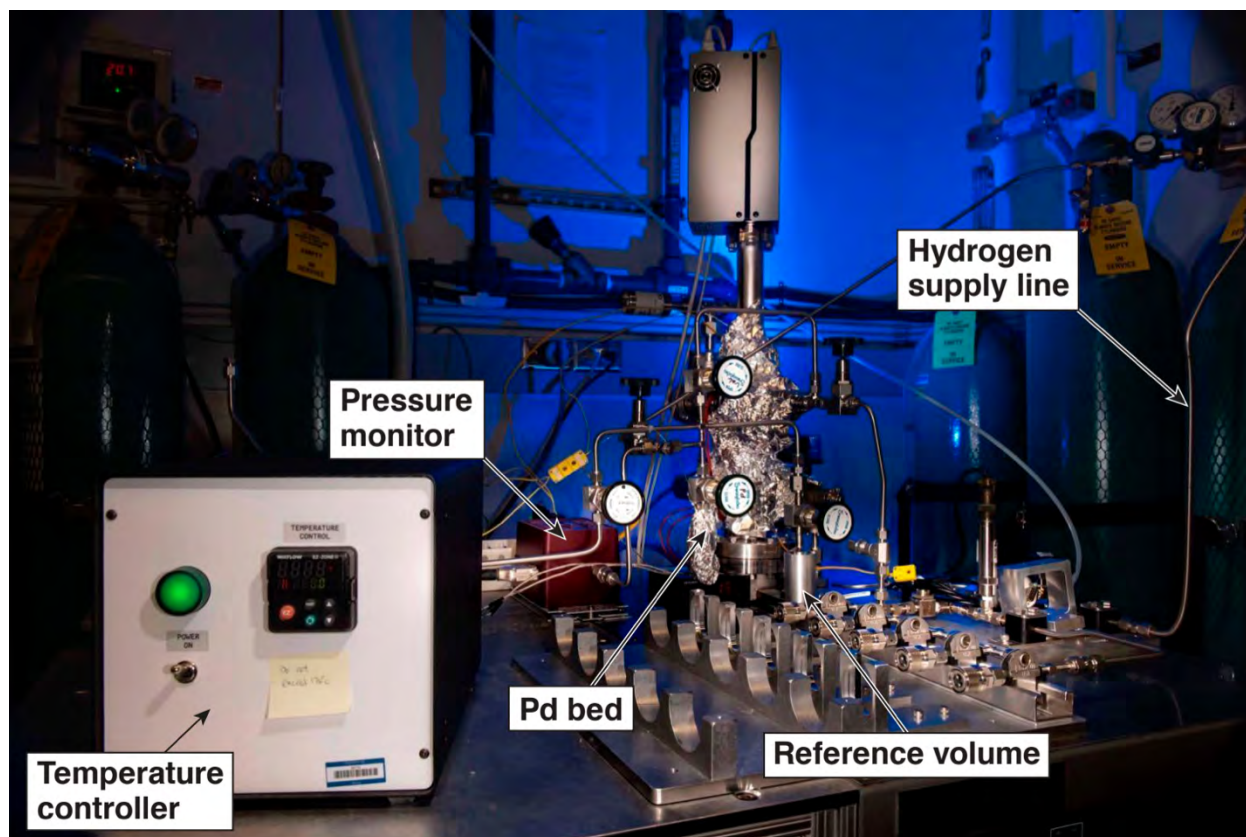
Figure 4: Photograph of the experimental setup.

The palladium bed consists of 2.4 grams (0.0226 moles) palladium sponge, which is held in a stainless-steel container with a head volume of 2.98 cubic centimeters. The palladium bed has foil wrapped around it as a means of insulation. The bed is connected to a turbomolecular vacuum pump that maintains a vacuum of less than 10^{-7} Torr.

The ion gauge is a low-pressure measuring device that measures the quality of the vacuum. The ion gauge uses a heated filament to emit electrons into an electric field. The electric field accelerates the electrons to 80 eV to ionize gas

molecules. The ions are collected on a cathode. The ion current is proportional to the gas density in the vacuum.

Helium gas was introduced into the system in order to measure the manifold volume, the palladium bed head volume, and the reference volume. Helium forms a monolayer on the palladium. This layer interferes with the palladium reacting with hydrogen. Therefore, the system must be baked for several days to remove all helium from the system after volume calibrations are complete.

Air was used to purge the space between the turbomolecular pump and the scroll pump. Hydrogen molecules are so small that the scroll pump cannot completely remove all hydrogen gas on its own. Hydrogen molecules back diffuse from the downstream side of the pump into the space between the two pumps, which becomes evident when hard vacuum cannot be achieved within minutes while the vacuum pumps are running. By purging the interspace with air, the larger molecules help flush the smaller hydrogen molecules from the downstream line.

The system was connected to a computer that used LabVIEW to show real-time measurements of temperature and pressure. LabVIEW is a systems engineering software for applications that involve tests, measurements, and control. A program was created to show the hardware of the system, collect data at various time intervals (standard data collection is in 5 second intervals), and provide data insights.

4. Experimental Procedure:

The collection of data for each isotherm consisted of loading and unloading procedures. The following loading procedure describes the steps for introducing hydrogen to the palladium bed. The hydrogen is administered sequentially in small aliquots, which are all part of a single "run" for a given isotherm. The loading procedure is detailed below:

1. Close all valves.
2. Start data acquisition in LabVIEW and collect background pressure.
3. Slowly open the hydrogen valve to pressurize the charge volume to the desired amount. Monitor the pressure gauges and close the hydrogen valve when finished.
4. Record pressure measurement in the charge volume (P_{Charge}).
5. Open V_{Pd}.
6. Allow gas to reach equilibrium (constant pressure).
7. Record pressure measurement over the palladium (P_{eq}).
8. Close V_{Pd}.
9. Repeat steps 3-8 until the isotherm is complete.
10. Close all valves.

The desired amount of hydrogen injected into the system depends on the region of the isotherm for which data is being collected. In the alpha region and the beta region, the system is pressurized by increments of about 150 Torr. In the mixed region, the system is pressurized by increments of about 900 Torr. In the transition regions between the alpha and mixed region or the mixed and beta

region, the system is pressurized by increments of approximately 75 Torr. Smaller aliquots (those that introduce small amounts of hydrogen and therefore smaller pressure increments) produce data points that are closer together. Larger aliquots produce larger differences in the H:Pd ratio, leading to data points that are farther apart in a plot of the equilibrium pressure vs. the H:Pd ratio. For this reason, it is crucial to introduce small loads during transitions between regions, in order to accurately measure the transition regions. However, it is acceptable to introduce large loads to the system during the mixed region because the equilibrium pressure remains relatively constant.

An isotherm is complete when several data points have been taken in the beta region, or when the pressure has reached 1000 Torr. The pressure gauge that was used had a maximum rating of 1000 Torr.

After each run, the hydrogen or deuterium must be removed from the system. The unloading procedure is detailed below:

1. Open V_{Pd}.
2. Slowly open V_{Vac} until the Hastings pressure gauge is greater than 1000 μmHg (1 Torr).
   a. If the pressure does not decrease within five minutes, close V_{Vac} and open V_{Air} briefly.
   b. When the pressure decreases to less than 50 μmHg on the Hastings pressure gauge, re-open V_{Vac}.
   c. Repeat steps 2a – 2b (air purge) as necessary.

3. Once the pressure on the MKS pressure gauge is at background pressure, open V_{Vac} fully and turn on the turbo pump.

4. After the turbo fully spins up, wait 30 seconds and turn on the ion gauge.

5. Evacuate for several hours.

6. Heat the Pd bed to 160°C.

    a. Turn the temperature up in increments of 10°C.

    b. Do not allow the system to exceed 170°C.

7. Evacuate while heating for at least 8 hours.

    a. The ion gauge should read less than 10^{-7} Torr.

8. Turn the heat down to the desired setting for the next isotherm.

9. Close V_{Vac} and $V_{Pd.}$

10. Turn off the turbo and wait 15 minutes for it to spin down before starting the next run.

5. Results and Discussion:

Measurements of pressure, temperature, and composition were used to create isotherms in the temperature range 293 K to 393 K, plotted in Figure 5. These isotherms illustrate the hydrogen absorption into palladium that is occurring in the alpha, mixed, and beta regions. The experimental data are represented by stars. Data in this temperature range followed the general trend published by Gillespie[2,3] and Lasser,[4] but differ from the data published by Cross,[1] which show some inconsistencies.

During each hydrogen loading onto the palladium bed, the pressure and temperature were recorded. This data was used to plot the isotherms of hydrogen

pressure versus the hydrogen to palladium atom ratio. Loadings were made from 293 K to 393 K. It is apparent that hydrogen vapor pressure increases as temperature increases.
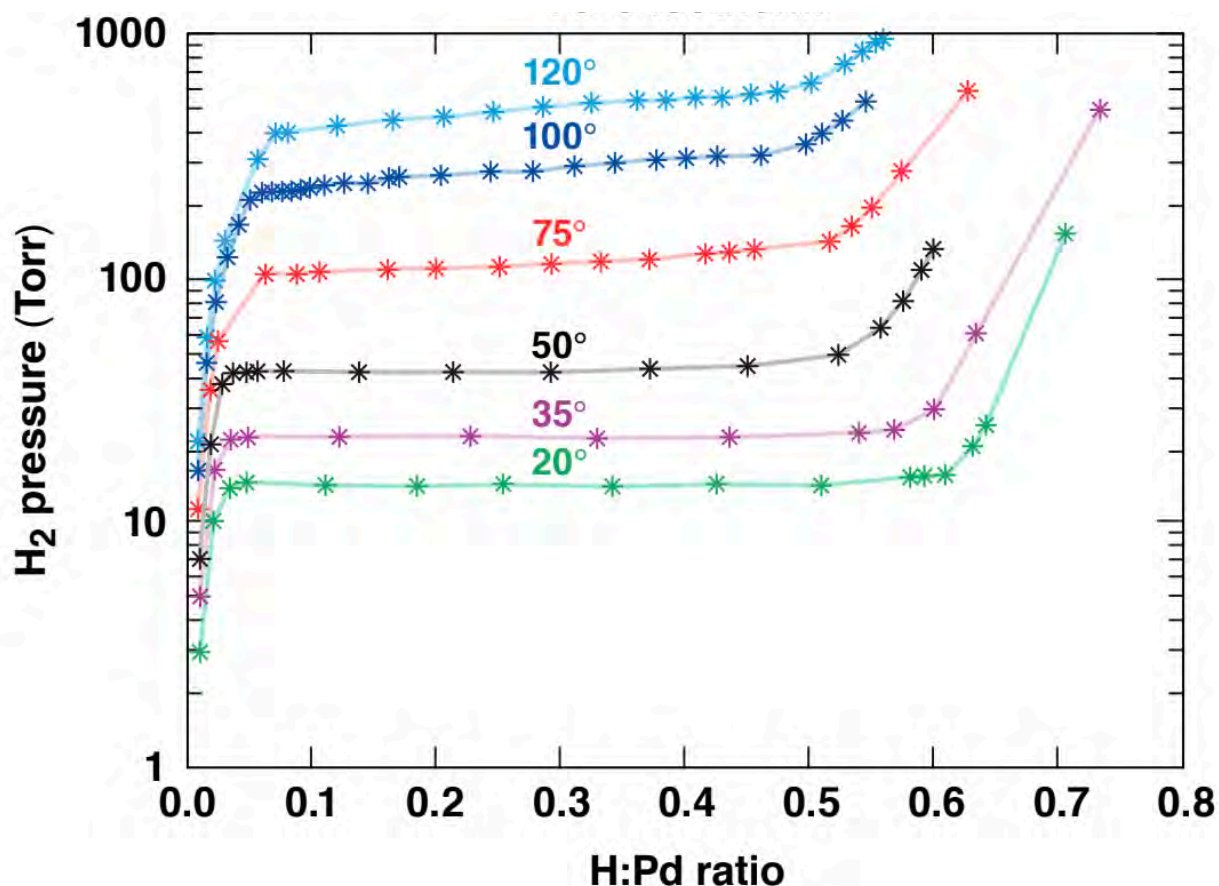

Figure 5: Hydrogen isotherms at various temperatures.

Each loading was duplicated to show consistency in the current study. Figure 6 shows two sets of data taken at the temperature 75°C. The data sets are highly consistent with each other, showing that the mixed region spans the H:Pd range of 0.08 to 0.54, and has an equilibrium pressure increasing from 105 to 110 Torr.
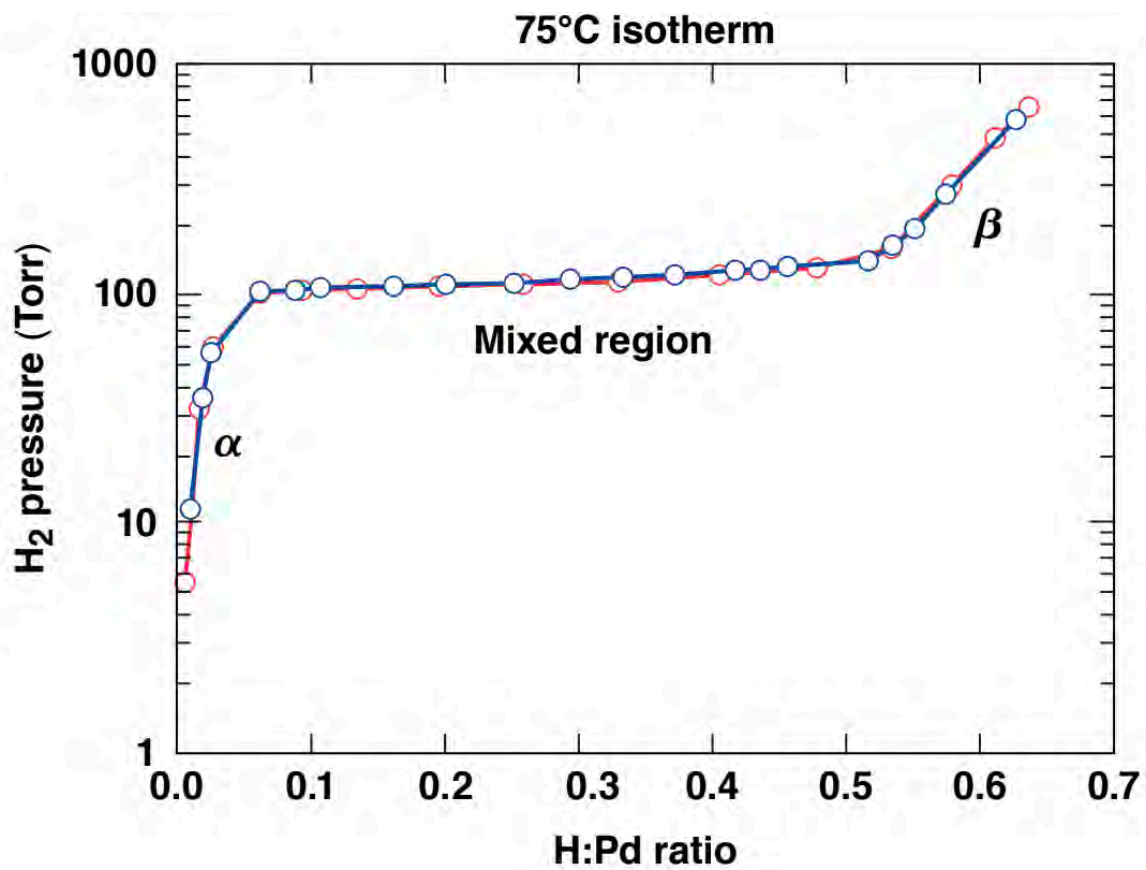
Figure 6: Two isotherms generated at 75º C to demonstrate reproducibility.

Figure 7 shows a plot of $\ln(P_{eq})$ vs. 1/RT for the 0.4 H:Pd ratio.
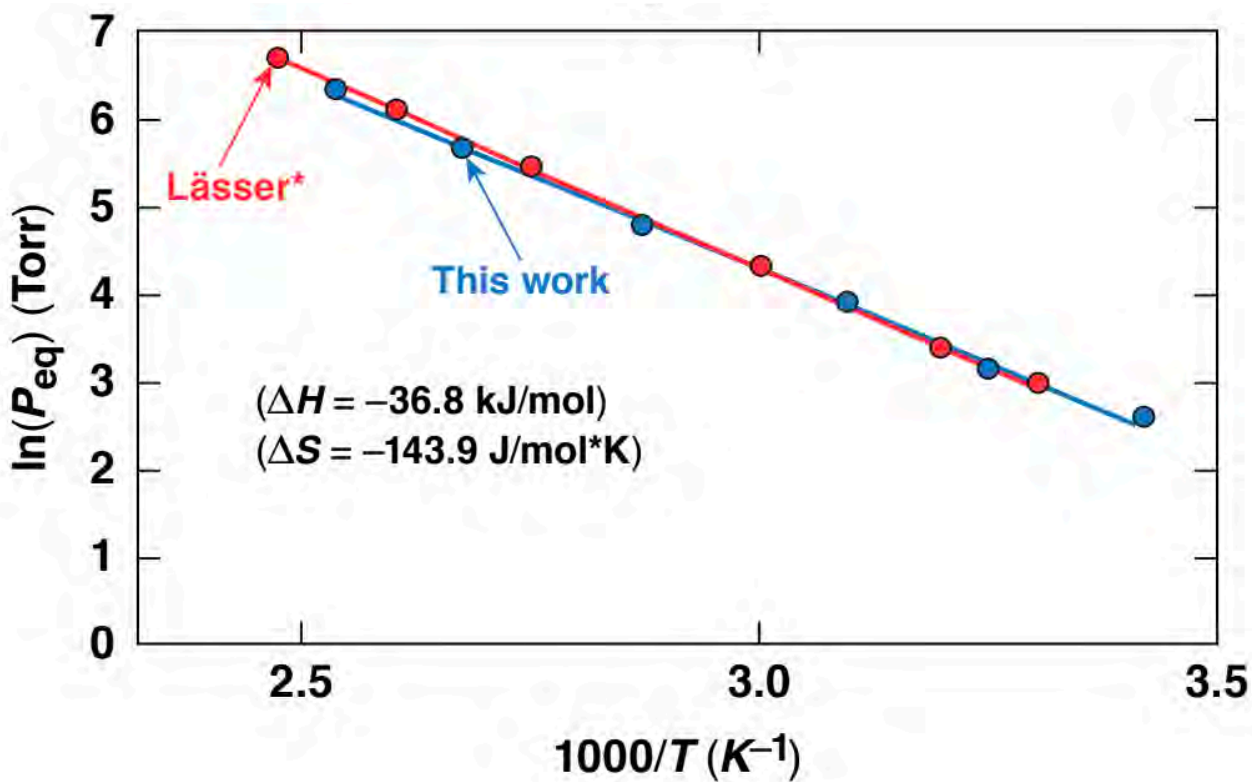
Figure 7: The van't Hoff plot at the 0.4 H:Pd ratio for Lasser (red) and this study (blue). The two van't Hoff plots match, indicating that the current work has reproduced literature data within experimental error.

The van't Hoff equation obtained from the current data set is

$$\ln(P_{eq}) = -36801/RT + 17.688.$$

Using this equation, the enthalpy of formation was determined to be:

$$\Delta H = -36.8 +/- 0.9 \text{ kJ/mol}$$

and the entropy of formation was determined to be:

$$\Delta S = -143.9 +/- 2.7 \text{ J/mol/K}.$$

6. Conclusion:

Palladium is a viable storage medium and pump for hydrogen, deuterium, and tritium. Palladium absorbs and reacts with hydrogen and deuterium to form palladium hydride and palladium deuteride, respectively. Palladium absorbs a significant amount of hydrogen within its crystal lattice. An experimental setup was used to measure the formation of palladium hydride at modest temperatures. The enthalpy and entropy of reaction can be used to predict the required pressure at a fixed H:Pd ratio and at a given temperature. A higher H:Pd mole ratio can be achieved at lower temperatures. This experiment validates prior data on the hydrogen-palladium system.

Now that the experimental setup has been validated, it can be used for several investigations. Future work is already underway for isotherms of the deuterium—palladium system. After that, work will be done on the hydrogen—deuterium—palladium system. This will address mixed isotopes and serve as a model for the deuterium—tritium—palladium system. Future work will also include isotherms at cryogenic temperatures, which is highly relevant to the new target-filling concept.

7. Acknowledgments:

8. <u>Works Cited</u>

1. Cross, Griffin. "Study of the Hydrogen Palladium System." Laboratory for Laser Energetics High School Research Program (2017).

2. Gillespie, Louis. "The Palladium-Deuterium Equilibrium." J. Am. Chem. Soc. **61**, 2496 (1939).

3. Gillespie, Louis. "The Palladium-Hydrogen Equilibrium and New Palladium Hydrides." J. Am. Chem. Soc. **58**, 2565 (1936).

4. Lasser, R. and Klatt, K.-H. "Solubility of Hydrogen Isotopes in Palladium." Phys. Rev. B **28**, 748 (1983).

Microscopy with Ultraviolet Surface Excitation in Life Science Education

Katherine Kopp

Victor Senior High School

Victor, NY

Advisor: Stavros Demos

1. Abstract

This project investigates how to integrate microscopy with ultraviolet surface excitation (MUSE) into a high school science classroom in order to enhance life science education as well as student interest and engagement. MUSE utilizes the unique property of ultraviolet light at wavelengths between 250 and 285 nm to propagate about ten µm into tissues, thus illuminating only the top cell layer. This allows for imaging of the cellular organization and microstructure without having to cut the sample into very thin sections. This capability has the potential to eliminate the need for pre-made slides, and be far more fascinating and informative for students. Laboratory experiments have been developed to directly expose students to plant and animal microanatomy with a personalized learning approach to producing high-quality microscope images. These exercises enable students to utilize autofluorescence and stained tissue samples to identify various microstructures relating to the Next Generation Science living environment core standards.

2. Introduction

Microscopy with ultraviolet surface excitation (MUSE) is based on the salient property of UV light at wavelengths between 250 and 285 nm to propagate only into the top 10 µm of a tissue specimen, illuminating only the top cell layer.[1–3] The resulting fluorescence images, arising from either the native tissue fluorophores or extrinsic contrast agents, are also localized within this narrow range. The MUSE technology was originally developed to examine defects on high-power laser optics, but has since been adapted to biological studies. This microscopy system enables one, with proper selection of imaging optics, to acquire high-quality images without implementing any additional optical sectioning method (such as confocal imaging) or physical sectioning of the specimen into very thin layers. In addition, UV light can photoexcite a wide range of common fluorescing stains, which subsequently emit light typically in the visible spectrum.[2,3] MUSE imaging relies on the visible structural differentiation caused by either the nonuniform cellular distribution of naturally occurring biomolecules or the use of fluorescing stains to highlight different cellular compartments. This allows one to image the cellular organization and

2

microstructure without laborious effort (fix, dehydrate, embed in wax, cut, and stain) to produce a thin stained section, which can take anywhere from many hours to several days before the slides become available for viewing under the microscope.

Tissues produce autofluorescence when exposed to any form of photoexcitation, but UV light causes a relatively larger amount of autofluorescence, typically dominated by the emission by tryptophan.[1] The autofluorescence provides immediate visualization of structural differentiation within the sample, which enables one to identify various microstructures without staining the sample. MUSE can also be used in combination with fluorescent stains designed to target specific structures within tissues, allowing for easier structural identification. These stains can be excited by 250 to 285 nm of UV light (typically via transition of ground-state electrons to the second singlet excited state, $S_0 \rightarrow S_2$) and emit light in the visible spectrum (from radiative transition from the first singlet excited state, $S_1 \rightarrow S_0$).

In this work, tissue samples were stained using Hoechst 33342 and Eosin Y, which stain the nuclei and cytoplasm, respectively, and are safe for classroom handling and use.[4] Premixed powders in a gelatin capsule have been made with 20 g of Eosin Y and 5 g of Hoechst 33342, and the capsule is readily soluble in 100 mL of de-ionized water, resulting in a stain solution that is plenty for a single class. A rapid and simple staining process has been developed so that any individual student can safely complete each step. The process is as follows: a 10-s phosphate-buffered saline (PBS) rinse, 20 s in isopropanol, a 10-s PBS rinse, 60 s in a stain solution, and a 10-s PBS rinse.[4] The isopropanol is not required for the stain, but it helps to enhance the nuclear stain. It is possible to use staining solutions other than Hoechst 33342 and Eosin Y to achieve the desired results, but these possibilities require further research and development.

The goal of this work was to develop a curriculum involving MUSE that can be adapted to life science education in order to inspire students to learn more about the natural world. To do this, laboratory exercises for a high school science class were created to enhance student interest with a personalized learning approach. High school life science education is responsible for shaping the scientists of the future

by capturing and sustaining students' interest in the natural world. As part of this work, laboratory experiments have been developed to directly expose students to plant and animal microanatomy. These exercises involve imaging tissue samples and using native fluorophores (autofluorescence) or fluorescent stains to identify various microstructures relating to the high school life science curriculum. The experiments are designed to teach students about scientific practices while reinforcing their knowledge of the life science core standards. This work suggests that implementation of MUSE technology in an educational setting has the potential to increase student engagement while complementing the Next Generation science living environment core standards currently used in the United States.
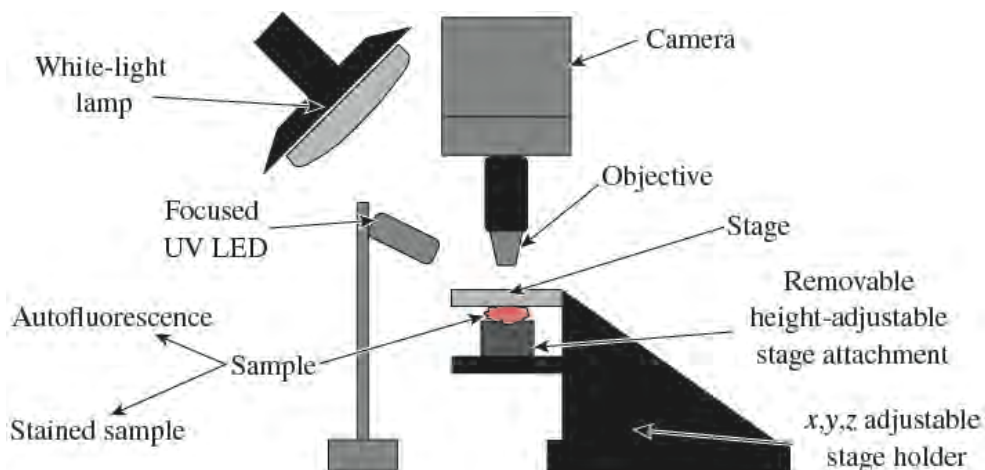
3. Laboratory Exercises

Figure 1: Schematic diagram of the MUSE experimental apparatus.

Figure 1 shows the schematic diagram of the MUSE setup. The UV LED illumination is at an oblique angle and focused on the sample directly under the objective. This system was used to view plant and animal microanatomy with a quick, simple, and inexpensive process. This system was also used to image tissues without any preparation, as well as stained tissue samples. Imaging experiments of various objects, plants, and animal tissues were performed toward (a) exploring the spectrum of MUSE imaging suitable for an education setting and (b) developing laboratory experiments relevant to the high school science classroom. Laboratory procedures, background, and examples were written for each experiment.

These exercises utilize MUSE technology while complementing the current life science curriculum standards. The labs bring a personalized learning approach to obtaining high-quality images of tissue microstructure that reinforce material learned through classwork. Each laboratory exercise is discussed in further detail in the next sections.

3.1 Introduction to MUSE

The first laboratory exercise titled "*Introduction to MUSE*" serves the purpose of exposing students to MUSE technology while promoting individual interest in microscopy and microanatomy. In this exercise, students gather everyday objects from around the classroom and school and image each object's autofluorescence with the microscope. Each student has unique samples; consequently, the set of images captured by each student is different. The examples of captured images in Fig. 2 show foam, paper towel, and sugar crystals, respectively. Students are able to complete every step of this lab exercise individually and obtain distinct resulting images, which allows for flexibility and creativity in the process. This approach has the potential to be more interesting and engaging for students while still being effectively informative. The exercise introduces students to the concept of microstructures, allowing them to view firsthand the microscopic structure of objects with which they are familiar. This reinforces knowledge of structural hierarchy and exposes students to the idea of fluorescence and the understanding of MUSE technology and how it can be used to capture fluorescence images.
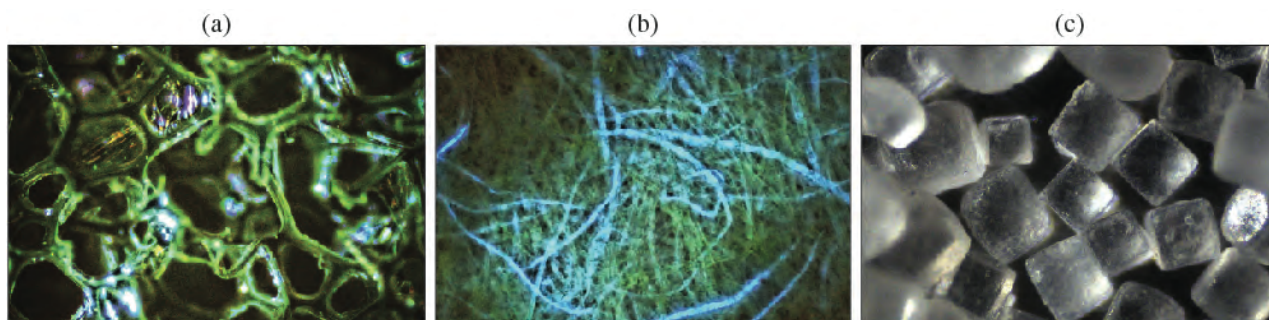

Figure 2: MUSE microscopy images based on native fluorescence (autofluorescence) from a foam sample (a), a piece of paper towel (b), and sugar crystals (c).

3.2 Living Organisms

The next exercise, "*Living Organisms*," introduces students to the staining process and reinforces students' knowledge of plant structures. The procedure for this experiment includes gathering living organisms such as leaves and flowers from the outdoors and imaging these samples with MUSE using their native fluorescence (autofluorescence) or staining to view in more detail. Figure 3 presents images obtained from a maple leaf: (a) the conventional color image of the leaf's surface, (b) the autofluorescent image, and (c) the maple leaf after it was exposed to staining. Students can gather samples from various plants or other small organisms and perform each step on their own, so they are free to choose samples that are of personal interest. Students can also identify structures from captured images, such as nuclei, cell walls, pollen, and leaf veins. In this experiment, students should focus on the staining process and identifying notable parts of each living sample.
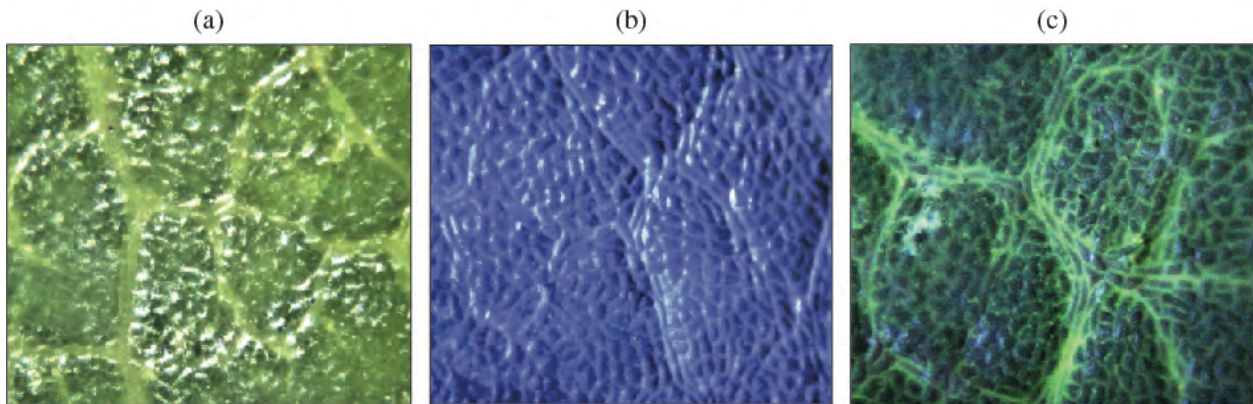

Figure 3: Images from the surface of a maple leaf: conventional white light illumination (a), autofluorescence (b), and following staining with Hoechst 33342 and Eosin Y (c).

3.3 Plant and Animal Cells

The third laboratory exercise titled "*Plant and Animal Cells*" focuses on emphasizing the structural and functional similarities and differences between plants and animals. In this exercise, students can use an onion, a flower, or a leaf as the plant sample and a cheek swab as the animal sample. Onion cells have been found to produce the best images, and due to the nature of MUSE, there is no need for thin sectioning. Autofluorescence or stained samples can be viewed and imaged, and the plant and animal

cell images can be compared in order to find structural similarities and differences. Figure 4(a) shows a stained onion sample, where the rectangular cell walls and dark red stained nuclei are clearly visible. Figure 4(b) shows an autofluorescent image from a cheek swab, allowing one to directly view the irregular-shaped cell membrane.

Through MUSE microscope captures, students can visualize the cellular organization and combine that with their knowledge of the functions of plant and animal cells. For example, students can compare rigid plant cell walls to the more abnormally shaped and flexible animal cells and study the structural and functional reasons for these differences. In this exercise, the presence or absence of fluorescing stains, as well as the different regions within a single sample, should be noted by students. Students can also focus on visualizing multiple types of specialized cells within a single sample.
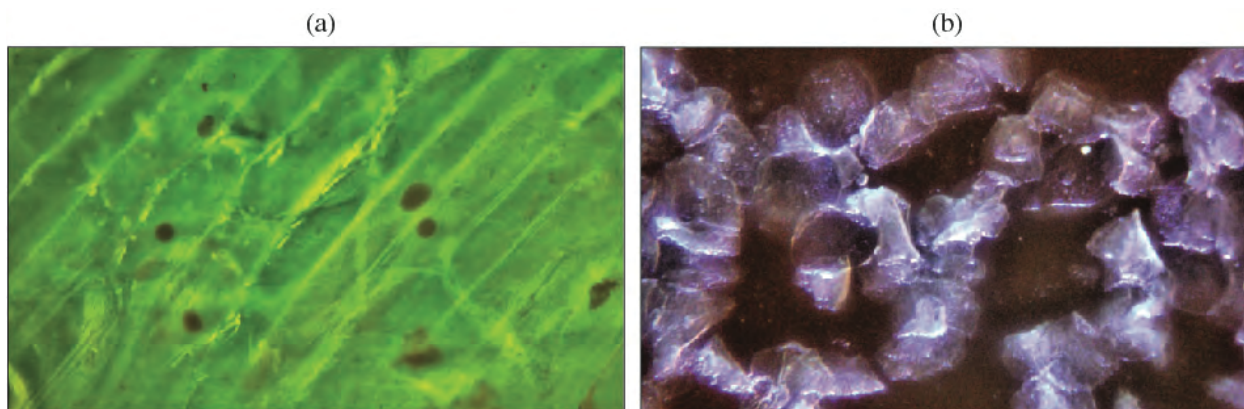

Figure 4: Onion cells in a thick sample visualized after staining with Hoechst 33342 and Eosin Y (a). Autofluorescence image of cheek swab cells (b).

3.4 Animal Dissection and Microanatomy

The next laboratory exercise is "*Animal Dissection and Microanatomy*," in which students dissect a preserved animal to view gross anatomy and use tissue samples to view microanatomy. This experiment can be implemented into units on the digestive or circulatory system, as students first identify the organ systems present in the animal. Then, students can identify individual organs and other structures, taking a tissue sample for further use. A kidney cross section, heart cross section, skeletal muscle surface, lung

surface, and liver cross section were found to be relatively easy to identify, cut, and view under the microscope. The representative organs used in this report are from a frog, but other animals may be used as well. Students can use images of the organs to locate and view various microstructures.

In Fig. 5 the images of a ranine lung obtained following nuclear and cytoplasmic stain clearly show the bronchioles and the nuclei. Specifically, Fig. 5(a) is a digitally stitched image comprised of a number of individual image captures that offer an enlarged view of the lung cross section. Figures 5(b) and 5(c) are individual images (single captures) that allow one to appreciate the information detail and volume available to the student with the higher magnification.

Figure 6 shows a stitched image of a kidney cross section. The kidney tubules are visible in the cross section either through their exposed surface (mostly on the right side of the image), or as cuts through individual tubules that expose the rounded tubular walls (mostly on the center and left sides of the image), where the higher concentration of exposed nuclei gives them the appearance of ring structures.

Figure 7(a) shows striated cardiac muscle, while Fig. 7(b) shows skeletal muscle fibers. This exercise directly exposes students to the structural similarities and differences between various organs from the same organism. Cardiac muscle is striated while skeletal muscle has fibers, and the lungs have bronchioles while the kidneys have tubules,[5] each displaying a unique structure that is related to its function within the body.

Through these experiments, students can focus on identifying how each organ's microstructure relates to its function. This questioning with an actual organism gives students a concrete example of hierarchal differentiation in multicellular organisms, which is an important concept in life science education.
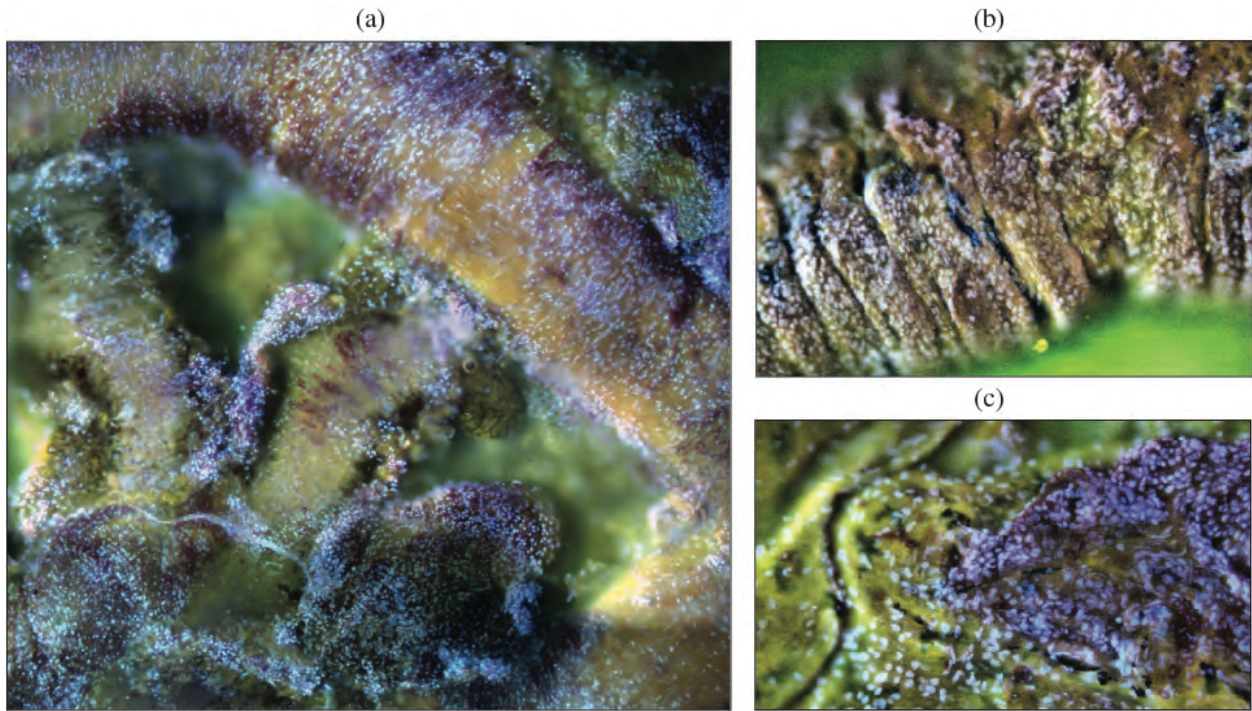
Figure 5: Ranine lung with nuclear and cytoplasmic stain. (a) This image is digitally stitched to show a larger field of view. The blue illuminated dots are nuclei of lung cells. Single image captures (b and c) as recorded by the microscope system reveal the microstructure of the cross sectioned tissue.
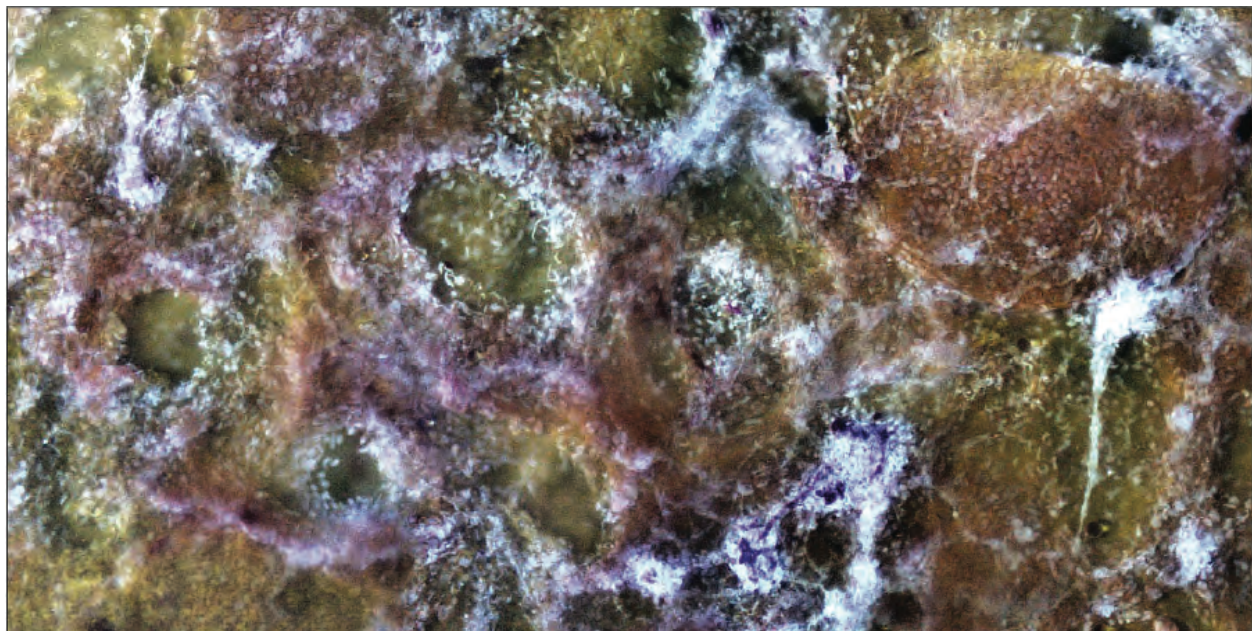

Figure 6: Ranine kidney cross section with nuclear and cytoplasmic stain. This image is digitally stitched to show a larger field of view. The round shapes in the image are the cross sections of kidney tubules.

(a)
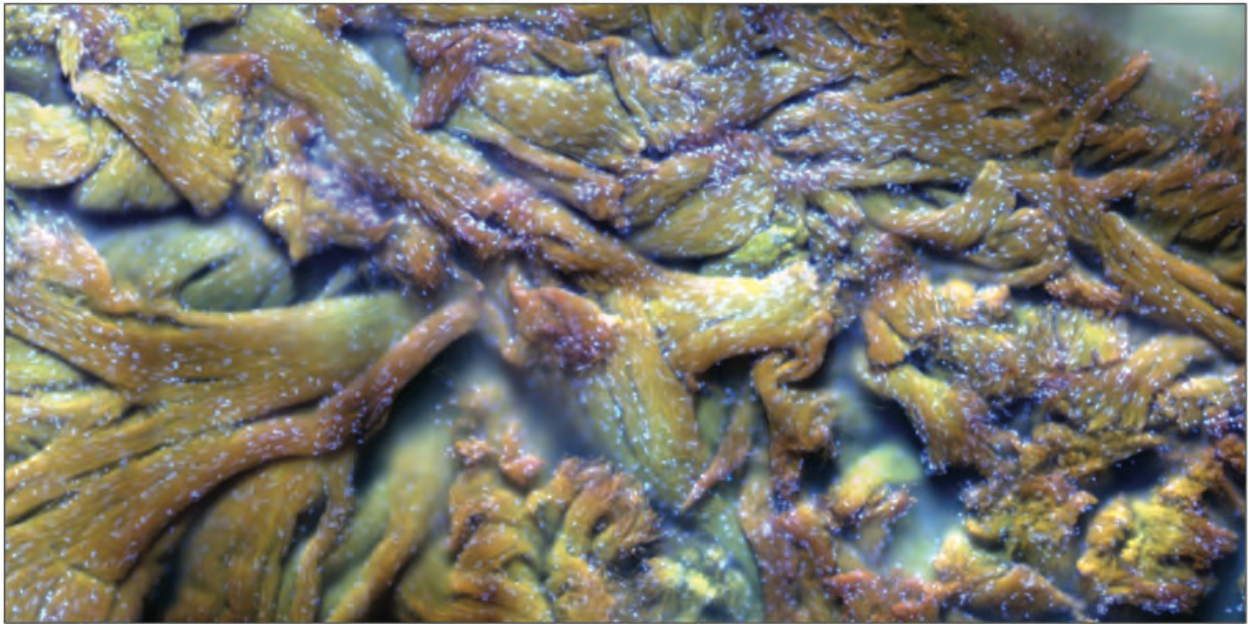
(b)
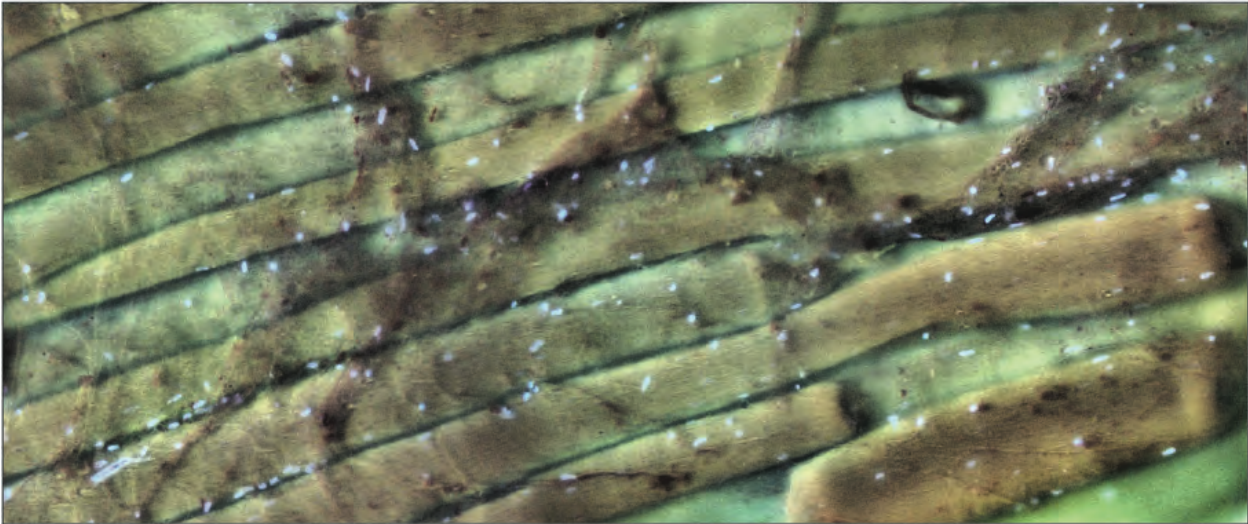
Figure 7: MUSE images of ranine cardiac muscle (a) and skeletal muscle (b) with nuclear and cytoplasmic stain. Muscle fibers and cell nuclei (illuminated dots) are visible. Each image is digitally stitched to show a larger field of view.

3.5 Leaf Cross Section and Microanatomy

The last laboratory exercise developed in this work, titled "*Leaf Cross Section and Microanatomy*," allows students to use a physical model of a leaf to identify various microstructures,

including the cuticle, xylem, phloem, stomata, and mesophyll layer. Students collect leaves of their interest, cut a thin strip, and place the sample on the stage so that the cross section is facing the microscope objective. The autofluorescence generated by the UV light creates clear structural differences in color and intensity, resulting in an image that students can use to easily identify the different parts of the leaf. Images of maple leaf cross sections are shown in Fig. 8.

With this exercise, students gain a physical model of a leaf cross section, which is generally taught from cartoon diagrams. With the images of actual leaf cross sections, students can identify structures and compare them to the schematic representations taught in class. Students can view the structure of different leaf parts and can question its relation to each part's function. For example, the cuticle is a layer on the top of the leaf with thin cells that act as a protective barrier. The xylem and phloem are tubes in leaf veins that transport water and nutrients throughout the plant. The mesophyll layers in the center of the leaf have cells that face the top of the leaf since they have chloroplasts that use sunlight for photosynthesis.[6] Students can explore these types of relationships with this exercise, which reinforces their knowledge of specialization and cellular differentiation.
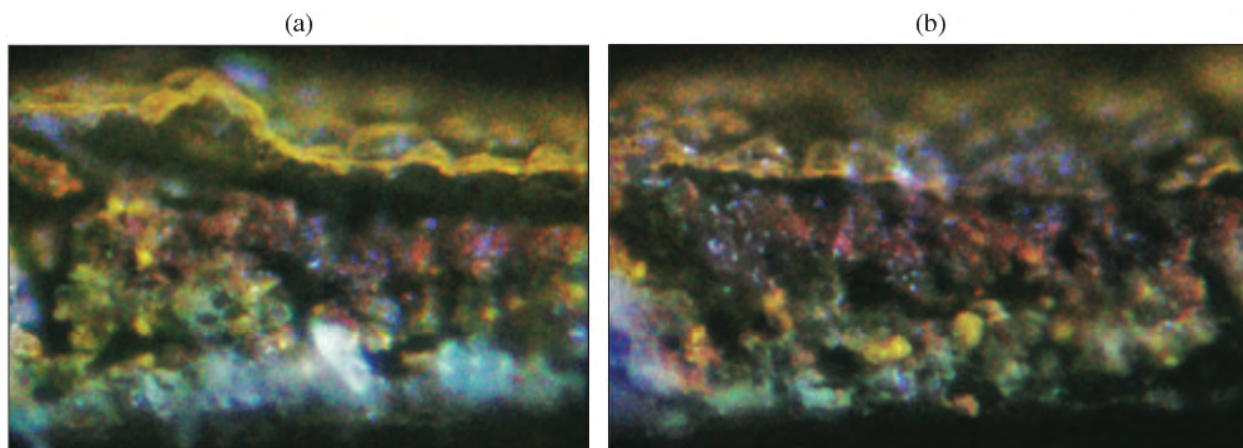

Figure 8: MUSE images of maple leaf cross-section using autofluorescence only.

4. Curriculum

The developed MUSE curriculum focuses on exposing high school students to scientific practices that reinforce their knowledge about life science. Each practice learned through the laboratory exercises is relevant to the public high school life science standards, and the coordinating Next Generation science standard is referenced.[7]

The first practice that this curriculum emphasizes is the identification of major structures in plant samples. Students can view organisms such as leaves, grass, and flowers under the microscope and use the resulting images to find certain microstructures, such as leaf veins. By looking at various cells and structures within one organism, students are learning about cellular specialization and organization. This practice reinforces the fact that while different cells within an organism have the same genetic information, they may not have the same structure or function, depending on which genes are expressed. This practice reinforces Next Generation standards HS-LS1-1 and HS-LS1-2.

The next scientific practice with which students are involved is the dissection of an organism to view gross anatomy as well as tissue microstructure. When students dissect an organism, they work to understand the hierarchical levels of organization within a multicellular organism. This corresponds to Next Generation standard HS-LS1-2. Students can identify organs and organ systems in an organism and can then take a tissue sample to view the same organism's microanatomy at the cellular level.

The last emphasized practice is the comprehension of the structure and function of plant and animal cells. This practice works on a microscopic scale and focuses on life processes at the cellular level. Plant and animal cells have different organelles to perform different functions, and each organelle and cell has specific structures that relate to its function. The various cells work together to perform life processes to maintain homeostasis within an organism. This is shown in Next Generation standard HS-LS1-2.

Additional laboratory exercises can be developed to offer unique experiences to a student. For example, experiments that enable dynamic response of cells and tissues to an external stimulus are

possible using the MUSE technology. In addition, MUSE can be used to visualize microanatomy of non-normal tissue such as tissue that has undergone some type of injury.

5. Conclusion

This work details the developed curriculum for the high school life science implementation of MUSE. Further optimization of the system, including the development of a design specifically for use of MUSE in education, must be done to enable the actual use of this technology in the classroom. Such an instrument can be based on the schematic diagram showed in Fig. 1 and should include a focused UV LED with wavelengths between 250 and 285 nm, a removable and adjustable sample holder, and an objective and tube lens for imaging. With the proper instrumentation and curriculum, MUSE can be effectively integrated into a high school life science classroom.

6. Acknowledgements

7. References

1. Lin, B., Urayama, S., Saroufeem, R. M. G., Matthews, D. L. and Demos, S. G., "Characterizing the origin of autofluorescence in human esophageal epithelium under ultraviolet excitation," Opt. Express 18(20), 21074–21082 (2010).

2. Levenson, R. M., Harmany, Z., Demos, S. G. and Fereidouni, F., "Slide-free histology via muse: UV surface excitation microscopy for imaging unsectioned tissue," Proc. SPIE 9703, 97030J (2016).

3. Fereidouni, F., Harmany, Z. T., Tian, M., Todd, A., Kintner, J. A., McPherson, J. D., Borowsky, A. D., Bishop, J., Lechpammer, M., Demos, S. G. and Levenson, R., "Microscopy with ultraviolet surface excitation for rapid slide-free histology," Nat. Biomed. Eng. 1(12), 957–966 (2017).

4. Huang, C. Z. R., Wood, R. W. and Demos, S. G., "Adaptation of microscopy with ultraviolet surface excitation for enhancing stem and undergraduate education," J. Biomed. Opt. 23(12), 121603 (2018).

5. Minkoff, E. C., [A Laboratory Guide to Frog Anatomy], Pergamon Press, New York (1975).

6. Upton, R., [Botanical Microscopy Handbook], CRC Press, Boca Raton, FL (2001).

7. [Next Generation Science Standards: For States, by States], The National Academies Press, Washington, DC (2013).

Computational Chemistry Modeling of Photoswitchable Liquid Crystal Alignment Materials

Hannah Lang

Rush-Henrietta Senior High School

Advisor: Kenneth L. Marshall

Laboratory for Laser Energetics

University of Rochester

Rochester, NY

Summer High School Research Program 2018

Abstract

The optical switching properties of spirooxazine in photoalignment command surfaces, used to control the molecular orientation of liquid crystals (LC), were modeled using density functional theory in order to identify the optimal molecular structure for a rewritable, photoswitchable LC beam shaper for high-peak-power lasers such as OMEGA EP. This photoswitchable device would replace existing laser beam-shaper technology, which is limited in its application scope by a low 1054-nm laser damage threshold. This work examined the effect of molecular structure on bistability (switching state lifetime) by modeling different functional groups attached to the spirooxazine chromophore, along with alkyl tethers ranging in length from 3 to 9 carbons to link the chromophore to a methacrylate polymer backbone, to find an ideal combination possessing high bistability. The most promising molecule that was modeled, a spirooxazine with a 1-(4-pyridyl)piperazine functional group and tether length of 4, exhibited the smallest isomerization-state energy difference and moderately high activation energy, and its larger functional group should prove effective at redirecting the orientation of the LC materials.

1. Introduction

Spirooxazine chromophores are under computational investigation in order to model their optical switching properties, which make them potential candidates for rewritable photoalignment materials for use in an all-optical liquid crystal (LC) beam shaper. The application of existing beam shaper technologies, for example metal-mask beam shapers and LC electro-optical spatial light modulators, is severely limited by a poor 1054-nm laser damage threshold of approximately 200 to 700 mJ/cm^2 [1]. A photoswitchable device (Fig. 1), currently in design at the Laboratory for Laser Energetics, presents a potential solution to this issue.
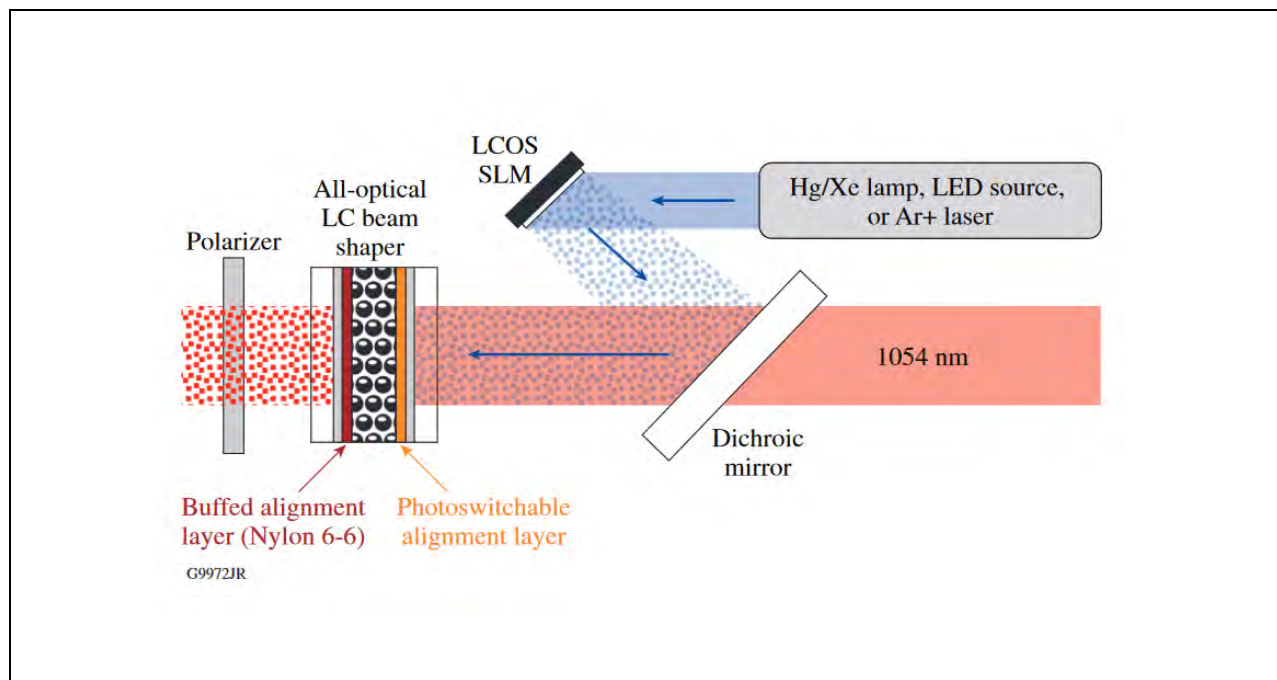
Fig. 1: Schematic of a photoswitchable device [1]. The 1054 nm laser beam is shaped using the all-optical photoswitchable device proposed. The all-optical LC beam shaper consists of a glass substrate, a photoswitchable alignment layer, liquid crystals (represented by the dotted pattern), and a buffed alignment layer, and is capped by a second glass substrate.

The schematic in Fig. 1 demonstrates how such a device would function. Here, the liquid-crystal-on-silicon spatial light modulator (LCOS SLM) electrically generates a pattern, which is reflected off the dichroic mirror and written onto the photoswitchable alignment layer, shown in orange. The molecules that make up the photoswitchable alignment layer generate the pattern in the LC layer (represented by the dotted pattern) by switching between the open and closed isomers upon exposure to light energy, and thereby physically redirecting the orientation of the liquid crystals. The buffed alignment layer produces a fixed LC orientation at its surface. Notably, unlike existing technology, this pattern will remain once the light source (provided by the Hg/Xe lamp, LED source, or Ar+ laser) is turned off.

In order for such a device to be useful, the photoalignment layer must have a significantly higher laser damage threshold than that of existing beam-shaper technologies. Spirooxazine chromophores were therefore chosen for examination in this work for their similarity to spiropyran (Fig. 2), which was recently shown to have a 1-on-1 laser damage threshold (found by irradiating separate sites of a material with increasing intensity, therefore giving information only on the peak of damage resistance for single shot operation) of 91.30 ± 6.87 J/cm^2 and an N-on-1 laser damage threshold (found by irradiating a single site with multiple shots of increasing intensity, giving a more complete picture of a material's survivability and operational lifetime) of 100.84 ± 5.51 J/cm^2 [2].

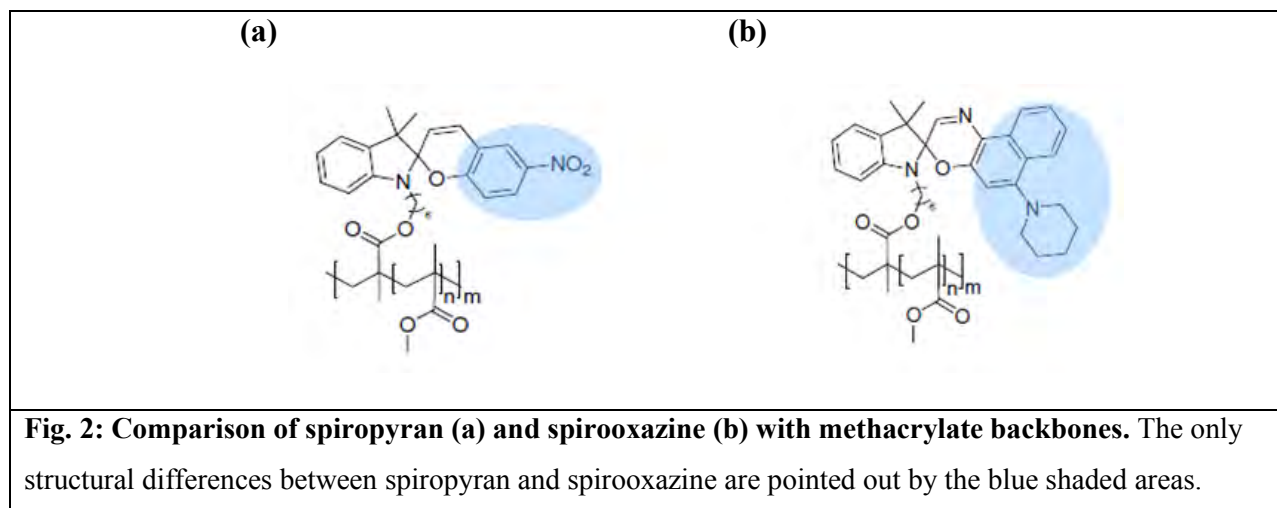**Fig. 2: Comparison of spiropyran (a) and spirooxazine (b) with methacrylate backbones.** The only structural differences between spiropyran and spirooxazine are pointed out by the blue shaded areas.

The similarity of spirooxazine and spiropyran, as seen in Fig. 2, allows spirooxazine to be modeled under the assumption that it would have a laser-damage threshold superior to existing technologies.
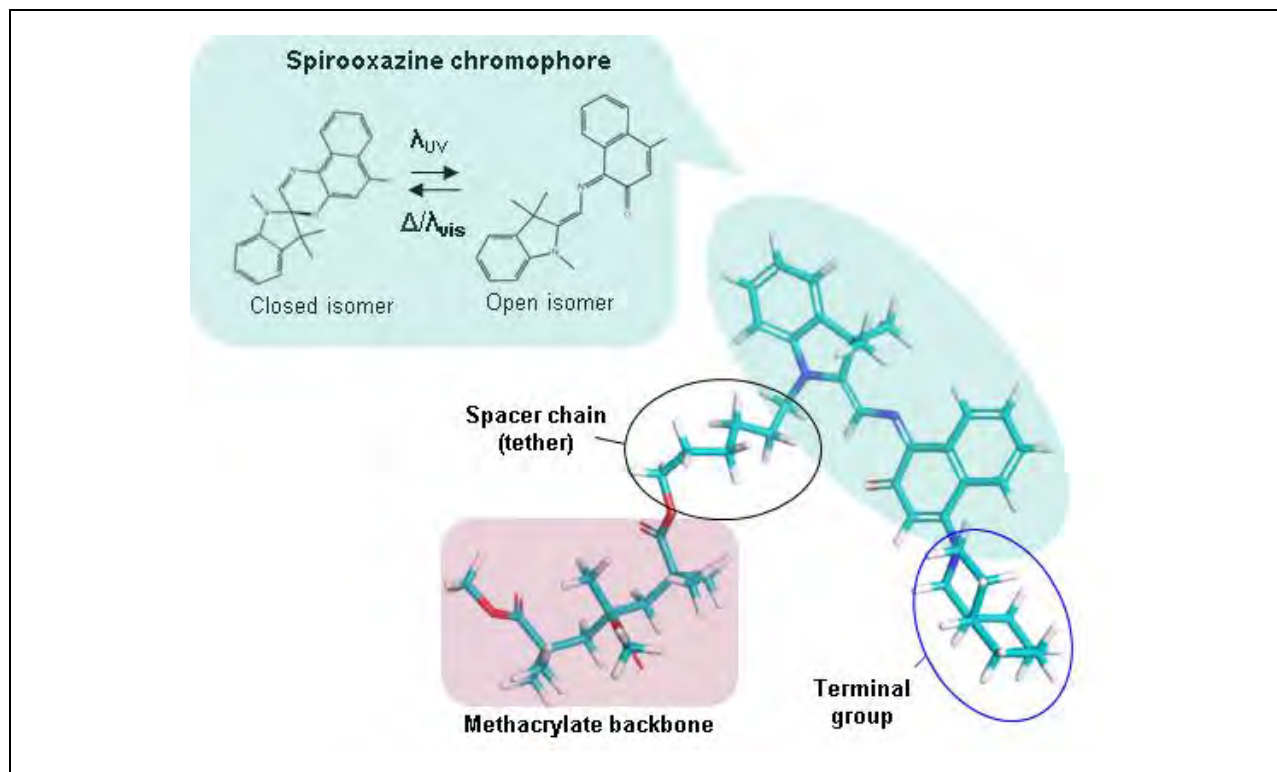
Fig. 3: Example of a spirooxazine molecule as displayed in computational models. The spirooxazine molecules modeled consist of four parts: the methacrylate backbone, carbon tether, spirooxazine chromophore (the component responsible for the actual mechanism that switches the molecule between the open and closed isomers upon exposure to light or heat energy), and terminal group, also known as functional group.

In the proposed device, spirooxazine molecules such as the one shown in Fig. 3 are found in the photoalignment layer of the command surface, pictured in orange in Fig. 1. The spirooxazine chromophore is photoswitchable, so exposure to UV light prompts the molecule to open and likewise exposure to visible light reverses the isomerization. In the photoalignment layer, this chromophore switching of spirooxazine would act as a mechanism to redirect the orientation of the LC materials and shape the laser beam. Fig. 4 shows a magnified view of the command surface, which consists of a glass substrate, the spirooxazine molecule – tethered to the command surface by its methacrylate backbone – and the LC molecules above [3]. This

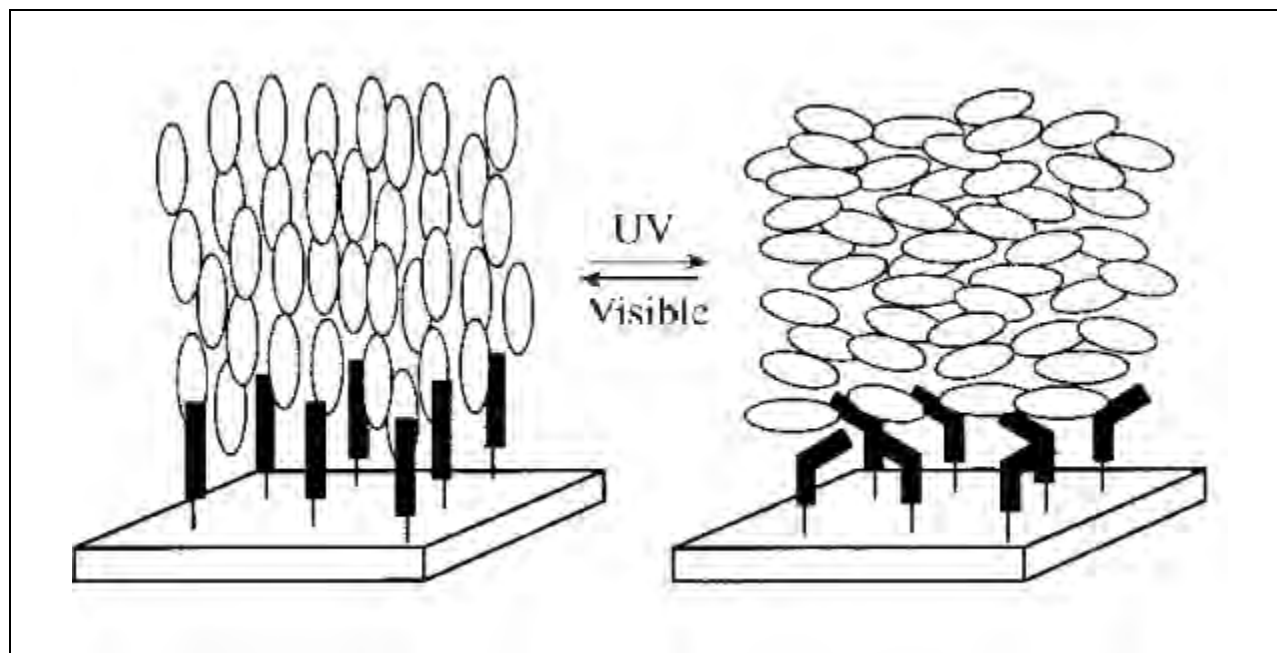command surface would be capped by a buffed alignment layer and a second glass substrate, as shown in Fig. 1.

Fig. 4: Command surface diagram. The command surface in a photoswitchable device (referred to as the all-optical LC beam shaper in Fig. 1) is shown here in greater detail. The black rectangles are representative of the photoswitchable molecules, anchored to the glass substrate by the molecule's backbone, and the ellipses represent the LC materials [3]. Note that this diagram is specific to trans/cis azobenzene chromophores; however, the idea holds for spirooxazine chromophores as well.

In order to identify molecules well suited for these photoalignment layers, the effect of molecular structure on bistability (Fig. 5) was modeled by performing isomerization and transition-state calculations for spirooxazine molecules with different functional/terminal groups and alkyl tether lengths ranging from 3 to 9 carbons. Bistability is defined as switching state lifetime, meaning how stable the molecule's orientation is when it switches between isomers. A molecule that stays as an open isomer for a longer period of time after being exposed to the correct amount of light energy, for example, would be considered to have a higher bistability.

Bistability is affected by a combination of the molecule's isomerization-state energy difference and activation energy [1].
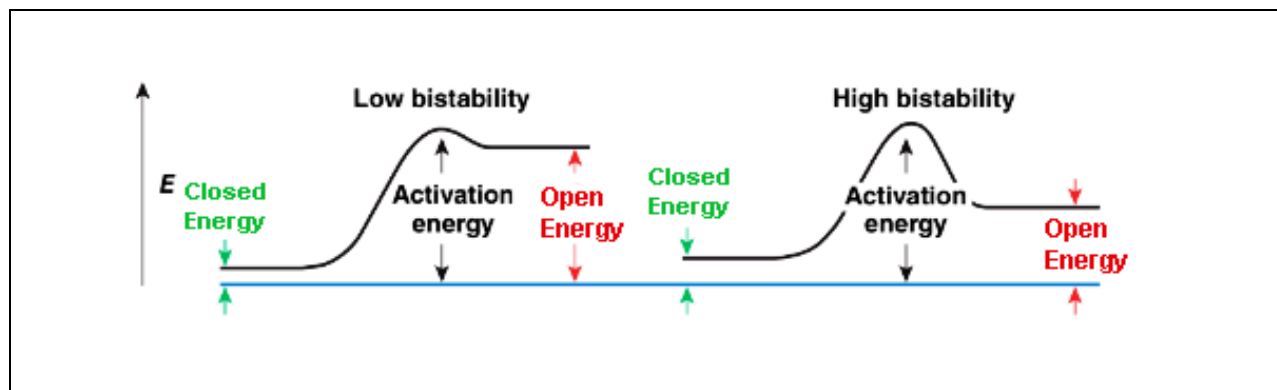

Fig. 5: Graph demonstrating bistability. Note that the energy barrier for the transition from the closed to open isomers is large in each case, but for the system with low bistability the reverse isomerization from the open to closed isomers has a low energy barrier. The graph of high bistability, on the other hand, shows a significant energy barrier for both directions of isomerization.

Molecules with high bistability are less likely to switch between isomers without deliberate interference, since, for example, environmental factors like heat are unlikely to prompt the molecule to switch back to the closed isomer [1]. The goal of this computational modeling was to identify candidate molecules for use in photoswitchable alignment layers by identifying those with the highest bistability. In order to identify such molecules, isomerization-state energy differences – the difference in potential energy between the open and closed isomers of a molecule – and activation energies necessary for the transition between isomers were calculated.

2. Previous Research

Previous research into molecules for potential use in photoswitchable alignment layers in an optically addressable LC device has largely focused on the use of computational modeling to predict the physical properties of molecules with azobenzene chromophores, thereby preserving time, labor, and money that would otherwise be spent on synthesis. The methods for such

computational chemistry modeling can be categorized as follows: (1) *ab initio*, which employ

only physical principles for calculations; (2) semi-empirical, whose calculations are based on

existing data in the literature; and (3) density functional theory (DFT) and time-dependent

density functional theory (TDDFT), more recent computational methods that use approximations

of the Schrodinger equation to calculate electron density [1]. Hartree-Fock is the most basic *ab*

initio method, and uses a many-electron wave function that assumes that all nuclei are

motionless with respect to the electrons [4]. As such, the accuracy of the Hartree-Fock method

decreases as molecular size increases, whereas DFT uses a 3D electron density function as

pictured in Fig. 6, and is therefore more efficient for molecules of greater complexity.

Fig. 6: A visualization of computed wave functions versus electron density functions for the same molecule [1].
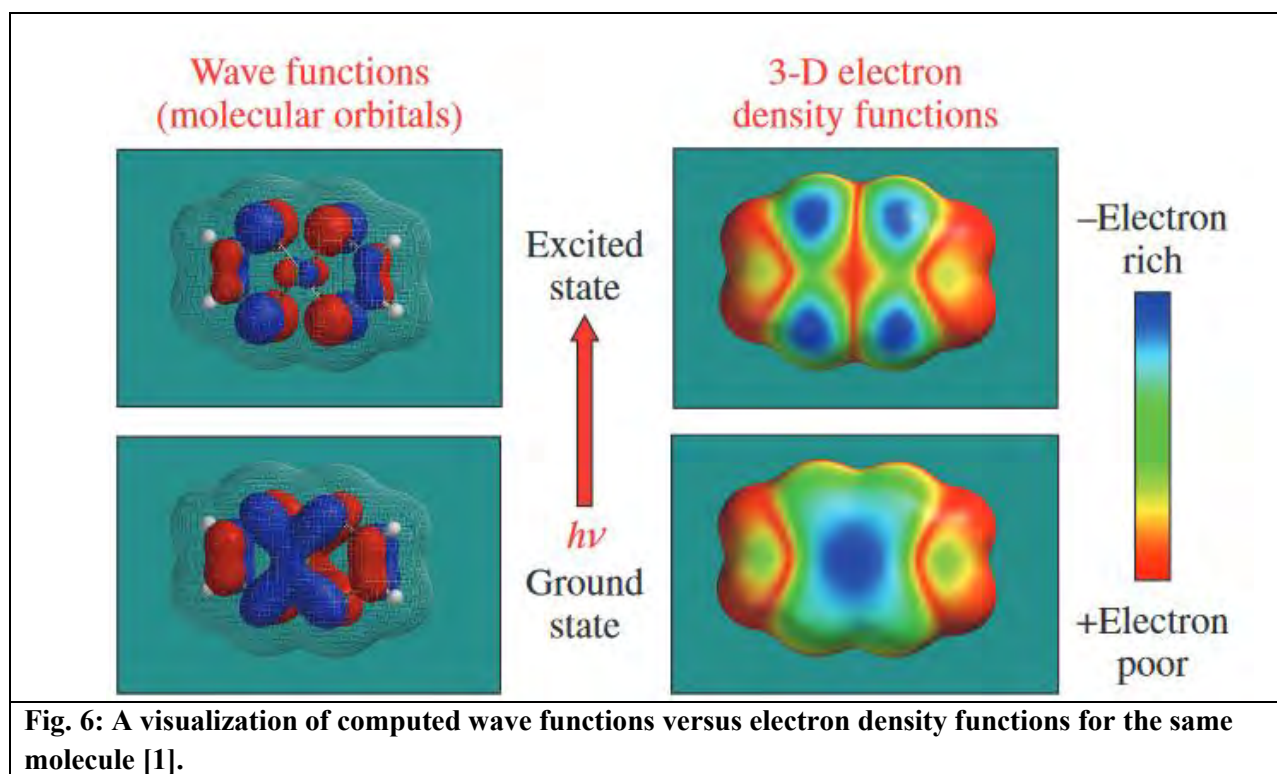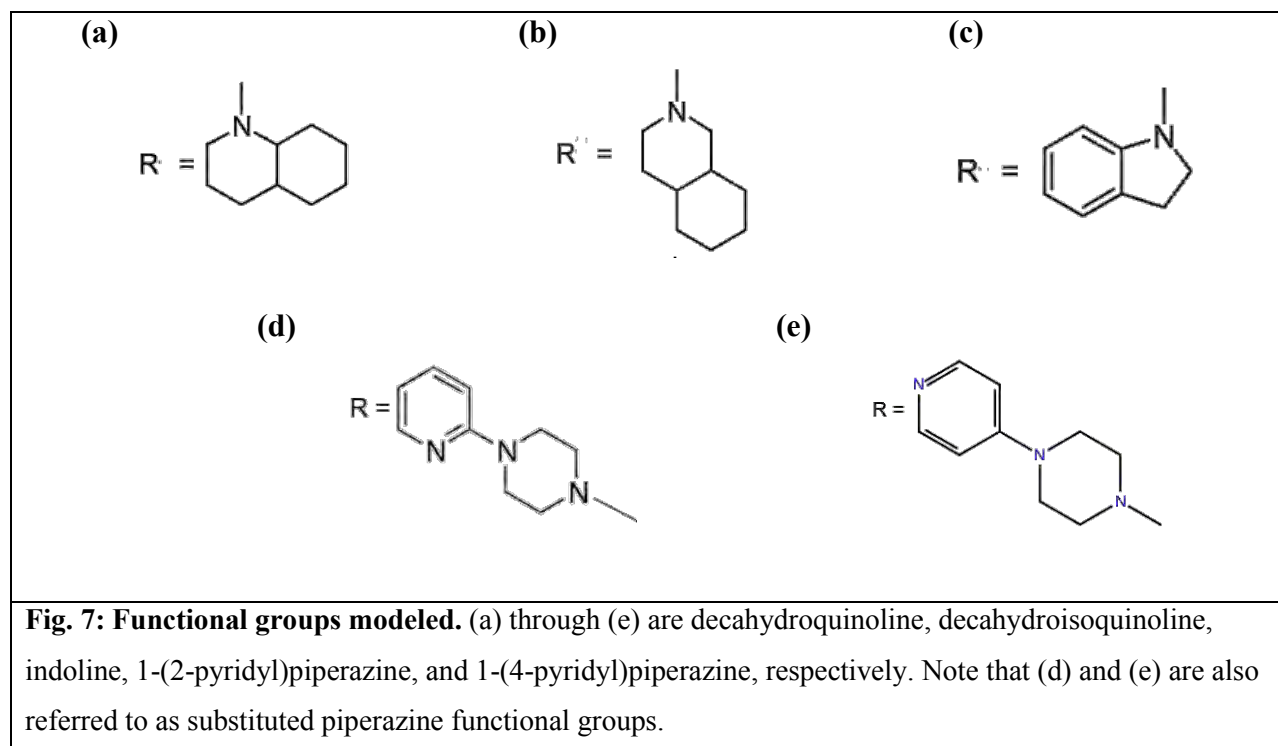
Past work that used DFT as the chosen computational method for the investigation of

azobenzenes for use in photoswitchable alignment layers has shown that a basis set of 6-31G**+

was the best compromise between efficiency and accuracy [2]. Note that a basis is a set of functions used to create the molecular orbitals in the computational model [5]. The notation ** indicates that all atoms, with the exception of transition metals, have polarization functions on them to describe additional electron orbitals, and the + places diffuse functions, which help to more accurately model electrons further from the nucleus, on all atoms excluding H and He [5].

3. Methodology

The optimal molecular structure for spirooxazine molecules was investigated by altering two factors: (1) the composition of the functional group, and (2) the length of the carbon tether attaching the spirooxazine chromophore to the methacrylate backbone. It was decided to vary the alkyl tether length between 3 and 9 carbons for relative ease of synthesis, as a tether length of less than 3 would be difficult to synthesize, while a tether longer than 9 carbons is expected to produce chain tangling and products with very low melting points that would be difficult to purify, and likely not well suited to use in photoalignment materials. Functional groups were initially chosen largely based on the work of Tan *et al* [6] in synthesis, characterization, and photochromic studies in spirooxazines containing heterocycle functional groups. These functional groups are depicted in Fig. 7 (a-c). However, extremely promising results from preliminary work with spirooxazines guided the modeling towards substituted piperazine functional groups, shown in Fig. 7 (d-e). It was theorized that like spirooxazine molecules with piperazine functional groups, the molecules with substituted groups would have relatively low isomerization-state energy differences, and that their larger size would make them more effective at redirecting the LC materials [7].

Fig. 7: Functional groups modeled. (a) through (e) are decahydroquinoline, decahydroisoquinoline, indoline, 1-(2-pyridyl)piperazine, and 1-(4-pyridyl)piperazine, respectively. Note that (d) and (e) are also referred to as substituted piperazine functional groups.

As with similar previous research, DFT was chosen in this work for optimization, single point energy, and transition state calculations to model the aforementioned different structures of spirooxazine molecules because of its combined efficiency and accuracy, since the models are highly computationally intensive. Geometry optimization of molecules for isomerization-state energy difference calculations, for example, takes approximately eight to sixteen hours, and transition state analysis averages a week (168 hours). Again based on previous research, this study selected the basis set 6-31G**+ for its efficiency and accuracy. In the interest of preserving computational resources, the length of the molecule was limited to contain only one tethered chromophore and four repeating units in the methacrylate backbone.

This work utilized the Schrodinger Materials Science Suite and the Maestro design and visualization interface for all calculations, more specifically employing Jaguar software for geometry optimizations, single point energy calculations, and transition state searches, and

Desmond for geometry minimizations [5]. These calculations were run on the Laboratory for Laser Energetics' supercomputing clusters.

With regards to transition state analysis, transition state searches were conducted only on molecules with isomerization-state energy differences of less than 5 kJ/mol, again in an effort to preserve time and computational resources. Transition state searches were run using linear synchronous transit (LST) along the lowest Hessian vector as recommended by the Schrodinger Materials Science Suite when input geometries are available [5]. In this case, the input geometries refer to the optimized open and closed isomers. Transition state searches were especially intensive computationally not only because they required the input for the open isomer to be manually built from the closed isomer in Maestro's 3D "drawer" in order to ensure that corresponding atoms in each isomer were properly numbered, but also because the resulting open isomer had to be minimized using Desmond and then re-optimized using Jaguar before the transition state search itself could proceed. Furthermore, vibrational frequencies were calculated for each transition state as a simple check on their accuracy, as transition states should have one vibrational frequency each.

4. Results and Discussions

Isomerization-state energy differences were calculated for spirooxazine molecules with five different functional groups for tether lengths 3 through 9, the most promising of which were then modeled in the transition state to gain further insight into the molecule's bistability. The five functional groups investigated in this work (Fig. 7) can be broadly categorized as nitrogen heterocycles or substituted piperazines. The isomerization-state energy differences for the spirooxazine molecules with the nitrogen heterocycle functional groups of Fig. 7(a-c) are shown

in Fig. 8. These values were all relatively small, with only the molecule with a decahydroisoquinoline functional group and tether length of 8 yielding an energy difference between the open and closed isomers of greater than 25 kJ/mol.
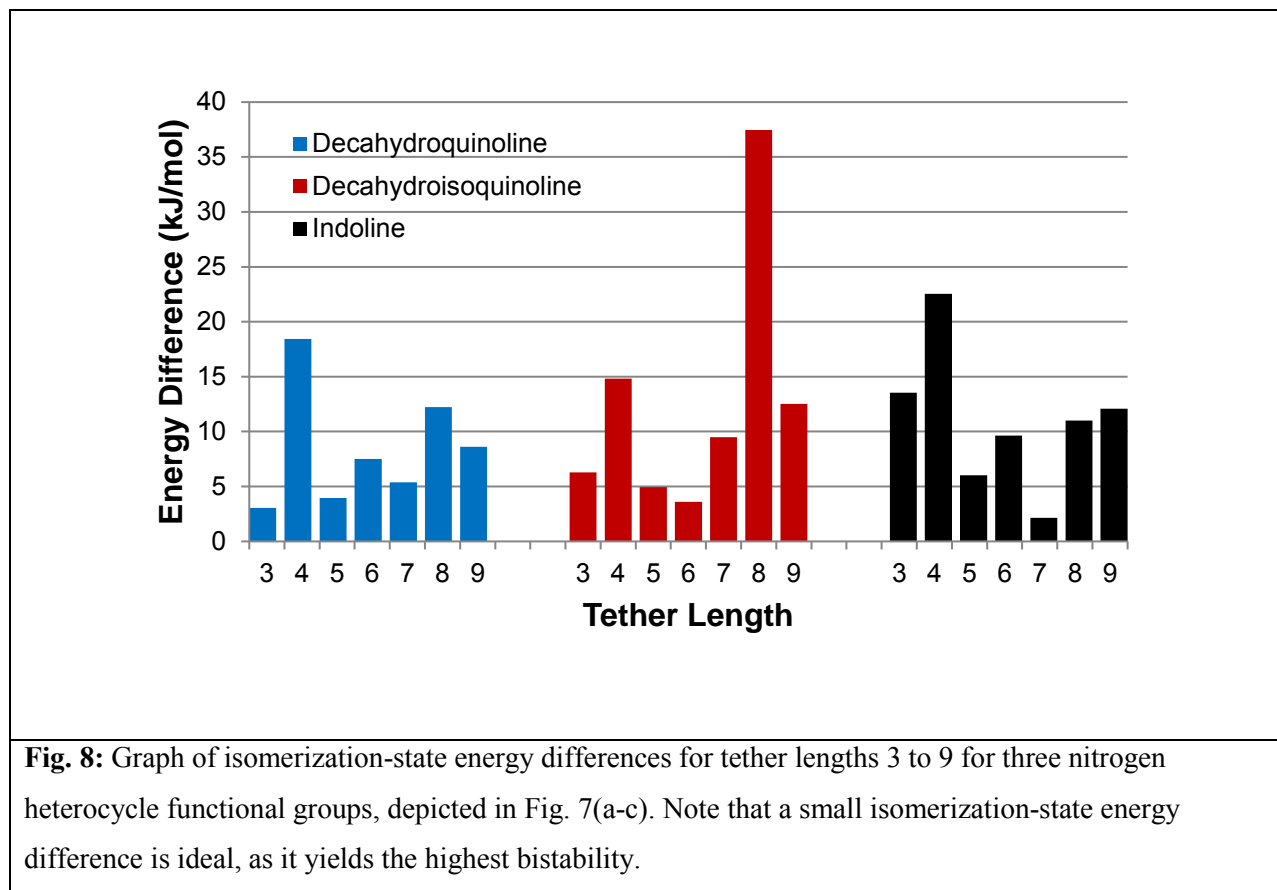

Fig. 8: Graph of isomerization-state energy differences for tether lengths 3 to 9 for three nitrogen heterocycle functional groups, depicted in Fig. 7(a-c). Note that a small isomerization-state energy difference is ideal, as it yields the highest bistability.

For spirooxazines with decahydroquinoline and indoline functional groups, an odd-even pattern is seen where the molecules with an even number of carbons making up its alkyl tether display a higher isomerization-state energy difference than that of the preceding odd tether length. This pattern has emerged in previous research with azobenzenes and is also a common phenomenon in LC materials, possibly due to steric effects caused by the folding of the alkyl chain [1].
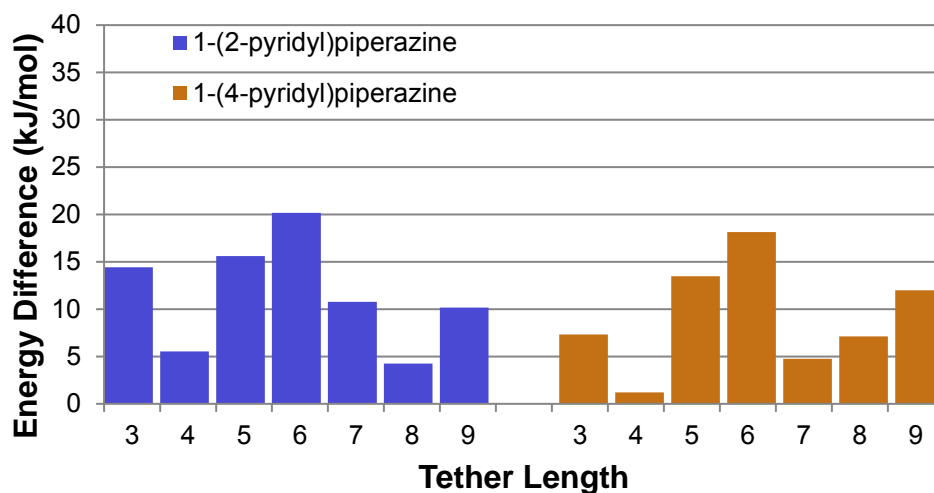
Fig. 9: Same as Fig. 8, but for substituted piperazine functional groups as depicted in Fig. 7(d-e).

The substituted piperazine functional groups of Fig. 7(d-e) also displayed promising isomerization-state energy differences, as seen in Fig. 9, although no similar odd-even pattern is evident. Notably, the spirooxazine molecule with a 1-(4-pyridyl)piperazine functional group and tether length of 4 yielded the smallest isomerization-state energy difference in this investigation of approximately 1.2 kJ/mol.

As previously described, transition state analysis was performed for molecules with an isomerization-state energy difference of less than 5 kJ/mole in order to gain further insight into the molecule's bistability by modeling the activation energy of the molecules' isomerization. These results are displayed in Table 1.
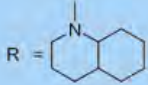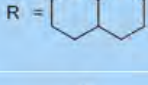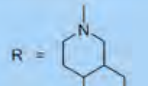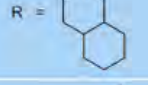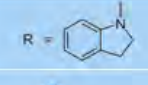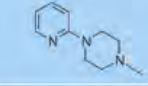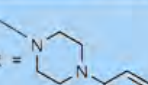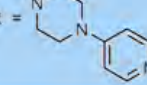
Terminal group	Tether length	Terminal group	Activation energy (kJ/mol)
Decahydroquinoline	3	R = (structure)	79.2
Decahydroquinoline	5		182.6
Decahydroisoquinoline	5	R = (structure)	80.6
Decahydroisoquinoline	6		70.6
Indoline	7	R = (structure)	68.8
1-(2-pyridyl)piperazine	8	(structure)	85.9
1-(4-pyridyl)piperazine	4	R = (structure)	78.0
1-(4-pyridyl)piperazine	7		57.7

Table 1: Activation energies for selected molecules

In general, activation energies ranged from approximately 60 to 80 kJ/mol with the exception of the spirooxazine molecule with a decahydroquinoline terminal group and tether length of five, whose activation energy (183 kJ/mol) was unusually high. However, the transition state search for this molecule returned three imaginary vibrational frequencies, when the transition state should only have one. Although two of the frequencies were small relative to the other, different options are being explored in the transition state search, for example quadratic synchronous transit (QST), to further examine this result. However, QST requires one to make a "guess" at the transition state structure as input; in this case, the transition state structure is relatively unknown.

Other than this outlier, the results displayed in Table 1 helped to identify the most promising candidate molecule, the spirooxazine molecule with a 1-(4-pyridyl)piperazine functional group and tether length of 4, noted in the discussion of Fig. 9. Computational

14

modeling of this molecule demonstrated both a low isomerization-state energy difference and significant activation energy, characteristics that combine for the high bistability necessary for molecules in a photoswitchable alignment layer. Although this molecule appears to be the most promising, many of the other molecules selected for transition state analysis display similar characteristics, and will be further examined experimentally for confirmation of their suitability.

5. Conclusions

Based on computational modeling, spirooxazine appears to be a highly promising chromophore for use in photoalignment materials. The vast majority of the molecules examined displayed isomerization-state energy differences of less than 25 kJ/mol, with several demonstrating extremely low isomerization-state energy differences of less than 5 kJ/mol. Furthermore, the molecules that qualified for transition state analysis also displayed significant activation energies, which, in combination with the low isomerization-state energy differences, are indicative of a high bistability as shown by Fig. 5. Of the molecules modeled, spirooxazine with a 1-(4-pyridyl)piperazine functional group and tether length of 4 appears to be the most promising. Not only did it display the lowest isomerization-state energy difference, but transition state analysis also yielded a significant activation energy; both of these characteristics yield high bistability, and the larger functional group should be able to more effectively redirect the orientation of the LC materials.

In the future, additional methods of transition state analysis, for example QST, will be explored to corroborate the abnormal result of spirooxazine with a decahydroquinoline functional group and tether length of 5. It is also hoped to explore other backbones in addition to methacrylate to examine the effect of the backbone on the molecule's bistability. Potential

backbone candidates for such research include acrylamide (which has been modeled extensively with azobenzenes) and siloxane.

The computational results described in this work are intended to guide the synthesis of molecules for use in photoalignment materials. In the future, experimental corroboration of this modeling is necessary before further development is done.

6. Acknowledgements

References

[1] Marshall, K. L. et al; "Optically-addressable liquid crystal laser beam shapers employing photoalignment layer materials and technologies" (Conference Presentation); SPIE proceedings vol. 10375, Liquid Crystals XXII, September 2018

[2] Marshall, K. L. *et al*; "Computational Chemistry Modeling and Design of Photoswitchable Alignment Materials for Optically Addressable Liquid Crystal Devices"; LLE Review, vol. 143, pp 150-161, August 2015

[3] Ubukata, Tatashi *et al*; "Modeling the Interface Region of Command Surface 1. Structural Evaluations of Azobenzene/Liquid Crystal Hybrid Langmuir Monolayers"; J. of Phys. Chem, vol. 104, pp 4141-4147, April 2000

[4] Wang, Rui, "Computational Modeling of Spectral Properties of Nickel Diethiolene Dyes"; LLE Summer High School Research Program, 2006

[5] Jaguar User Manual, Schrodinger Press, May 2015

[6] Tan, Ting-Feng *et al*; "Synthesis, characterization and photochromic studies in film of heterocycle-containing spirooxazines"; Tetrahedron, vol. 61, 8291-8198, 2005

[7] James Savino, Private Communication

Oxidation of Copper Zinc Alloy

Maia Raynor

Brighton High School

LLE Advisors: Walter Shmayda and Cody Fagan

Abstract

A copper zinc (Cu/Zn) alloy was characterized for its use as an alternative concept to traditional techniques for extracting tritium from air streams. The molecular tritium is oxidized to form tritiated water which is then captured on a molecular sieve. The Cu/Zn alloy consists of 40 wt% of Cu and Zn and balance support alumina. In this work, hydrogen is used in place of tritium to mitigate any radiological hazards. Oxygen is loaded onto the bed preceding the hydrogen oxidation. The oxygen gettering dependence on alloy temperature has been measured at various bed temperatures. Gettering capacity increases as the temperature increases from 30°C to 150°C and approaches 100% at 150ºC. Oxygen gettering efficiency of the bed is not influenced by temperature and is also independent of the range of total flow rates and oxygen concentrations examined. During hydrogen oxidation, conversion efficiency of hydrogen to water decreases as oxygen inventory on the bed increases. The results indicate that the Cu/Zn alloy can oxidize hydrogen at significantly lower temperatures than the traditional method and can be implemented as an alternative in the nuclear industry to remove molecular hydrogen isotopes from air streams.

1. Introduction

Catalytic oxidation of molecular hydrogen species has potential applications in industry to treat hydrogen waste streams to form non-hazardous waste water. This same process can also be used in the nuclear industry to remove molecular tritium from air streams [1]. Tritium process systems are typically enclosed in gloveboxes to minimize exposure to radioactive material. An inert gas, helium, is utilized in the glovebox because elemental hydrogen that escapes from process loops can be recaptured and re-used [2]. Traditionally, a copper (Cu) bed operating in the realm of 700°C is used to convert molecular tritium to tritiated water, which is then captured on a molecular sieve. This process can be repeated once the Cu bed is reloaded with oxygen. The equation for reducing the Cu alloy is: $T_2 + CuO \rightarrow T_2O + Cu$. Alternatively, a Cu/Zn alloy is able to oxidize tritium at significantly lower temperatures (~150°C) than the tradition Cu metal [3]. The equation for reducing the Cu/Zn alloy is: $T_2 + Cu/ZnO \rightarrow T_2O + Cu/Zn$. The alternative tritium removal system is shown in Fig. 1.1.

Figure 1.1: Schematic of alternative elemental tritium removal system where the Cu/Zn alloy is employed. An air stream containing molecular tritium is flown over a Cu/Zn bed that converts molecular tritium to tritiated water which is then captured on a molecular sieve.
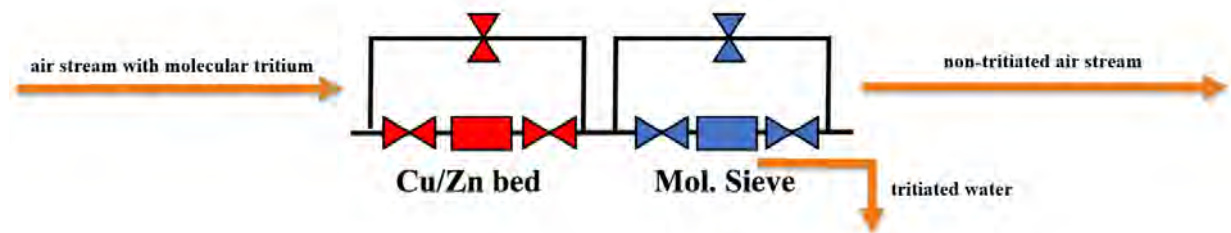
In this experiment, a Cu/Zn alloy was characterized as an alternative to replace Cu. Specifically, this experiment investigated the oxygen gettering efficiency (defined as the bed's efficiency of adsorbing oxygen) and capacity (the percentage of copper that is oxidized) as a function of bed temperature during the oxygen regeneration process and the bed's conversion efficiency of hydrogen to water as a function of oxygen inventory during the hydrogen oxidation process.

2. Experimental

The gettering experimental setup is shown in Fig. 2.1. This setup was used to determine the hydrogen oxidation oxygen gettering efficiencies of the Cu/Zn bed at various temperatures. Gas flow (H_2, 20% O_2 in N_2, and He) can travel over the Cu/Zn bed or through a bypass line. The bypass line, system lines, and capillary tubing are heated to prevent water from condensing in the system. The bypass line and system lines were heated to 100° C and the capillary tubing was heated at 150° C. To monitor these temperatures, thermocouples are located in the outlet stream of the Cu/Zn bed and adjacent to the Residual Gas Analyzer (RGA). The RGA is a mass spectrometer that finds the chemical composition of a gas by measuring the distribution of mass to charge ratios of the ionized gas molecules. The bed is surrounded by a heater and packed with insulation to preserve the desired temperature for each experiment. The bed's temperature ranges from 30° C to 200°C and is measured with a thermocouple attached directly to the bed. The dew point monitor, thermocouples, and RGA are utilized in data acquisition.

Figure 2.1: Schematic of experimental system.

3
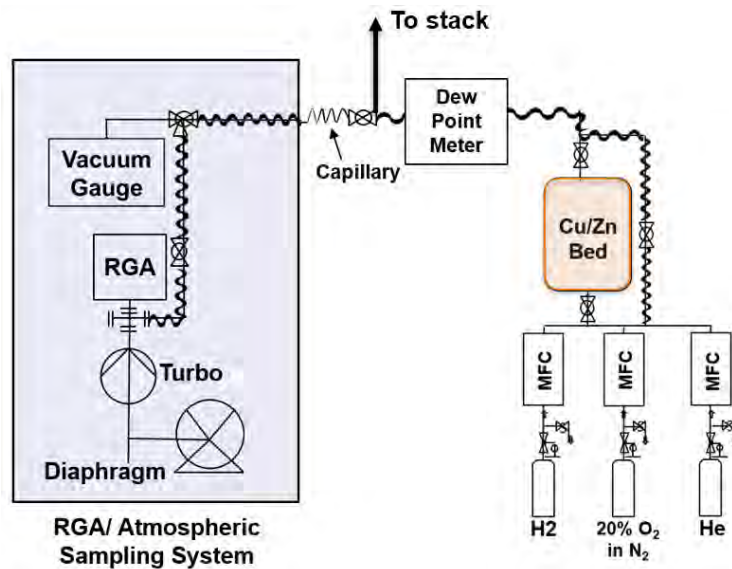
2.1 Properties of the Cu/Zn Alloy and the Bed

The 188 gram Cu/Zn alloy (Gettermax 133), 140 cm^3 internal volume bed utilized for this experiment was comprised of 40% Cu and 40% Zn with alumina for balance. The particle size/shape of the pellets composing the Cu/Zn alloy is 3 × 3 mm. The bed cavity is cylindrical with a diameter of 5.4 cm and length of 6.1 cm. The tapped density (defined as the increased density of the bulk attained after mechanically tapping the container) of the alloy in the bed is 1.35 g/cm^3. The ratio of the particle diameter to the bed diameter is 0.0556, which implies that slippage flow between the alloy and the wall represents less than 1% of the total flow through the alloy (according to calculations).

The gas flow enters through the inlet valve, passes through a 100 μm stainless steel filter, interacts with the Cu/Zn alloy, and then leaves the bed through a second 100 μm filter, as shown in Fig. 2.2. At a flow rate of 1 L/min the superficial velocity through the bed (=volumetric flow rate ÷ cross-sectional area of the bed) is 1 cm/s and the residence time in the bed (= bed volume ÷ volumetric flow rate) at the flow rate is 8.4 s. Under these conditions the modified Reynolds number (=particle diameter × superficial mass flux ÷ gas viscosity) is 0.2 and indicates the flow through the bed is laminar. The flow can be visualized as a slug of gas moving through the getter material.

Figure 2.2: Schematic of the getter bed.
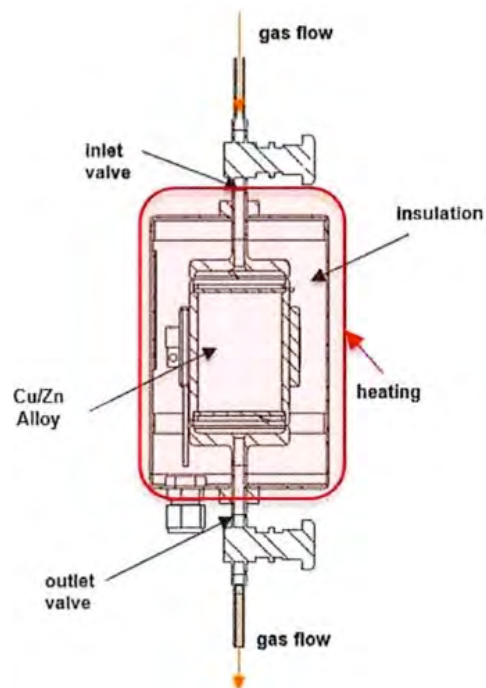
2.2 Gases

Three gases, helium, hydrogen, and 20% oxygen in nitrogen were used during the experiment. Helium gas functioned as a carrier gas while the hydrogen and 20% oxygen in nitrogen were the actual experimental gases used to test the bed's oxygen gettering capacity, oxygen gettering efficiency, and conversion efficiency of hydrogen to water. The flow rates of the gases were controlled by three mass flow controllers (Alicat) which were controlled by a LabVIEW program. The gases could either be sent over the Cu/Zn bed or through the bypass line for control and calibration (see Fig. 2.1). Helium was used as an inert carrier gas flown at a rate of 1 L/min to purge the system of atmospheric air and other residual gases as well as to carry the low quantities of hydrogen and oxygen through the system. A mixture of 20% oxygen in nitrogen was passed over the Cu/Zn bed during oxygen gettering experiments to load the bed with oxygen. Hydrogen was sent over the oxidized Cu/Zn species to regenerate the bed during hydrogen oxidation experiments.

2.3 Oxygen Gettering Experiment

For an oxygen gettering experiment 47.6 sccm (standard cubic centimeters per minute) of 20% oxygen in nitrogen is co-blended with 1 L/min of helium. Figure 2.3 is a graph of the percentage of oxygen gettered over the course of the experiment.

Figure 2.3: Percentage of oxygen adsorbed (gettered) by the Cu/Zn bed over the course of an oxygen gettering experiment. A nonlinear scale is used during the initial portion to better display the early time behavior.
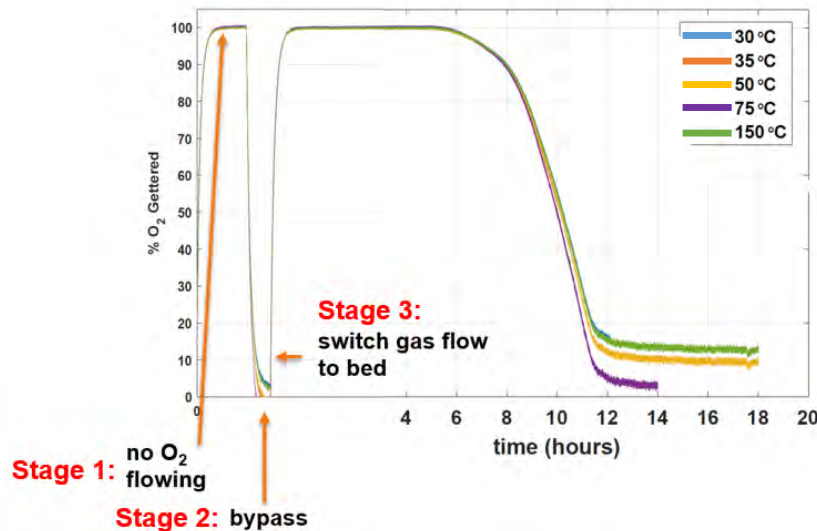
At the beginning of the experiment (Stage 1 in Fig. 2.3), there is no oxygen being passed through the system. During Stage 1, there appears to be 100% oxygen gettered according to the figure. This is because there is close to 0% oxygen in the outlet stream of the bed. Oxygen flow is then sent through the bypass line to calibrate the RGA signal (Stage 2 in Fig. 2.3). Once calibrated, the gas flow is then sent over the Cu/Zn bed (Stage 3 in Fig. 2.3), which is expected to getter oxygen to form Cu/ZnO. Close to 100% of the oxygen is gettered until the bed is no longer able to absorb all of the oxygen in the gas stream at that temperature. This is known as break through. Break through level in these experiments is arbitrarily defined as the point when the oxygen gettering efficiency drops to 80% i.e., when the fraction of oxygen in the outlet stream is 20% of the total oxygen in the inlet gas stream. Figure 2.3 shows that the bed has a relatively high gettering efficiency, meaning the bed is absorbing all of the oxygen in the inlet stream. This experiment determined the gettering efficiency of the bed for several temperatures between 30°C and 150°C.

2.4 Hydrogen Oxidation Experiment

During hydrogen oxidation experiments, 10 sccm of hydrogen was co-blended with 1 L/min of helium and passed over the Cu/Zn bed loaded with oxygen from the preceding oxygen gettering experiment. The bed was heated at 200°C and experiments were conducted at varying oxygen inventory levels on the copper alloy. Figure 2.4 is a data graph of the hydrogen and water flow in the system over the course of a typical run.

Figure 2.4: Partial pressure of H_2 and H_2O in the outlet stream of the Cu/Zn bed over the course of a hydrogen oxidation experiment.
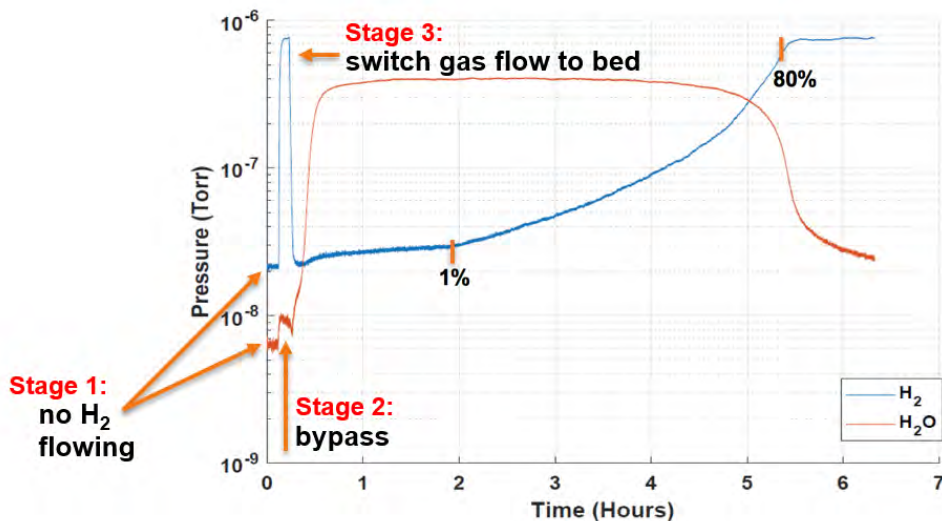
Initially, there is no hydrogen being sent through the system (Stage 1 in Fig. 2.4). Hydrogen is then passed through the bypass line to calibrate the RGA signal (Stage 2 in Fig. 2.4). Once the RGA signal is calibrated, hydrogen gas is passed over the Cu/Zn bed (Stage 3 in Fig. 2.4). When the gas flow is initially switched to the bed, the hydrogen concentration in the outlet stream decreases rapidly and the water concentration increases because the hydrogen being passed over the bed bonds with the adsorbed oxygen to produce water. Once the oxygen inventory on the bed is exhausted, the hydrogen concentration in the outlet stream increases while the water concentration decreases. Break through level is defined as the point when the hydrogen concentration in the outlet stream returns to 80% of the feedstock concentration. Once the partial pressure of hydrogen in the outlet stream matches that of the inlet stream, there will be no oxygen bonded to the copper alloy and the alloy will be fully regenerated.

3. Results and Discussion

3.1 Oxygen Gettering Capacity

Oxygen gettering capacity is defined as the percent copper oxidized on the bed at a specified temperature when the maximum quantity of oxygen has been adsorbed onto the bed. The temperature dependence of the oxygen gettering capacity and efficiency was determined by fixing the flow rate of oxygen and helium and changing the temperature of the bed over several runs. The concentration of oxygen in the outlet stream was measured as a function of time. The results for the percentage of oxygen gettered as a function of time measured by the RGA are show in Fig. 2.3. It is found that the oxygen gettering capacity of the Cu/Zn alloy increases with increasing bed temperature from 30°C to 150°C. The percentage of the copper oxidized up to the breakthrough for five bed temperatures is shown in Table 3.1 and demonstrates that the percentage of copper oxidized increases with increasing temperature.

Table 3.1: Quantity of copper oxidized as a function of temperature for five different bed temperatures.

Temperature (°C)	% of Cu Oxidized
30	5.0
50	7.0
75	15.6
100	29.0
150	41.9

3.2 Oxygen Gettering Efficiency

The oxygen gettering efficiency of the Cu/Zn bed was determined by comparing the concentration of the oxygen in the outlet stream to the concentration of oxygen in the inlet stream. Fig. 3.1 shows the fraction of oxygen gettered as a function of time magnified prior to breakthrough. It reveals that there is a slight difference between the oxygen concentrations in the outlet stream when there is no oxygen flowing through the system compared to when oxygen is initially being flown over the bed. This indicates that when the oxygen is initially flown over the Cu/Zn bed the bed is gettering 99.8% of the oxygen flow. This trend perpetuates for different temperatures showing that oxygen gettering efficiency is independent of temperature.

Figure 3.1: Same as Figure 2.3 except that it is magnified at low times.
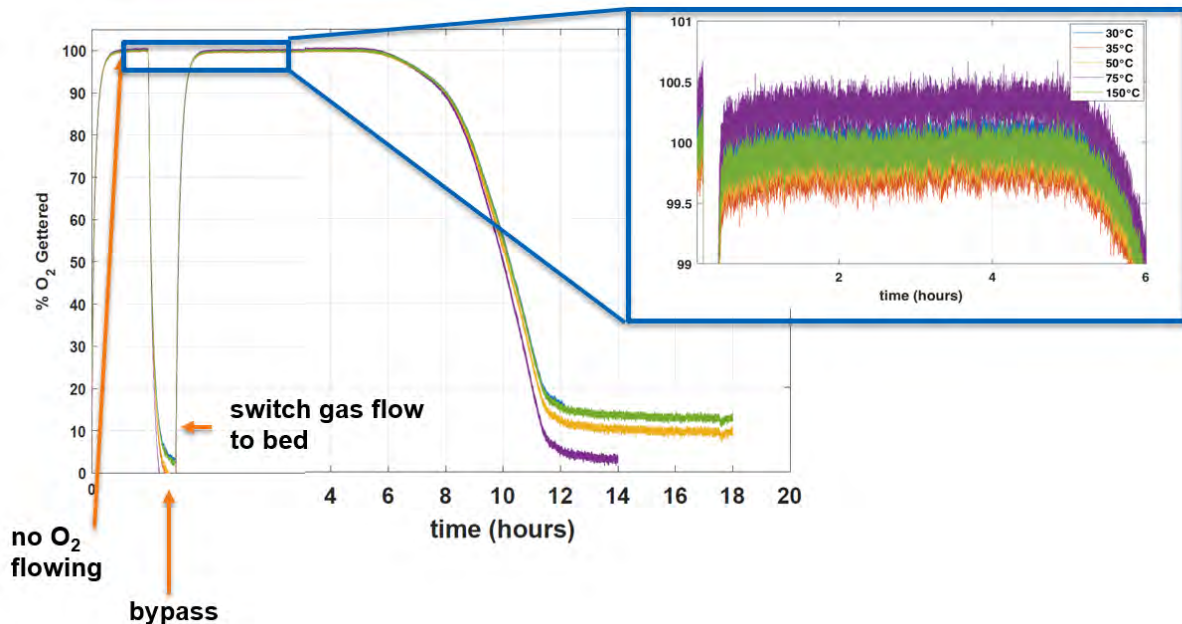
Delivering oxygen to the bed results in an exothermic reaction which produces watts of heat. When less oxygen is delivered to the bed, less heat is generated. Through a series of calculations summarized below, it was determined that varying the amount of oxygen delivered to the bed, and therefore changing the amount of heat the exothermic reaction generates, does not affect the bed's efficiency. The heat of formation of CuO is 157 kJ/mol of CuO. With 0.087 mol/L of 20% oxygen in nitrogen and 1 L/min of helium, there are 455 watts generated in the getter bed. If the helium flow rate is reduced to 0.25 L/min the heat generated by the exothermic

reaction is only 114 Watts. Heat loss from the bed is mostly by conduction through the medium to the walls of the getter bed (although 8W will be carried away by hot gas). Despite the considerable decrease in heat produced by the reaction, it is found that there is negligible change in the efficiency. This is another indication that the oxidation rate is not sensitive to temperature.

The oxygen gettering efficiency of the Cu/Zn bed was measured as a function of total flow rate. A concentration of 0.087 mol/L of 20% oxygen in nitrogen was held constant for total flow rates varying from 0.25 L/min to 2 L/min. Fig. 3.2 shows the gettering efficiency as a function of total flow rate and demonstrates that as total flow rate increases, the oxygen gettering efficiency remains constant.

Figure 3.2: Oxygen gettering efficiency dependence on total flow rate.
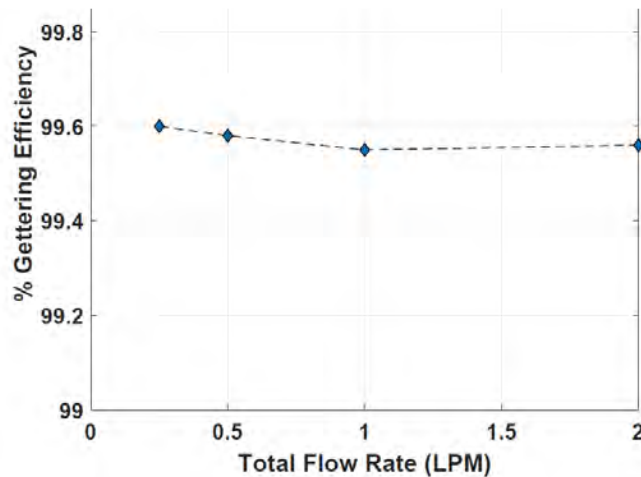
The gettering efficiency was also tested as a function of oxygen concentration. The concentration of oxygen in the carrier stream was varied from 0.14×10^{-3} mol/L to 1.1×10^{-3} mol/L of oxygen per liter of carrier gas. Fig. 3.3 shows the gettering efficiency as a function of oxygen concentration and demonstrates, within experimental error, that as the oxygen concentration increases the oxygen gettering efficiency of the Cu/Zn bed does not change.

Figure 3.3: Oxygen gettering efficiency dependence on oxygen concentration in the carrier. Dashed lines connect data points but there is no significant trend.
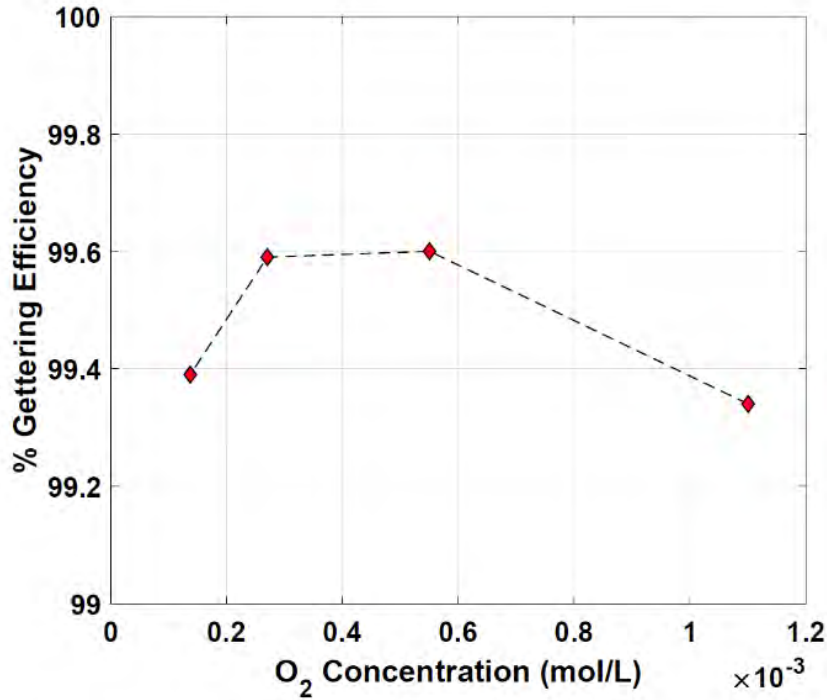
3.3 Hydrogen Oxidation Efficiency

The Cu/Zn hydrogen oxidation efficiency, shown in Fig. 2.4, was measured by fixing the hydrogen and helium flow rates as well as the alloy temperature and varying the oxygen inventory on the bed at the start of each experiment. The concentrations of hydrogen and water species in the outlet stream were measured as a function of time, as shown in Fig. 2.4. It is seen that the hydrogen concentration in the outlet stream when hydrogen is initially passed over the bed is slightly greater than the hydrogen concentration when no hydrogen is being flown through the system. This indicates that during hydrogen oxidation, the conversion efficiency of hydrogen to water is less than 100%.

The water production efficiency of the Cu/Zn bed was measured for varying oxygen inventories. The oxygen inventory of the bed is equivalent to the percentage of copper oxidized. Figure 3.4 shows the water production efficiency of the bed at varying oxygen inventories on copper.

Figure 3.4: H_2O production efficiency as a function of percentage Cu oxidized, measured at 200°C
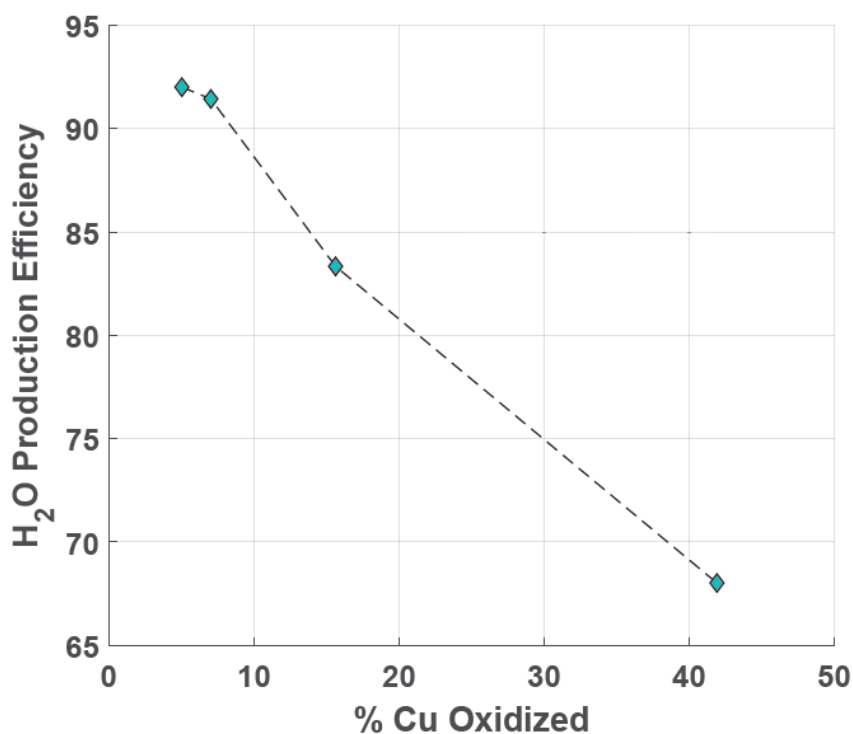
This figure demonstrates that water production efficiency of the Cu/Zn bed decreases as the fraction of oxidized copper increases. This is due to the position of the mass transfer zone (defined as the portion of a packed column where the adsorption occurs) moving along the length of the bed with increased oxidized copper. Eventually, this zone which is required for complete conversion of $Cu/ZnO + H_2 \rightarrow Cu/Zn + H_2O$ is small enough that the conversion cannot be completed. This decreases the water production efficiency of the bed. This supports that the oxidized Cu/Zn bed will convert hydrogen to water as long as there is available oxygen on the bed, but at a reduced efficiency.

Conclusion

The goal of this research was to use Cu/Zn as a more efficient alternative of capturing tritium. This work looked at oxygen gettering dependence on alloy temperature, total gas flow rates, and oxygen concentrations. It also looked at the conversion efficiency of hydrogen to water as a function of oxygen inventory. It was found that oxygen gettering capacity increases as the temperature of the alloy increases from 30°C to 150°C. Gettering efficiency of the Cu/Zn bed is not influenced by temperature and is independent of total flow rate and oxygen concentration over the range tested. During hydrogen oxidation, conversion efficiency of hydrogen to water is less than 100% at 200°C and decreases as the oxygen inventory on the bed increases. The Cu/Zn bed will convert hydrogen as long as there is available oxygen on the bed, but at a reduced efficiency as the oxygen inventory increases. These results signal that the Cu/Zn alloy has the ability to perform at significantly lower temperatures than the traditional method. They also support the conclusion that the alloy could be implemented in the nuclear industry to remove molecular hydrogen from air streams.

Acknowledgments

References

[1]   *Technologies for Mitigating Tritium Releases to the Environment*. (2005). *LLE Review*. Volume 103, Page 142.

[2]   Gnolek, S. (2013, November). *Catalytic Oxidation of Hydrogen in Air Streams*. LLE Summer High School Research Program.

[3]   Hanchett, M. (2012, December). *Oxygen Uptake Using a Nickel Catalyst*. LLE Summer

High School Research Program.

Protective Polymer Coatings for Laser Optics

Margaret Rudnick

Pittsford Mendon High School,
Rochester NY, 14534
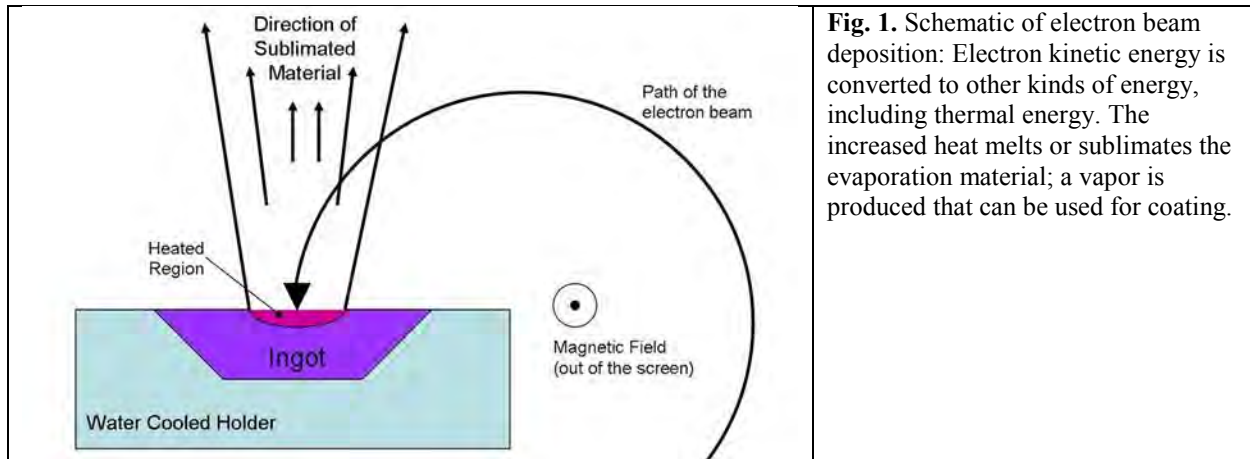
Advisor: Kenneth L. Marshall

Abstract

Mirrors and laser glass used in OMEGA and OMEGA EP are sensitive to water. When water vapor works its way into the pores of high-reflectance mirror coatings, the wavelength of peak reflectance shifts, leading to a reduced reflectance at the intended beam wavelength. Water exposure leads to pitting and eventually clouding on phosphate laser glass, causing light from the laser beam to scatter. Both of these effects ultimately lead to a loss of energy as the beam makes its way to the target. Different organosilanes and coating processes were tested on both mirrors and phosphate laser glass with the overall goal of slowing the absorption of water into the samples. An effective coating process was found for the mirrors that involves vapor depositing organosilanes in a nitrogen-purged atmosphere. Although vapor depositing organosilane coatings onto laser glass did not afford a sufficient level of protection from water vapor, polydimethylsiloxane (PDMS) applied by rod-coating was found to effectively protect the glass from water damage in an environment of 99% relative humidity.

1. Introduction: Importance of the Sensitivity of Optics to Water Vapor

1.1 High Reflective Coatings

High power lasers are used to investigate the use of fusion as a practical source of energy. Many of these lasers use high reflective (HR) coatings composed of hafnia and silica layers on a glass substrate as mirrors to redirect the laser beam. Various methods of coating the substrate with hafnia and silica layers (sputtering, ion assisted deposition, e-beam deposition) can result in porous coatings. Electron beam deposition (**Fig. 1**) is the coating method primarily used at the Laboratory for Laser Energetics (LLE) for OMEGA and OMEGA EP, the Lawrence Livermore National Laboratory for the National Ignition Facility (NIF), and the Megajoule Laser Facility for CEA in France.[1, 2]

Fig. 1. Schematic of electron beam deposition: Electron kinetic energy is converted to other kinds of energy, including thermal energy. The increased heat melts or sublimates the evaporation material; a vapor is produced that can be used for coating.

Because deposition of the hafnia and silica is not uniform, many pores exist in the HR coatings for water vapor to infiltrate. When water works its way into the pores of the HR coating, both the refractive index and the narrow absorption band of the coating change (example shown in **Fig. 2**), which leads to major energy losses as the beam travels to the target.

Fig. 2.[3] Averaged spectral characteristics of 22 NIF transport HR coating runs (vertical line width represents one standard deviation from the mean); note the presence of the narrow %reflectance peak from ~350-400 nm. If this peak shifts even slightly, the ability of the HR coating to reflect beam energy at 351 nm may be greatly reduced. This fact illustrates the importance of preventing water infiltration into HR coatings.

HR coatings in the OMEGA and OMEGA EP lasers redirect laser beams primarily at 351 nm and 1054 nm wavelengths. The HR coating samples experimented with are intended for use with a 351 nm laser pulse. However, these coatings could also be used with a 1054 nm laser pulse, which has a higher laser damage threshold.
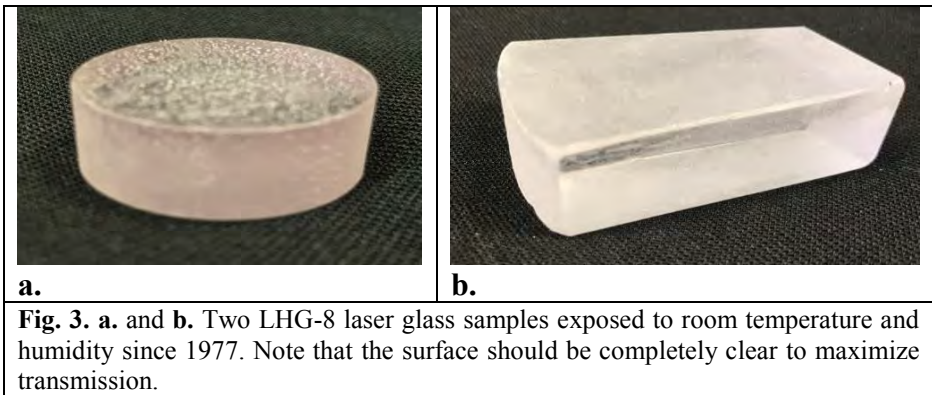
1.2 Laser Glass

LHG-8 is a phosphate-based laser glass used in many high-peak-power lasers (OMEGA, OMEGA EP, the NIF, Gekko-XII, LFEX (PW), Vulcan, and LIL[4]) as a gain medium to amplify

the beam. This glass was chosen, in part, for its athermal properties. LHG-8 has a nearly zero temperature coefficient of optical path length ($+0.6 \times 10^{-6}$ / ºC). This property is important because repeated laser shots raise the temperature of the glass, causing a change in optical path length and disturbance in the spatial oscillation pattern and overall oscillation performance of the beam.[5]

LHG-8 laser glass possesses desirable athermal properties, but it is sensitive to water vapor. The rods and disks in OMEGA and OMEGA EP experience "chalking" and pitting (**Fig. 3**), due to incremental lapses in atmospheric control of the nitrogen environment that the equipment is housed in.[6, 7] The chalking is a

Fig. 3. a. and **b.** Two LHG-8 laser glass samples exposed to room temperature and humidity since 1977. Note that the surface should be completely clear to maximize transmission.

result of leaching and pitting, and is caused by network dissolution.[8, 9] In the laboratory, some degree of macroscopic chalking was observed on laser glass samples kept at room temperature and humidity only two weeks after polishing. After this observation, freshly polished laser glass samples were housed in a desiccator at ~25% relative humidity (RH).

The overall effect of chalking and pitting on the laser glass surface is a loss of beam energy. The chalking lowers the sample's %transmission and the pitting causes the beam to scatter. To minimize the effect of chalking and pitting, a 50/50 mixture of ethylene glycol and water is used to cool the LHG-8 rods in the OMEGA laser, which significantly reduces (but does not completely eliminate) degradation of the optical quality of the laser glass rods.

2. Methodology: Vapor Phase Organosilylation

To combat water sensitivity of both the HR coatings and LHG-8 laser glass, coatings that render the surface hydrophobic by preventing the penetration of water were developed. Organosilazanes were first investigated for generation of hydrophobic coatings because of their successful application as contamination-resistant coatings on multi-layer dielectric gratings.[10, 11] Silazanes, a subcategory of silanes, are hydrides of silicon and nitrogen (analogous to siloxanes with -NH- replacing -O-). Hexamethyldisilazane (HMDS), tetramethyldisilazane (TMDS), bis(trifluoropropyl)-tetramethyldisilazane (FTMDS), and trimethylchlorosilane (TMCS) were chosen specifically due to their high laser damage threshold performance on these MLD gratings.[10, 11]

Organosilanes chemically modify surfaces containing hydroxyl groups through the process of silylation (**Fig. 4**). HR coatings are known to have surface hydroxyl groups due to hydration of their hafnium oxide and silica oxide composition. The LHG-8 laser glass composition also indicates that surface hydroxyl groups are present for silylation to take place (**Fig. 5**).[4]
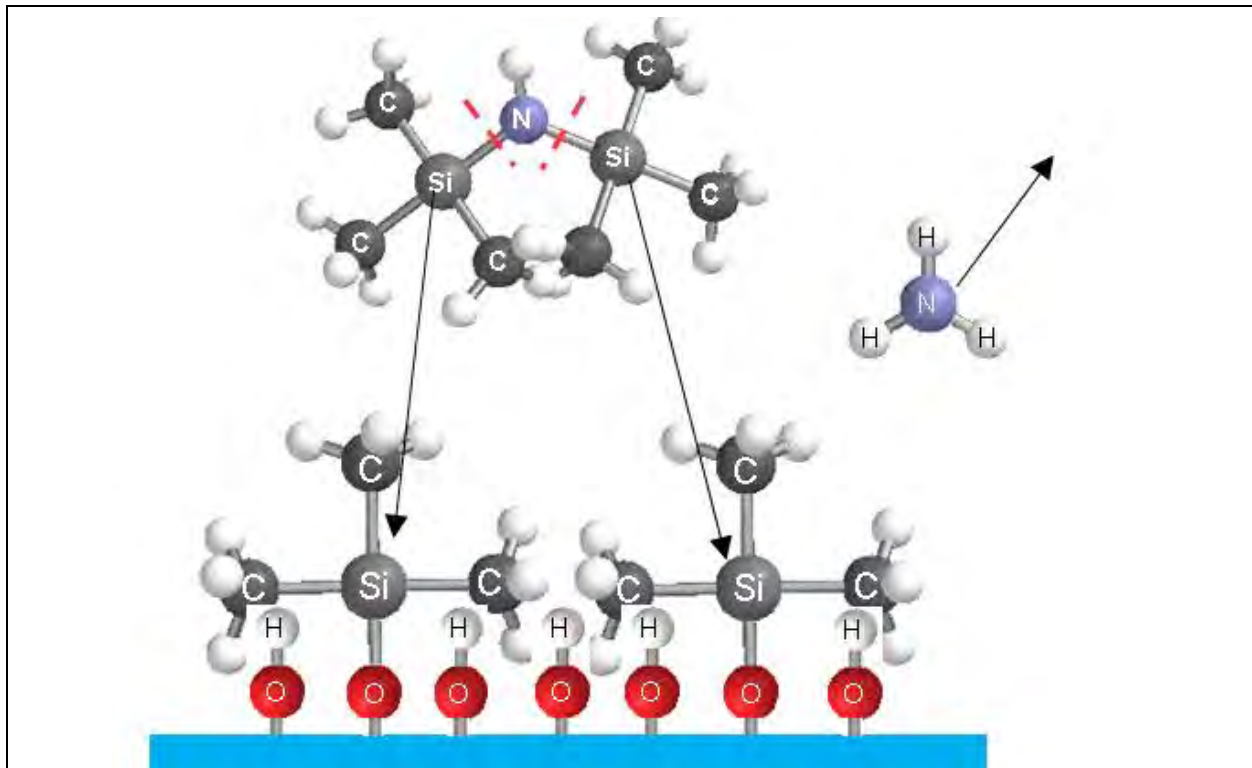
Fig. 4. Silylation occurs when silane groups break off from the disilazane and bond to hydroxyls on the substrate's surface; ammonia is produced as a byproduct. It should be noted that TMCS reacts with the surface hydroxyl groups by depositing a single trimethylsilane group through a similar (but simpler) one-step process, forming hydrogen chloride gas as a byproduct.

Component oxide equivalent (mol%)	LHG-8 [8]	LG-770 [8]	LG-750 [8]	HAP-3 [52]	Nd-SG [78]
P_2O_5	55-60	58-62	55-60	60	-
Al_2O_3	8-12	6-10	8-12	10	1.64
SiO_2	-	-	-	15	98.1
K_2O	13-17	20-25	13-17	-	-
Li_2O	-	-	-	13	-
BaO	10-15	-	10-15	-	-
MgO	-	5-10	-	-	-
Nd_2O_3[a]	0-2	0-2	0-2	0-2	0.23
Other	<2	<2	<2	<2	0
O/P ($\pm$0.1)	3	3	3	3.2	NA

[a] Nd-doping levels vary depending on use.

Fig. 5.[4] Representative compositions of commercial Nd-doped laser glasses and one developmental glass. The boxed compounds indicate compounds that form surface hydroxyl groups, enabling silylation to occur.

The vapor deposition experimental setup initially followed the same procedure as used to coat MLD gratings[10] and consisted of a sealed jar containing either an HR-coated substrate or a piece of polished laser glass and a 5 mL beaker with 1-2 mL of the chosen organosilane (**Fig. 6**). Most of the organosilanes used are volatile enough to vaporize at room temperature and then deposit on the surface of the sample as a vapor, inducing silylation. In some experiments, increased heat (50ºC) was applied by a programmable hot plate, and a watch glass replaced the screw-on lids in order to prevent a pressure buildup within the glass jars. Both reflectance and transmission spectra were taken using a Perkin Elmer Lambda 900 UV-VIS NIR spectrophotometer equipped with an integrating sphere detector or a 6º fixed spectral reflectance accessory for the HR coatings before and after
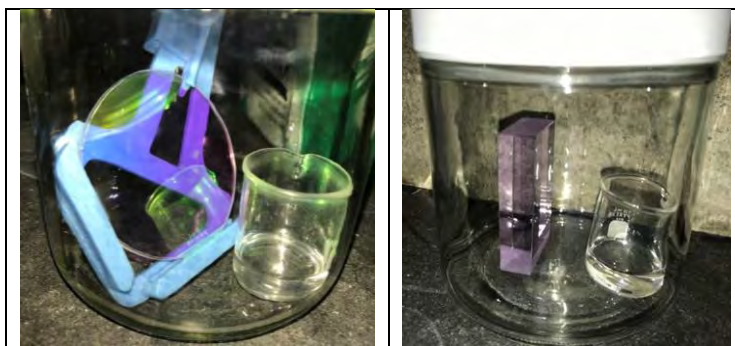

Fig. 6. Original silylation setup. HR coating on left and laser glass sample on right. Same size glass jars and glass beakers were used.

silylation, and then again after an interval of exposure in either a room-temperature humidity chamber (99% RH) or a "vapor temp" chamber (saturated humidity environment at 50ºC) to determine the effectiveness of the organosilane coatings. For HR coating samples, a fully effective coating would result in no changes in either the magnitude or location of the reflectance and transmission peaks before and after humidity exposure. For the LHG-8 laser glass, only transmission spectra were taken, because laser glass reflectance properties are not essential to the functioning of the lasers. For these samples, analysis of the surface quality of the laser glass surface by Nomarski differential interference contrast (DIC) microscopy (Zeiss AxioScope A.1) in reflection was used as a measure of coating effectiveness. If the average number of microscopic

surface pits per viewing area increased after humidity exposure, then the coating did not effectively protect the laser glass from water vapor.

The results obtained from this initial experimental setup were unexpected for both HR coatings and laser glass. Both the reflectance and transmission peaks for the organosilylated HR coatings shifted after exposure to humidity (explanatory results shown in **Fig. 7**). Microscopy observations showed an increased number of pits on the organosilane-coated laser glass surfaces after humidity exposure, with a resulting drop in the transmission of the sample. These results were similar for almost every organosilane attempted, even when increased temperature was employed during the vapor deposition coating process. Attempts to dip-coat the samples with HMDS and FTMDS did not yield coatings with improved hydrophobic properties.

In the one of the initial experiments, vapor-phase organosilylation of HR coatings was first undertaken by exposure to a saturated environment of HMDS at room temperature for 30 hours. The contact angle of a droplet of water was measured before and after HMDS exposure using an AST contact angle goniometer instrument (the contact angle is the angle between a line tangent to the droplet's surface and the sample surface and is a useful metric for determining the hydrophobicity and surface energy of the substrate surface—here, the contact angle measurement was used to determine the presence of a hydrophobic coating on the HR coatings and laser glass samples). There was a significant increase in the contact angle of the HR coating after HMDS exposure (from below the instrument's level of detection to 100.5º). The sample was then moved to the humidity chamber, and both reflectance and transmission spectra were measured after 23 hours of humidity exposure. The results (**Fig. 7**) showed a horizontal shift to the left in both the reflectance and transmission peaks from the initial time=0 reading to after the coating was applied, then a horizontal shift back to the right after 23 hours in the humidity chamber. These results

indicate that the HMDS coating, which is assumed to be present based on the increased contact angle, is not sufficiently effective to prevent water vapor infiltration into the sample.
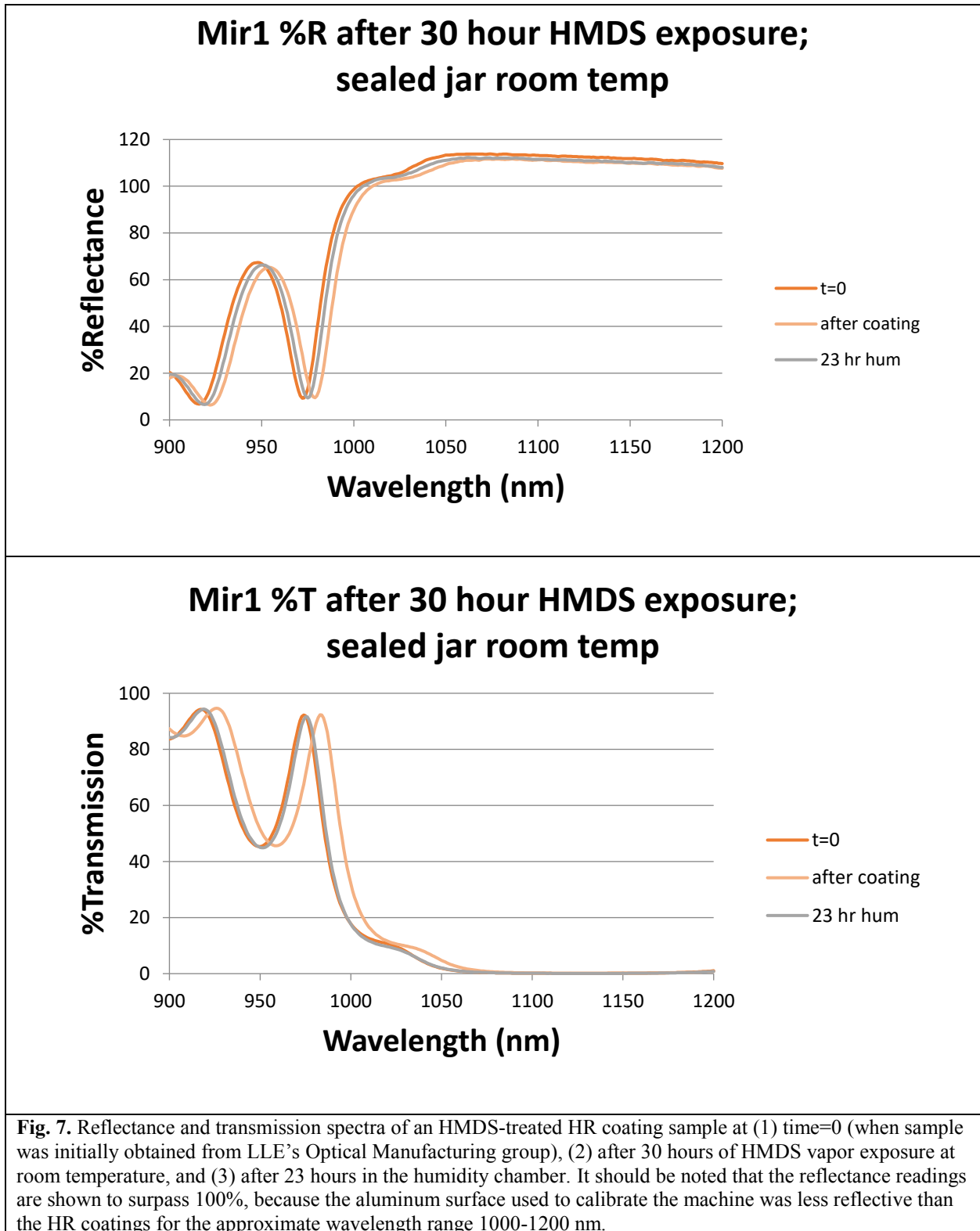
Fig. 7. Reflectance and transmission spectra of an HMDS-treated HR coating sample at (1) time=0 (when sample was initially obtained from LLE's Optical Manufacturing group), (2) after 30 hours of HMDS vapor exposure at room temperature, and (3) after 23 hours in the humidity chamber. It should be noted that the reflectance readings are shown to surpass 100%, because the aluminum surface used to calibrate the machine was less reflective than the HR coatings for the approximate wavelength range 1000-1200 nm.

The poor performance of these vapor-phase deposited HMDS coatings points to the possibility that there may have been water molecules bound to the OH groups on the coating surface that were reacting with the HMDS and consuming a sufficient quantity of organosilane to slow down the silylation rate or reduce the effective HDMS concentration available at the surface. Disilazanes react *non-selectively* with surface hydroxyl groups and water (both bound and un-bound) in a porous coating. To overcome this problem, vapor-phase depositions were conducted under a nitrogen atmosphere as described in Section 3 below.

3. Nitrogen Atmosphere Silylation of HR Coatings

Because the presence of bound surface water to the hydroxyl groups on the HR coatings can interfere with the silylation process, samples were equilibrated in a purged nitrogen atmosphere prior to vapor deposition of HMDS in a dry, oxygen-free environment (**Fig. 8**).
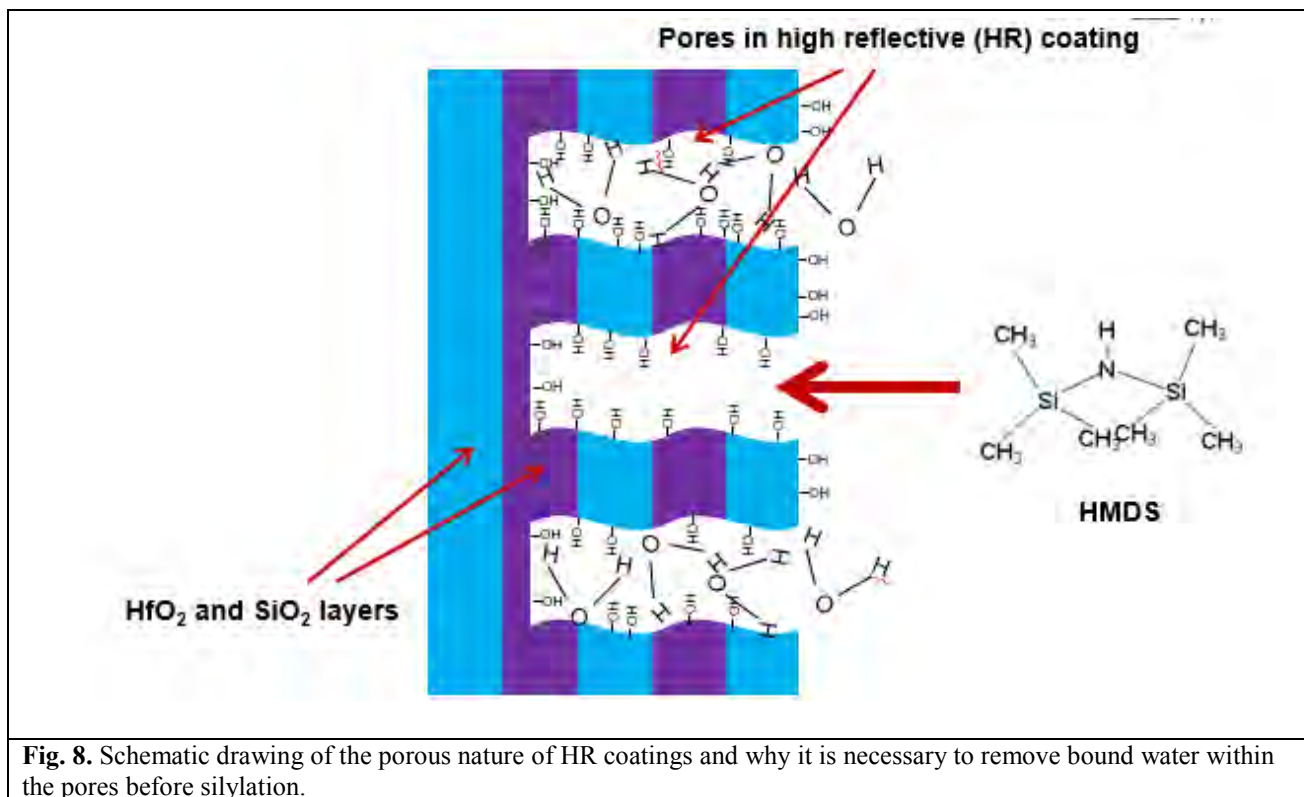

Fig. 8. Schematic drawing of the porous nature of HR coatings and why it is necessary to remove bound water within the pores before silylation.

Fig. 9 displays the setup for the nitrogen purge and silylation process at room temperature. The following procedure was used:

- Place the sample in the silylation chamber, open the chamber stopcocks, and purge with nitrogen for 24 hours.

- Turn off the nitrogen flow at the regulator, close both chamber stopcocks, and add 10 ml of organosilane to the gas bubbler reservoir.

- Open both chamber stopcocks and bubble nitrogen through the silylating agent until the contents of the gas bubbler have been depleted to saturate the chamber atmosphere with organosilane.

- Turn off the nitrogen flow and close both chamber stopcocks; allow the sample to equilibrate in a disilazane-saturated environment for 24 hours.

- Open both chamber stopcocks and purge the chamber with nitrogen to expel any remaining silylating agent before removing the sample.
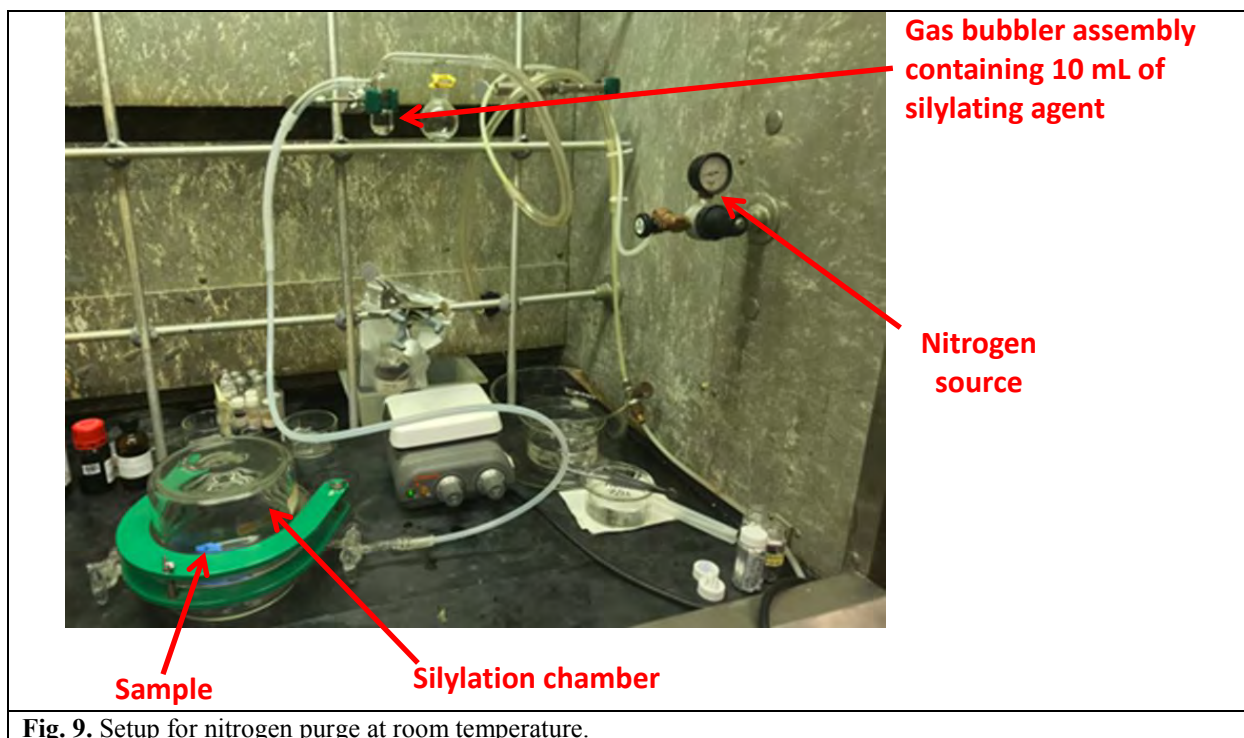

Fig. 9. Setup for nitrogen purge at room temperature.

Fig. 10 compares the reflectance spectra for HR samples before and after silylation with HMDS, as well as after exposure to high relative humidity environments. For HR samples silylated in air, peaks in the spectra shifted significantly after humidity exposure, whereas the spectra for those samples that were silylated after 24 hours equilibration in dry nitrogen were essentially unchanged. These results imply that nitrogen purging before HMDS silylation is much more effective in protecting HR coatings from moisture-induced changes in optical properties. Similar results were also obtained with other disilazane materials (TMDS and FTMDS).
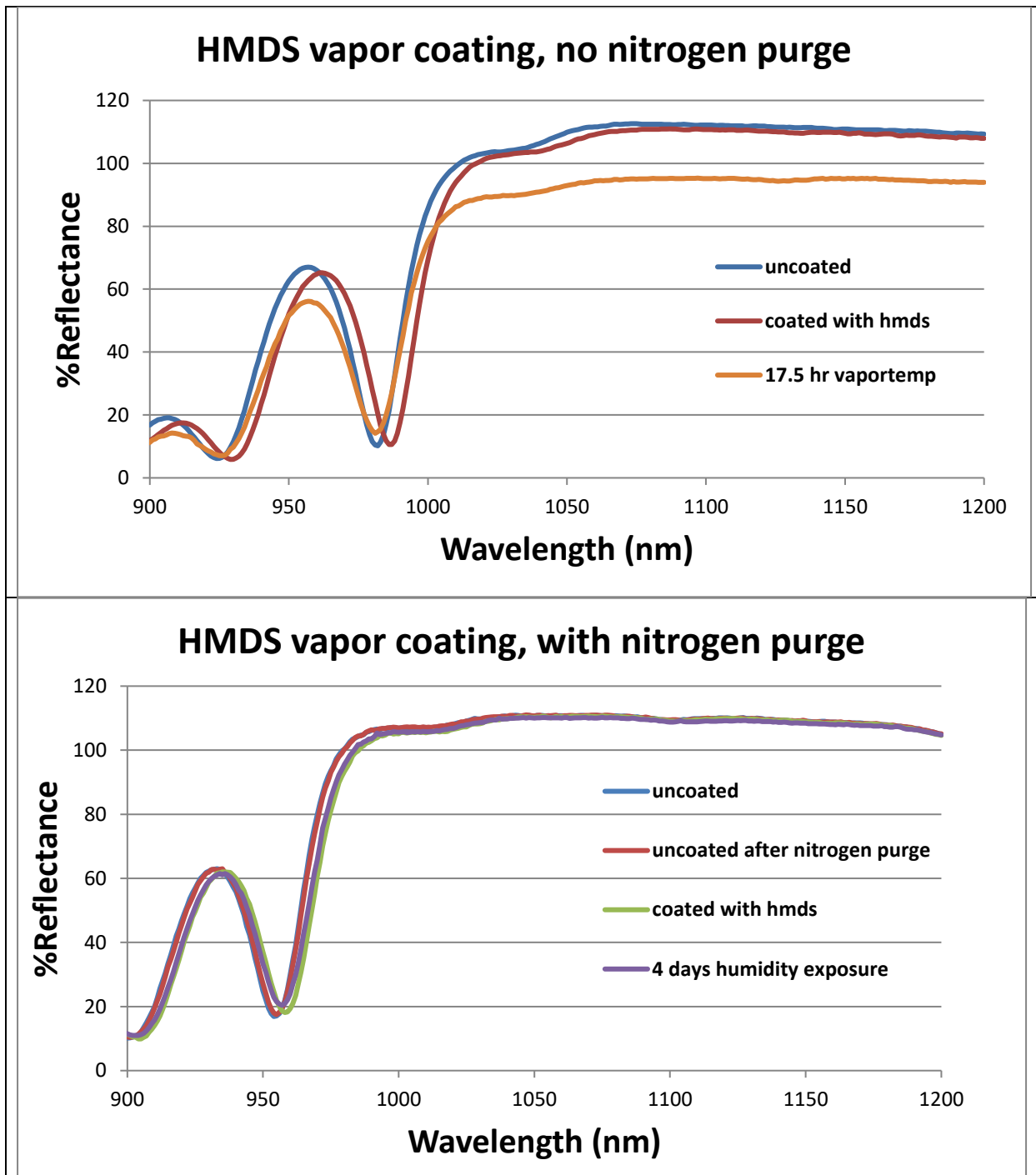
Fig. 10. Reflectance spectra for two samples coated with HMDS, (a) without and (b) with a nitrogen purge. Samples equilibrated in nitrogen exhibited superior performance to samples that had been silylated directly. TMDS and FTMDS coatings also show superior performance when the nitrogen purge coating method is used.

4. Hydrophobic Organosilane Laser Glass Coatings

Unlike for HR coatings, neither vapor-phase deposited nor dip-coated disilazane coatings could prevent pitting of LHG-8 phosphate laser glass at the long term, high humidity exposure levels (10-day 99% RH exposure at 25 °C) used in accelerated aging tests (**Fig. 11)**. Microscopies show that the average number of pits per microscope frame for samples coated with silazanes increased after intense exposure to humidity. Under less harsh conditions, these materials may provide sufficient protection for day-to-day laser bay operations, but more work must be done to verify the level of protection possible. In terms of other optical properties, a 4% increase in transmission through the laser glass was observed after disilazane application, implying that disilazanes can act as anti-reflective coatings (**Fig. 12**). Transmission peaks generally increase after laser glass is coated, showing that disilazanes are acting as anti-reflective coatings. These increases in transmission peaks were consistent for HMDS and FTMDS, on both vapor deposition and dip-coated surfaces.
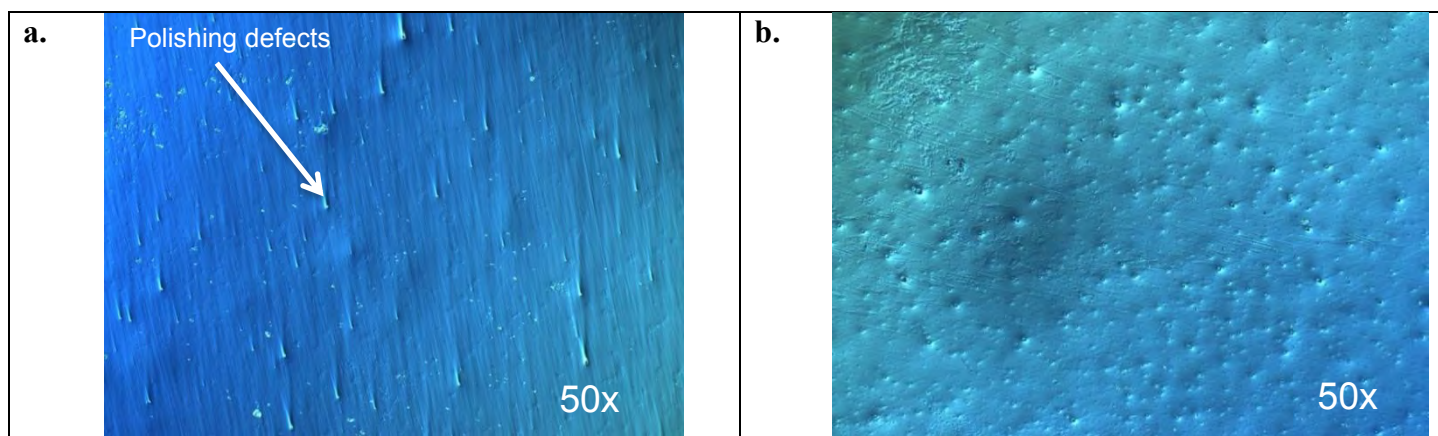

Fig. 11. a. Control sample before exposure; surface is covered with regular microscopic polishing defects. **b.** Sample vapor-phase coated with HMDS after 10 day 99% RH exposure at 25 °C.
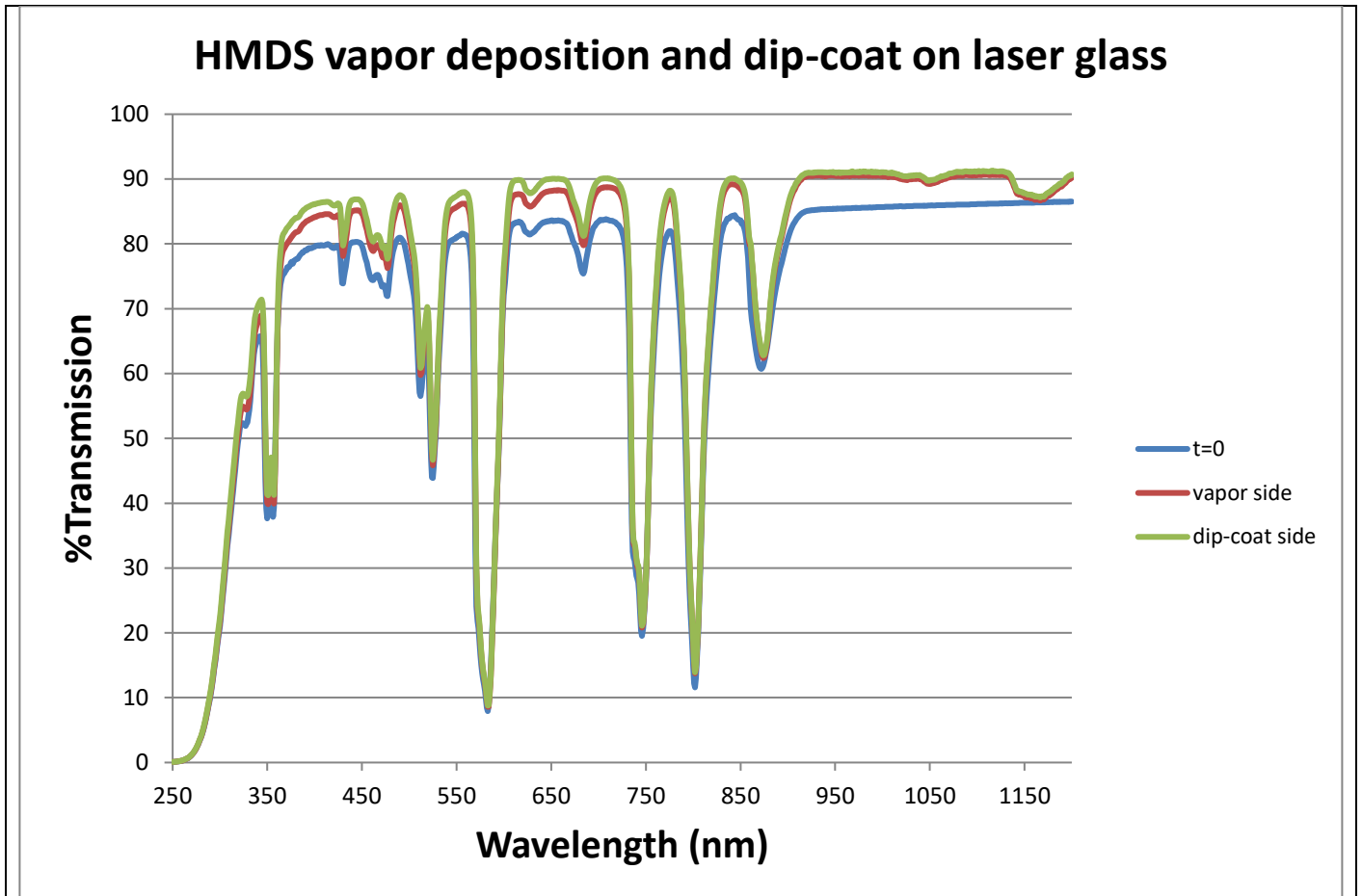
Fig. 12. The transmission spectra for a laser glass sample (rectangular prism shape) with a vapor-deposited coat of HMDS on one half and a dip-coating of HMDS on the other half. A time=0 reading was taken when no coating was present on the sample. Notice that the transmission peaks increased after the sample received the HMDS coating.

Additional experiments were conducted using Dow Corning Sylgard polydimethylsiloxane (PDMS) elastomer applied to polished laser glass surfaces by rod-coating. This material provided adequate protection of the polished LHG-8 surface from pitting over a 16-day exposure at 99% RH and 25 °C (**Fig. 13**). In addition to providing a good level of protection from water damage under harsh environmental conditions, this coating is transmissive and anti-reflective at an average thickness of ~ 3.2 μm.

15

Fig. 13. Nomarski DIC images of PDMS-coated and uncoated LHG-8 laser glass samples after exposure to high humidity. **a.** PDMS coated on laser glass surface with a plastic stirring rod (no solvent), after a 16-day exposure at 99% RH and 25 °C; **b.** Uncoated laser glass surface after an 18-day exposure at 99% RH and 25 °C.
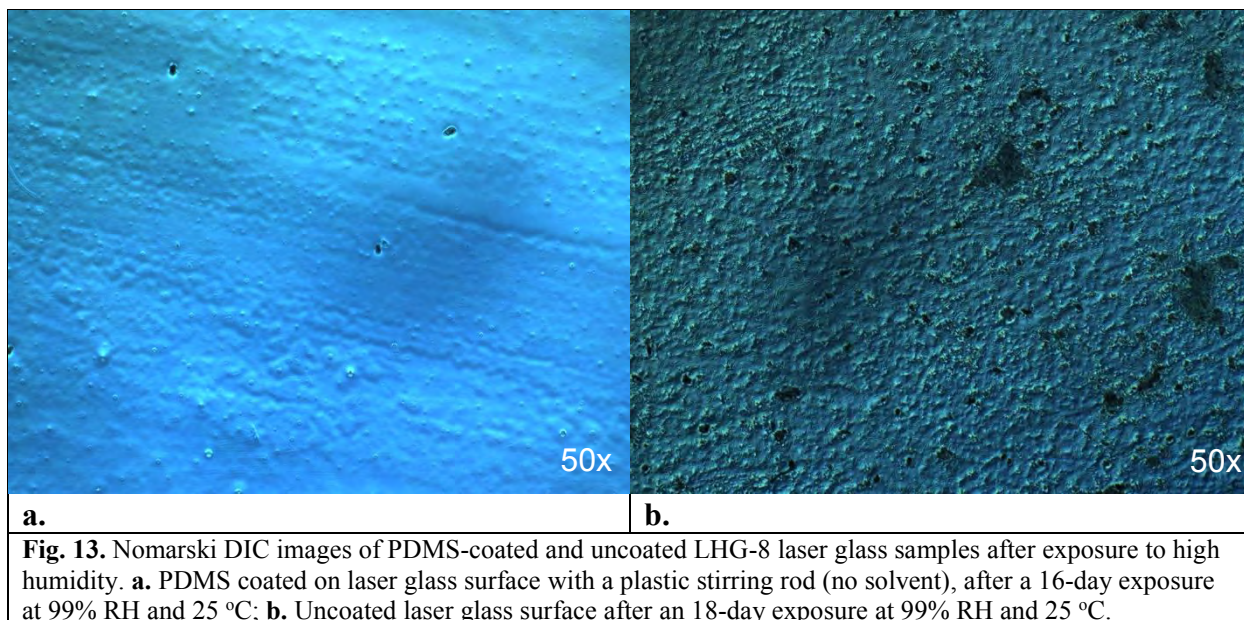
5. Conclusion

Many organosilanes were investigated to coat laser optics (HR mirrors and laser glass) in order to protect them from humidity damage. At first, organosilanes were vapor coated onto both kinds of optics. However, the HR coatings required a nitrogen purge prior to vapor deposition to remove water already present in the coatings' pores in order to produce an effective hydrophobic organosilane coating. In the case of laser glass, organosilanes (both vapor deposited and dip-coated) did not protect samples under extreme conditions from humidity damage. PDMS was found to provide a sufficient hydrophobic coating on laser glass.

These experiments determined that effective coatings (no changes in reflectance or transmission peak positions upon humidity exposure) can be produced when water molecules are removed from porous HR coatings prior to vapor phase deposition of disilazanes. Although disilazane coatings deposited on LHG-8 phosphate laser glass did not provide a sufficient level of protection from water under extreme humidity conditions, Sylgard PDMS coatings virtually eliminated surface pitting of the laser glass when exposed to a prolonged saturated humidity

environment. More investigations are needed on the effectiveness of PDMS coatings at different thicknesses, RH levels, and lengths of humidity exposure.

Future experiments should also include optical characterization and damage threshold testing on both Sylgard PDMS and vapor-phase deposited organosilane HR coatings for eventual application in OMEGA and OMEGA EP. Other materials may prove to be even more effective and should be investigated. For example, another well-know and widely characterized "glassy" polysiloxane resin, GR-650, which in the past has been used as a protective coating for hygroscopic potassium dihydrogen phosphate (KDP) frequency conversion crystals on OMEGA and other large high-peak-power lasers, is a promising candidate. Additionally, multifunctional organosilane compounds that react with both the laser glass surface and cross-link among themselves (e.g., derived from efforts at LLE to develop contamination-resistant and abrasion-resistant sol-gel anti-reflective coatings)[12, 13] should be considered.

Acknowledgements

References

(1). J. B. Oliver, P. Kupinski, A. L. Rigatti, A. W. Schmid, J. C. Lambropoulos, S. Papernov, A. Kozlov, C. Smith, and R. D. Hand, *Stress compensation in hafnia/silica optical coatings by inclusion of alumina layers,* Opt. Express, Vol. 20, p. 16596-16610, 2012.

(2). Francois Y. Genin, Christopher J. Stolz, *Morphologies of laser-induced damage in hafnia-silica multilayer mirror and polarizer coatings*, Proc. SPIE 2870, Third International Workshop on Laser Beam and Optics Characterization, 20 November 1996.

(3). Christopher J. Stolz, *Status of NIF mirror technologies for completion of the NIF facility*, https://e-reports-ext.llnl.gov/pdf/364178.pdf.

(4). J. H. Campbell, J. S. Hayden, A. J. Marker, *High-Power Solid-State Lasers from a Laser Glass Perspective*, LLNL-JRNL-464385, 22 Dec. 2010.

(5). S. D. Jacobs, *LHG-8 Athermal Laser Glass*, personal Hoya products notes, 5 May 2009.

(6). *Chemical Durability of Phosphate Laser Glasses Polished with Pitch, Pads, or MRF*, LLE Review, Vol. 100, p. 257-268, Jul.-Sep. 2004.

(7). S. D. Jacobs, email correspondence with A. Rigatti of Optical Manufacturing Group, 27 Aug. 2004.

(8). Arun K. Varshneya, *Fundamentals of Inorganic Glasses*, Harcourt Brace & Company, p. 397-408, 1994.

(9). S. D. Jacobs, email correspondence with A. K. Varshneya, 8 Jun. 2004.

(10). Z. Culakova, *Improved Laser Damage Resistance of Multi-Layer Diffraction Gratings Vapor-Treated with Organosilanes*, Laboratory for Laser Energetics High School Program, Aug. 2006.

(11). K. L. Marshall, Z. Culakova, B. Ashe, C. Giacofei, A. L. Rigatti, T. J. Kessler, A. W. Schmid, J. B. Oliver, and A. Kozlov, *Vapor-phase–deposited organosilane coatings as "hardening" agents for high-peak-power laser optics*, Proc. of SPIE - The International Society for Optical Engineering. 6674. 10.1117/12.734723.

(12). M. Rutan, *Abrasion Resistant Anti-Reflective Sol-Gel Coatings*, Laboratory for Laser Energetics High School Program, Aug. 2011

(13). Xiaodong Wang, Jun Shen, *A review of contamination-resistant antireflective sol-gel coatings*, Journal of Sol-Gel Science and Technology 61(1), 10.1007/s10971-011-2615-4, December 2010.

A Containerized Approach for Data Analysis on Omega

Aidan Sciortino
Wilson Magnet High School

Advisor: Richard Kidder
University of Rochester Laboratory for Laser Energetics

January 2019

Abstract

Scientific data analysis is critical to the work done at LLE. An important part of this is enabling easy access to data and compute resources for scientists, both on the day of a shot and afterwards. Current systems for accessing data for analysis are old, hard to access, and have long download times. This makes quick analysis between shots very difficult. This project explores possible ways to remedy this, presenting a container-based system allowing web-based development of analysis programs, with easy access to data on the webpage itself. This is part of a larger study of containerization as a way to provide compute resources across the lab, scaled according to need.

1 Introduction

1.1 Challenges at LLE

One of the major challenges that needs to be addressed at LLE is how data access is provided to scientists, both for on-site PIs as well as for visiting PIs. Currently on-site PIs connect directly to the facility SQL database, or scrape data off statically generated webpages based on technologies popular in the 1990s.

While external PIs can access these webpages beyond the firewall, they are unable to access the SQL database and must rely on on-site scientists to share any data that can't be found on the webpages with them by email.

HTML scraping or writing SQL is inefficient and inhibits productivity, forcing scientists to write extra code—and in the case of SQL learn a new programming language—instead of allowing them to focus in on their specific research. In addition, writing SQL requires somewhat intricate knowledge of the data structures within the database in order to build queries, without which pulled data may be inaccurate.

Another major challenge encountered at LLE is the amount of time it often takes for a scientist to access and analyze data from a shot. In order to access data scientists must download it to their workstations, where analysis code must then be run. While some analyses may be run well after the day of the shot, others are optimal to run in between shots in order to catch and rectify any problems in the experimental setup. The process of loading data

and running these procedures is inconsistent, varying according to many factors including but not limited to the age of the computer, the speed of the user's internet connection, and the amount of data that must be loaded. In cases where resources are unavailable, running analyses between shots is not feasible. A containerized approach for scientific data analysis provides a solution for consistent, secure access to data, services, and resources that will help scientists formulate new methods for checking data in between shots, allowing further sharing of responsibilities and better utilization of facility resources.

1.2   Modern Technologies

Since the SQL database and HTML pages were set up in the late 1990s, countless new approaches to provisioning programmatic data access for users have emerged. In addition, many new technologies have emerged to allow for easier allocation of computing resources, including the concept of containerization. Containerization builds on the concept of Unix process isolation, in which the root directory of a process is changed such that it doesn't affect other processes. This concept evolved, through the concept of "Jailing" processes by partitioning a full system into several smaller systems, each of which is assigned its own IP address and system configuration. As cloud-based hosting grew and there became more and more demand for technologies allowing allocation of compute resources for various cloud websites, the concept of the container was embraced by many providers as a system for isolating and allocating resource usage in cloud data centers.

In 2013 the Docker container system was introduced, which made containers significantly easier to create. With Docker emerged Docker Hub, a platform that allows users to share container images for other users to download and use. In 2014 Google introduced Kubernetes, an open source container orchestration platform. Kubernetes solves the problems that Docker does not, coordinating the way in which multiple containers share resources and interact.

In the past five years containerization has grown from a fringe technology used by few companies for very specialized purposes in web hosting to the de-facto standard for deploying

modern applications, databases, and other stateless infrastructure.

2 Approaches to Service Compartmentalization

2.1 Bare Metal

In a bare metal architecture (shown in figure 1) an operating system runs directly on the hardware, and holds libraries that all applications hosted on the server share.
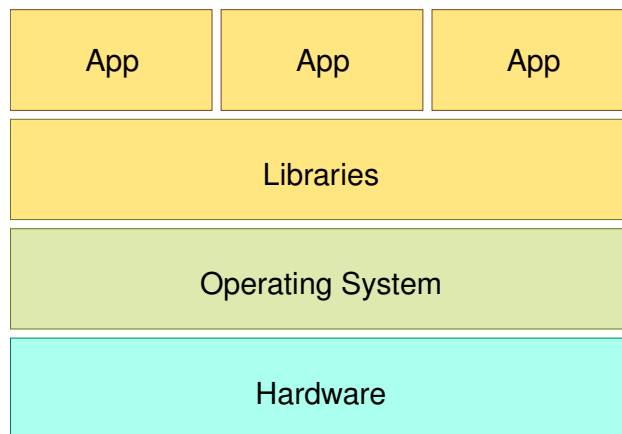

Figure 1: Traditional Bare-Metal System Architecture

This architecture prevents inefficient usage of storage space and processing power because the applications share libraries and operating system resources with each other. However, since applications share libraries, dependency conflicts (in which one application requires a different version of a library than another) are common.

2.2 Virtualization

In a virtualized architecture (shown in figure 2) an operating system still runs directly on the hardware, but its sole purpose is to run the virtualization software. The virtualization software allows for the creation of multiple virtual machines, each of which has its own operating system, and can hold its own libraries and applications.
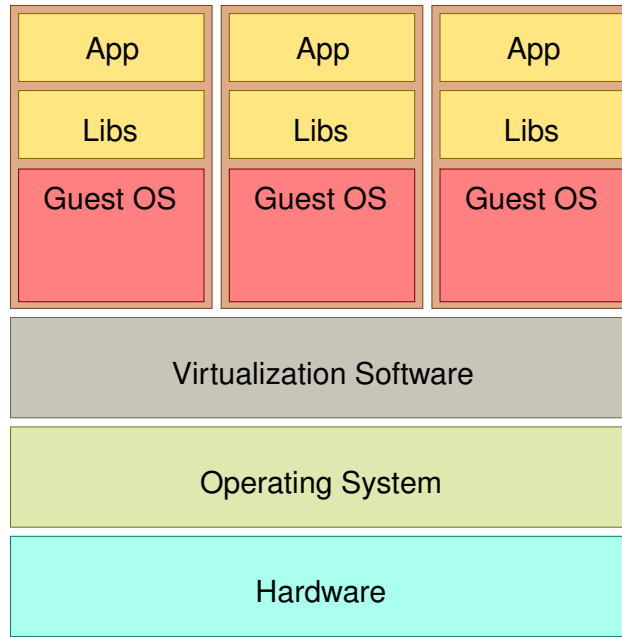
Figure 2: Virtualized System Architecture

This architecture avoids the dependency conflicts described in section 2.1 by providing each application with its own individual dependencies. In many cases this architecture is also more secure due to the compartmentalized nature of the virtual machines. If one application is compromised it does not mean that the entire system is; solely that machine. In comparison, in a bare-metal architecture if one application is compromised all other applications on the machine are vulnerable.

The primary disadvantage of virtualization is that an entire computer must be simulated and an entire operating system must be virtualized, which uses significant overhead. This results in less efficient systems and often has a negative impact on the performance of processes running in virtual machines.

2.3 Containerization

A containerized system (shown in figure 3) presents a hybrid of the two previously mentioned approaches. The operating system runs a container engine, similarly to how the operating system in a virtualized system runs virtualization software. However, this container engine

does not simulate an entire machine for the apps contained in containers. Instead it passes through core parts of the underlying host operating system, focusing on modularising only the dependencies for each app in each container.
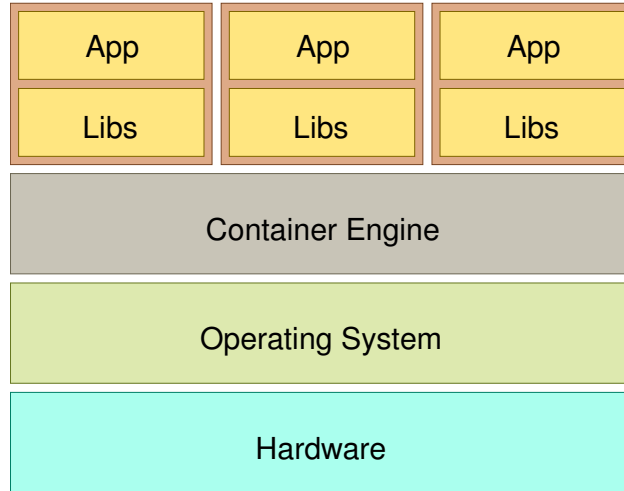

Figure 3: Containerized System Architecture

By sharing core parts of the operating system to each container, containerization avoids the inefficiency of simulating entire computers and virtualizing entire operating systems as described in section 2.2. However, it also avoids the dependency conflicts described in section 2.1 by providing individual libraries based on containers, and maintains many of the security benefits of a virtualized architecture.

In addition, by passing through core parts of the host operating system, containerization avoids the performance costs associated with virtualization.

3   Proof of Concept Application

The *Shotday* web application was planned and developed to demonstrate the possibilities that containerization offers for data analysis solutions internally and externally. The application builds upon modern container technology with modern web technologies such as Angular[1]

---
[1] https://angular.io/

and NodeJS[2], and data analysis solutions such as Jupyter[3].

3.1 Application Architecture

The application is based around the architecture depicted in figure 4. A frontend, written using the Angular web framework, connects a user to a Linux container that serves as a backend. This backend runs a Jupyter data analysis kernel that allows the user to write code in Python 3 or Matlab. This container has access to the LLE database using the user's authentication, such that code written in it can be executed anywhere, and still access facility resources.
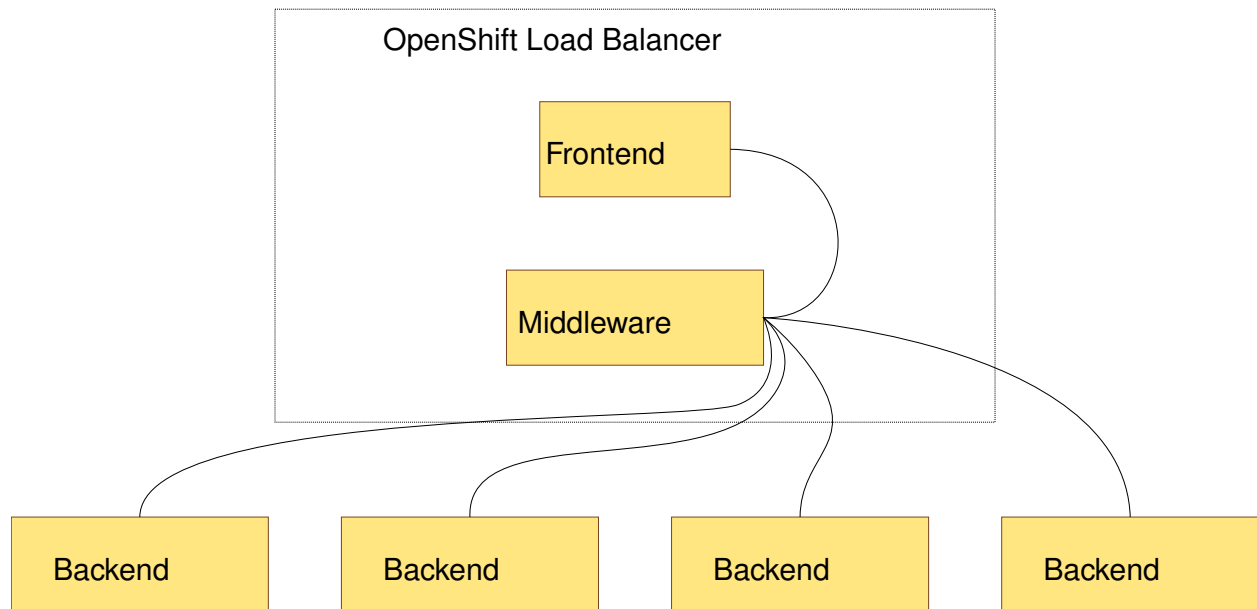
Figure 4: *Shotday* Architecture

The containers are all contained within the OpenShift[4] containerization platform. This platform extends the Kubernetes[5] container orchestration platform, which is the industry standard for managing containers in a production environment. This platform provides easy management of container infrastructure that is easily scalable. It also automates tasks such as load

---

[2]https://nodejs.org/
[3]https://jupyter.org/
[4]https://www.openshift.com/
[5]https://kubernetes.io

balancing and allocating resources such as processing power, memory, and storage space to containers.

The frontend and middleware are both designed to be stateless, such that the containers themselves can be destroyed and recreated without users losing data. They are also designed to be load balanced using the load balancing technologies included in OpenShift.

The backend containers are also designed to be stateless, with user programs being stored in the facility's Gitlab code management system. However, the backend containers are managed by the Jupyter Enterprise Gateway, a piece of software designed by developers at IBM and several other companies that manages Jupyter kernel deployment in High Performanc Computing (HPC) and containerized environments.

4   Integration with Current Infrastructure

4.1   Current LLE Infrastructure

Currently LLE possesses an Oracle SQL database that stores data from laser shots. This database provides data to webpages, which are used by different people across the lab for different purposes.

Many scientists run data analysis routines on personal computers—generally either workstations or laptops. The lab also has several sources of high performance computing (HPC) power, two on site as well as one off site, that are used for data analysis as well as for simulations and other HPC-based experiments.

In addition, there is an existing code management tool called Gitlab that allows easy sharing of and collaboration on code.

4.2   Proposed Containerized Architecture

The proposed containerized application provides scientists with a secure Linux container that has easy access to all of the existing resources from anywhere in the world; not solely behind the LLE firewall.

These containers have libraries that are designed to make pulling from the database simple, have access to the facility Gitlab system, and are designed with the intention of eventual expansion allowing jobs to be executed on facility HPC resources.

Containers can be managed using existing facility infrastructure including the authentication servers already in use for both existing web services and user authentication into desktop computers. In addition, containers present further security benefits as discussed in section 2.3, as such presenting a method that is as secure, and possibly even more secure, than the methods currently used for data analysis.

5   Conclusions

The proof of concept presented in this paper serves only the function of providing scientists with a web-based interface for doing data analysis. While containerization serves this specific application well, it also holds significant opportunities and advantages that could be used to enhance the lab's existing infrastructure.

For example, stateless containers could be used to provide access to the facility database via a web Application Programming Interface. This allows access to data without needing to learn SQL or other programming languages. It also allows for easier integration of modern web applications with facility data. Data services such as these are growing more common, as more and more applications become web based. Containerization presents a thoroughly future-proof method for implementing such services, and thus is a valid route forwards that should be taken into consideration for use in the lab.

6 Acknowledgements

First and foremost I'd like to thank my advisor, Richard Kidder, for all of his guidance on this project. Without Rick's vision this project would not exist at all, and without his guidance in connecting me with people around the lab, as well as his immense knowledge of the operations of the facility, I would not have been able to get anywhere close to the proof-of-concept presented in this paper.

I'd also like to thank Michael Charissis, who set up the infrastructure required for the project and from whom I've learned immense amounts about server administration and what todays enterprise technology landscape looks like.

In addition I'd like to thank the informatics team (Andrew Zeller, Tyler Coppenbarger, and Mathew Schweigardt), with whom I worked extensively investigating the feasibility of integrating the proof of concept into their existing code.

Finally I'd like to thank Dr. Craxton for organizing and running the summer intern program, as well as all of the other summer interns with whom I had countless discussions in topics in computer science, physics, and philosophy, and whom challenged me every day to think harder and longer about many problems in all spheres of my work.

Optimization of Cone-in-Shell Targets for an X-ray Backlighter on the National Ignition Facility

Anirudh Sharma

Webster Schroeder High School

Advisor: Dr. R. S. Craxton

Laboratory for Laser Energetics

University of Rochester

November 2018

1. Abstract

A double cone-in-shell plastic (CH) target imploded by laser beams has been optimized for the purpose of x-ray backlighting a hohlraum-heated iron sample in an opacity platform at the National Ignition Facility (NIF). The cones, which are located at the poles of a spherical shell, allow the target to produce a short pulse of x rays that probe the sample at a specified time. Both the parameters of the available laser beams and specifications of the cones have been optimized using the 2D hydrodynamics simulation code *SAGE*. By placing all the beams in best focus and appropriately selecting the pointings of the beams, a uniform implosion has been achieved. The behavior of the cone has been optimized by selecting a sufficiently small cone half-angle that laser rays do not enter the cone and a sufficiently large distance from the cone tip to the target center that the cone's obstruction of the implosion is minimal. An x-ray diagnostic code, *Orion*, has been created for the purpose of calculating the x-ray output from the targets. The optimized design has been found to produce a short (~350 ps) point source (~100 µm) of x rays as desired, effectively eliminating emission produced by the target before peak compression ("run-in"). The parameters of the design are chosen to ensure that the convergence of the cone on the vertical axis prevents hot compressed plasma from escaping through the cone after peak compression. This design has also been compared to a conventional target lacking cones. Calculations from *Orion* have shown that the conventional target produces significant run-in emission and a longer x-ray pulse than the optimized cone-in-shell design. This work suggests that a double cone-in-shell target is a viable candidate for improved backlighting of opacity experiments at the NIF.

2. Introduction

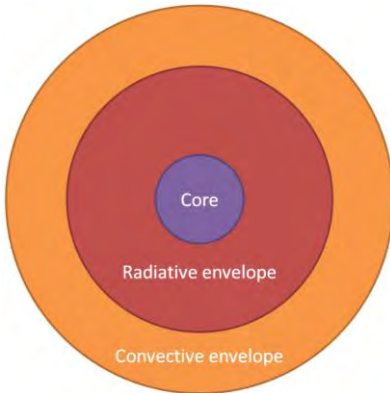### 2.1. Iron Opacity Experiments at the NIF

Figure 2.1: The radiative and convective zones of the sun. The transition radius between the two is unknown.

In the sun, heat is transferred by two different methods: radiation and convection, as shown in Fig. 2.1. Currently, the transition radius, or the distance at which the method of heat transfer changes from radiation to convection, is unknown. Experiments are being carried out to determine the opacity of iron, a value that the transition radius depends on. The current setup at the National Ignition Facility (NIF) at Lawrence Livermore National Laboratory for such experiments, designed by Heeter et al.,[1] is shown in Fig. 2.2 (a). The proposed setup, which is the focus of this work, is shown in Fig. 2.2 (b).

In both setups, laser rays heat the inner wall of a hohlraum (a chamber made of a high-atomic-number material such as gold) and x rays emitted by the hohlraum wall heat an iron sample. Laser rays are also used to implode a backlighter target. The target in Fig. 2.2 (a) is a plastic (CH) shell, often known as a capsule. The imploded target is indicated with dotted lines in Fig. 2.2. The backlighter is intended to produce a short pulse of x rays. The proposed design [Fig. 2.2 (b)] uses a double cone-in-shell target instead of a conventional target.
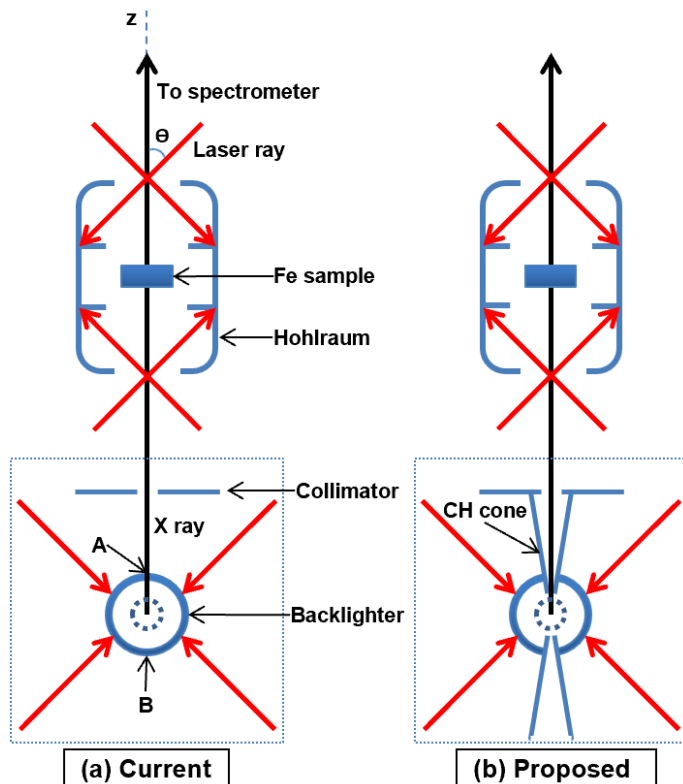

Figure 2.2: The current (a) and proposed (b) setups for the NIF Opacity Platform. In the proposed design (b), the conventional backlighter is replaced with a double cone-in-shell target.

X-ray emission from the backlighter is transmitted axially through a collimator and then through the hohlraum-heated iron sample (Fig. 2.3). The collimator is necessary to ensure that the sample's self-emission E (see Eq. 1) is measured without contamination from the backlighter x rays. At the spectrometer, different regions of emission can be used to determine the initial intensity of the emitted x rays, the final intensity, and the self-emission from the sample. Using the simple formula

$$T = \frac{U - E}{V - E}$$ (1)

where T is the transmittance, U is the intensity in the direction of attenuated x rays that pass through the sample, and V is the intensity in the direction of unattenuated x rays that do not pass through the sample, the transmittance and thus the opacity of the heated sample can be found.[1] These regions of emission are shown in Fig. 2.3, which demonstrates how the sample's self-emission E contributes to the measurements of U and V, and consequently must be subtracted from both values to ensure an accurate transmittance calculation.

The backlighters in Fig. 2.2 are imploded using direct drive.[2, 3] In direct drive implosions, a small spherical plastic capsule is irradiated with laser rays. As the laser rays heat the capsule, a layer of hot plasma (known as coronal plasma) forms around the capsule as the outer portion of the capsule ablates outward, causing an equal opposing force to drive the inner portion of the capsule inward. This process creates conditions of high temperature and pressure in a small, compressed core. Such conditions lead to the emission of x rays.
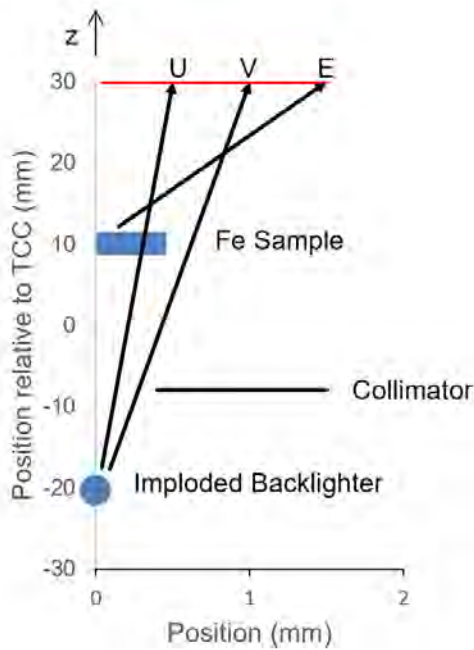

Figure 2.3: Regions of emission formed by the sample and backlighter. The spectrometer is located 600 mm from target chamber center (TCC). The horizontal scale has been greatly enlarged.

The iron sample used in NIF opacity experiments is brought to solar-interior temperatures via indirect drive.[4] In indirect drive, the laser rays enter and heat a hohlraum, which contains the primary target. As the hohlraum is heated, it emits x rays, which then irradiate and heat the target.

Typically, there is a spherical capsule in the hohlraum that is imploded by these x rays. This implosion process, accomplished using either direct or indirect drive, is generally used for inertial confinement fusion (ICF). Capsules used for ICF are filled with deuterium-tritium fuel. High temperatures and densities provide the deuterium and tritium nuclei with sufficient energy to overcome

their Coulombic repulsion and fuse, producing a helium nucleus and a high-energy neutron. In the setup of Fig. 2.2, the iron sample is simply being heated rather than imploded as a target would be in ICF.

The NIF is configured for indirect drive, and the laser beams are arranged in rings of quads (where each quad has 4 beams) oriented at polar angles Ө (indicated in Fig. 2.2) of 23°, 30°, 45°, and 50°. Indirect drive requires laser rays to enter through a hole at the top of the hohlraum; it is difficult to accomplish this using beams with Ө>50°. Lasers configured for direct drive (such as the OMEGA laser[5] at the Laboratory for Laser Energetics) have beams oriented more uniformly around the entire target.

Only certain quads are available for the backlighter. The primary target is heated in the hohlraum by the 45° laser beams and the backlighter is driven by the 23° and 30° beams and every other 50° quad, as some of the 50° quads are blocked by the target holder.

While direct drive presents the obvious advantage of greater efficiency in energy deposition, indirect drive produces a smoother implosion in ICF and more consistent heating of a sample in opacity experiments. Direct drive can be accomplished at the NIF by repointing the laser beams toward the equator of the target, a process known as polar drive.[6, 7] A similar repointing is done in this work in order to optimize the implosion of the backlighter.

2.2. Cone-in-Shell Backlighters

In current experiments at the NIF [Fig. 2.2 (a)], backlighters have presented the issue of "run-in," or x-ray emission produced prior to peak compression as the laser rays continually heat the coronal plasma.[8] Such emission interferes with the transmittance measurements of the primary sample, as it creates a temporally spread signal which extends the duration of the spectrometer's time-integrated measurements. Since the primary sample is evolving with time and it is desired to probe the sample at a specific time, this affects the accuracy of those measurements. While the collimator blocks much of this emission, run-in from regions A and B [Fig. 2.2 (a)] cannot be blocked as they directly view the sample. To resolve this issue, Heeter[9] proposed a double cone-in-shell target [Fig. 2.2 (b)]. The new capsule includes cones at both the poles that limit the view of the sample to a central region of the spherical backlighter capsule. Specifically, the design eliminates the portions of the shell in the polar regions A and B and thus the run-in from those areas. Consequently, there should be no detected emission until the capsule implodes, as there is no polar emission and the cone and collimator [Fig. 2.2 (b)] block the sample from run-in associated with the whole surface of the capsule.

Cone-in-shell targets have been fabricated for such applications as fast ignition,[10] but a double cone-in-shell target for the backlighting of opacity experiments, as explored in this work, is a new concept. This research proves that such a target is viable and may offer significant benefits over current capsules, especially in terms of producing a short-pulse signal.

The findings of this work are divided into three sections. In section 3, an initial cone-in-shell design that exhibits high uniformity is presented. In section 4, an x-ray diagnostic code *Orion* is developed and used to assess emission from the initial design. In section 5, an optimized design that produces a short pulse of x rays is shown and compared to current backlighters in use at the NIF.

3. Initial Design

Fig. 3.1 (a) shows the specifications for the initial cone-in-shell design. To develop this design, five parameters of the cone were investigated: length, distance from tip to target center, tip radius, thickness, and half-angle. The pointings and defocuses of the relevant beams (23°, 30° and 50°) were varied as well. Fig. 3.1 (b) shows the laser pulse that was used to implode the target. The total laser energy is 300 kJ and 66.6% of the total energy is absorbed. The laser turns off at 2.8 ns.
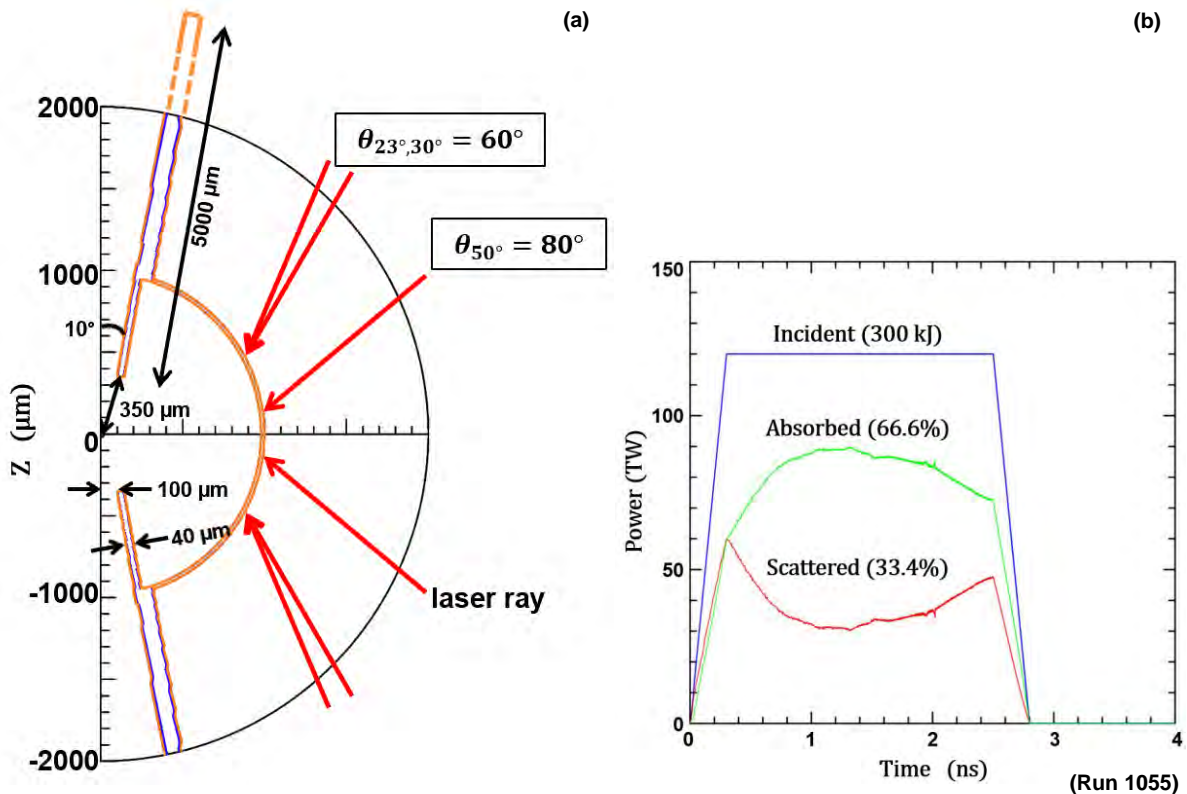

Figure 3.1: (a) The specifications for the initial cone-in-shell design and (b) plot of power versus time for the laser pulse used in all simulations. The red arrows indicate where the laser rays at the centers of the beams are aimed on the initial capsule surface.

These initial optimizations focused on preventing laser rays from entering the cone (which would cause the formation of unwanted radiating plasma inside the cone) and ensuring implosion uniformity, as this is necessary for achieving high densities and thus high x-ray output. It was found that 10° was a sufficiently small cone half-angle and 5000 μm was a sufficiently large cone length to prevent laser ray entry into the cone. In actual experiments, a greater length will be used since the cone must be mounted

on the collimator [Fig. 2.2 (b)]. A cone thickness of 40 μm was chosen to maintain the integrity of the cone during the implosion: a cone that is significantly thinner than 40 μm would collapse early and block x rays from the backlighter whereas a cone that is too thick limits the amount of shell material that can be driven inward during the implosion. A cone tip radius of 100 μm was selected to ensure that the imploded core would be in the view of the sample. For the distance from cone tip to target center, 350 μm was found to be large enough to not impede the implosion. The beam pointings were optimized to ensure adequate equatorial drive: the 23° and 30° beams were pointed at an angle of 60° on the initial target surface and the 50° beams were pointed at 80°. All of the beams were placed in best focus (which increased laser energy deposition at the equator), thereby achieving the desired uniformity.

The time evolution of the initial design is shown in Fig. 3.2, which shows electron-density contour plots at three times. The critical density (orange) is the highest density that laser rays can penetrate to. The initial design implodes with a high degree of uniformity, as clearly evidenced by the spherical appearance of the shell before and during peak compression. At 1500 ps, before the implosion, the shell (indicated by the concentrated blue contours) seems to be very uniformly driven across its entire surface. At 2300 ps, during the peak compression, the imploded core still appears spherical, suggesting a high-quality implosion. At 3500 ps, after the implosion, the plasma has expanded outward.
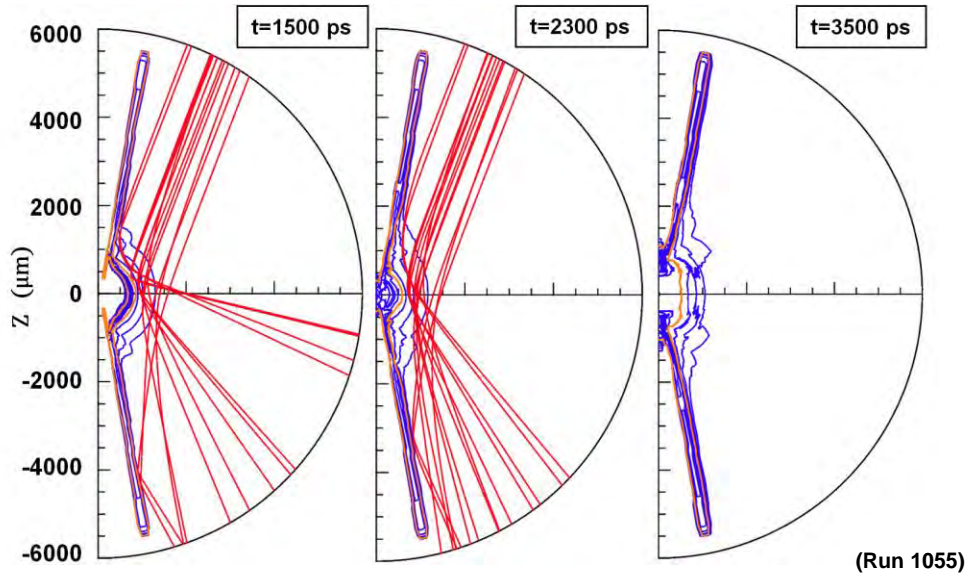

Figure 3.2: The time evolution of the initial cone-in-shell design. Incident laser rays are represented in red, and electron densities (of successive powers of ½ times the critical density) are indicated with blue contours (the critical density n_c is shown in orange). The shell implodes very uniformly.
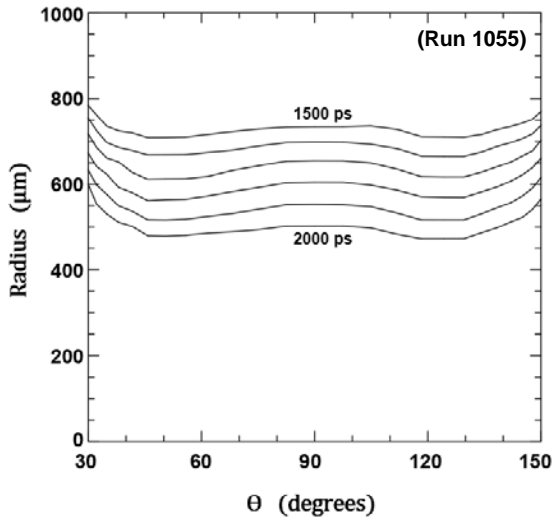
Figure 3.3: Center-of-mass radius plots superposed for 100 ps intervals from 1500 ps to 2000 ps. The implosion exhibits a high degree of uniformity.

A center-of-mass radius plot (for angles outside the range of the cone, where it can be defined) is shown in Fig. 3.3. The center-of-mass radius is the distance from the center of the target to the center of mass at some angle Θ. This plot shows that the center-of-mass radius is extremely consistent across the surface of the target leading up to the implosion. Both the time evolution plots of Fig. 3.2 and the center-of-mass radius plot show that the design exhibits a uniform implosion.

Blowups of the initial design (Fig. 3.4) reveal a new issue: hot compressed plasma escapes into the cone at late stages. The early appearance of this plasma is apparent at the time of implosion [Fig. 3.4 (a)], at which point compressed material already appears to be expanding along the axis. By 3000 ps [Fig. 3.4 (b)], the hot plasma has escaped further into the cone. The expansion of this hot plasma is indicated by the separation between the n_c and $\frac{n_c}{2} - \frac{n_c}{8}$ contours. Due to the high temperatures and density of this material, it will emit x rays long after the implosion has ended, thus extending the x-ray pulse beyond what is desired.
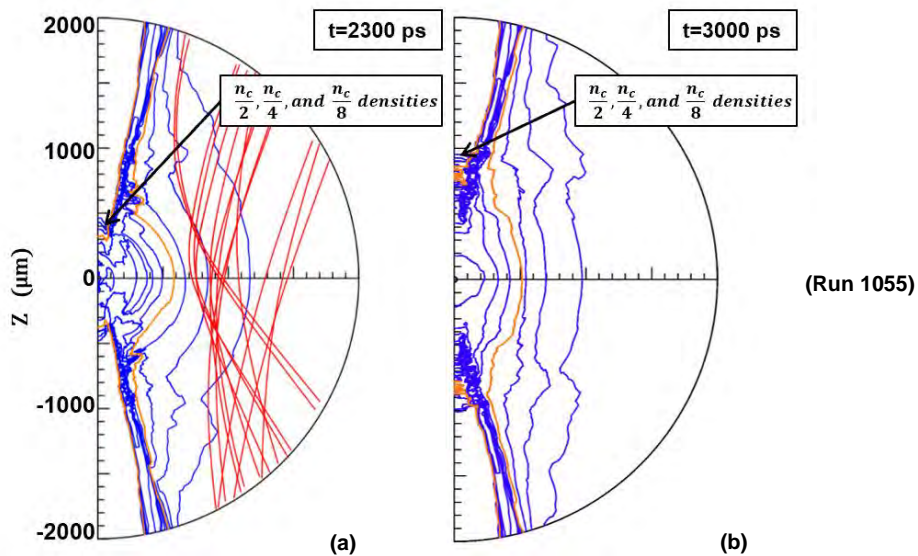

Figure 3.4: Density contour blowups for the initial design at the time of implosion (a) and after the implosion (b). Note the evolution of the expanding hot plasma in the cone as it escapes further up the axis.

Density contour plots (as in Fig. 3.2) show that the cone is pushed inward as the target implodes. If the cone continued to move inward, it would have converged onto the vertical axis, thus shutting off the x-ray signal. In the initial design, this did not occur due to the expanding hot plasma along the axis shown in Fig. 3.4.

It was found that if the cone is too thin, it will move at a greater velocity toward the axis, collapsing before peak central emission. Similarly, if the tip radius is too small, the convergence happens earlier than desired. A small tip radius also has the consequence of decreased output overall, as it limits the area of emission.

Other parameters, such as the distance from cone tip to target center and the beam pointings, affected the behavior of the cone as well, yet how they would affect x-ray emission was not completely clear. Since optimizing these features was dependent on how emission from the backlighter was distributed (both temporally and spatially), a code, *Orion*, was written to predict x-ray output from targets and aid in further optimizations.

4. Development of X-ray Diagnostic Code

4.1. The Code Orion

To diagnose a target that will be used as an x-ray backlighter, it is important to know how much emission it will produce. A simple differential equation can be used to find the intensity of an x ray as it passes through a radiating object.

The radiation transfer equation is given by

$$\frac{dI_v}{ds} = k_v' B_v - k_v' I_v \tag{2}$$

and is used here to model the spectral intensity of an x ray of frequency v traveling on a path through the plasma, where I_v is spectral intensity in $\frac{ergs}{sec \times cm^2 \times sr \times freq}$, B_v is the blackbody spectral intensity, s is distance, and k_v' is opacity.[11] Note that there are both a positive term, which represents self-emission, and a negative term, which represents absorption. By starting with an x ray of zero intensity and calculating its spectral intensity as it passes through the capsule (growing due to self-emission and being attenuated due to absorption), the x-ray spectral intensity at a specific position and time can be determined.

The blackbody function B_v is given by

$$B_v = \frac{2hv^3}{c^2} \times \frac{1}{e^{\frac{hv}{k_B T}} - 1} \tag{3}$$

where h is Planck's constant, c is the speed of light, k_B is Boltzmann's constant, and T is temperature. For a given x-ray frequency, the blackbody intensity is solely a function of temperature.

By selecting a sufficiently small step ds that a constant temperature and thus an unchanging blackbody intensity, as well as a constant opacity, can be assumed along the step, the following relation is obtained from Eq. 2:

$$\frac{dI_v}{ds} = \frac{d(I_v - B_v)}{ds} = -k'_v(I_v - B_v) \tag{4}$$

Eq. 4 shows that I_v approaches B_v, regardless of whether $I_v > B_v$ or $I_v < B_v$. The spectral intensity can be obtained as a function of position by integrating Eq. 4 to give I_v at a position that is an interval of ds greater than the original position s:

$$I_v(\mathbf{s} + \mathbf{ds}) = I_v(\mathbf{s})e^{-k'_v ds} + B_v(\mathbf{s})(1 - e^{-k'_v ds}) \tag{5}$$

Here, the absorption term is the first term on the right while the self-emission term is the second. The spectral intensity is decreased by a damping factor that depends on the opacity, and is increased by a term that depends on the blackbody value and the opacity.

An x-ray diagnostic code *Orion* was built using Fortran that models the spectral intensity of x-ray emission using this numerical integration technique. *Orion* can obtain solutions for Eq. 5 for single x rays and also calculate space and time integrals.

4.2. X-ray Emission from the Initial Design

Orion can plot the intensity for an x ray as it passes through the target at some radius x. A simple example of this is shown in Fig. 4.1 for an imploded target. Two intensity plots are shown: that of an x ray passing unimpeded through the emitting center of the target (blue) as well as that of an x ray that experiences significant absorption upon reaching the optically thick cone (green). Here, intensity is plotted as $\hat{I}_v$, such that

$$\hat{I}_v = \frac{I_v}{h} \tag{6}$$

where h is Planck's constant. Since I_v is the spectral intensity in $\frac{ergs}{sec \times cm^2 \times sr \times freq}$, $\hat{I}_v$ is the spectral intensity in $\frac{ergs}{sec \times cm^2 \times sr \times ergs}$ (since the product hv gives energy in ergs), which is equivalent to $\frac{1}{sec \times cm^2 \times sr}$. In the figures presented here *Orion* plots are for an x-ray energy hv of 700 eV (which is in the range of interest for opacity measurements).
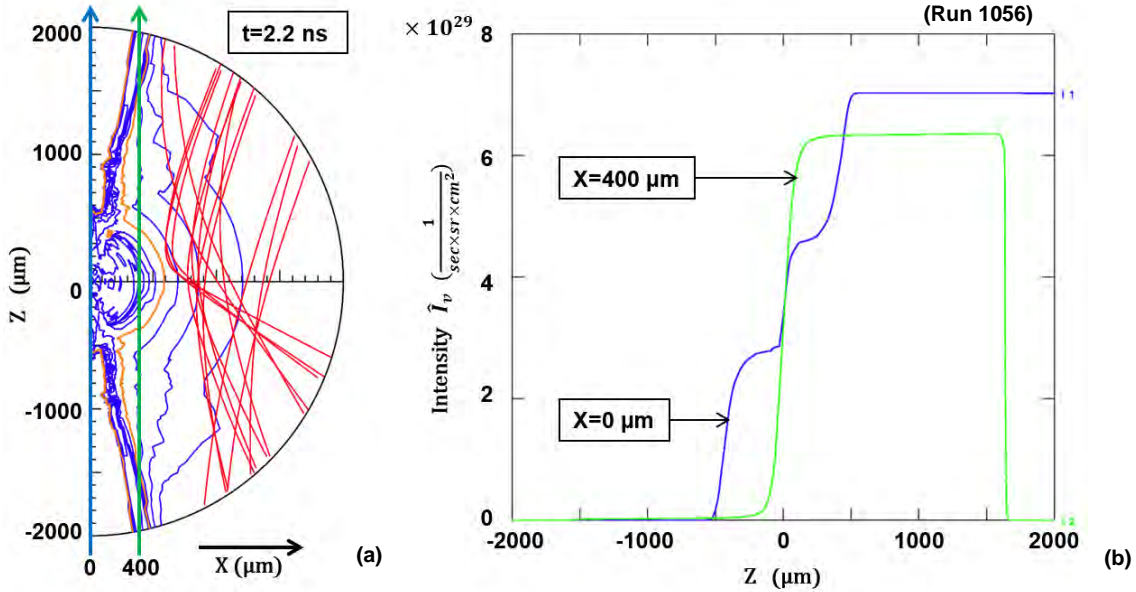
Figure 4.1: Density contour plot of an imploded target (a) and intensity lineouts produced by Orion at two radii (b). The paths of a ray through the center and one at a radius of 400 μm are shown in (a). Their respective intensities as a function of their z-position are plotted in (b). Note the sharp attenuation of the ray at a radius of 400 μm when it reaches the cone at z~1500 μm.

The first ray, indicated in blue, increases in intensity as it passes through the hot plasma and the compressed core of the target, a region extending from approximately z = -500 μm to 500 μm. The high temperature and density of this area cause the significant self-emission that is evidenced by the rise in spectral intensity in Fig. 4.1 (b). The second ray, indicated in green, also passes through a region of hot, compressed material, leading to a rise in intensity as it crosses the x axis; the green ray grows over a smaller range of z. Upon reaching the cone (z~1500 μm), the intensity is rapidly attenuated to virtually zero [Fig. 4.1 (b)]. This is caused by the high opacity and low temperature of the cone, which lead to low self-emission and high absorption.

The output intensity of x-ray emission can be spatially integrated at a given time over some circular region. Thus, the total emission at that time can be found, allowing the pulse duration to be determined. The space-integrated intensity is defined as

$$\int_{0}^{x_c} \hat{I}_v \cdot 2\pi x dx \tag{7}$$

where $\hat{I}_v$ is the spectral intensity as previously defined and x_c is the radius of the collimator (400 μm). Since the intensity is integrated over space, its units are $\frac{1}{sec \times sr}$.

A plot of space-integrated intensity versus time for the initial design is shown in Fig. 4.2. The effects of the hot plasma escaping into the cone [Fig. 3.4 (b)] are evident. The emission produced in the

initial design after peak compression, due to this hot plasma, far outstrips that produced during the actual implosion and causes an extended pulse. Note that the maximum is $3.8 \times 10^{26} \frac{1}{sec \times sr}$ or $61 \frac{GW}{keV \times sr}$.
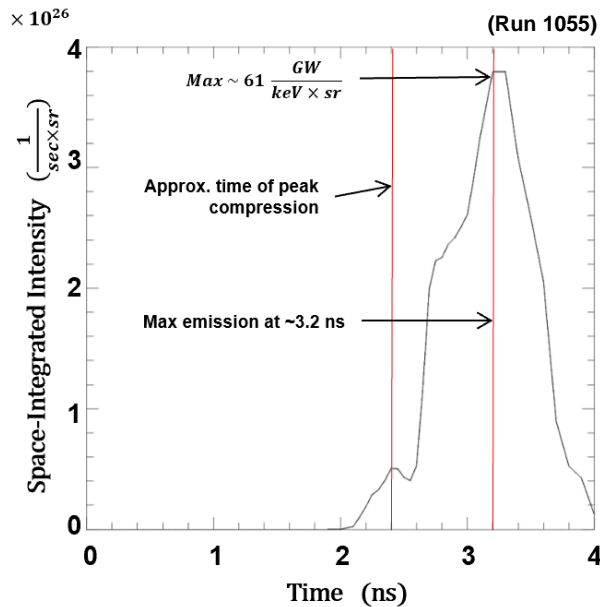

Figure 4.2: Plot of space-integrated intensity versus time for the initial design. Note that the maximum occurs long after the time of peak compression, significantly extending the duration of the pulse. This late-stage emission is caused by hot, emitting plasma that escaped into the cone (see Fig. 3.4)

  Orion was used to guide the development of subsequent designs, which aimed to eliminate this late-stage emission in order to shorten the x-ray pulse.

5. Optimized Design

5.1. Improving the Initial Design

  In the initial design, the inward movement of the cone was impeded by the expansion of hot compressed plasma. If the hot plasma had not flown out of the cone tip, the cone would have converged onto the vertical axis, thus preventing late-stage emission by sealing off the compressed material from view of the spectrometer. Later designs aimed to produce this convergence before imploded material could escape into the cone. *Orion* total emission (space-integrated intensity) plots against time were especially useful in diagnosing these designs, as they confirmed whether or not undesired emission was being blocked, depending on whether the target continued to emit after the implosion had occurred.
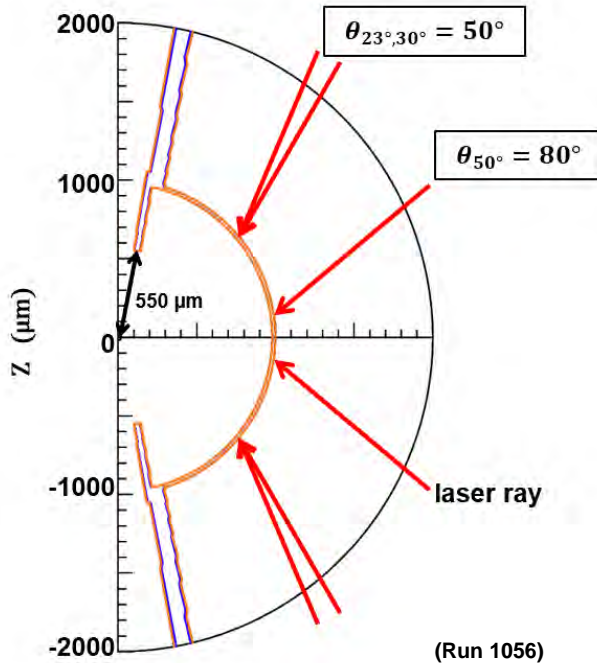
Figure 5.1: The parameters that were adjusted in order to optimize the cone-in-shell design [compare to Fig. 3.1 (a)].

Fig. 5.1 shows the optimized design and the key parameter changes from the initial design [Fig. 3.1 (a)]. The distance from cone tip to target center was increased from 350 μm to 550 μm and the theta pointings of the 23° and 30° beams were decreased from 60° to 50°. The pointings of the 50° beams were not adjusted in order to maintain sufficient drive at the equator. All beams remained in best focus.

It was found that capsules with a greater distance from cone tip to target center minimized the cone's obstruction of the implosion and extended the time it took for the hot plasma to flow to the cone tip, thus allowing the cone tip more time to converge onto the axis. Similarly, a decreas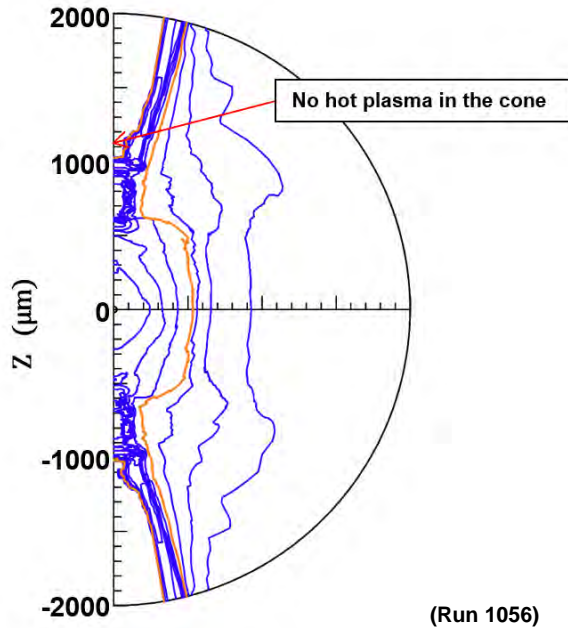ed repointing of the 23° and 30° beams increased the time it took for the equatorial material (which now received less drive) to reach the center and travel up and down the vertical axis, allowing the cone to converge onto the axis before the hot compressed material could escape. The repointing also increased the force driving the polar parts of the shell toward the target center. This inward force opposes the outward flow of compressed material from the cone tip, consequently producing the same effect.

Density contour plots of the new target (Fig. 5.2) showed no hot plasma in the cone after the implosion due to its earlier closing. The absence of contours below the critical density inside the cone, in contrast to the initial design in Fig. 3.4 (b), indicates clearly that no compressed material escaped into the cone. This suggests that no x-ray emission would be detected at this time.

Figure 5.2: Late stage (t=3 ns) density contour blowup for the new design. The optimized parameters have led the cone to converge onto the vertical axis.

Parts of the cone (indicated by the compact distribution of blue density contours close to the axis from z=600 μm to 1000 μm) appear open, but the tip itself and higher portions of the cone (at z~1000 μm) have converged onto the axis. While some hot plasma has escaped through the tip, it cannot emit through the cold and dense cone material at z~1000 μm. It is possible to ensure that the convergence occurs sooner by decreasing the radius of the tip, but this would also drastically limit the amount of x-ray emission.

One-dimensional lineouts of density, velocity, and temperature along the vertical axis of Fig. 5.2 at the corresponding time of 3 ns are shown for both the initial and optimized designs in Fig. 5.3. In the initial design [Fig. 5.3 (a)], there are a positive velocity and fairly high temperature that extend to z~2000 μm as well as a relatively high density beyond 1000 μm, suggesting the presence of a hot, expanding plasma as seen in Fig. 3.4 (b). In contrast, the optimized design [Fig. 5.3 (b)] has no significant plasma past z~1000 μm. This is consistent with the cone converging at z~1000 μm and stopping the expanding implosion material.

Together, the density contour plot and the one-dimensional lineouts suggest that the issue of hot plasma in the cone at late stages has been resolved in the optimized design.
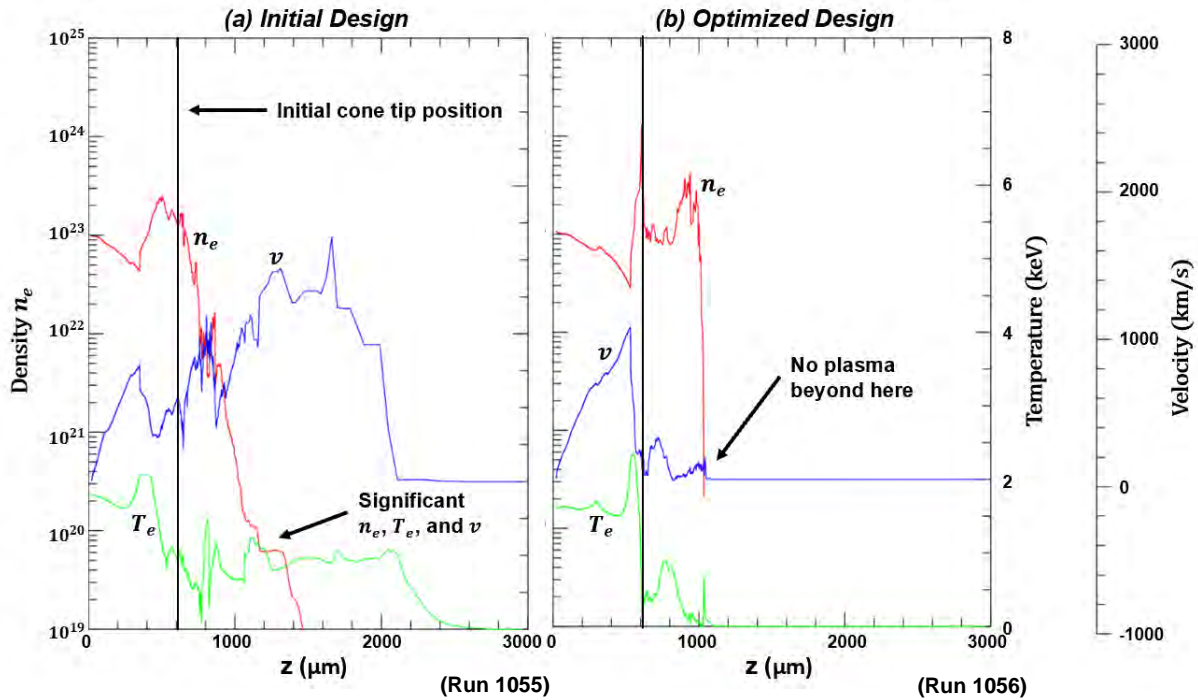
Figure 5.3: One-dimensional lineouts at t=3 ns along the z-axis for electron density (n_e, red), velocity (v, blue) and electron temperature (T_e, green) for the initial (a) and optimized (b) designs. The sharp drop off in density and temperature as well as the absence of a non-zero velocity past 1000 μm in (b) indicates the lack of an expanding, hot plasma inside of the cone, in contrast to the initial design (a).
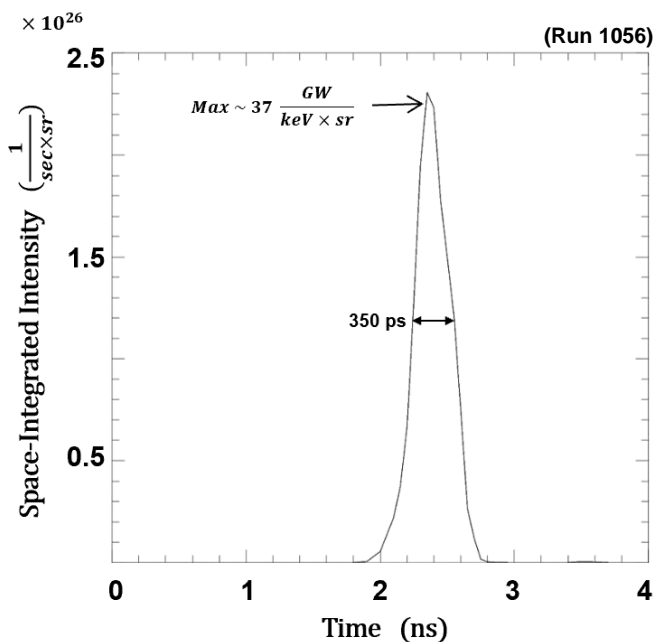

Figure 5.4: Plot of space-integrated intensity versus time for the optimized design. The optimized design produces a short, 350 ps pulse.

An *Orion* plot of space-integrated intensity versus time for the optimized design (Fig. 5.4) clearly shows how the elimination of late-stage hot plasma in the cone affects x-ray emission: a short, 350 ps x-ray pulse is achieved in the optimized design, contrasting the extended pulse in the initial design (Fig. 4.2). Fig. 5.4 highlights two key features of the optimized design: the lack of run-in emission prior to the implosion and the elimination of post-implosion emission. The first feature, which represents the original purpose of the cones, is also observable in the initial design, but the second is not. The post-implosion emission

that characterized the initial design (Fig. 4.2) is very noticeably not present in the optimized design, and indicates the success of the cone's convergence in sealing off x-ray emission. Together, these differences lead to a short-pulse source of x rays with no run-in emission, which is the primary purpose of the cone-in-shell design.

5.2. Comparisons to Conventional Backlighters

In order to better illustrate the advantages of a cone-in-shell backlighter, x-ray output calculations were also carried out for a conventional capsule lacking cones. This design had beam pointings that had been optimized by Y. Yang[12] in order to create a highly uniform implosion. As evidenced by the plot of spatial integral of intensity versus time in Fig. 5.5, the conventional capsule produces a longer pulse with significant run-in when compared to the cone-in-shell design (Fig. 5.4). The duration of the pulse is 600 ps, almost twice as long for the design lacking cones, and there is clearly late-stage emission that is present as late as 4 ns.

The cone-in-shell design produces far less emission overall: $37 \frac{GW}{keV \times sr}$ compared to $1362 \frac{GW}{keV \times sr}$ in the conventional design, suggesting that the conventional design produces 37 times more emission during the implosion than the cone-in-shell design. This is caused by two main factors. First, the cone-in-shell design produces virtually all of its detectable emission over a 100 μm radius due to the narrow cone tip. The cone tip cannot be enlarged, as this would hinder the cone's ability to converge on the axis in order to prevent late-stage emission. In contrast, the conventional design produces emission over the entire 400 μm radius of the collimator
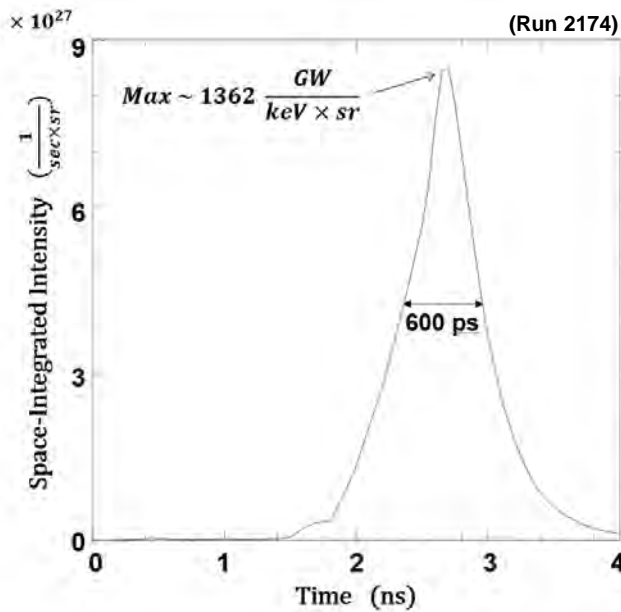
Figure 5.5: Plot of space-integrated intensity versus time for the design lacking cones. Note the extended duration of the pulse as compared to the optimized cone-in-shell design in Figure 5.4.

since there is no cone present to block the x rays.

The output intensities of x rays passing through the target can be temporally integrated to determine the total emission from different positions (x values) over some timespan, allowing the source size to be determined. The time-integrated intensity is defined as

$$\int_0^{t_{max}} \hat{I}_v \, dt \qquad (8)$$

where $\hat{I}_\nu$ is the spectral intensity as previously defined and t is time. The upper bound of the integral t_{max} is 4 ns in order to include emission before, during, and after the peak compression, all of which contribute to the spectrometer's measurements. Fig. 5.4 and Fig. 5.5 show that there is negligible emission at t_{max}. Since the integral is over time, its units are $\frac{1}{sr \times cm^2}$.
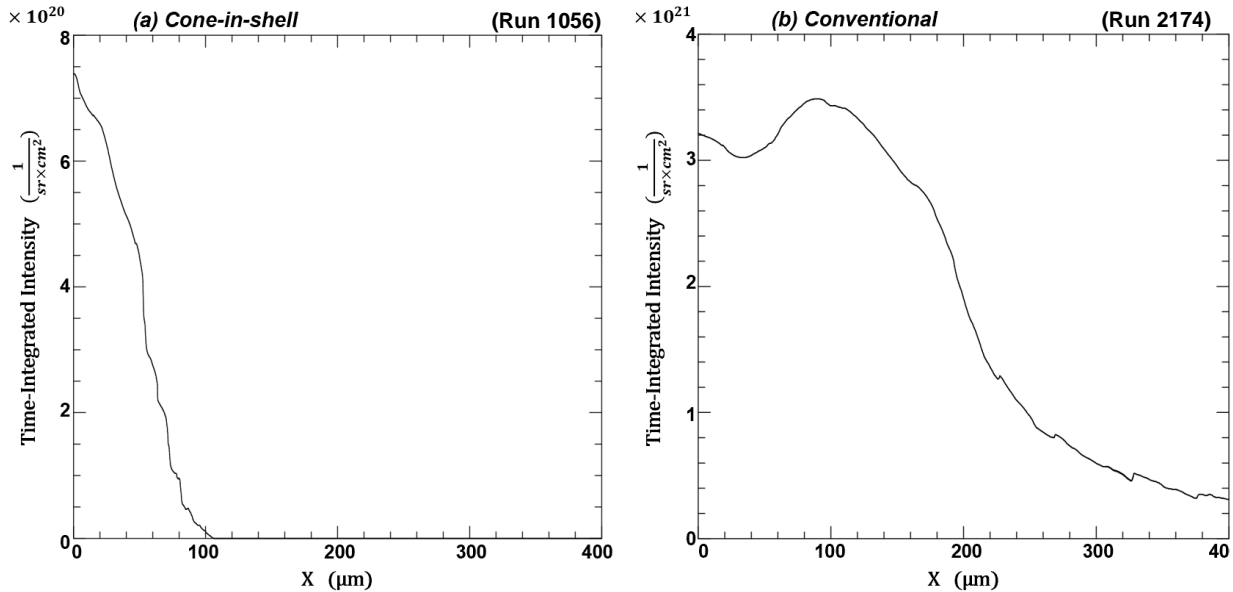

Figure 5.6: Plots of time-integrated intensity versus position for the cone-in-shell (a) and conventional (b) designs. Note the significantly wider radius from which emission is detected for the conventional design as compared to the cone-in-shell design.

Plots of the time-integrated intensities for the two designs, shown in Fig. 5.6, illustrate the difference in source size. The conventional design has a significantly larger radius from which emission is available. This four-fold increase in radius translates to a sixteen-fold increase in area, a factor that would be directly reflected when integrating over space to determine the total emission.

Second, it is not possible to achieve the same quality of implosion for a cone-in-shell design as there is no polar material to implode. This limits the densities and temperatures that can be reached at peak compression, further decreasing the x-ray output. The difference in quality of implosion can be observed by comparing the central emission from the two targets. In Fig. 5.6 (a), the central emission (at x=0) is $\sim 7.5 \times 10^{20} \; \frac{1}{sr \times cm^2}$, whereas in Fig. 5.6 (b), the emission at the same point is $\sim 3.2 \times 10^{21} \; \frac{1}{sr \times cm^2}$, a factor of 4.3 higher. This difference is much smaller than the factor of 16 that distinguishes the two areas of emission.

These two factors explain the majority of the difference in maximum x-ray emission seen in the plots of space-integrated intensity (Fig. 5.4 and Fig. 5.5). The cone-in-shell target can produce the desired short pulse of x rays, but at the cost of a reduced signal as compared to a conventional backlighter.

6. Conclusion

In this work, a double cone-in-shell backlighter was optimized using the 2D hydrodynamics code *SAGE* and the x-ray diagnostic code *Orion*, which was developed to aid in the prediction of emission from imploding targets. The capsule was optimized to produce a short, 350 ps pulse of x rays for the backlighting of Fe opacity experiments at the NIF. The design eliminates undesired run-in produced by current backlighters. The optimized convergence of the cone on the vertical axis following the implosion prevents contributions from emission produced after peak compression.

This design could allow for significantly improved opacity measurements, offering insight into the question of the solar radiative-convective transition radius. *Orion* is able to guide the further development of this backlighter on the NIF.

7. Acknowledgements

8. References

[1] R. F. Heeter et al., "Conceptual Design of Initial Opacity Experiments on the National Ignition Facility," J. Plasma Phys. **83**, 595830103 (2017).

[2] J. Nuckolls et al., "Laser Compression of Matter to Super-High Densities: Thermonuclear (CTR) Applications," Nature **239**, 139 (1972).

[3] R. S. Craxton et al., "Direct-Drive Inertial Confinement Fusion: A Review," Phys. Plasmas **22**, 110501 (2015).

[4] J. D. Lindl, "Development of the Indirect-Drive Approach to Inertial Confinement Fusion and the Target Basis for Ignition and Gain," Phys. Plasmas **2**, 3933 (1995).

[5] T. R. Boehly et al., "Initial Performance Results of the OMEGA Laser System," Opt. Commun. **133**, 495 (1997).

[6] S. Skupsky et al., "Polar Direct Drive on the National Ignition Facility," Phys. Plasmas **11**, 2763 (2004).

[7] A. M. Cok et al., "Polar-Driven Designs for Optimizing Neutron Yields on the National Ignition Facility," Phys. Plasmas **15**, 082705 (2008).

[8] Y. P. Opachich et al., "Capsule Implosions for Continuum X-ray Backlighting of Opacity Samples at the National Ignition Facility," Phys. Plasmas **24**, 063301 (2017).

[9] R. F. Heeter, Lawrence Livermore National Laboratory, private communication (2018).

[10] R. Kodama et al., "Fast Heating of Ultrahigh-Density Plasma as a Step Towards Laser Fusion Ignition," Nature **412**, 798 (2001).

[11] Ya. B. Zel'dovich and Yu. P. Raizer, "Physics of Shock Waves and High-Temperature Hydrodynamic Phenomena," Academic Press Inc. (1967).

[12] Y. Yang, Laboratory for Laser Energetics, private communication (2018).

Complex Ray Tracing and Cross-Beam Energy Transfer for Laser-Plasma Simulations

Alan Tu

Pittsford Sutherland High School

Pittsford, New York

Advisor: Dr. Adam Sefkow

Alan Tu

ABSTRACT

A ray-tracing code was developed that propagates laser beams by representing them as bundles of rays and then evolving the rays in time according to a set of differential equations. These equations account for the dispersion relation of the electromagnetic waves and the density profile of the background plasma. The energy deposited by the beams, as well as the beam intensities and electric fields, can be calculated and plotted onto a grid. Cross-beam energy transfer (CBET) occurs when laser beams overlap in a plasma and was implemented into the program for two interacting beams. This new program performs the CBET calculation faster than current programs in use. Furthermore, an alternative ray-tracing method was investigated, namely, complex ray tracing, which represents a laser beam with only five rays. The results are identical to those of the standard ray tracing but are achieved faster and can model additional effects such as diffraction and interference. In the future, this work will be implemented into the 3-D hybrid fluid-kinetic code *TriForce*.

Alan Tu

I.   INTRODUCTION

Current experiments being done on OMEGA involve shooting up to 60 laser beams at a

target in an attempt to achieve nuclear fusion. This method is called direct-drive inertial

confinement fusion (ICF).[1] The target is an ~l-mm-diam cryogenic capsule that contains a

mixture of deuterium and tritium fuel. The energy from the laser beam ablates the outer shell of

the capsule, causing the inner fuel to implode by Newton's third law; because of its extremely

high temperature and pressure, the ablating material becomes a very hot ionized gas known as

plasma.[1] Light propagation in plasma is quite complex since electromagnetic waves can interact

with the freely floating electrons of a plasma. Accordingly, many phenomena related to laser–

plasma interactions are not well understood.

Ray-tracing algorithms are important in designing and interpreting ICF experiments

because they can predict the quantity and location of energy deposited by the laser beam. Based

on these simulations, the optimal pointing of laser beams, as well as their respective intensities,

can be determined and tested. Ray-tracing models are currently used at the Laboratory for Laser

Energetics (LLE) in the hydrodynamic codes *LILAC* and *DRACO*. *LILAC* is a 1-D code that

assumes spherical symmetry and consequently cannot take nonuniformities into account.

DRACO is a 2-D code that assumes azimuthal symmetry and can model some types of

perturbations. Both *LILAC* and *DRACO* are fluid-based models, which means that particle

velocity distributions are assumed to follow a Maxwell–Boltzmann distribution at each point in

the plasma and can be described by a single temperature. Therefore, the fluid model does not

follow individual particles to determine the general behavior of the plasma.

TriForce is a 3-D hybrid fluid-kinetic code for ICF and high-energy-density physics

research. A pure kinetic model does follow individual particles and does not assume a form for

Alan Tu

the particle velocity distribution; therefore, it can more accurately model a plasma that is not in equilibrium (e.g., when a laser beam creates hot electrons and waves). In exchange for greater accuracy, however, kinetic models use more computation time. *TriForce* is a hybrid code in the sense that it uses kinetic algorithms where necessary and fluid algorithms everywhere else.

In this work, preliminary algorithms were developed for use in *TriForce*. These algorithms include a standard ray-tracing code, in which rays simply propagate through plasma; a cross-beam energy transfer code, which models the interaction of two laser beams in resonance with the plasma; and a complex ray-tracing code, which may be a powerful alternative to standard ray tracing because it includes extra physics while requiring fewer rays to model a laser beam.

II.   STANDARD RAY TRACING

Light acts as both a particle and a wave. The dispersion relation describes the relation between a wave's angular frequency and wavevector while traveling through a given medium. In this case, the medium is plasma, and the dispersion relation for high-frequency electromagnetic waves can be expressed as follows:[2]

$$\omega^2 = \omega_p^2 + c^2 k^2, \tag{1}$$

where ω is the wave frequency, c is the speed of light, k is the wave number, and ω_p is the plasma frequency defined by

4

Alan Tu

$$\omega_{\mathrm{p}} = \sqrt{\frac{n_{\mathrm{e}} e_{\mathrm{c}}^2}{m_{\mathrm{e}} \varepsilon_0}}, \qquad (2)$$

where n_{e} is the electron density, e_{c} is the elementary charge, m_{e} is the mass of an electron, and ε_0 is the permittivity of free space. The plasma frequency describes the rate of electron oscillations in the plasma.
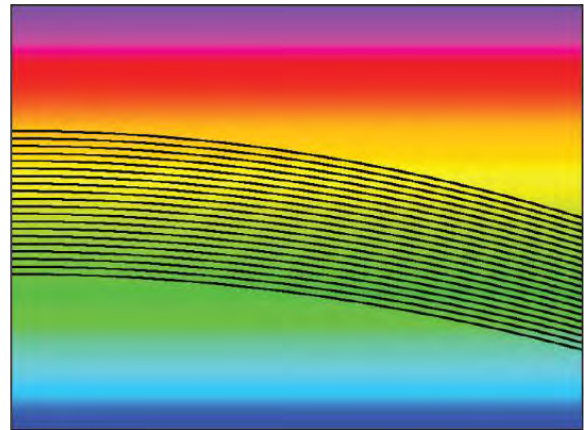
An electron density gradient in the plasma will cause a ray to refract toward a region of lower electron density. The critical density [see Eq. (6)] is the density at which the laser light frequency is equal to the plasma frequency; when this happens, the k value in the dispersion equation must equal zero. Therefore, a ray cannot freely propagate in a region with a density above the critical density.

TC14826J1

FIG. 1. A bundle of rays propagating through a plasma. Note that the rays refract toward a region of lower electron density (shown in blue). Fewer rays have been traced for clarity; for best results, hundreds or thousands of rays must be used.

In standard ray tracing, a laser beam is statistically represented by a finite bundle of rays, as shown in Fig. 1. Each ray is traced individually and propagates according to the following differential equations:[3]

$$\frac{d\mathbf{x}}{dt} = \mathbf{v}_{\mathrm{g}}, \qquad (3)$$

$$\frac{d\mathbf{v}_{\mathrm{g}}}{dt} = -\frac{c^2 \nabla n_{\mathrm{e}}}{2 n_{\mathrm{c}}}, \qquad (4)$$

Alan Tu

where $\mathbf{x}$ is the position vector, t is time, and $\mathbf{v}_g$ is the group velocity vector, defined by

$$\mathbf{v}_g = \frac{\partial \omega}{\partial \mathbf{k}} = \frac{c^2 \mathbf{k}}{\omega}, \tag{5}$$

where ω is the angular frequency, $\mathbf{k}$ is the wave number vector, and n_c is the critical density, defined by

$$n_c = \frac{\omega^2 m_e \varepsilon_0}{e_c^2}. \tag{6}$$

Note that, by Eq. (1), the phase velocity ω/k is greater than the speed of light. By Eq. (5), however, the group velocity, which is the rate at which energy propagates, is less than c.

Because these equations have no closed analytic solution for arbitrary electron density, one must numerically evolve each ray in time using small discrete steps, while updating the position and velocity vectors at each time step. An example of tracing ten rays is shown in Fig. 2. The smaller the time step, the more accurate the solution.
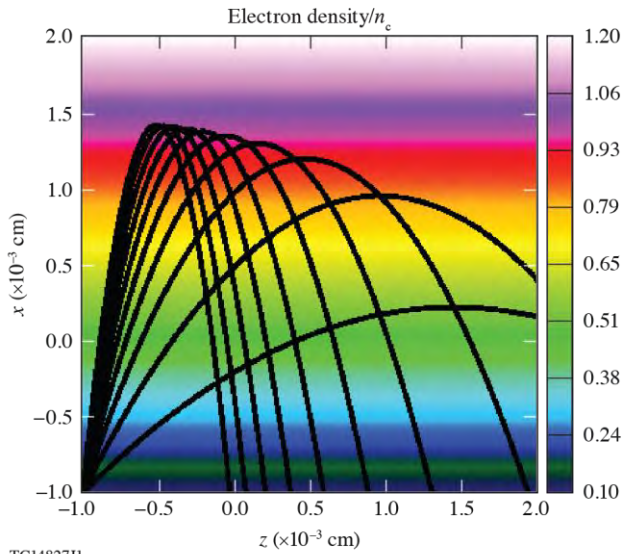

TC14827J1

FIG. 2. The numerical trajectories of ten rays traced in a plasma with a linear density gradient. Note that the rays turn at the critical density and follow parabolic paths, as expected by theory.

6

Alan Tu

As the rays travel through the plasma, they deposit energy in the plasma. The amount of energy deposited by a ray in an interval dt is given by the following relation:[4]
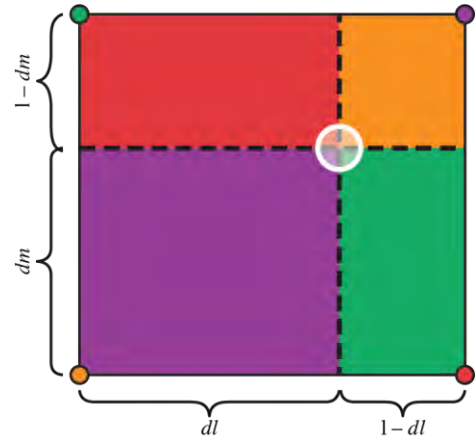
$$E_{dep} = \frac{v_{ei} n_e}{n_c} E_{inc} dt, \tag{7}$$

where E_{inc} is the energy of the ray incident on the interval, dt is the time step, and v_{ei} is the electron–ion collision rate given by

$$v_{ei} = \frac{n_e e^2}{m_e} \eta, \tag{8}$$

where η is the plasma resistivity.

We deposit energy using a first-order linear interpolation method, which is shown in Fig. 3. For each time step, we determine the location of the ray and find its nearest node. We calculate the distances dl and dm as shown in the figure, therefore dividing the cell into four quadrants. We split the energy deposited into the four surrounding cells based on the fractional area of each

TC14828J1

FIG. 3. First-order interpolation method for one grid cell.

quadrant. This is more effective than zeroth-order interpolation, the so-called nearest neighbor method, because a ray that barely passes through a cell will not deposit all of its energy in that cell.

7

Alan Tu

Figure 4 shows results from this ray-tracing code when applied to an OMEGA capsule electron density distribution, as calculated by *LILAC*. The plot in Fig. 4(a) is from the ray-tracing code developed in this project; the plot in Fig. 4(b) is from a different ray-tracing code in use at LLE that has already been validated. The density profiles are the same but represented with different color maps. The ray trajectories match very closely.
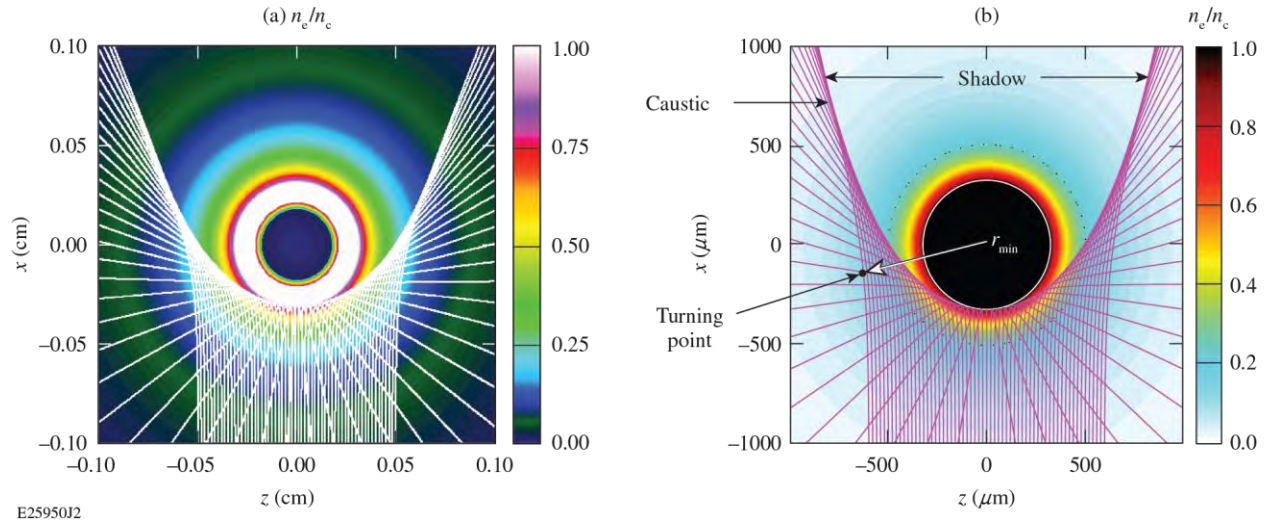

E25950J2

FIG. 4. (a) Results from the ray-tracing code developed in this work and (b) another ray-tracing code in use at LLE, both using an OMEGA capsule electron density profile. Notice the close similarities.

III.   CROSS-BEAM ENERGY TRANSFER

Figure 5 shows two laser beams overlapping without any mutual interaction or energy deposition in the plasma. The electric-field contours are expressed in terms of a_0, a dimensionless quantity defined by

$$a_0 = e_c E / (m_e c \omega), \tag{9}$$

8

Alan Tu

where E is the electric field. In this figure, the chosen width of the laser beam is arbitrary. To obtain the electric field on the grid, we let each ray carry electric field information, which is then "deposited" (using the first-order linear interpolation method shown in Fig. 3) in each cell along its trajectory.
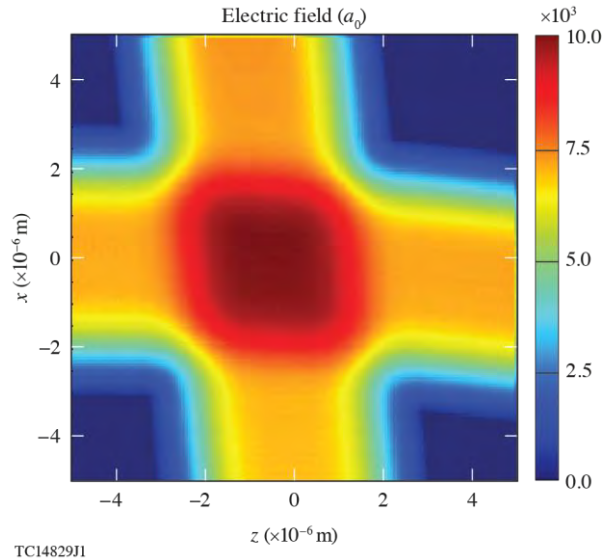

FIG. 5. Electric field of two intersecting laser beams that do not transfer energy between each other. One beam travels from bottom to top, and the other beam travels from left to right.

In reality, however, many complex effects occur when laser beams overlap with each other within a plasma. One of these effects is cross-beam energy transfer (CBET), which is driven by ion-acoustic waves, one of many collective modes that a plasma can exhibit. The plasma flow velocity causes a Doppler shift; therefore, two interacting beams will have slightly different frequencies relative to each other. Beat waves will result, and the acoustic waves will act as a grating to divert energy from one beam to another. Generally speaking, the beam traveling more "against" the bulk plasma flow will lose energy. In OMEGA implosions, the plasma flows radially outward and the rays are shot inward, so incoming rays will lose energy to outgoing rays, significantly decreasing energy deposition in the desired areas around the capsule. CBET may be responsible for up to a 50% decrease in hydrodynamic efficiency in OMEGA implosions.[5]

A simulation program was developed that models CBET for the simple case of two intersecting beams. To properly model CBET, a five-step process was used: (1) obtain electric fields at each point on the grid; (2) map the ray trajectories to the grid; (3) find all the

Alan Tu

interactions (i.e., where the rays intersect); (4) calculate the gain coefficients for the interactions; and (5) solve by iteration.

As mentioned, we have already determined the electric field on the grid. Now let us take a closer look at the following steps:

A. Mapping ray trajectories and finding interactions

The determination of ray intersections requires finding and saving the locations where individual rays cross the half-grid, as shown in Fig. 6, which has a reduced grid size of 10×10 for clarity.
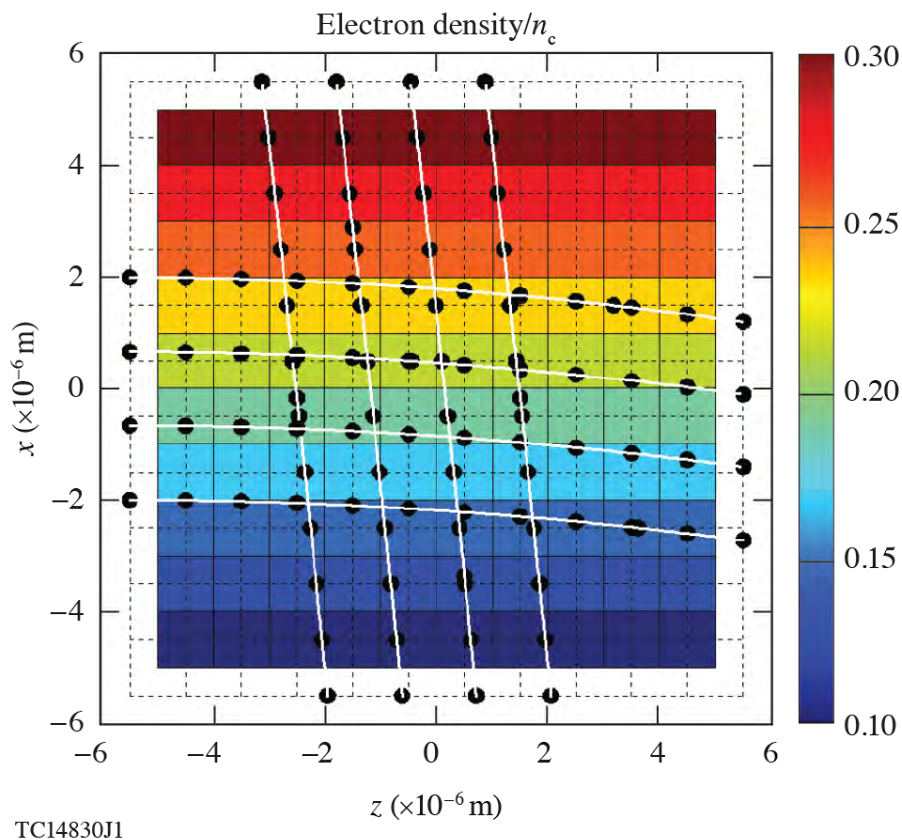

TC14830J1

FIG. 6. Keeping track of ray intersections with the grid. The solid lines define the normal grid, and the dashed lines define the half-grid. The half-grid has been used because it allows a node (the place where two normal grid lines intersect; also, where we store electric field and electron density information) to be at the center of each cell. The rays are the white lines and their intersections with the half-grid are the black dots.

10

Alan Tu

For each ray, we store an array of the ray's coordinates along its trajectory. At each time step, we check if the ray has crossed a grid line. For example, if there is a grid line at $x = 0.100$ cm and the ray's x coordinate changes from 0.098 to 0.101, then the ray would have crossed a grid line. We interpolate to find the coordinates of the crossing and save them as well; these coordinates will be used later in the calculation of energy transfer. A multidimensional array keeps track of the cells passed through by each ray.

Two rays are said to intersect if they both pass through the same grid cell, even if they do not physically intersect. For each intersection between rays from different beams, we calculate the amount of energy transfer, which is explained below.

B.   Calculating gain coefficients for interactions and updating energies

For each interaction, we calculate the gain coefficient from the following formula:[6]

$$\left(L_s^{ijkl}\right)^{-1} = \frac{e^2|E_{k0}|^2}{4m_ec\omega_{ij}k_BT_e\left(1+3T_i/ZT_e\right)}\frac{n_e}{n_c}\frac{\omega_s}{v_{ia}}P\left(\eta_{ijkl}\right), \tag{10}$$

$$P(\eta) = \frac{\left(v_{ia}/\omega_s\right)^2\eta}{\left(\eta^2-1\right)^2+\left(v_{ia}/\omega_s\right)^2\eta^2}, \tag{11}$$

$$\eta_{ijkl} = \frac{\omega_{kl}-\omega_{ij}-\left(k_{kl}-k_{ij}\right)\cdot u}{\omega_s}, \tag{12}$$

Alan Tu

where L_s^{ijkl} is the laser absorption length (ij refers to the ith ray at the jth location on its path, and

likewise for kl), e is the elementary charge, E_{k0} is the initial electric field of the pump ray, m_e is

the electron mass, c is the speed of light, ω_{ij} and ω_{kl} are the frequencies of the seed beam and the

pump beam, respectively, k_B is the Boltzmann constant, T_e is the electron temperature, T_i is the

ion temperature, Z is the ionization state, n_e is the electron density, n_c is the critical density, ν_{ia} is

the ion-acoustic wave energy damping rate, $\mathbf{k}_{ij}$ and $\mathbf{k}_{kl}$ are the seed and pump ray vectors,

respectively, $\mathbf{u}$ is the plasma flow velocity, and ω_s is the acoustic frequency given by

$$\omega_s = k_{iaw} \, c_s, \tag{13}$$

where c_s is the ion-acoustic wave speed given by

$$c_s = \sqrt{\frac{k_B (ZT_e + 3T_i)}{m_i}}, \tag{14}$$

where m_i is the ion mass, and

$$k_{iaw} = \left| \mathbf{k}_{kl} - \mathbf{k}_{ij} \right|. \tag{15}$$

We have access to the electric field value in the current cell because we saved it to the

grid at an earlier step. The vectors $\mathbf{k}_{ij}$ and $\mathbf{k}_{kl}$ can be deduced simply from the coordinates of

each ray's intersection with the two grid lines of the cell, as shown in Fig. 7.

Alan Tu

Finally, the energy transfer is determined by the following formula:[6]

$$W_{i,j+1} = W_{ij}\exp\left(\frac{s_{ij}W_{kl}}{L_s^{ijkl}\sqrt{\varepsilon}}\right),$$

(16)

where W_{ij} is the seed ray's energy (normalized to the incident energy) in the current cell, $W_{i,j+1}$ is the seed ray's energy in the next cell, s_{ij} is the distance traveled by the seed ray in the current cell, W_{kl} is the pump ray's energy in the current cell, L_s^{ijkl} is the gain coefficient for the interaction in the current cell, and $\varepsilon = 1 - n_e/n_c$.
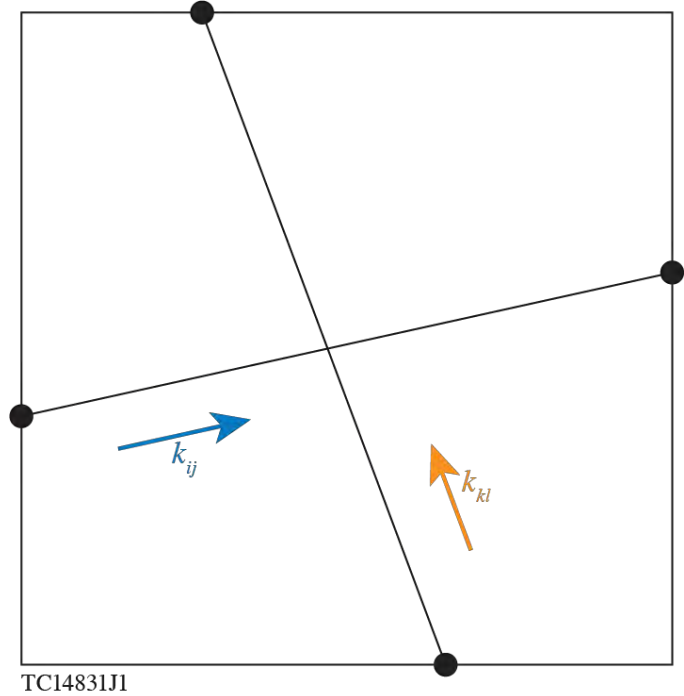

TC14831J1

FIG. 7. The $\mathbf{k}_{ij}$ and $\mathbf{k}_{kl}$ vectors. One grid cell is shown.

Once we determine the energy transfer for a single intersection, we must propagate the energy change to all downstream cells. After doing this for all possible ray intersections, we iterate the process if necessary, a step that is discussed in more detail below. In the case where a ray from one beam intersects multiple rays from another beam in a given cell, we calculate the energy transfer using the vector of only one of the crossing rays while using the total intensity of all the crossing rays.

13

Alan Tu

C.   Results

After writing this program, we compared our results to those from a CBET program

developed by R. K. Follett[6] that uses the same equations [Eqs. (10)–(12)] but different numerical

algorithms. The comparison is shown below in Fig. 8.

The ray-tracing code developed matches Follett's CBET results very closely; in addition,

the calculations are performed 10× faster. At higher intensities, however, our results differ

significantly from Follett's. This is most likely because we have not yet implemented the final

step in the CBET process which is solving by iteration. Each energy update affects CBET

interactions downstream, so it is critical that we calculate the interactions in the correct order that

would occur physically. This is not always possible, however, especially in more-complicated

cases, so we perform iteration; that is, we recalculate all the CBET interactions with our newly

modified values and repeat this until the change in values becomes very small. Essentially, we

get closer and closer to the true answer. Future work will implement iteration into this process.

IV.   COMPLEX RAY TRACING

Complex ray tracing, as described by Harvey *et al.*,[7] is a powerful alternative to standard

ray tracing. In complex ray tracing, a beam is represented by only five rays (in 2-D): a chief ray

(a.k.a., base ray), two waist rays, and two divergence rays, as shown in Fig. 9.

The electric field or intensity at any point can be calculated by finding the distance

between the point and three of the rays along a line perpendicular to the chief ray, as shown in

Fig. 10.[8] The method therefore assumes a functional relation between the rays themselves,

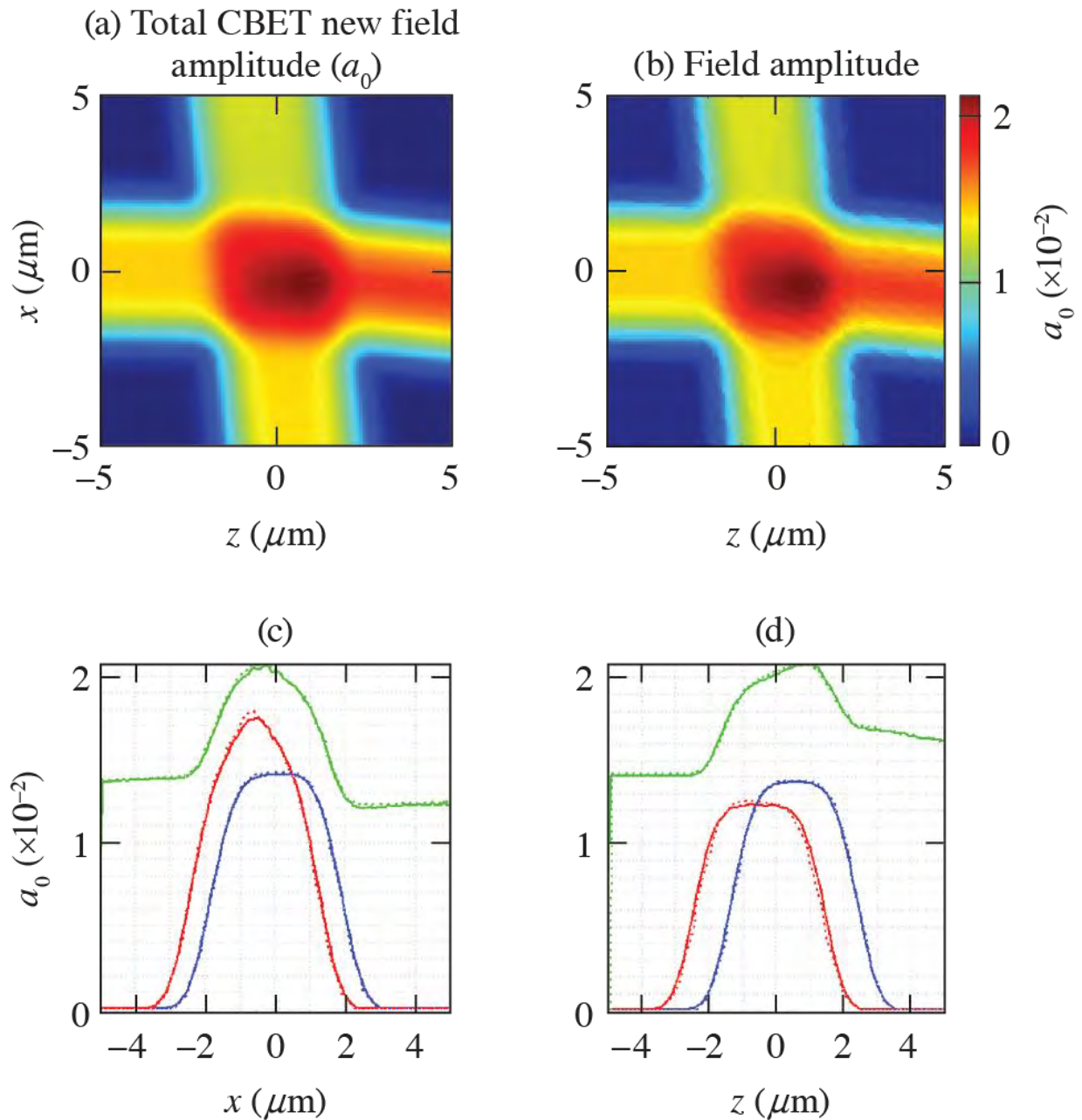whereas all rays are independent in standard ray tracing. To find the (normalized) electric field at

FIG. 8. [(a),(b)] Comparison of Follett's code with the developed code: (a) Our results and (b) Follett's results. Energy from the upward-traveling beam has been transferred to the rightward-traveling beam (cf., Fig. 5). [(c),(d)] Our results are shown as solid lines and Follett's results are shown as dotted lines. The blue, green, and red lines show the electric-field profiles taken at the minimum z (or x) value, midpoint value, and maximum value, respectively.
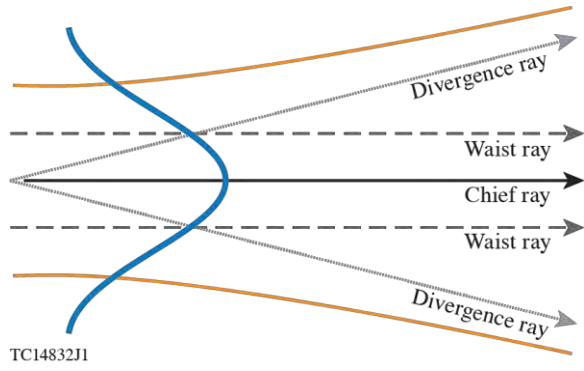
Alan Tu

FIG. 9. The rays needed for complex ray tracing. The solid blue line is the transverse profile of the beam intensity.
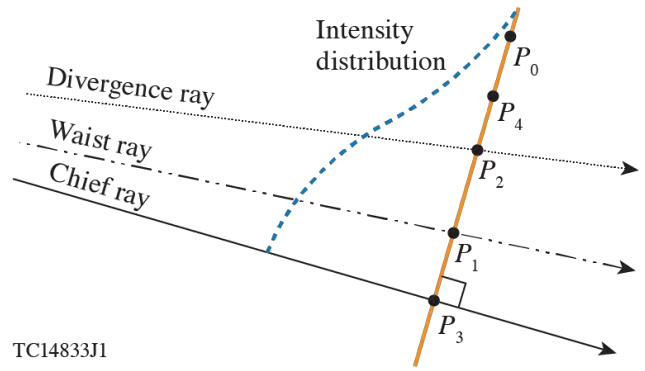
FIG. 10. Determining the intensity at an arbitrary point. Adapted from [8].

P_0, we simply calculate the distances from P_3 to P_0, P_1, and P_2 along the orange line (which we denote as p_0, p_1, and p_2, respectively) and then use the following formula:[8]

$$E(p_0) = \frac{w_0}{p_4} \exp\left[-\left(\frac{p_0}{p_4}\right)^2\right], \tag{17}$$

where

$$p_4 = \sqrt{p_1^2 + p_2^2}. \tag{18}$$

The intensity can then be calculated by squaring the electric field.

A.   Gaussian Beams in the Diffraction Limit

Consider the case where the power distribution of a laser can be described using the Gaussian function. Such a beam remains Gaussian throughout its path, and the Gaussian function

16

Alan Tu

solves the wave equation, making it an ideal candidate for modeling purposes. The transverse

profile of the intensity of a Gaussian beam can be described as follows, using r–z coordinate

axes:[7]

$$I(r,z) = \frac{2P}{\pi w^2(z)} \exp\left\{-2\left[\frac{r}{w(z)}\right]^2\right\}, \tag{19}$$

where

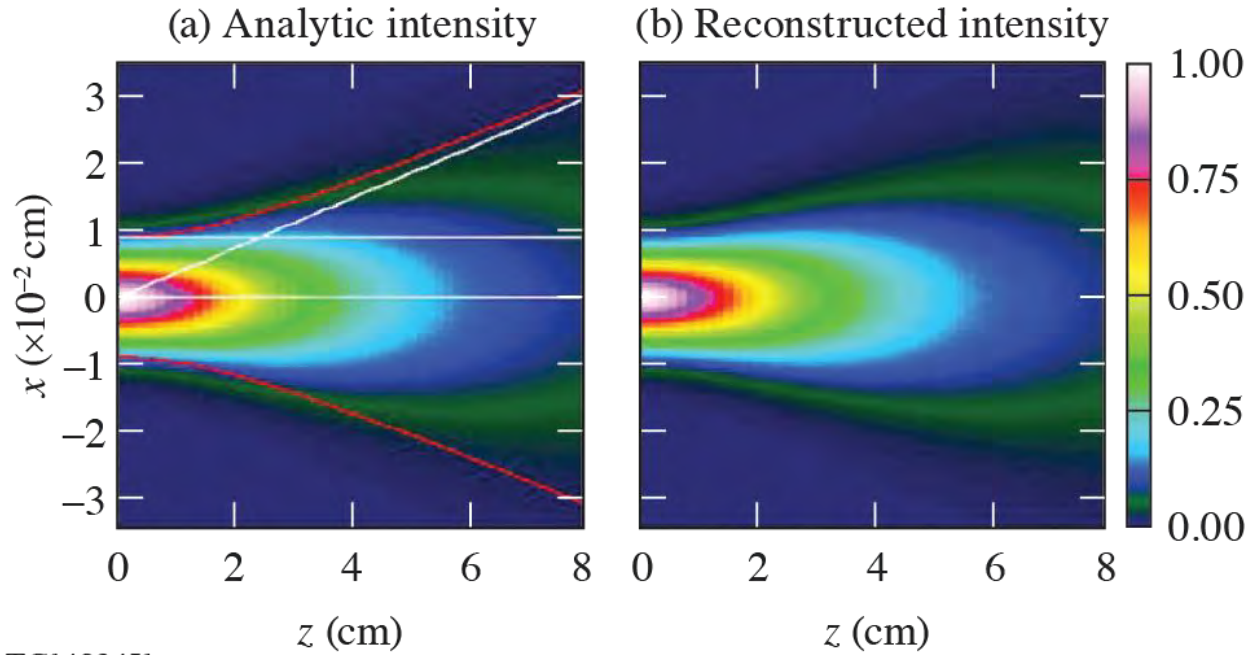$$p = \frac{\pi w_0^2}{2} I_0, \tag{20}$$

I_0 is the initial beam intensity and w_0 is the initial beam waist, and

$$w(z) = w_0\sqrt{1+(z/z_R)^2}, \tag{21}$$

where z_R is the Rayleigh range defined by

$$z_R = \frac{\pi w_0^2}{\lambda}. \tag{22}$$

The intensity function is plotted in Fig. 11(a).

FIG. 11. Analytic formula versus complex ray tracing for a diffraction-limited Gaussian beam in vacuum. The white lines are three of the complex rays (chief, waist, and divergence) and the red lines denote the beam waist.

To model a Gaussian beam via standard ray tracing, we must statistically weight the powers of each ray, with the rays closest to the center receiving the highest powers, in the case that the rays are spaced equally apart (however, standard ray tracing does not properly model the behavior near the focal plane, as it does not include diffraction). The power distribution is Gaussian and is given by the following, where x is the ray position relative to the beam center:

$$P = \exp\left\{ -\left[\left(\frac{x}{\sigma} \right)^2 \right]^{n/2} \right\}. \tag{23}$$

A standard Gaussian beam has $n = 2$, whereas the OMEGA laser uses $n = 4$ to 5, a super-Gaussian.

Alan Tu

Equations (17) and (18) were used to create a complex ray-tracing program. The test case of a Gaussian beam in vacuum is shown in Fig. 11; this plot was easy to create because all the perpendicular lines were vertical and lined up with the grid.

When a beam refracts (such as in plasma), however, or its propagation direction does not line up with the grid axes, then a different method must be used. Two methods were attempted, and the results are discussed below.

B.   Cell-by-Cell Approach

In this method of complex ray tracing, we trace all five rays at the beginning and then go cell by cell along the trajectories to calculate the intensity for all the cells. To do this, we must trace the perpendiculars from each cell (P_0) to the chief ray so that we may determine distances along this perpendicular. Figure 12 shows the perpendiculars drawn in red. Note that in this figure, P_0 is taken to be at the corner of each cell, rather than the
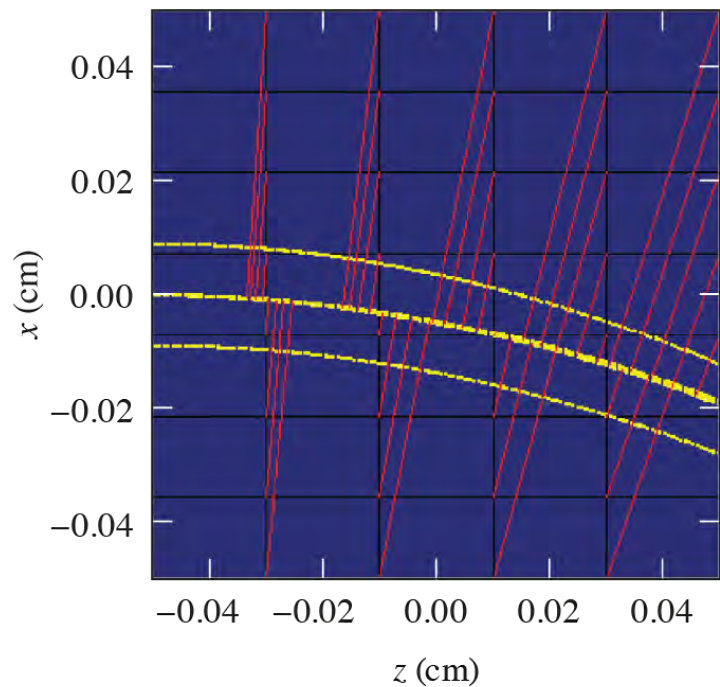
TC14835J1

FIG. 12. Perpendicular lines (shown in red) drawn from each cell to the chief ray. The yellow lines show the five complex rays; at this scale, the chief ray and divergent rays are extremely close together. The colors of the density profile have been removed for clarity.

center; as the number of cells increases, this discrepancy is negligible.

The following method is used to find the perpendiculars. Our first task is to determine the point on the chief ray P_3 that defines the perpendicular line. To do this, we move along the time

Alan Tu

steps of the chief ray and for each point P on the chief ray's trajectory, we calculate the chief

ray's directional vector $\mathbf{k}$ as well as the vector connecting P_0 to P. We take the dot product of

these two vectors and save it to compare with the next point P. Two vectors are perpendicular if

their dot product is zero; since the two vectors in question are never truly perpendicular, we wish

to find the P that makes them closest to perpendicular; that is, the P that produces a dot product

closest to zero. We stop the search when the dot product changes from negative to positive or

vice versa (i.e., "crosses" zero) and then choose the one with the smaller absolute value.

While this method is very accurate, it is very slow when the number of cells becomes

large. In addition, it requires us to move along each of the rays for each cell calculation. To fix

these issues, we chose a new approach.

C.   Update Outward Along the Chief Ray

This improved algorithm starts by tracing the waist and divergence rays; then, while the

chief ray is traced, we update the intensities outward from the chief ray and use the energy

deposition method again to "deposit" intensity. For each point on the chief ray, we find the

equation of the line perpendicular to the chief ray's $\mathbf{k}$ vector and determine where it intersects the

waist and divergence rays. To do this, we find the waist/divergence ray's $\mathbf{k}$ vector at each time,

thereby creating another linear equation (the equation of the line tangent to the ray's trajectory),

which we solve in tandem with the equation of the line perpendicular to the chief ray. If the

solution to this system of equations is located on the waist/divergence ray, we have found the

correct point of intersection and simply determine its distance from the chief ray. To speed up

the process, we start with the point at the same time step as the current chief ray's time step and

then move outward.

Alan Tu

Once the distances p_1 and p_2 are determined, we return to the chief ray and move outward along the perpendicular line. At each point, we calculate the intensity using Eq. (17), and then deposit that intensity using the energy deposition algorithm from above. Therefore, each cell may receive multiple intensity contributions which are summed at the end. For the case of a Gaussian beam refracting in plasma, as shown in Fig. 13, this method worked quickly and accurately. It ran 4× faster than the standard ray-tracing method and produced a smoother plot, which is also important for simulation accuracy. If we were to make a comparison based on the quality of the solution, we would have to use many more rays in the standard case, so the difference in speed would be even greater.

With these tools in hand, we attempted to reproduce a famous interference pattern in order to demonstrate the advanced capability of complex ray tracing.
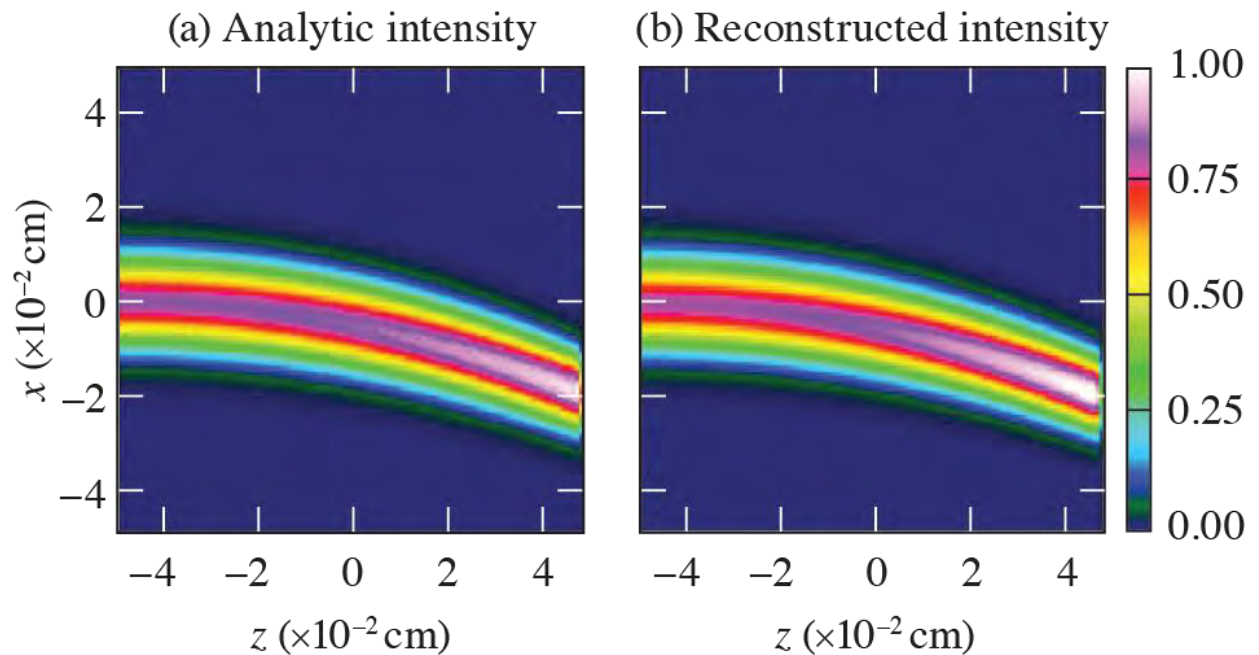
TC14836J1

FIG. 13. (a) Standard ray tracing versus (b) complex ray tracing.

Alan Tu

D.   The Double-Slit Experiment

In 1801, Thomas Young performed the first double-slit experiment, in which he passed light through two small apertures, producing interference patterns on the viewing board. This showed that light has both particle and wave characteristics. Standard ray tracing cannot reproduce this phenomenon because it does not account for the wave nature of light and therefore does not include its phase.

With complex ray tracing, it is possible to include the phase of a laser beam by adding a phase term to Eq. (17):[2]

$$E(P_0) = \frac{w_0}{p_4} \exp\left[-\left(\frac{p_0}{p_4}\right)^2\right] \cos(-kz),$$

(24)

where

$$k = \frac{2\pi}{\lambda}.$$

(25)

We modeled Young's experiment by shooting two point sources spaced a small distance apart. Each point source was composed of 17 complex "beamlets," each of which was shot in a different direction to span a given angle. We time-averaged the intensities over a period to obtain an accurate cycle-averaged plot, shown in Fig. 14.
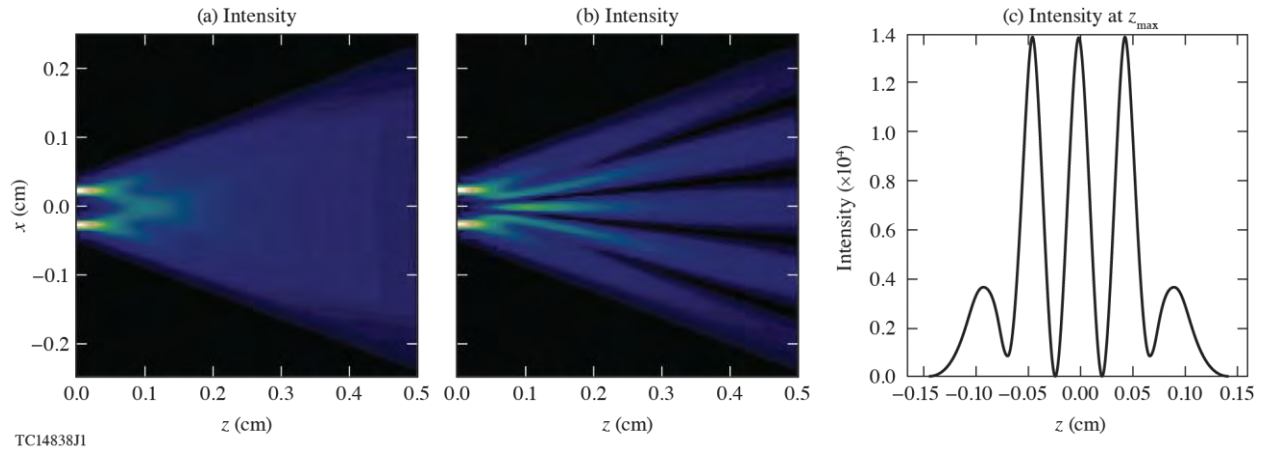
Alan Tu

FIG. 14. Interference pattern for Young's double-slit experiment with complex ray tracing. (a) The point sources contain no phase information; therefore, there is no interference. (b) The inclusion of phase information makes the interference clearly visible. (c) The intensity profile taken at the maximum z value. The beam waist is 0.025 cm and the wavelength is 0.01 cm.

V.   CONCLUSION

In this work, several programs were developed for implementation into the 3-D hybrid-fluid kinetic code *TriForce*. These programs include a standard ray-tracing program that traces bundles of rays to represent beams and can determine energy deposition, intensity, and electric field; a CBET feature that accurately models energy transfer between two beams in plasma; and a complex ray-tracing program that can perform the same tasks as standard ray tracing (but faster) as well as model interference. Attention was paid to speed and efficiency in the algorithms since they must run in *TriForce* without slowing it down. *TriForce* will be used in the future to design and interpret ICF experiments and other high-energy-density physics research experiments.

Alan Tu

ACKNOWLEDGMENTS

Alan Tu

REFERENCES

1.   R. S. Craxton, K. S. Anderson, T. R. Boehly, V. N. Goncharov, D. R. Harding, J. P. Knauer, R. L. McCrory, P. W. McKenty, D. D. Meyerhofer, J. F. Myatt, A. J. Schmitt, J. D. Sethian, R. W. Short, S. Skupsky, W. Theobald, W. L. Kruer, K. Tanaka, R. Betti, T. J. B. Collins, J. A. Delettrez, S. X. Hu, J. A. Marozas, A. V. Maximov, D. T. Michel, P. B. Radha, S. P. Regan, T. C. Sangster, W. Seka, A. A. Solodov, J. M. Soures, C. Stoeckl, and J. D. Zuegel, Phys. Plasmas **22**, 110501 (2015).

2.   E. R. Tracy, A. J. Brizard, A. S. Richardson, and A. N. Kaufman, *Ray Tracing and Beyond: Phase Space Methods in Plasma Wave Theory* (Cambridge University Press, Cambridge, England, 2014).

3.   T. B. Kaiser, Phys. Rev. E **61**, 895 (2000).

4.   F. F. Chen, *Introduction to Plasma Physics and Controlled Fusion*, 3rd ed. (Springer International Publishing, Cham, Switzerland, 2016).

5.   J. F. Myatt, R. K. Follett, J. G. Shaw, D. H. Edgell, D. H. Froula, I. V. Igumenshchev, and V. N. Goncharov, Phys. Plasmas **24**, 056308 (2017).

6.   R. K. Follett, J. G. Shaw, J. F. Myatt, V. N. Goncharov, D. H. Edgell, D. H. Froula, and J. P. Palastro, Phys. Rev. E **98**, 043202 (2018).

7.   J. E. Harvey, R. G. Irvin, and R. N. Pfisterer, Opt. Eng. **54**, 035105 (2015).

8.   H. Yu, G. Rossi, A. Braglia, and G. Perrone, Appl. Opt. **55**, 6530 (2016).